

https://dspace.org/

Micro-to macro-structural investigations of faulting in deep South African gold mines

Mngadi, Siyanda B

2021
https://hdl.handle.net/10539/33157

Downloaded from a DSpace repository. https://dspace.org/

UNIVERSITY OF THE
WITWATERSRAND,
JOHANNESBURG

Micro- to macro-structural investigations of faulting in deep South African gold mines

A Dissertation submitted to the Faculty of Science, University of the Witwatersrand, Johannesburg, in fulfilment of the requirements for the degree of Doctor of Philosophy.

Siyanda B. Mngadi

335401

PhD Thesis

July 2021

Supervision: Professor Musa S.D. Manzi and Professor Raymond J. Durrheim

School of Geosciences

The University of the Witwatersrand

Declaration

I declare that this dissertation is my own work. This dissertation is submitted at the University of the Witwatersrand, Johannesburg to be examined for the fulfilment of the degree of Doctor of Philosophy in Geophysics. It has not been submitted before for any degree or examination in any other University.

Siyanda Mngadi:

Day of **02 August 2021**, at the **University of the Witwatersrand, Johannesburg**.



_____

Abstract

Deep and high stress South African gold and platinum mines (1000 m – 4000 m) are important for sustainable economic development. These mines are critical for foreign currency earnings, creating employment, alleviation of poverty and reducing inequality. However, deep level mining operations are subject to seismicity, falls of ground (FOG) and rockbursts, which pose a risk to the safety of mineworkers, infrastructure and people living in mining regions. On the other hand, deep mines offer a unique and cost-effective opportunity to examine the physics and mechanics of earthquake processes at some seismogenic depths. A reliable scientific method has been developed in the last decade, to drill into 'active faults' at seismogenic depths. Analysis of the core has shown that it is possible to resolve fundamental seismological questions in earthquake and faulting processes. This study is part of the international collaboration under the International Continental Scientific Drilling Programme (ICDP) Drilling into Seismogenic zones project (DSeis). As the continuation of the Science And Technology Research Partnership for Sustainable development (SATREPS) project, a 5-year Japanese – South African collaborative project named "Observational studies in South African mines to mitigate seismic risks", drilled into seismogenic zones in several deep South African gold mines. The ICDP-DSeis project identified three active seismogenic zones: (a) the Moab Khotsong mine M_L 5.5 earthquake; (b) the Savuka mine M 3.5 earthquake; and, (c) the Cooke 4 mine M 1-2 earthquakes. The PhD research focused on two seismogenic zones: Cooke 4 mine and Moab Khotsong mine. At Cooke 4 mine, the research examined seismicity associated with the extraction of a highly-stressed 1-km-deep shaft pillar intersected by large normal faults. At Moab Khotsong mine, the research focused on the largest mining-related earthquake M_L 5.5 that occurred below the mining levels. The M_L 5.5 fault had an uncommon left lateral strike-slip mechanism.

Specific to this PhD thesis, the micro (microns – millimetres) to macro (metres – kilometres) mechanics and physics of mining-induced and mining-related earthquakes in deep and highly stress Witwatersrand Basin gold mines was examined. The study endeavoured to answer open seismological questions such as: (1) What influences fracture patterns and geometry, both in space and in time?; (2) What is the role of geology?; (3) How do earthquakes propagate along shear zones?; and (4) How do earthquakes scale (i.e., fracturing dependency on scale)? Answering these fundamental seismological questions will help to mitigate the risks posed by seismicity, falls of ground and rockbursts.

Systematic and detailed comprehension of fracture patterns forming in the hangingwall and ahead of the stope face will assist miners recommend tailor-made support systems that will prevent the falls of ground in stopes. In addition, understanding rupture propagation and the influence of gouge will help mining practitioners appreciate the origin of unstable rupture propagation and factors controlling the severity of seismicity and rockbursts in deep mines. This will assist in the development of early warning systems and evacuation plans.

The thesis is based on the total of five manuscripts: two manuscripts were published in peer-reviewed international journals, while three manuscripts have still to be submitted to journals. The first manuscript describes the development of fractures ahead of the stope in both space and time. An integrated fracture model obtained from underground mapping, petrographic analysis using thin sections, rock mechanics and high-resolution microseismic analysis at Cooke 4 mine is presented. Underground mapping and petrographic analysis reveal that the shaft pillar is largely comprised of quartzites, pebbly quartzites, argillaceous quartzites and conglomerates, which are characterised by different uniaxial compressive strengths (UCS), with quartzite being the strongest. In addition, underground mapping reveals that the shaft pillar is characterised by several minor to macro-scale discontinuity sets. Microseismic data revealed the formation of shear fractures ahead of the mining excavation (van Aswegen (2013) referred to as ‘Ortlepp shears'), and that the shear fracture 'turning-point' occurs in the soft strata (weak hangingwall lavas). The integration of these datasets enabled the development of the fracture model for different geotechnical zones (i.e., weak/soft lava hangingwall and quartzite/conglomerate footwall). This fracture model has significant safety implications.

The second manuscript, examines how earthquakes propagate along these fractures occurring ahead of the stope, and what controls rupture propagation. The ICDP-DSeis team drilled into this seismogenic zone, and successfully recovered fragile ruptures, fault rocks and fault gouge material using a specialised triple-tube core barrel. Several dynamic friction-experiments were performed under room-dry conditions, some with gouge recovered from deep drilling, and others without fault gouge particles. These experiments were conducted from low to high slip velocities (~1.0 mm/s to 1200 mm/s). The experiments reveal a difference in the dynamic friction weakening behaviour (e.g., the 'no fault gouge' rock-on-rock experiments show a sudden reduction in fault strength at a significantly lower slip velocity than the specimens with the gouge material). The study shows that the presence of the fault gouge and its formation during rupture propagation controls fault rupture propagation processes along

underground brittle shear fractures (i.e., the presence of the fault gouge causes a fault to temporarily strengthen at lower slip velocities). These results of friction experiments have implications for the severity of rockbursts.

The third manuscript, examines the architecture, physics and mechanics of the unusual M_L 5.5 strike-slip earthquake that occurred below the Moab Khotsong mine. This is compared to the shear fractures with the common normal-slip displacement that occur ahead of the stope at Cooke 4 mine. In a serendipitous circumstance, the M_L 5.5 earthquake occurred within an area mapped by the 2-D reflection seismic data acquired by Anglo Gold Ashanti in 1992 for gold exploration. This legacy data was re-processed using modern techniques and re-interpreted to make clear the architecture of geological structures that hosted the M_L 5.5 earthquake. Similar to Cooke 4 mine, seismicity was recorded by underground seismic sensors near the source region. This enabled the DSeis team to spatially delineate the M_L 5.5 earthquake rupture, and drilled into this active seismogenic zone with its upper edge at a depth of 3.5 km. The DSeis team successfully drilled and recovered the fragile core, host rocks, rock breccia, sampled hypersaline brine, dolerite sills and a lamprophyre dyke. The fault rupture zone was characterised by the lamprophyre dyke, sandy fault gouge material and a core-loss zone. Interestingly, the re-processed and re-interpreted legacy 2-D reflection seismic data revealed that the geological structure that hosted the M_L 5.5 earthquake crosscut the Transvaal Supergroup strata, and potentially the base of the Karoo Basin. In addition, the legacy 2-D reflection seismic data revealed several dolerite sills characterised by high seismic amplitude reflections, while seismic attribute analysis was able to image vertical structures such as faults and/or dykes. The integration of the reflection seismic data and mine seismicity data, including the DSeis drill core (geological core logging) and geophysical borehole logging (gamma, density and velocity), allowed a full description to make clear a near-vertical structure, striking NNW-SSE. The relatively younger and highly-altered lamprophyre dyke intruded into this existing fault and older dolerite dykes. The fault was reactivated as a left-lateral strike-slip fault.

The X-ray diffraction (XRD) analysis and measurements of the particle size distribution of the fault gouge material were conducted. The fault gouge consists predominantly of talc and biotite minerals (> 40%) and the particle size approach a minimum of ~ 10 µm. The abundance of talc and biotite minerals may control the friction weakening mechanism, acting as a lubricant during rupture propagation. The study conducted friction experiments on the Moab Khotsong sandy fault gouge

sample at a slip velocity of ~100 mm/s and normal stress of 2 MPa. These experiments revealed that the peak friction coefficient of ~1.0 decreased exponentially to steady-state friction of ~0.66 over a slip weakening distance of ~9.1 m. The friction weakening behaviour and steady-state friction values are comparable with results obtained from normal faults occurring ahead of the mining stope at Cooke 4 mine at similar slip velocity and normal stress.

The investigation shows that there may be three active processes that influence the M_L 5.5 earthquake seismogenic zone: (a) the architecture of the fault zone (e.g., intersection of lamprophyre dyke and dolerite sills); (b) the mechanical process induced by tectonic and/or mining-related stresses; and (c) the chemical processes caused by hypersaline fluids. This is different from Cooke 4 mine normal faults that are largely controlled by the mechanical processes induced by mining-related stress.

The fourth manuscript, will be developed to a paper at a later stage. The Cooke 4 shear fractures induced by mining activities are compared to shear ruptures induced by triaxial laboratory experiments conducted up to 20 MPa confining stress, similar to underground conditions at Cooke 4 mine. The experiments and underground observations showed clear similarities - characterised by rough rupture surfaces and fault gouge material. The energy required to create a new fracture surface was computed and found that very little energy (0.15% and 0.56% of the total energy budget) was consumed during the creation of a new fracture. This was found to be in the same order of magnitude as the seismic efficiency.

The fifth draft manuscript (see Appendix) discussed and developed new criteria that could be used to identify shear ruptures in drill core. The primary focus was on El Teniente mine and the Cooke 4 mine drill cores.

Keywords: Mining-induced normal faults, brittle shear fractures, high-resolution microseismicity, fracture model, seismic source, rupture propagation, frictional sliding and low to high-velocity friction experiments.

Dedication

"Without mining and agriculture, the world as we know it cannot survive. In fact, agriculture's productivity is doubled through the products that mining produces. So, we believe that if mining is not the most important industry on the face of the planet, it's right up there with the top two or three," Mr. Mark Cutifani.

Dedicated to family, friends, and the people of Lamontville.

Acknowledgements

I would like to express my sincere appreciation and gratitude to my supervisors Prof. Raymond Durrheim and Prof. Musa Manzi for their academic and financial support throughout the study. The DSeis Project team Prof. Hiroshi Ogasawara and Prof. Yasou Yabe for guidance, advice and support. I also like to thank Prof. Akito Tsutsumi, Dr. Gerrie van Aswegen, Dr. Neta Wechsler, Dr. Martin Ziegler and Dr. Thomas Wiersberg for their technical support and experience. Special thanks goes to Mr. Tony Ward, Mr. Sylvester Morema and Mr. Bennie Liebenberg.

I would also like to thank my late mother Mbali Joyful Mngadi-Gumede, beautiful daughter Simphiwe Mngadi and my supportive and lovely wife Siyabulela Manengele. I thank, my amazing grandmothers - Ntombizonke Mngadi and Khuluza Shandu, supportive and caring aunt Nokulunga Mngadi-Bulose, her husband Ezra Bulose, mother in law Thuletu Manengele and my father Nkanyiso Malinga. I thank my siblings Slungile Mngadi, Sinenhlanhla Olwethu Mngadi, Manqoba Gumede and Ayabonga Gumede. My family – Noluthando Ntshangase, Wonder Ntshangase, Khanyo Shandu, Zeh Shandu, Vale Shandu, Nelly Shandu, Mdu Mchunu, Siphiwe Mngadi and Qiniso Shabalala for love, encouragement and unwavering support.

I would like to thank my supportive colleagues – Akimasa Ishida, Hiroyuki Ogasawara, Shunye Kaneki, Noda Taku, Kosuke Sugimura, Zamo Nkosi and Onyebueke Emmanuel Onyebuchi. My great and wonderful friends - Sihle Mkhize, Phelelani Mpanza, Sthembele Moloi, Bonga Myeza, Rhandzu Ngobeni, Sikhanyiso Dlamini, Khulekani Nkwanyane, Mthandeni Ntuli, Mzwakhe Mbili, Mvuyisi Ndaba, Mbongeni Hlubi, Siyanda Khumalo, Bongani Khoza and Sitchaba Khumalo. My mentors Mr. Mosa Mabuza, Mr. Mike Teke, Mr. Ndaba Ntsele, Mr. Lesiba Mothata and Mrs. Tryphosa Ramano.

Thanks also goes out to the technicians from the various laboratories who helped me with sample preparation and conducting the various analyses, Mr. Caiphus Majola and Mr. Andrew Carpede. Sincere thanks must go to the ICDP-DSeis project team members, JSPS Core-to-Core Program, JSPS - NRF Bilateral Research Program. Sibanye Stillwater gold limited is acknowledged for providing permission to publish the results. The authors thank the School of Geosciences, University of the Witwatersrand, Department of Geology and Mineralogy, Kyoto University, CIMERA, Council for Geosciences and the CSIR Centre for Mining Innovation, for the use of their resources and facilities. RJD acknowledges the support of the South African Research Chairs Initiative of the Department of Science and Technology and National Research Foundation.

List of Papers

The following papers have been published during the course of the PhD research programme, or are in preparation for submission:

1. Mngadi, S.B., Durrheim, R.J., Manzi, M.S.D., Ogasawara, H., Yabe, Y., Yilmaz, H. Wechsler, N., van Aswegen, G., Roberts, D., Ward, A.K., Naoi, M., Moriya, H., Nakatani, M., Ishida, A., SATREPS Team and ICDP DSeis Team. (2019). Integration of underground mapping, petrology, and high-resolution microseismicity analysis to characterise weak geotechnical zones in deep South African gold mines*. International Journal of Rock Mechanics and Mining Sciences*, 114, 79–91.
2. Mngadi, S.B., Tsutsumi, A., Manzi, M.S.D., Onoe, Y., Durrheim, R.J., Yabe, Y., Ogasawara, H., Kaneki, S., Wechsler, N., Ward, A., Naoi, M., Moriya H., Nakatani, M. and the DSeis team. (2020). Effect of gouge generation on rupture propagation along underground brittle shear fractures. *International Journal of Rock Mechanics and Mining Sciences, 137, 104454.* doi.org/10.1016/j.ijrmms.2020.104454.
3. Mngadi, S.B., Manzi, M.S.D., Nkosi, N.Z., Durrheim, R.J., Ogasawara, Jr. H., Noda, T., Ogasawara, H., Yasou, Y. and DSeis team. (In preparation). Making clear the dolerite sills, strike-slip fault and lamprophyre dyke hosting the M_L 5.5 earthquake with related complexities of factors controlling the physics and mechanics.
4. Mngadi, S.B. Wechsler, N., Manzi, M.S.D., Durrheim, R.J., Yabe, Y., Ogasawara, H., Kaneki, S., Ward, A., Tsutsumi, A., Onoe, Y., Naoi, M., Moriya H., Nakatani, M. and the DSeis team. (In preparation). Particle-size distribution and energy budget of the mining-induced shear fractures in Deep South African gold mines.
5. van Aswegen, G., Mngadi, S., Padilla, R. and Stonestreet, P. (In preparation). Detecting mining induced seismic sources in borehole core.

Conference contributions during my PhD research comprise:

1. Abe, S., Yabe, Y., Ishida, A., Funato, A., Ito, T., Kato, H., Yilmaz, H., Durrheim, R.J., Mngadi, S.B., Hofmann, H. and Ogasawara, H. (2018). Stress States in the Source Regions of M2-3 Earthquakes Estimated by the DSeis Drilling in South African Deep Gold Mines. *15th Annual*

*Meeting of the Asia Oceania Geosciences Societ*y (AOGS), 03 - 08 June 2018, Honolulu, Hawaii.

2. Durrheim, R.J., Ogasawara, H., Nakatani, M., Yabe, Y., Naoi, M., Moriya, H., Cichowicz, A., Satoh, T., Hironori, K.H., Milev, A., Kgarume, T., Brink, V.Z., Ward, A.K., Ribeiro, L., Manzi, M.S.D., Mngadi, S.B. and SATREPS. (2017). Observational Studies in South African Mines to Mitigate Seismic Risks: Challenges and Achievements. In: Proceedings of the *AfriRock International Symposium.* 3-5 October 2017, Cape Town; South Africa.
3. Ishida, A., Sugimura, K., Liebenberg, B., Rickenbacher, M., Mngadi, S.B., Kato, H., Abe, S., Yabe, Y., Noda, T., Funato, A., Ito, T., Nakatani, M., Ward, A.K., Durrheim, R.J. and Ogasawara, H. (2018). Stress measurement using cores of drilling into seismogenic zone of M2.0-M5.5 earthquakes in South African gold mines (ICDP DSeis project). *Japan Geosciences Union Meeting*, 20-24 May 2018, Chiba, Japan.
4. Mngadi, S.B., Durrheim, R.J., Yilmaz, H., Musa, M.S.D., Kgarume, T., Kuijpers, J., Ward, A., Roberts, D., Naoi, M., Ogaswara, H. snr., Ishida, A. and SATREPS. (2017). Integrated petrographic, geomechanical and seismological studies of rockmass behaviour during the final phase of ore extraction at Cooke 4 shaft in South Africa*. Joint Scientific Assembly of the International Association of Geodesy and international Association of Seismology and Physics of the Earth's Interior* (IAG-IASPEI), 30 July – 4 August 2017, Kobe, Japan.
5. Mngadi, S.B., Durrheim, R.J., Yilmaz, H., Manzi, M.S.D., Kgarume, T., Kuijpers, J., Ward, T., Roberts, D., Naoi, M., Moriya, H., Ogasawara H. snr., Ishida, A. and SATREPS. (2017). An integrated approach to understanding different geotechnical zones using high resolution microseismicity in underground mines. *South African Geophysical Association's (SAGA) 15th Biennial Conference & Exhibition*, 10 – 13 September 2017, Cape Town, South Africa.
6. Mngadi, S.B., Durrheim, R.J., Yilmaz, H., Manzi, M.S.D., Kgarume, T., Kuijpers, J., Ward, T., Roberts, D., Naoi, M., Moriya, H., Ogasawara H. snr., Ishida, A. and SATREPS. (2017). An integrated approach to understanding different geotechnical zones using high resolution microseismicity in underground mines. *DST-NRF CIMERA & UJ PPM Colloquia*, 24 - 26 October 2017. Held at the University of Johannesburg, Auckland Park Campus.
7. Mngadi, S.B., Durrheim, R.J. and Manzi, M.S.D. (2017). Integrated Petrographic, Geomechanical and Seismological studies of rockmass behaviour at Cooke 4 mine, South

Africa. *The Wits Cross-Faculty Mine Health & Safety Research Group (WMHSRG) 1st Seminar*, 22 February 2017, Held at Johannesburg, South African.

8. Mngadi, S.B. (2018). Fracture energy estimation from grain size distribution generated from simulated fractures. *NRF-JSPS DSeis workshop: ICDP-DSeis Scientific Drilling & Rock Physics*, 27 June 2018. University of the Witwatersrand Johannesburg, South Africa & Tshimologong Digital Innovation Precinct.
9. Mngadi, S.B., Durrheim, R.J., Yilmaz, H., Manzi, M.S.D., Kgarume, T., Kuijpers, J., Ward, T., Roberts, D., Naoi, M., Moriya, H., Ogasawara, Snr. H., Ishida, A., and SATREPS. (2018). An integrated approach to understanding different geotechnical zones using high resolution microseismicity in deep underground mines, South Africa. *American Association of Petroleum Geologists (AAPG)*, 20 - 23 May 2018, Salt Lake City, Utah.
10. Mngadi, S.B. (2019). Update of my research work in relation to DSeis drilling project. *DSeis Workshop during AGU: ICDP-DSeis Scientific Drilling & Rock Physics* on Thursday, 12 December 2019, Parc 55 Hilton hotel, San Francisco, California.
11. Mngadi, S.B., Manzi, M.S.D., Durrheim, R.J., Tsutsumi, A., Yabe, Y., Ogasawara, H., Onoe, Y., Kaneki, S., Wechsler, N., Nakatani, M., Naoi, M., Moriya H. and the DSeis Team. (2019). The effect of gouge formation on fault propagation along underground brittle shear fractures. *AGU Fall Meeting*, 9 – 13 December 2019, San Francisco, California.
12. Mngadi. S.B. (2019). Effect of gouge generation on rupture propagation along underground brittle shear fractures. *DSI-NRF CIMERA annual colloquium*, 7- 8 November 2019, Johannesburg, South Africa.
13. Mngadi. S.B. (2019). Predicting rupture propagation along underground brittle shear fractures. *The 14th Annual Africa Array workshop*. 7-12 July 2019. Johannesburg, South Africa.
14. Ogasawara, H., Liebenberg, B., Yabe, Y., Yokoyama, Y., Hirono, T., Nisson, D.M., Onstott, T.C., Kieft, T.L., Esta van Heerden, Wiersberg, T., Noda, T., Manzi, M.S.D. Mngadi, S.B. Durrheim, R.J., Yamamaoto, Y., Ito, T., Funato, A., Ziegler, M., Mori, J.J., Carsten, D. and The ICDP DSeis team. (2020a). The seismogenic zones of an M2.0-5.5 earthquakes successfully recovered in deep South African gold mines: the outcomes and the follow-up plan. *EGU General Assembly 2020*. 4–8 May 2020, Online.

15. Ogasawara, H., Noda, T., Manzi, M.S.D., Durrheim, R.J., Yabe, Y., Hirono, T., Yuhji Yamamoto, Y., Matsuzaki, T., Higashi, M., Yoshida, S., Yokoyama, Y., Suzuki, K., Ligaraba, D., Masondo, N., Nkosi, Z., Mngadi, S.B., Liebenberg, B Esta van Heerden. (2020b). ICDP DSeis: an altered lamprophyre dike identified at the M5.5 seismogenic zone by the analyses of the 3D reflection data and drilled core at Kochi Core Center. 12-15 July 2020, Online.

16. Ogasawara, H., Liebenberg, B., Rickenbacher, M., Ziegler, M., van Esterhuizen, H., Onstott, T.C., Durrheim, R.J., Manzi, M.S.D., Mngadi, S.B., Yabe, Y., Ogasawara, H., Kaneki, S., Cason, E., Vermeuren, J-G., van Heerden, E., Wiersberg, T., Zimmer, M., Kujawa, C., Conze, R., van Aswegen, G., Wechsler, N., Ward, A.K., Enslin, S., Tau, S. and Bucibo, M.S. (2019). 2019 status report: Drilling into seismogenic zones of M2.0–M5.5 earthquakes in South African gold mines (DSeis project), in W Joughin (ed.), Proceedings of the *Ninth International Conference on Deep and High Stress Mining,* The Southern African Institute of Mining and Metallurgy, Johannesburg, 375-384.

17. Ogasawara, Sr. H., Yabe, Y., Onstott, T.C., Liebenberg, B., Rickenbacher, M., Ishida, A., Abe, S., Sugimura, K., Ito, T., Funato, A., Mngadi, S.B., Ogasawara, Jr. H., Manzi, M.S.D., Yasutomi, T., Noda, T., Durrheim, R.J., Ziegler, M., Wechsler, N., Van Aswegen, G., Ward, A.K., Bucibo, S., Nkosi, Z.N., Roberts, D. and the DSeis team. (2018). Near-completion of ICDP drilling into M2.0 – M5.5 seismogenic zones in South African gold mines (DSeis). *Japan Geosciences Union Meeting*, 20-24 May 2018, Chiba, Japan.

18. Ogasawara, H. snr, Durrheim, R.J., Yabe, Y., Ito, T., van Aswegen, G., Grobbelaar, M., Funato, A., Ishida, A., Ogasawara, H,, Mngadi, S.B., Manzi, M.S.D., Ziegler, M., Ward, Tony., Moyer, P., Boettcher, M., Ellsworth, B., Liebenberg, B., Wechsler, N., Onstott, T., Berset, N., and the DSeis team. (2017a). Initial report on drilling into seismogenic zones of M2.0 – M5.5 earthquakes from deep South African gold mines (DSeis). *European Geosciences Union General Assembly*, 23–28 April 2017, Vienna, Austria.

19. Ogasawara, H., Durrheim, R.J., Yabe, Y., Ito, T., van Aswegen, G., Grobbelaar, M., Funato, A., Ishida, A., Ogasawara, Jr. H., Mngadi, S.B., Manzi, M.S.D., Ziegler, M., Ward, A.K., Hofmann, G., Moyer, P., Boettcher, M., Dight, P., Ellsworth, W., Liebenberg, B., Wechsler, N., Onstott, T., Berset, N. and the DSeis Team. (2017b). Drilling into seismogenic zones of M2.0 – M5.5 earthquakes from deep South African gold mines (DSeis): establishment of research sites. In:

Proceedings of the *AfriRock International Symposium*. 30 September–6 October 2017, Cape Town, South Africa.

20. Wechsler, N., van Aswegen, G., Yabe, Y., Mngadi, S.B., Kamhaji, L., Ward, A., Morema, S., Durrheim, R.J., Ogasawara, H. and ICDP DSeis team. (2017). Recovery of ruptures from seismogenic zones at Cooke 4 mine (ICDP scientific drilling project in the South-African gold mines). *European Geosciences Union General Assembly*, 8-13 April 2017, Vienna, Austria.
21. Yabe, Y., Kanematu, M., Higashi, M., Tadokoro, R., Yoshida, S., Sugimura, K., Ogasawara, H., Ito, T., Funato, A., Ziegler, M., Liebenberg, B., Watson, B., Mngadi, S.B., Manzi, M.S.D. and Durrheim, R.J. (2020). Stress state in the upper margin of the aftershock zone of the 2014 Orkney earthquake (M5.5), South Africa, estimated from analyses of drill cores and borehole breakouts of ICDP-DSeis drillings. *EGU General Assembly 2020*. 4–8 May 2020, Online.
22. Yabe, Y., Abe, S., Ito, T., Ishida, A., Sugimura, K., Kanematsu, M., Higashi, M., Tadokoro, R., Ogasawara, H., Funato, A., Kato, H., Watson, B., Mngadi, S.B., Durrheim, R.J., Hofmann, G. and Scheepers, L. (2019). In-situ stress around source faults of seismic events in and beneath South African deep gold mines, in W Joughin (ed.), Proceedings of the *Ninth International Conference on Deep and High Stress Mining*. The Southern African Institute of Mining and Metallurgy, Johannesburg, pp. 399-411, https://doi.org/10.36487/ACG_rep/1952_30_Yabe.
23. Ziegler, M., Rickenbacher, M., Berset, N., Liebenberg, B., Ishida, A., Sugimura, K., Noda, T., Ogasawara, H., Mngadi, S.B., Durrheim, R.J., Ito, T., Funato, A. and the ICDP DSeis team. (2018). Logging of core and borehole and stress measurements of a 817 m long hole drilled from 2.9 km depth toward the Moab Khotsong 2014 M5.5 aftershock zone (ICDP DSeis project in South Africa). *European Geophysical Union Assembly*, 9-13 April 2018, Vienna, Austria.
24. Ziegler, M., Rickenbacher, M., Berset, N., Liebenberg, B., Ishida, A., Sugimura, K., Noda, T., Ogasawara, H., Mngadi, S.B., Durrheim, R.J., Ito, T., Funato, A., and the ICDP DSeis team. (2017). Logging and stress measurements of a 817 m long borehole drilled from 2.9 km depth toward the Moab Khotsong 2014 M5.5 aftershock zone (ICDP DSeis project in South Africa). *European Geosciences Union General Assembly*, 8-13 April 2017, Vienna, Austria.

Training and workshops:

1. Funato, A. and Ito, T. (2019). DCDA stress measurements. NRF-JSPS DSeis workshop: ICDP-DSeis Scientific Drilling & Rock Physics - DCDA stress measurements, 21 August 2019, CSIR Nelson Mandela Mining Precinct, Johannesburg, South Africa.
2. ICDP Training Course on Continental Scientific Drilling. (2018). This training course covered relevant aspects for managing a scientific drilling project, including: Proposal Writing & Multi-Source Fundraising; Drilling Workflow & Terminologies; Health, Safety and Environment; On-Site Management; Sample Handling and Curation; Downhole Logging Planning and Execution; Data Management; Outreach. 15-17 May 2018, GeoZentrum KTB, Germany.
3. DSeis team. (2018). How core is archived and sample cores. JSPS-NRF and JSPS Core-to-Core joint seminar and meeting: ICDP-DSeis Drilling & Sampling. 6 - 7 September 2018, CSIR Mandela Mining Precinct, Johannesburg.

Table of Contents

Declaration i

Abstract ii

Dedication vi

Acknowledgements vii

List of Papers viii

Table of Contents xiv

List of Figures xvi

List of Tables xviii

Abbreviations xix

1. Introduction 1

2. Research objectives 2

2.1. Microscale (microns – millimetres) 2

2.2. Mesoscale (millimetres – metres) 3

2.3. Macroscale (metres – kilometres) 3

3. Background: Mining, Rockbursts and Seismicity in South Africa 3

3.1. Seismicity 7

3.2. Reflection seismic 9

4. Witwatersrand Basin 9

5. Basic descriptions and methods 12

5.1. Mining-induced shear fractures 12

5.2. Fault gouge 14

5.3. Methodology 15

5.3.1. Mine seismicity data 17

5.3.2. Triple-tube drilling 20

5.3.3. Petrography and geophysical borehole logging 20

5.3.4. Identifying mining-induced shear ruptures in ‘triple-tube’ drill core 21

5.3.5. Frictional sliding experiments 22

5.3.6. Particle size distribution analysis 23

5.3.7. Slip friction experiments 24

5.3.8. Petrophysical properties 27

5.3.9. Reflection seismic method 29
6. Summary of manuscripts 33
6.1. Geometry of brittle shear fractures occurring ahead of tabular mining stopes 33
6.2. Dynamic rupture propagation of brittle shear fractures 34
6.3. Factors controlling the physics and mechanics of M5.5 rupture 35
6.4. The energy budget of the mining-induced brittle shear fractures 37
6.5. Detecting mining induced seismic sources in borehole core. 38
7. Geometry of brittle shear fractures occurring ahead of tabular mining stopes 40
8. Dynamic rupture propagation of brittle shear fractures 74
9. Factors controlling the physics and mechanics of M5.5 rupture 122
10. The energy budget of the mining-induced brittle shear fractures 180
11. Discussion 244
12. Conclusion and Future work 255
12.1. Conclusion 255
12.2. Future work 257
13. The ICDP DSeis team 259
14. References 260
15. Appendix 275
15.1. Detecting mining-induced seismic ruptures in borehole core 275

List of Figures

Figure 1: Geographical location of selected active mines in South Africa that include platinum, manganese, chrome, vanadium and gold (modified from Vorster, 2003). 4

Figure 2: The study areas are located in Western Areas (6) and Klerksdorp Goldfields (8) at Cooke 4 mine and Moab Khotsong mine in the Witwatersrand Basin (modified from Dankert and Heim, 2010; Nkosi, 2016). The location of Greefswald farm, site of the capital of the pre-colonial gold-trading Kingom of Mapungubwe, is shown in the inset. 5

Figure 3: This is the general stratigraphy of the Witwatersrand Supergroup, showing Central Rand and West Rand Groups (modified from Robb and Meyer, 1995; Dankert and Heim, 2010). 11

Figure 4: The 2-D vertical geometry of the shear fractures occurring ahead of the mining excavations 'Ortlepp shears', which are often associated with large seismic events (Mw 1-4) (modified from Adams et al., 1981). 13

Figure 5. Multidisciplinary approach used in this PhD thesis - geology, geochemistry, geomechanics and geophysics. Specific methods used include: X-ray powder diffraction (XRD), X-ray fluorescence (XRF), Energy Dispersive X-Ray Spectroscopy (EDS) and scanning electron microscopy (SEM). 16

Figure 6. The remnant shaft pillar that was investigated at Cooke 4 mine is situated at 1000 - 1200 m depth; shows extensively mined out areas vs unmined areas. This also shows the borehole configurations drilled by SATREPS team. These boreholes were used to install acoustic emission sensors and accelerometers to monitor and delineate shear fractures occurring ahead of the stope. The DSeis project borehole location, stope face, and the location of shear fractures associated with the stope face are shown. 18

Figure 7. The top view of microseismicity data spatial distribution related to active stopes is shown. b) Perpendicular view of microseismic data spatial distribution showing steeply dipping planar seismic clusters. c) Lithological, geophysical and shear rupture logs. 19

Figure 8. Moab Khotsong mine a) Location of recorded seismicity. DSeis drilling plan (in red) is shown and in mine geophones. b) The aftershock data delineated the rupture plane generated by M5.5 earthquake. The location of drilled Hole A and Hole B are shown (Ogasawara et al., 2019). 19

Figure 9. Graphic representation of the experimental set-up of two friction experiments: (a) with the fault gouge, and (b) without the fault gouge 'rock-on-rock'. Friction experiments were conducted on the

sample using a rotary-shear apparatus at low, Intermediate to high-velocities similar to Ujiie and Tsutsumi (2010). 25

List of Tables

Table 1. Multidisciplinary approach to scientific drilling. 15

Abbreviations

ICDP	International Continental Scientific Drilling Programme
DSEIS	ICDP-DSeis project, “Drilling into seismogenic zones of M2.0 to M5.5 earthquakes in South African gold mines”.
JSPS	Japan Society for the Promotion of Science
NRF	National Research Foundation
CIMERA	Centre of Excellence for Integrated Mineral and Energy Resource Analysis
CSIR	Council for Scientific and Industrial Research
JICA	Japan International Cooperation Agency
JST	Japan Science and Technology Agency
SATREPS	Science and Technology Research Partnership for Sustainable Development
PGM	Platinum Group Metals
FOG	Fall of Ground

1. Introduction

The research presented in this thesis examines the micro to macro characteristics of mining-induced and mining-related faulting in deep and high stress South African gold mines. The study addresses the following issues: (a) the spatial and temporal evolution of shear fractures forming ahead of the stope face; (b) the role of geology in controlling shear fractures; and (c) earthquake propagation along brittle shear zones. The thesis consists of 11 chapters - introduction, research objectives, background, geology of the study areas, theoretical aspects and methods applied, summaries of each manuscripts and the contribution of the candidate, and lastly, full manuscripts presented either as the published manuscripts, or as draft manuscripts prepared according to journal requirements.

Chapter 1 of the thesis provides the introduction, which sets out the structure of the thesis. Chapter 2 outlines the specific objectives of the research work and motivation. Chapter 3 describes the background to the study. The background chapter comprises of the overview of the International Continental Scientific Drilling Program (ICDP) project, “Drilling into Seismogenic zones in deep South African gold mines” (Dseis) (https://www.icdp-online.org/projects/world/africa/orkney-s-africa/details/).

Chapter 4 briefly presents the geology of the Witwatersrand Basin, with a focus on the study areas, Cooke 4 mine (situated in the Central Rand Group) and the Moab Khotsong mine (situated in the West Rand Group). Chapter 5 provides a basic theoretical framework and a description of the research methods applied throughout the study to address the research questions.

The manuscripts form the basis for this PhD thesis. Chapter 6 presents summaries of the two manuscripts published in peer-reviewed international journals and four unpublished draft manuscripts during the PhD study. In addition, these summaries clearly outline my contribution to each manuscript. Chapter 7 and Chapter 8 are manuscripts that are published in peer-reviewed international journals. These are presented according to peer-reviewed journal standards. Chapter 9 and Chapter 10 are draft manuscripts that can be further developed into full manuscripts. Chapter 11 is the discussion, which links all the manuscripts, published and unpublished. Chapter 12 is the conclusion and recommended future work.

Attached to the PhD thesis is Appendix, which contains a draft manuscript that may be further developed into full manuscripts to be published in peer-reviewed journals. This manuscript is presented last since the candidate is the second author, but still relevant to this PhD thesis.

2. Research objectives

This project involves a collaboration of experts in seismology, rock engineering, geochemistry, geology and microbiology from South African, Japan, India, Israel, Germany, Switzerland and the United State of America (USA). The ICDP (https://www.icdp-online.org/projects/naturalhazards/faults/) has vast experience drilling into seismogenic depths and has conducted several active fault-zone drilling projects around the world such as the San Andreas Fault, Chelungpu Fault, the Nojima Fault, Nankai Trough, and Pretorius Fault (Reches and Ito, 2007; Mori and Ellsworth, 2013). Grounded in these successes, Mori and Ellsworth (2013) recommended that in the next decade the ICDP should focus on topics such as: How do earthquakes propagate? Why do they start or stop?

These universal unsolved seismological questions cannot be answered solely by using far-field monitoring techniques and observations (Ogasawara et al., 2017). Therefore, near-field borehole observations are necessary. Drilling into seismogenic zones in South African mines provided new insights into resolving these longstanding seismological questions (Durrheim et al., 2017; Ogasawara et al., 2017). South African mines also bridge the gap between small-scale laboratory studies and natural earthquake field studies. In South African mines, faults often occur in centimetre to metre scale ahead of the stope face. Metre to kilometre scale faults are often encountered in field observations, while micrometre to centimetre scale faults are often analysed in laboratory experiments. This PhD study will focus on answering these questions:

1. What influences the spatial and temporal development of fractures?
2. What is the role of geology?
3. How do earthquakes propagate along shear zones?; and
4. How do earthquakes scale?

The research scope and objectives are separated into carefully planned scale-based approach:

2.1. Microscale (microns – millimetres)

To understand the rupture propagation and the weakening behaviour laboratory rock testing were conducted and the fault gouge analysed. Friction experiments were performed using fresh fault gouge and host rocks recovered from recent earthquake ruptures in source regions (Cooke 4 and Moab Khotsong mines) to determine the dynamic rupture weakening behaviour during slip propagation along earthquake ruptures in deep mines. In this study, it is critical to determine the rock mass composition.

Therefore, X-ray fluorescence (XRF) analysis was used to determine the elemental composition of fragile core samples and fault gouge material recovered from drilling endeavours. In addition, the scanning electron microscopy (SEM) analysis was used for particle microanalysis of earthquake ruptures. The XRD analysis was used for mineral composition determination.

2.2. Mesoscale (millimetres – metres)

This work focused at Cooke 4 mine, where mesoscale normal faults occurred ahead of the stope face and were a primary investigation. The study involved the use of geological core logging, geophysical borehole logging, underground mapping and microseismic data analysis (i.e., acoustic emissions) ($-5 < M < 0$). The triple-tube core barrel drilling technique was used at Cooke 4 mine to maximise the recovery of the fracture system forming ahead and around the stope face. We conducted laboratory uniaxial compressive strength (UCS) and triaxial compressive strength tests. We further used the recovered borehole core samples to measure seismic velocities, density and elastic properties. The integration of these datasets has enabled the development of a fracture model at seismogenic depths (fracture geometry and failure patterns under triaxial load) (Figure 14; Manuscript 1).

2.3. Macroscale (metres – kilometres)

This work focused at Moab Khotsong mine, where a macroscale M_L 5.5 strike-slip fault occurred below the mining levels. We integrated the analysis of the drill hole and core, reflection seismic data and seismicity data to identify structures that hosted the largest mining-related seismic event yet to occur in South Africa. Seismic reflection and mine seismology data were used to delineate the macroscale structures. The DSeis team drilled into this earthquake rupture and successfully recovered fragile host rocks, fault rocks and gouge material. The drill also intercepted hypersaline brine water. We compared the findings at Moab Khotsong with those in Cooke 4 mine.

3. Background: Mining, Rockbursts and Seismicity in South Africa

The South African economy, in line with those in developing countries, was and still is significantly reliant on the mining industry. In 2017, the Gross Domestic Product (GDP) of South Africa was estimated at ~R4.7 trillion (~US$ 348 billion) with the GDP per capita of US$ 13 500 (Statistics South Africa, 2018). In the same year, South Africa exported and imported US$ 108 billion and US$ 81.9

billion, respectively. The South African economy exports close to 200 products, and was ranked 34th in the world as the largest export economy. The highest foreign currency earner (exports) in South Africa is the mining industry: Gold (US$ 16.9 billion), Diamonds (US$ 9.8 billion), Platinum (US$ 9 billion), etc. mostly trading with China and the USA (https://oec.world/en/profile/country/zaf/). The selected active mines including commodities that are listed above are shown in Figure 1.

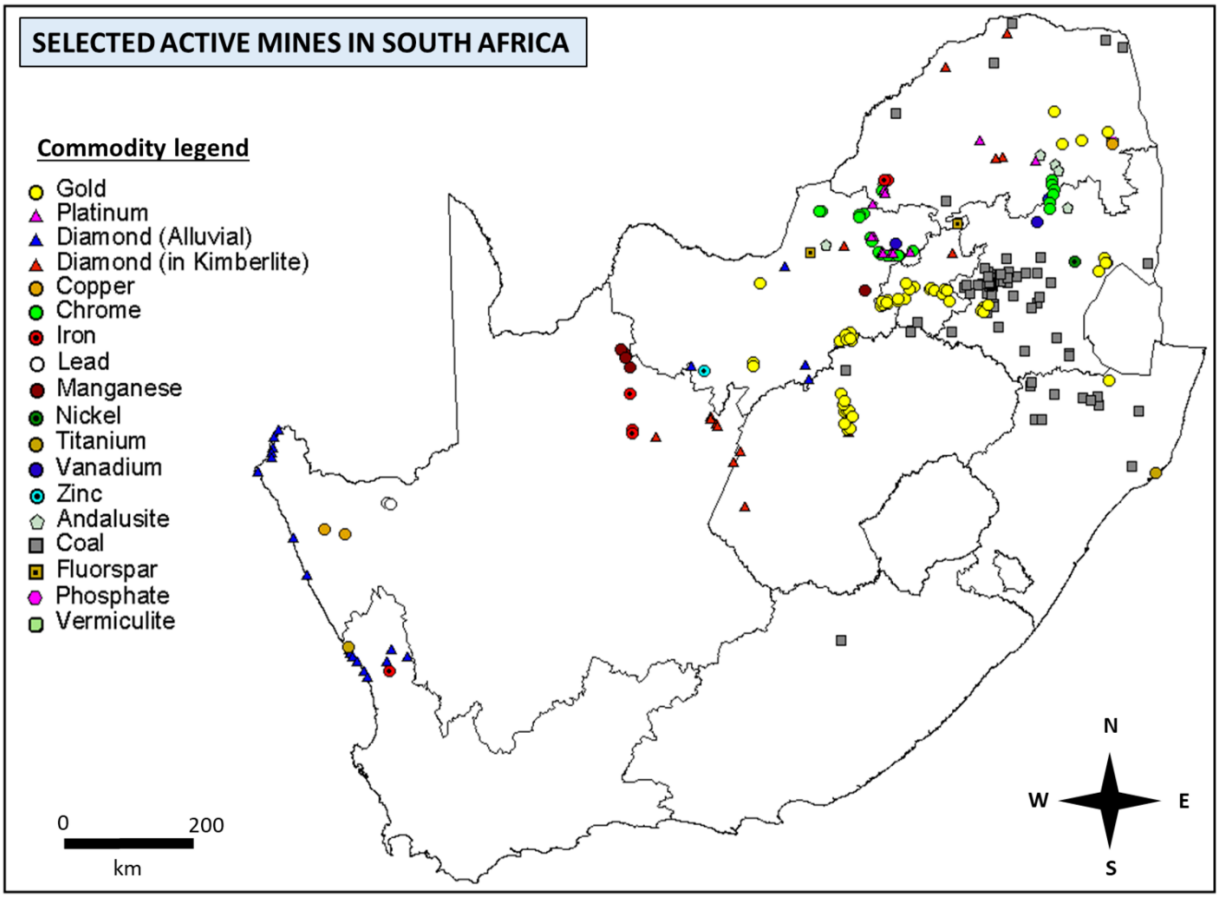


Figure 1: Geographical location of selected active mines in South Africa that include platinum, manganese, chrome, vanadium and gold (modified from Vorster, 2003).

Therefore, it is important that South Africa develops a strong and safe gold mining industry that contributes meaningfully to 'a better life for all' envisaged by the democratic government under the leadership of African National Congress (ANC) (Durrheim et al., 2010). The gold resources are finite – and are being depleted and more difficult to mine at greater depth. This has led to declining production, mine closures and creation of ghost towns, which eventually results to huge social problem for governments such as job losses, increasing poverty and widening inequality. Thus, finding innovative and safer solutions for mining operations to continue mining at deep levels (1 – 4 km) is important to maintain and create employment.

This study focuses on the deep and high stress gold mining operations in the Witwatersrand Basin. In South Africa, the gold mining industry played a critical role in the infrastructure and economic development. However, with deeper gold mining operations and the risk posed by seismicity and rockbursts, it is increasingly important for South Africa to develop safer gold mines to achieve “zero harm”. Achieving zero harm will enable the gold mining industry to continue mining deep ore bodies, and contribute meaningfully to the economic growth, foreign currency earnings and enhance the quality of life of all citizens. The study areas (Cooke 4 mine and Moab Khotsong mine) are situated in the Witwatersrand Basin, which has been a critical source of gold mining in the world (Figure 2).

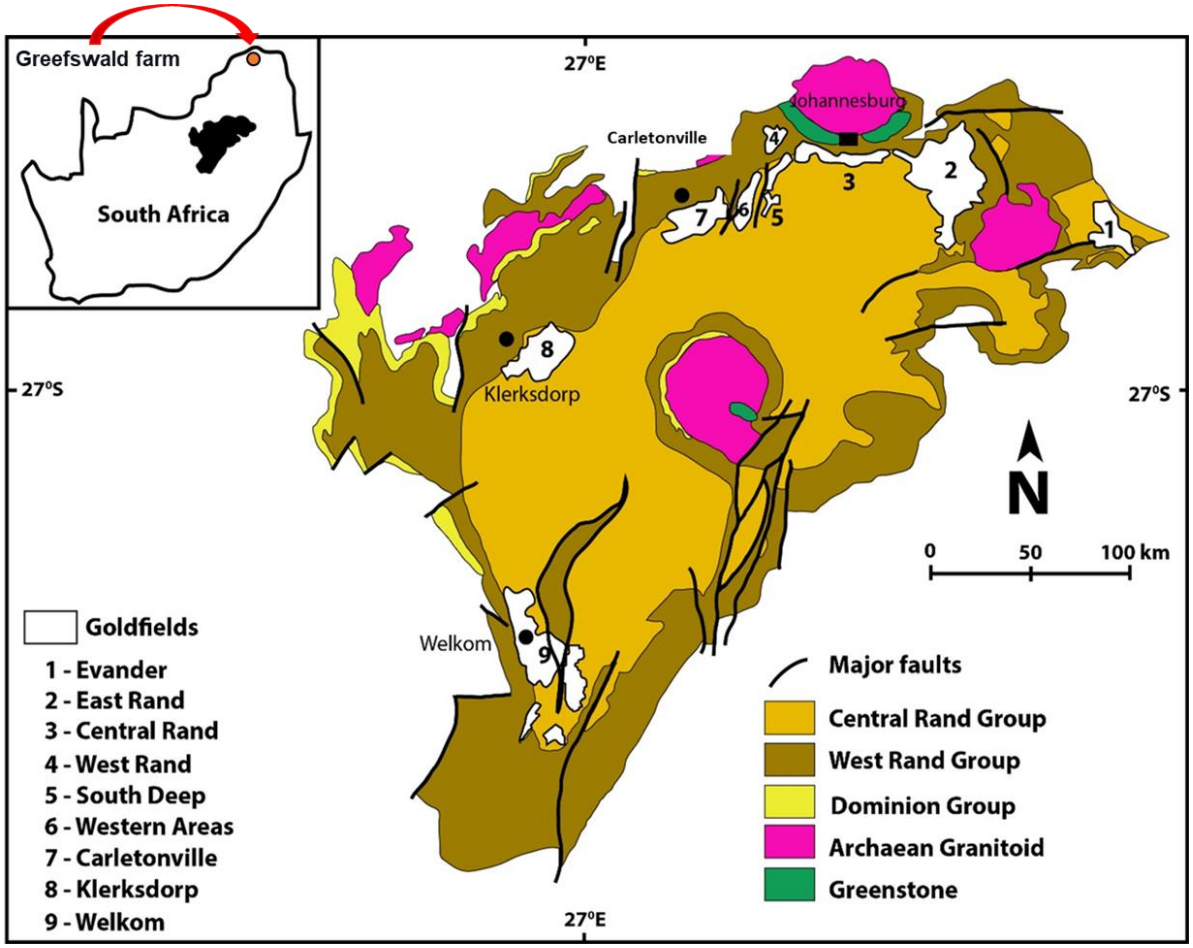


Figure 2: The study areas are located in Western Areas (6) and Klerksdorp Goldfields (8) at Cooke 4 mine and Moab Khotsong mine in the Witwatersrand Basin (modified from Dankert and Heim, 2010; Nkosi, 2016). The location of Greefswald farm, site of the capital of the pre-colonial gold-trading Kingom of Mapungubwe, is shown in the inset.

The history of gold in Southern Africa predates the great discovery of gold in the Witwatersrand Basin. A pre-colonial Kingdom of Mapungubwe located in the present-day Greefswald farm, Limpopo Province (see Figure 2) appears to have traded gold and ivory with Asian and North African countries

(China, India and Egypt) from ~ 1200 to 1300 AD (Duffey, 2012; Bam et al., 2018). The colonial or 'modern day' gold mining in South Africa started in Barberton in 1874 with the discovery of alluvial gold.

The discovery of gold in the Witwatersrand Basin in 1886 resulted in an unprecedented gold rush that created the South Africa we know today. Many towns were born out of gold mining, such as Johannesburg, Klerksdorp, Carletonville and Welkom (Durrheim et al., 2010). De Kiewiet (1941) perfectly describes the discovery of gold in the Witwatersrand, “A change so unexpected and a development never known before were due to the discovery in 1886 of the greatest gold mines of all history, ancient and modern.”

Following the discovery, mining operations rapidly got deeper. Communities such as the Ophirton village and Boksburg near the goldfields began to experience damaging seismic events in the Witwatersrand Basin (Anon, 1924; Durrheim et al., 2006). As the gold mining industry expanded, the severity of the problem amplified. This resulted in the formation of several committees to investigate these seismic events and their association to mining operations – 1908, 1915, 1924 and 1964 (Durrheim et al., 2006). Seismic monitoring systems were deployed (the first seismograph were installed in 1910, at Ophirton) and for over a century South Africa has conducted extensive research of mining-induced and related seismicity and rockbursts (Durrheim et al., 2012). Gane et al. (1946) were the first to report the direct relationship between the seismicity and deep gold mining operations in the Witwatersrand Basin using a surface seismic monitoring network (Gibowicz and Kijko, 1994; McGarr, 2000; Durrheim et al., 2006). Subsequently, Cook (1962) used an underground seismic monitoring network deployed near source regions to delineate the spatial relationship between the mining-induced seismicity and active mining stopes. McGarr and Green (1975) conducted measurements of tilt in deep-level gold mines and their relationship to mining excavations and seismicity.

Further research using broadband seismic monitoring systems, physical underground observations from exhumed fault surfaces and laboratory experiments revealed that mining-induced seismicity displayed similar physical and mechanical signatures to natural earthquakes occurring in active tectonic regions (Ortlepp, 1978; McGarr et al., 1979; Gay and Ortlepp, 1979; Spottiswoode, 1980; Olgaard and Brace, 1983). Since then, these mining-induced earthquakes have attracted a lot of interest both locally and internationally from researchers trying to understand fundamental seismological questions about near source regions (Ortlepp, 1997; Bosman and van Aswegen, 2003; Reches and Dewers, 2005; Wilson et al., 2005; van Aswegen, 2008; van Aswegen, 2013).

3.1. Seismicity

Near plate boundaries, earthquakes pose an even greater risk to human lives and public infrastructure. For instance, on 26 December 2004, a large earthquake of magnitude Mw 9.1 occurred 160 km off the western coast of northern Sumatra, Indonesia at 00:58:53 UTC. The earthquake was one of the most devastating natural disasters recorded in history, killing over 230 000 people in 14 countries. In addition, an estimated 125 000 people were injured and more than 600 000 people were displaced (IIEES, 2004). In Kobe, an earthquake occurred on 17 January 1995 at 05:46:53 JST with the moment magnitude of Mw 6.9. The earthquake killed 6 400 people and caused estimated total damage of US$ 200 billion (Reches and Ito, 2007). This led to the drilling of boreholes in various seismogenic zones (including human-induced seismicity such as in South African gold mines) around the world. The first boreholes were drilled into the Nojima Fault, Japan, which hosted another deadly and costly earthquakes, 'the Great Hanshin earthquake', which was the name given to the earthquake that struck Kobe in 1995.

This was followed by several endeavours to drill in active fault zones (Kikuchi et al., 2003; Tsuru et al., 2005; Reches and Ito, 2007; Tanioka and Satake, 2001): (1) Chelungpu Fault - a major thrust in an active Orogenic Belt, where the 21 September 1999 magnitude Mw7.7 Chi-Chi earthquake in Taiwan created large zones of surface rupture, with a maximum displacement of 8 m (Tanaka et al., 2002; Ma et al. 2005); (2) Nankai Thrust - a major subduction thrust that poses a seismic and tsunami threat to densely-populated coastal cities in Japan. The last two large earthquakes to occur on the Nankai thrust, which were accompanied by tsunamis occurred in 1944 and 1946 off the Kii Peninsula, Tonankai (M 8.1) and Nankaido (M 8.3) events, respectively (Katsuichiro et al., 2017); (3) The San Andreas Fault - a continental transform fault that spreads approximately 1200 km through California (Hickman et al, 2004; Zoback et al., 2006). This fault makes up the tectonic boundary between the North American Plate and Pacific Plate, with right-lateral strike-slip horizontal motion; (4) Aigion Fault - a rapid extension and active normal faulting in an active rift zone in Greece (Cornet et al., 2004; Forster et al., 2005); and (5) Pretorius Fault- a 'reactivated' Archean fault in South Africa (McGarr et al., 1979; Heesakkers et al., 2005; Reches et al., 2006). These studies revealed important information on in-situ stresses, fault-zone structure, fault-rock composition, mechanical properties, heat flow and near-field seismicity.

Below is a brief discussion of some of the endeavours that have contributed to our understanding of falls of ground, seismicity and rockbursts in deep South African gold mines. Between 2005 and 2008, the DAFSAM (Drilling Active Faults Laboratory in South African Mines)-NELSAM (Natural Earthquake Laboratory in South African Mines) projects focused on building an earthquake laboratory in a deep South African gold mine (TauTona mine) to examine the oblique strike-slip Pretorius fault (Reches and DAFSAM- NELSAM, 2006). In 2004, the fault was reactivated by mining activity and induced a magnitude M2.2 earthquake (Heesakkers et al., 2011a; Heesakkers et al., 2011b). The project drilled 18 underground boreholes covering a surface area of ~ 90 000 m^2 at 3.6 km depth. The study found that the M2.2 slip only occurred along the pre-existing fault segments, and had a maximum oblique-normal slip of ~ 25 mm. They identified three structural zones within the fault: (1) outer damage zone characterised by brittle deformation of widely spaced fractures (~ 100 m wide); (2) inner damage zone characterised by dense anastomosing sets of fault and fractures (~ 25 – 30 m wide); and (3) a cataclasite zone that accommodated most of the Archaean slip (~ 50 cm wide) (Ogasawara et al., 2017).

Between 2007 and 2008, the JAGUARS group (JApanese-German Underground Acoustic emission Research in South Africa) conducted seismic monitoring studies at Mponeng gold mine, which neighbours TauTona gold mine in the West Wits operations. Sensors were deployed at a depth of ~3.5 km consisting of eight acoustic emission (AE) sensors, one tri-axial accelerometer; and two tiltmeters to monitor the highly-stressed dyke that intruded into the host rock, quartzite (Yabe et al., 2009). In one-year (between June 2007 and June 2008) of monitoring, close to 500 000 AE events were successfully recorded. On 27 December 2007, the sensor network recorded a magnitude Mw 1.9 event with 21 000 aftershocks. Detailed analyses of aftershocks accurately defined the fault plane (Naoi et al. 2011). This assisted with the assessment of the stress on the fault and estimation of fault strength. Yabe et al. (2015) found the traces of ancient hydrothermal alteration on the mainshock rupture plane, which indicated that the foreshock event occurred on a pre-existing weakness (Ogasawara et al., 2017).

This was followed by a 5-year Japanese – South African collaborative project, "Observational studies in South African mines to mitigate seismic risks" by the Science and Technology Research Partnership for Sustainable Development (SATREPS) group which investigated three sites (Cooke 4 mine, Moab Khotsong mine and West Kloof-Driefontein Complex) between 2010 and 2015 (Durrheim et al., 2017). Through this ambitious project, more than 80 boreholes were drilled totalling a combined

core length of 2.8 km. This was followed by the installation of acoustic emission sensors and accelerometers to delineate the spatio-temporal evolution of ruptures ahead of mining faces (Ogasawara et al., 2014).

As the continuation of SATREPS project, following the 'spatio-temporal' delineation of these mining-induced fractures that occurred ahead of the mining front and the Orkney M_L 5.5 earthquake that occurred below mining levels on 5 August 2014 (Naoi et al. 2011, 2014, 2015 a and b; Moriya et al., 2015), the ICDP-DSeis team drilled into earthquake ruptures to recover fresh fragile rupture surfaces, rock breccia, fault gouge and host rocks. This study formed part of the ICDP-DSeis project, "*Drilling into seismogenic zones of M2.0 to M5.5 earthquakes in South African gold mines*". The study examined the physics and mechanics of mining-induced earthquakes from micro to macro scale near source regions in deep and high stress Witwatersrand Basin gold mines.

3.2. Reflection seismic

Making clear tectonic structures occurring in the seismogenic zone is crucial to understand the earthquake generation and propagation mechanism. One of the proven techniques for making clear subsurface tectonic structures is the seismic reflection method (e.g., Manzi et al, 2012; Nkosi, 2016). When gold was discovered in the Witwatersrand Basin in the late 1880s, potential field methods, (i.e., magnetic and gravity) were popular and often used for exploration, such was the case in the Witwatersrand Basin (see Johan H de Beer, 2016 in the History of Geophysics in Southern Africa). The reflection seismic technique was invented in the early 1920s. Since then, it has been used with a great deal of success in the exploration for oil and gas resources and has been the most popular applied geophysics method for over 80 years (Reddy, 2012). In this study, reflection seismic is used to delineate the spatial extent of the fault structure hosting the M5.5 earthquake. This was done through reprocessing and reinterpretation of the legacy exploration data.

4. Witwatersrand Basin

The geology of the Archaean Witwatersrand Basin (3.07 - 2.71 Ga) has been described by many authors (Robb and Meyer, 1995; McCarthy and Rubidge, 2005; Dankert and Hein, 2010) and we do not intend to repeat those details in this thesis. The Witwatersrand Supergroup sediments were deposited over ~ 360 Ma on the Archaean Kaapvaal Craton and terminated by a period of thrust folding (Robb

and Meyer, 1995; McCarthy and Rubidge, 2005; Dankert and Hein, 2010). For the duration of the deposition period, the basement granite terrains and greenstone belts were eroded by multiple streams, allowing sediments to be deposited into the inland sea. The Witwatersrand Supergroup is covered by volcanic rocks of the Ventersdorp Supergroup (2.72 - 2.63 Ga) (Dankert and Hein, 2010).

The Witwatersrand Supergroup comprises of two groups, the West Rand Group and the Central Rand Group (Figure 3) (Myers et al., 1989; McCarthy, 2006). The average thickness of the strata is ~ 4.6 km. The West Rand Group and Central Rand Group thickness tend to decrease towards the SE basin margin. The West Rand Group mainly comprises clastic sedimentary rocks such as quartzites, shales and minor conglomerates; whereas, the Central Rand Group mainly comprises quartzite and conglomerate packages and minor bands of shale and lavas – and hosts ~70% of gold reefs in the Witwatersrand Basin (SACS, 1980; SACS, 2006).

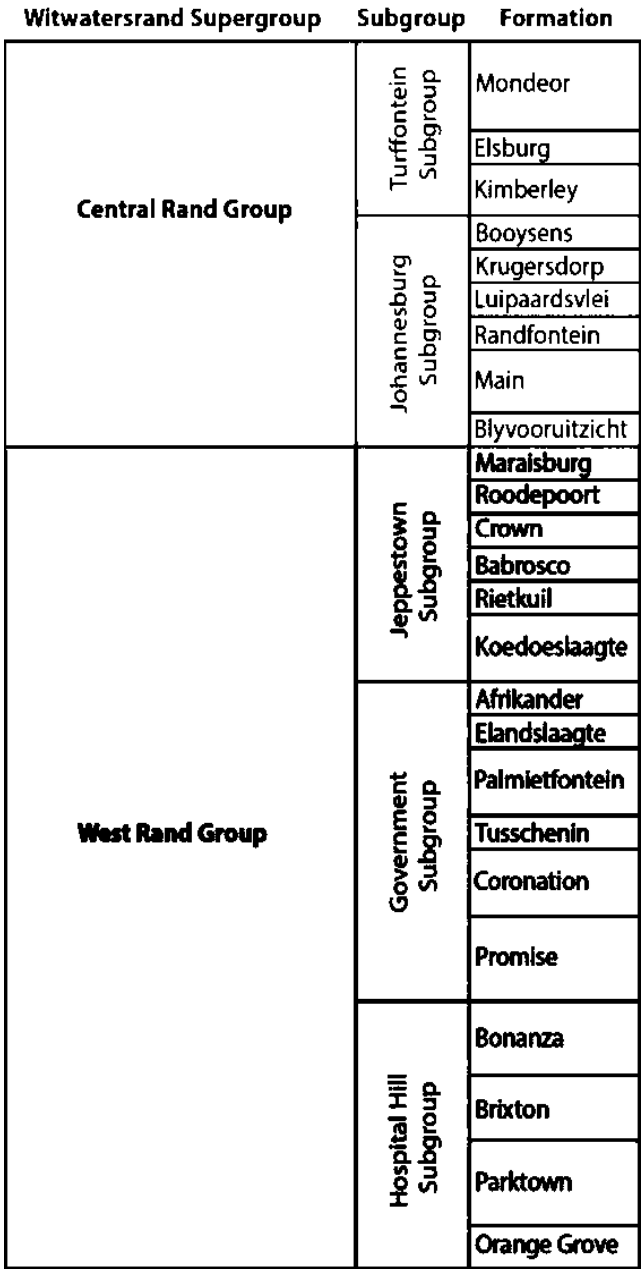


Figure 3: This is the general stratigraphy of the Witwatersrand Supergroup, showing Central Rand and West Rand Groups (modified from Robb and Meyer, 1995; Dankert and Heim, 2010).

The Witwatersrand Basin has listric faults, with associated drag folds, originating from an episode of extensional tectonics that affected the deposition of the Ventersdorp Supergroup (Vermaakt and Chunnet, 1994; Coward et al., 1995; Beach and Smith, 2007). The Basin is intruded by various dolerite sills and syenite dykes of Karoo (~150 Ma), Pilanesberg (~1.30 Ga), Transvaal (~2.20 Ga) and Ventersdorp (2.60 Ga) age. These structures often disturb the ground in the mining vicinity and displace gold reefs, creating an unstable and complex mining environment (Ligege, 2013). These unstable

structures are associated with stress concentration (redistributed by mining activities) and rock failure causing large damaging seismic events (Durrheim et al., 2012; Ogasawara et al., 2009).

5. Basic descriptions and methods

5.1. Mining-induced shear fractures

Mining-induced shear fractures have been widely studied in deep and high stress South African gold mines, and a nomenclature has been developed for fractures forming ahead and around the stope (Jager and Ryder, 1999; Ryder and Jager, 2002; van Aswegen and Stander, 2012). This study focuses on these specific mining-induced shear fractures known as “Ortlepp shears” (see p. 43 of Ortlepp, 1997; Manuscript 5, Figure 11). These shears constitute a subset of dynamic brittle shears that form in deep mines. Ortlepp shears (van Aswegen, 2008) are large shear fractures often associated with seismic events (Mw 1-4). Their genesis is believed to be similar to ‘conjugate shears’ forming under triaxial load in laboratory experiments (van Aswegen, 2008). Ortlepp shears occur ahead of the stope and are characterised by normal displacement. They dip towards the stope face when in the hangingwall, and dip away from the stope face when in the footwall (Figure 4).

Ortlepp shear fractures are characterised by two mechanical features: a) extension fractures, which occur in an en-echelon type geometry (van Aswegen, 2008), and b) a breakthrough shear rupture (Ortlepp, 1992; p. 43 of Ortlepp, 1997; Jager and Ryder, 1999; van Aswegen, 2008; Manuscript 5, Figure 11). A breakthrough rupture is also characterised by two features: rock pulverization and shear displacement (van Aswegen, 2008). The typical characteristics of brittle-ductile shear zones such as R1, R2 (Riedel), and P- and Y-shears are notably absence (Tchalenko, 1970; Logan et al., 1979; van Aswegen, 2008). However, it is worth mentioning that not all shear zones display a typical breakthrough shear rupture (Wibberley et al., 2000; van Aswegen, 2008).

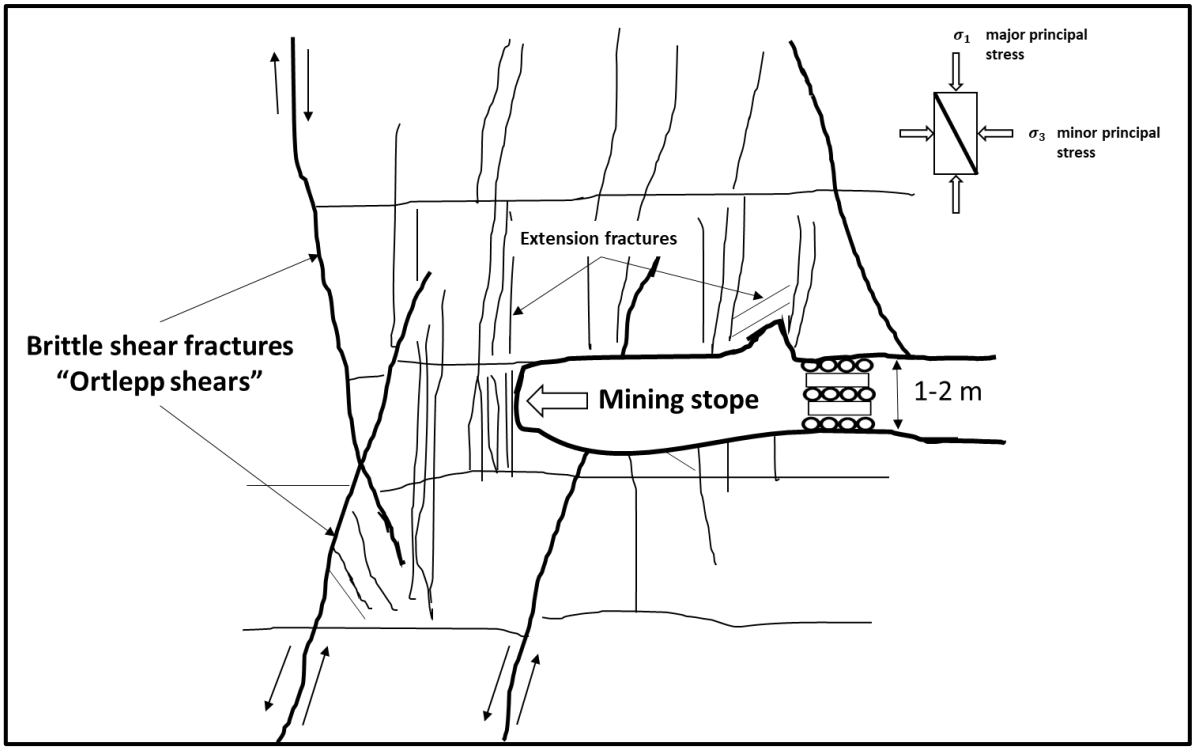


Figure 4: The 2-D vertical geometry of the shear fractures occurring ahead of the mining excavations 'Ortlepp shears', which are often associated with large seismic events (Mw 1-4) (modified from Adams et al., 1981).

Breakthrough shear ruptures should leave slickensides (striations on rock surfaces) as evidence of fault slip. These are parallel scratches or grooves on rocks that are created by the frictional sliding between two sliding rock surfaces (van Aswegen, 2013; Rowe and Griffith, 2015). Slickensides are used to determine the sense and direction of fault slip, and for mining-induced shear fractures, this sense of slip is normal as stated above (Jager and Ryder, 1999; van Aswegen, 2008). In the mines, newly formed slickensides resulting from Ortlepp shears are often soft, and merely indicate the direction of an unstable rock block that slid into the free space (van Aswegen, 2013). These rock surface traces are not well documented for Ortlepp shears, primarily because of the restricted access to "true physical rupture surfaces" and a past focus on the 2-D geometry of these fractures (van Aswegen, 2013). Our study through advanced triple-tube drilling exposes rare fresh rupture surfaces and provides an opportunity to examine these features in unprecedented detail.

Similar to brittle faults of all sizes, Ortlepp shear rupture zones are characterised by (a) fault gouge "rock flour" and (b) shear displacement (Gay and Ortlepp, 1979; McGarr et al., 1979; Spottiswoode, 1980; van Aswegen, 2008; van Aswegen, 2013). Several researchers reported that the fault gouge formation is a product of wear and attrition of sliding surfaces or implosive loading during

earthquakes (Brune, 2001; Scholz, 2002; Ben-Zion and Sammis, 2003). Models of wear and attrition suggest that progressive shear within gouge zones should lead to grain size reduction due to amplified stresses at grain contacts (Steacy and Sammis, 1991). Reches and Dewers (2005) studied the fault gouge from San Andreas Fault and South African gold mines and concluded that the formation of the 'fault gouge' is primarily through dynamic volumetric strain and that the extreme strain is associated with the 'fast mode II' deformation field near the fracture tip. Furthermore, Wilson et al. (2005) reported that fault gouge exhumed and collected in deep South African gold mines is a product of dynamic rock pulverization during the propagation of a single earthquake. Fault gouge recovered in deep mines was compared to gouge recovered from larger displacement faults (Wilson et al., 2005). van Aswegen (2013) further emphasised that faster dynamic deformation results in finer rock flour.

5.2. Fault gouge

Fault gouges can be seen in almost all natural earthquakes observed in the field, including the normal faults occurring ahead of the stope, strike-slip faults, and in controlled laboratory experiments such as frictional sliding experiments (Sammis et al., 1987; Marone and Scholz, 1989; Scholz, 2002; Reches and Lockner, 2010). Fault gouges reveal several important earthquake properties and fault processes (e.g., friction behaviour). Moreover, since observations of diverse fault gouge along fault zones have raised questions about their role to physical and mechanical processes of earthquake and faulting, particularly as they affect earthquake rupture propagation behaviour (Dieterich, 1978; Reches and Lockner, 2010). Some authors have argued that the fault gouge can become a "third layer", which acts as a lubricant during seismic slip, and can form for a wide range of fault configurations, compositions and temperatures (Ben-Zion and Sammis, 2003; Reches and Lockner, 2010). Furthermore, previous laboratory frictional experiments studies revealed that the presence of gouge, the mineralogy of the gouge, the particle size distribution and the gouge thickness all influence the earthquake instability process, dynamic rock friction and fault weakening behaviour (Biegel et al., 1989; Reches and Lockner, 2010). This important aspect of the mining-induced and mining-related earthquakes as it relates to unstable rupture propagation and resulting seismic damage.

5.3. Methodology

The DSeis scientific drilling endeavour is different from any ordinary routine in-mine or exploration drilling projects. The DSeis scientific drilling endeavour is primarily driven by the scientific objectives, and therefore, should be viewed as a giant “multidisciplinary” scientific experiment. There are three critical aspects of a scientific drilling endeavour: (1) the technologies deployed have a serious impact on drilling, drill core recovery, preservation of geological structures in drill core, sampling, on-site measurements and geophysical borehole logging; (2) the analysis of the acquired data; and (3) modelling of the data (Wöhrl and de Wall, 2014). This study focused on a comprehensive ‘multidisciplinary’ approach, analysing: geology, geochemistry and geophysics (Table 1 and Figure 5).

Table 1. Multidisciplinary approach to scientific drilling.

Measurements	Geological description	petrography; macrostructures; microstructures; microscopy, core orientation; scanning electron microscopy (SEM); and Laser digital particle size analyser (LDPSA)
	Geochemistry	X-ray powder diffraction (XRD), X-ray fluorescence (XRF) and Energy Dispersive X-Ray Spectroscopy (EDS)
	Petrophysics	density, magnetic properties, ultrasonic velocities
	Mechanical properties	uniaxial compressive strength; triaxial compressive strength; elastic constants
Output	samples (host rock, rock breccia, rupture surfaces, fault gouge particles); thin sections; lithological log; petrophysical properties; mechanical properties; geochemical log; digital database	



Figure 5. Multidisciplinary approach used in this PhD thesis - geology, geochemistry, geomechanics and geophysics. Specific methods used include: X-ray powder diffraction (XRD), X-ray fluorescence (XRF), Energy Dispersive X-Ray Spectroscopy (EDS) and scanning electron microscopy (SEM).

We used borehole core recovered by the SATREPS team using conventional diamond drilling techniques, and the newly recovered borehole core drilled by ICDP-DSeis team using advanced triple-tube drilling. The SATREPS team drilled 29 boreholes at Cooke 4 mine with an average length of ~100 m. These were drilled into the remnant shaft pillar to install acoustic emission sensors and accelerometers for seismic monitoring of Ortlepp shears "normal faults" at seismogenic depths (1.0 – 1.2 km) (Durrheim et al., 2017). The recovery of the drill core for SATREPS project was poor compared to the ICDP-DSeis project. The ICDP-DSeis project drilled a hole using advanced triple-tube technology and the core recovery was high, with minor core losses in some areas. The borehole length is ~41.5 m, with the core diameter of 42 mm (Azimuth: 30^{o}; Plunge: 24^{o}; Direction: north-northeast, NNE). The combined available core for petrographic analysis and rock physical and mechanical testing amounted to ~ 3.0 km in length.

Similarly, DSeis conducted drilling at Moab Khotsong mine to investigate the M5.5 strike-slip earthquake rupture. A chamber (6 m x 6 m x 6 m) was excavated and used as a drilling site at ~ 2.9 km depth near the seismogenic zone to minimise drilling costs. The drill hole plunged at ~35^{o}– 45^{o} to intersect the earthquake rupture and recover fault rocks (Ogasawara et al., 2019). Since the drilling length was greater here than at Cooke 4 mine, we deployed a 3 m long double-tube core barrel and near the rupture zone we deployed a 1.5 m long triple-tube core barrel to fully maximise core recovery (similar to Cooke 4 mine). Three holes were drilled, Hole A (~817 m) which deviated and did not intersect the rupture; Hole B (~700 m), and Hole C (~96 m), a short branch hole drilled from Hole B to sample the rupture with the triple-tube core barrel.

5.3.1. Mine seismicity data

Mining-induced microseismicity down to Mw –5 was monitored during active mining in the remnant shaft pillar at Cooke 4 mine using 28 high-resolution acoustic emission (AE) sensors and six accelerometers (Figure 6). The 3-D sensor spacing is average 15 m, covering 100 m in diameter (Kgarume et al., 2013). Sensors were grouted inside boreholes, and more than one sensor were installed in a borehole (Ogasawara et al., 2009). See Naoi et al. (2015a) and Naoi et al. (2015b) for more information on the installation of the acoustic emission sensors, accelerometers and catalogue development.

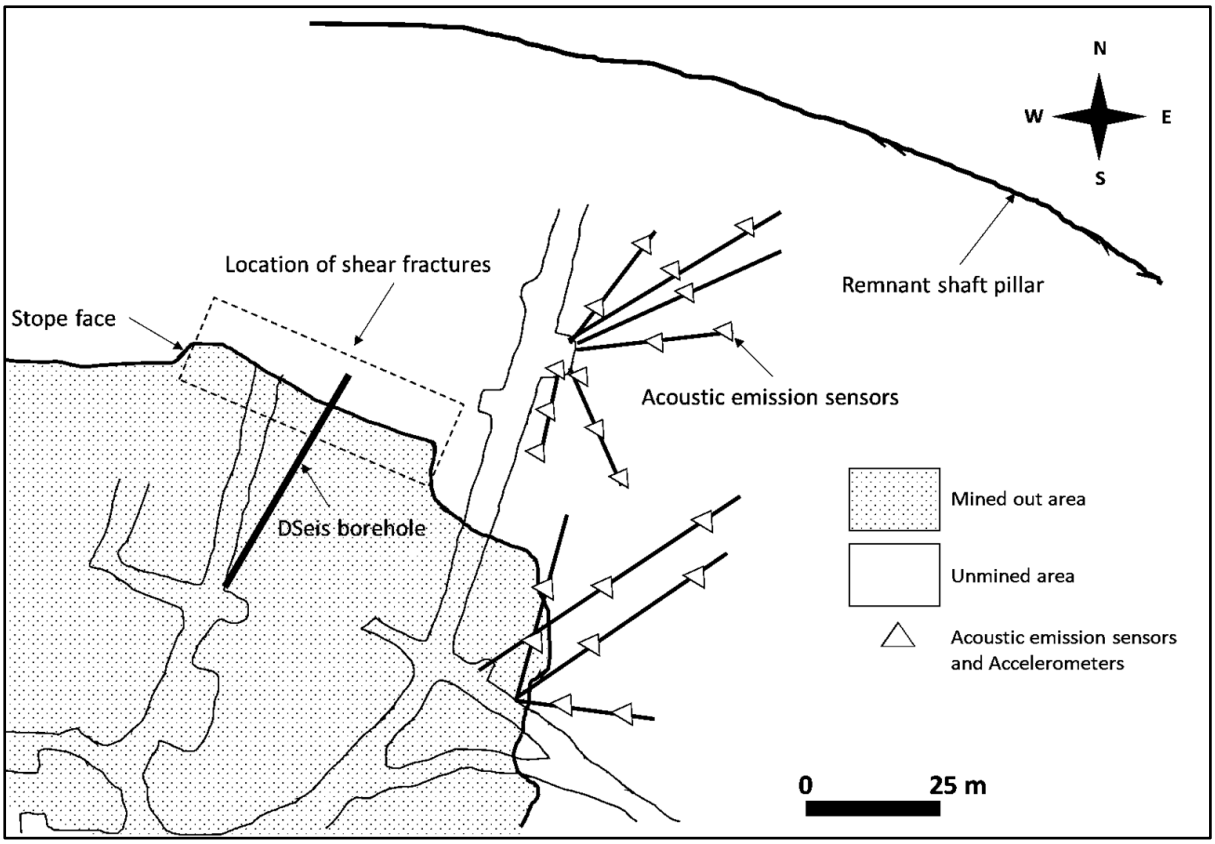


Figure 6. The remnant shaft pillar that was investigated at Cooke 4 mine is situated at 1000 - 1200 m depth; shows extensively mined out areas vs unmined areas. This also shows the borehole configurations drilled by SATREPS team. These boreholes were used to install acoustic emission sensors and accelerometers to monitor and delineate shear fractures occurring ahead of the stope. The DSeis project borehole location, stope face, and the location of shear fractures associated with the stope face are shown.

Moriya et al. (2015) conducted microseismic monitoring to delineate mining-induced fractures occurring ahead and around the stope. In this PhD thesis, microseismic data was further analysed in the hangingwall and ahead of the stope to identify fracture patterns and fracture turning points. The study could successfully identify and map seismic sources and monitor localised damage, fracture patterns and fracture turning point (Figure 7a and Figure 7b). The integration of data enabled the development a fracture model for shear fractures occurring ahead of the stope face in deep and high stress mines (Figure 3 and Figure 4, Manuscript 1). In addition to microseismic data, in-mine seismicity data were used to delineate the M5.5 earthquake rupture (Figure 8a and Figure 8b). This information made clear the orientation and position of the fault structure. This information was used to plan the drilling project to intercept these ruptures (Figure 8a and Figure 8b).

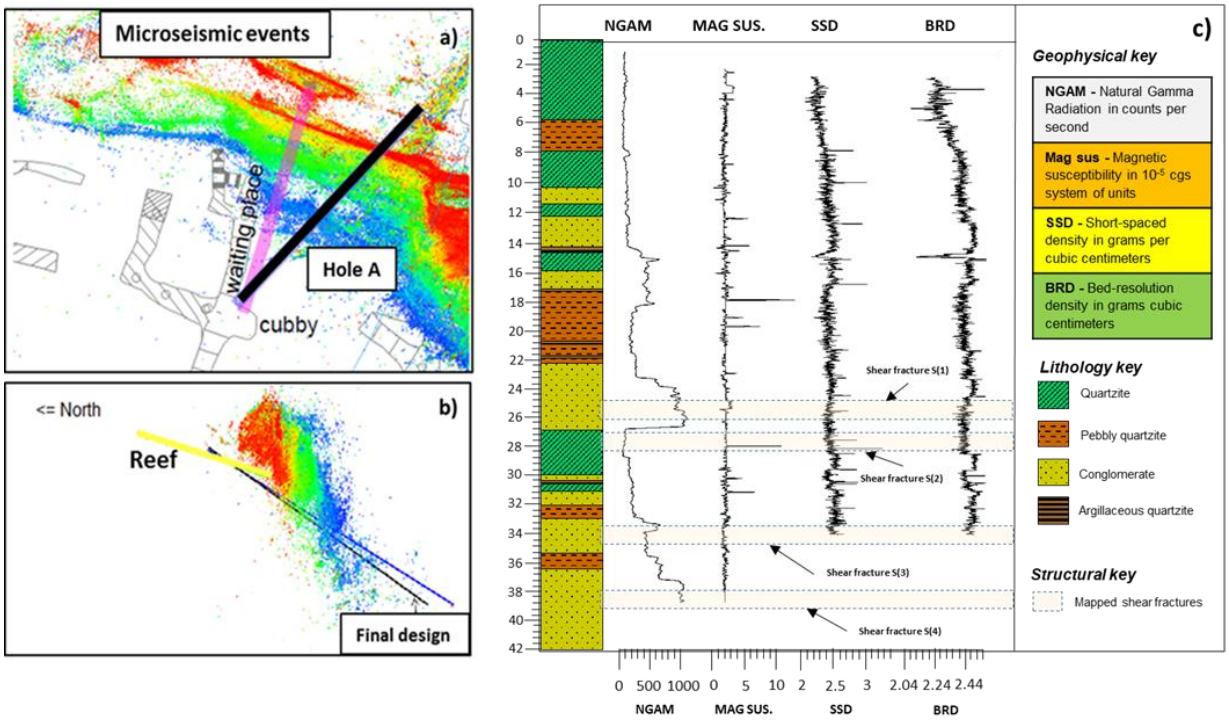


Figure 7. The top view of microseismicity data spatial distribution related to active stopes is shown. b) Perpendicular view of microseismic data spatial distribution showing steeply dipping planar seismic clusters. c) Lithological, geophysical and shear rupture logs.

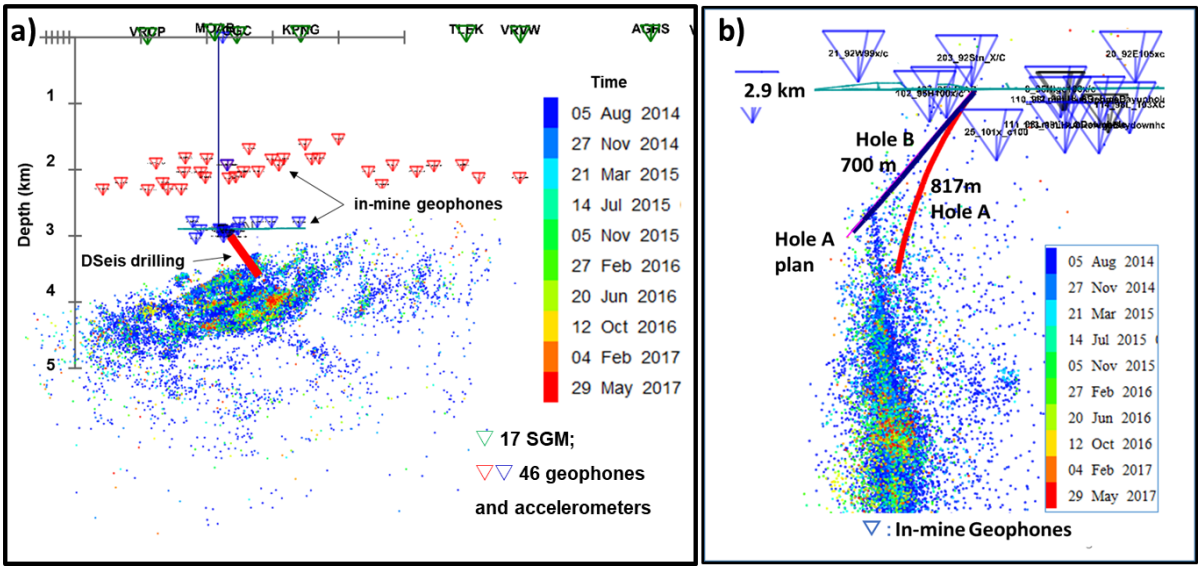


Figure 8. Moab Khotsong mine a) Location of recorded seismicity. DSeis drilling plan (in red) is shown and in mine geophones. b) The aftershock data delineated the rupture plane generated by M5.5 earthquake. The location of drilled Hole A and Hole B are shown (Ogasawara et al., 2019).

5.3.2. Triple-tube drilling

We successfully delineated the Ortlepp shears associated with normal faults (M1-2) and M_L 5.5 strike-slip earthquake rupture using seismicity data. The ICDP-DSeis team drilled into these delineated earthquake ruptures occurring ahead of the stope in the remnant shaft at Cooke 4 mine and below Moab Khotsong mine mining levels. In both drilling endeavours, we successfully recovered the host rocks, fragile ruptures, rock breccia and fault gouge material.

Drilling into deep and highly stressed intensely fractured rock mass at seismogenic depths requires special care, skill and attention. Conventional single and double tube core barrels are not suitable for these delicate settings. The double tube samplers often rotate (some inner tubing can be fixed), which often disturbs or shears the drill core samples along intensely-fractured zones. In addition, drilling fluids are notorious for disturbing core samples through erosion and displacement. Hence, to attain the best core recovery rate near seismogenic zones, we used the triple-tube core barrel. The triple-core barrel comprises of a double core barrel sampler including a stationary liner (some inner tubing can rotate with the inner tube if allowed to rotate) that protects the cored samples during the extraction.

5.3.3. Petrography and geophysical borehole logging

Qualitative and quantitative petrographic assessment of rock properties are well known to provide indications of the mechanical behaviour and seismic response of rocks when subjected to uniaxial or triaxial loads, and may provide a good qualitative indication of rock strength (Brace, 1961; Heap et al., 2009). The American Association of Petroleum Geologists (AAPG) recommends that when conducting petrographic analysis for sedimentary rocks the procedure and order of recording parameters should be: rock type; colour; grain size, roundness and sorting; matrix composition; sedimentary structures; and porosity (Wöhrl and de Wall, 2014). On the other hand, Knill et al. (1970) recommends that mechanical properties should be recorded first. Therefore, the following order of recording parameters is recommended: weathering condition of rocks; rock structure; major grain size and minor particle size; texture, alteration, cementation state; and rock strength.

The petrographic analysis focused on examining the rocks forming the remnant shaft pillar at Cooke 4 mine and around the M5.5 earthquake below the mining levels at Moab Khotsong mine by means of: (i) underground observations in the stope; (ii) geological core logging; (iii) geochemical

analysis of drill core; (iv) geophysical borehole logging; (v) unrolled and rolled scans of the drill core; (vi) ultra-high-resolution imagery of the drill core; and (vii) rock quality designation (RQD) index of drill core and sampling. The RQD is a high level measure of a degree of fracturing (or jointing) in a drill core. It is defined as the sum length of all recovered core samples greater or equal to 10 cm in length (good quality) divided by the total length of the drilled core. This measure is expressed in percentage.

At both drilling sites, the ICDP-DSeis team completed drilled a full-core wire-line NQ hole (~76 mm diameter); NQ is the minimum borehole diameter that allows downhole geophysical logging (Ogasawara et al., 2017). At Cooke 4 mine, the geological core logging, true physical observations of shear ruptures in the drill core and observations in the stope, were correlated with geophysical borehole logging. The geophysical borehole logging includes density, magnetic susceptibility and natural gamma logs (see Figure 7c). At Moab Khotsong mine, similarly, the geological core logging, reflection seismic data, mine seismology data were correlated with the geophysical borehole logging (See Figure 8). On the surface, we performed both unrolled and rolled scans of the drill core. The International Continental Scientific Drilling Program protocol was used to conduct the digital scanning of the core. These images clearly showed fractures, different lithology, and geological features such as veins.

For geochemical analysis of these rocks, the X-ray fluorescence (XRF) and X-ray powder diffraction (XRD) methods were used. The XRF analysis was used to identify major elements in a core, and the XRD analysis was used for mineral identification. The material was prepared using a back-loading preparation method. It was analysed with a Malvern Panalytical Aeris diffractometer with PIXcel detector and fixed slits with Fe filtered Co-Kα radiation. The phases were identified using X'Pert Highscore plus software. The relative phase amounts (weight %) were estimated using the Rietveld method. Major elements were determined using the Norrish Fusion (Norrish and Hutton, 1969) technique and Panalytical PW2404 X-ray fluorescence spectrometer.

5.3.4. Identifying mining-induced shear ruptures in 'triple-tube' drill core

One unresolved aspect is a set of clearly defined rules that can be used to identify the intersection of a seismic source in diamond drill core drilled into the rock mass ahead and around the stope, particularly in the hangingwall rocks. This information is critical for the delineation of the geometry of mining induced shears around a stope. The aim of this study was to develop criteria that could be used to identify seismic sources in drill core. The investigation results are mainly presented in ultra-high-

resolution imagery. We focus on examples from the DSeis borehole core from Cooke 4 mine remnant pillar (Ogasawara, et al., 2017). The core was drilled specifically to intersect a series of shear rupture surfaces detected by AE monitoring (Moriya et al., 2015) and verified by underground observations.

Core examination for scientific drilling is very delicate and requires extraordinary carefulness and skills. To map and identify seismic sources in drill core, it is imperative that observations are systematically described and logging is approached in a set order so that no important evidence is left out during logging. The core was characterised by rock breccia and several comminuted rock fragments, which made it impossible to orient the core in certain areas. To quantify the intensity of fracturing, we used the RQD index. Several fractures were mapped in detail on the core and distinguished. Some of the observed fractures were drilling-induced, and others formed 'naturally' from in-situ stress concentration induced by mining excavations. Therefore, the intersection of seismic sources in the diamond drill core were identified successfully (Figure 7c).

5.3.5. Frictional sliding experiments

Because of the lengthy mining history at Cooke 4 mine, which was established in the 1960s, absolute stress levels in the remnant shaft pillar are extremely high compared to the original virgin stresses. The vertical virgin stresses in South African gold mining regions can be estimated from the equation below (Jager and Ryder, 1999):

$$\sigma_v = 0.027 * h \quad (1)$$

where, h (m) is the depth, and

σ_v (MPa) is the vertical component of the virgin stress.

Therefore, the vertical component of the virgin stress in our study area at depths of 1000 – 1200m is expected to be ~ 27 MPa - 32 MPa. Ogasawara et al. (2014b) used the Compact Conical-ended Borehole Overcoring (CCBO) method to measure absolute stresses in the remnant shaft pillar at Cooke 4 mine during mining activities. The measured values of principal stresses: major principal stress (σ_1) (~ 123 MPa – 136 MPa) and minor principal stress (σ_3) (~ 28 MPa – 35 MPa) (Ogasawara et al. 2014b). The measured major principal stress orientation is almost vertical, and the minor principal stress is almost horizontal. From these stress measurements, we could compute the average k-ratio, defined as horizontal stress (σ_h) over vertical stress (σ_v):

$$k = \frac{\sigma_h}{\sigma_v} \quad (2)$$

We computed the average prevailing k-ratios in the remnant shaft pillar (k ~ 0.2 - 0.3). Previous studies on the origin and formation of Ortlepp shears are well documented. They are analogous to 'conjugate shears' occurring under triaxial compressive stresses in laboratory experiments, and are characterised by normal displacement (van Aswegen, 2008). Spottiswoode (1979) conducted triaxial compressive experiments using East Rand Proprietary Mines (ERPM) quartzite at confining stresses of ~ 13 MPa – 28 MPa, which is equivalent to ~ 1000 m - 2000 m depths, respectively, to examine the energy required to produce new surfaces during failure.

In this study, we designed frictional sliding experiments that produced ruptures that closely resemble Ortlepp shears with comparable underground absolute stress conditions – updated k-ratio ~ 0.3 and confining stresses up to 20 MPa. Frictional sliding experiments were performed on drill core samples recovered near mining-induced normal faults under uniaxial and triaxial loads (5 MPa, 10 MPa, 15 MPa and 20 MPa). The experimentally induced gouge along the sliding rupture surfaces was carefully collected with a brush and analysed using Energy Dispersive X-Ray Spectroscopy (EDS) for chemical microanalysis, and scanning electron microscopy (SEM) in conjunction with laser particle size analyser for particle size distribution. The amount of experimentally induced gouge generated from frictional sliding experiments was measured and sieved into size fractions.

5.3.6. Particle size distribution analysis

We used the thin section micrographs to constrain the grain size distribution (PSD) of host rocks, before conducting frictional sliding experiments. This indicates the average original grain size. One of the pitfalls of using thin section micrographs is that the minimum size of measurable grains is ~2 µm (Keulen et al., 2007).

Laser diffraction particle size analysis has been used widely to measure the particle size distribution of the fault gouge material recovered from fault zones (Chester et al., 2005; Wilson et al., 2005; Keulen et al., 2007; Wechsler et al., 2011). We used the Malvern Mastersizer 2000 laser diffraction particle size analyser. The instrument provides a detection limit of submicron (0.02 µm – 2000 µm) of wet or dry materials of milligram quantities (Spectris plc., 2005). The fault gouge was collected and sieved following the frictional sliding experiments. The weight of the sieved fault gouge samples was measured. However, the experiments analysed the fault gouge particle samples that are less than 1 mm to micron scale due to the instrument resolution detection limit.

The fault gouge was mixed with distilled water and stirred to minimise aggregation of fault gouge particles. Further, to minimise aggregation, a vibrator was used to separate the particles into individual gouge particles. The sample was then gradually added to 800 ml of distilled water and once the sample reached the desired obscuration range the measurement was started. The laser particle analysis cannot distinguish between agglomerates (or aggregation of particles) and individual gouge particles. Therefore, the effects of agglomeration are further minimised when sampling a fresh rupture, which comprises of a minimal clay fraction (except in argillaceous material). In addition, the recovered fresh fault gouge has undergone limited alteration and weathering.

To complement the thin section micrographs and sieving and laser diffraction particle analyser methods, we used scanning electron microscopy (SEM) to measure the particle sizes of both the experimentally -created and naturally-occurring gouge (Sammis et al., 1987; Shao and Zou, 1996). For sample preparation, the fault gouge was glued to a SEM stub using double-sided tape, and a 30 nm thick carbon coating was applied. The coating was applied by heating the carbon source until it evaporates, resulting in deposition of carbon material onto specimens. This was done before samples were analysed under the SEM microscopy. The data collected were analysed for particle size distribution. In addition, to determine the chemical composition of the gouge particles measured, the energy-dispersive x-ray spectroscopy (EDS) was used.

5.3.7. Slip friction experiments

The study conducted friction experiments from low to high slip velocity (~1.0 mms^{-1} - 1200 mms^{-1}), characteristic of tectonic earthquakes slip velocities (Mizoguchi et al., 2007). We used the rotary-shear apparatus machine with the ability to conduct low to high-velocity friction experiments (Shimamoto and Tsutsumi, 1994; Tsutsumi et al., 2011). We conducted two types of friction experiments with (1) fault gouge (Figure 9a), and (2) without fault gouge 'rock on rock' (Figure 9b). The fault gouge volume recovered was very limited for Ortlepp shear fractures as compared to the Moab Khotsong fault rupture zone. Consequently, for Cooke 4 mine friction experiments, we crushed rock 'breccia' collected from the fault gouge and used it as additional fault gouge material. We called it 'artificial gouge'. This was done to increase the amount of 'fault gouge' material available for friction experiment work.

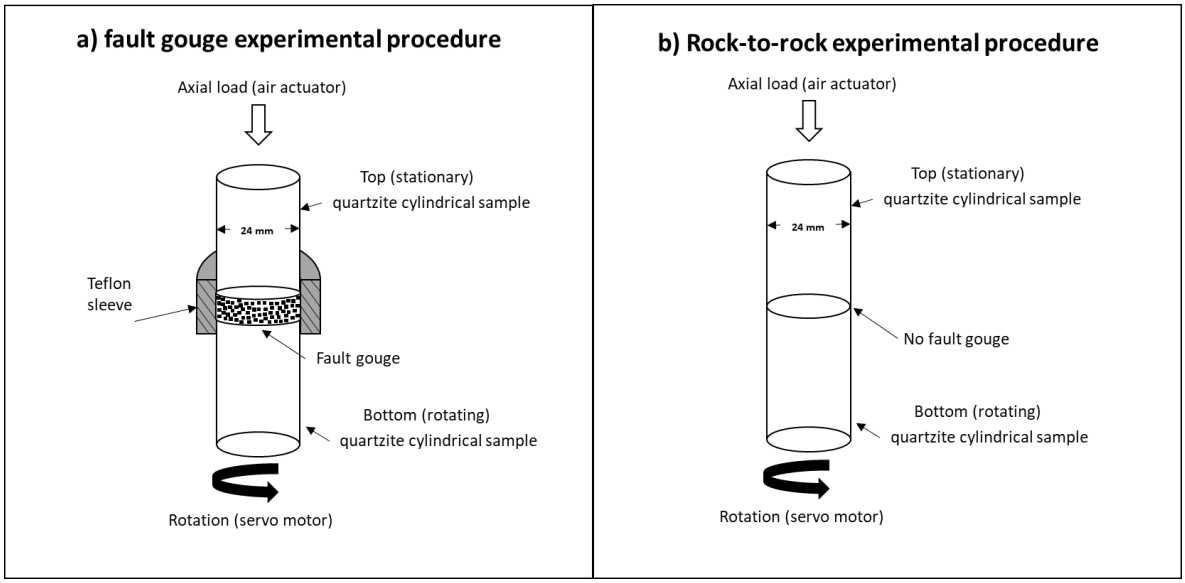


Figure 9. Graphic representation of the experimental set-up of two friction experiments: (a) with the fault gouge, and (b) without the fault gouge 'rock-on-rock'. Friction experiments were conducted on the sample using a rotary-shear apparatus at low, Intermediate to high-velocities similar to Ujiie and Tsutsumi (2010).

5.3.7.1. Fault gouge experimental procedure

For the first set of experiments, we inserted fault gouge between rock sliding surfaces. The procedure involves the use of a Polytetrafluoroethylene PTFE (Teflon) sleeves to prevent the fault gouge from leaking during shearing or rotation process. We used host rocks recovered from the remnant shaft pillar similar to the mining environment. They were prepared to be cylindrical shapes with parallel rough ends to make sure that deformation of the fault gouge is evenly distributed along sliding surfaces. The 80# SiC abrasive powder was used to roughen sliding surfaces. The '80# SiC' abrasive powder used is equivalent to ~180 µm roughness (Boulton et al., 2017). To achieve parallelism on roughened sliding surfaces, a pressure sensitive paper was used to check parallelism. We used quartzite cylinders with the diameter of ~24 mm and length of ~33 mm. These laboratory experiments were conducted at room temperature and in dry conditions since there is usually little water in mining environments because it is pumped out and only allowed to flood after the life of mine. The weight of the fault gouge used for each experimental run was measured to be ~ 0.5 g, and sandwiched between the pair of quartzite cylinders prepared from host rock samples. This gouge layer is approximated to be equivalent of ~0.5 mm thickness of the initial gouge before the experimental run starts. The experimental set-up with the fault gouge is illustrated in Figure 9a. The fault gouge is pre-loaded in the

axial direction between 30 - 60 minutes. The fault gouge is sheared by two sliding surfaces under 2 MPa normal stress.

The second set of experiments did not use the fault gouge between sliding surfaces. For the rock-on-rock experiments, we drilled a small 1 mm hole at the centre of each rock quartzite cylinders, and fastened the tip with the wire. This is done to mitigate tensile failure at the edges of the rock cylinders during friction experiments (i.e., during rotation). We also ensured that rotating and stationary cylinder surfaces were parallel, touching each other completely (Figure 9b).

Since the samples are cylindrical, the slip rate increases with sample radius from the centre of the axis of rotation to the edges of a sample. Therefore, the equivalent slip velocity (V_{eq}) is computed such that ($\tau \cdot V_{eq} \cdot S$) is the rate of frictional work on the sliding surface area S, assuming that the shear stress τ is constant over the entire fault surface (Shimamoto and Tsutsumi, 1994). This velocity is given by:

$$V_{eq} = \frac{4\pi}{3}\varphi R \quad (3)$$

where R is the radius of the samples, and

φ is the angular velocity.

5.3.7.2. PTFE (Teflon) sleeves friction and effect of confinement

We conducted friction experiments to assess and measure the effects of the Teflon sleeve on friction measured. We used a fixed velocity of 10 mms^{-1} and changed the normal stress: 2 MPa, 3 MPa, 4 MPa and 5 MPa. We calculated the shear stress and the friction coefficient of the Teflon sleeve from the slope of the shear stress and normal stress curve. Furthermore, we examined the influence of confining pressure induced by the Teflon sleeve on cylindrical samples on the measured friction.

In addition, to examine the stress exerted (confinement) by the Teflon sleeve on the measured friction, three runs of rock-on-rock experiments (with and without the Teflon sleeve) were conducted. The size of the Teflon sleeve inner diameter was varied to further investigate the relationship between the loose and tighter Teflon sleeves on measured friction. A fixed slip velocity of 10 mms^{-1} and normal stress 2 MPa were used. In these experiments a wire to reinforce the samples was not used, since we needed to put a PTFE sleeve on the cylinders.

A relatively large PTFE sleeve was used during the first experimental run (MVR944_1). The difference between the outer diameter of the stationary-side quartzite cylinder and an inner wall of the

PTFE sleeve was ~0.05 mm (e.g., the diameter difference is the same as sample in MVR918). During the second experimental run (MVR944_2), the PTFE sleeve was removed and the gouge powder was vacuumed (removing it from sliding surfaces). The PTFE sleeve was not used during this experimental run. During the third experimental run (MVR944_3), another PTFE sleeve was put around the samples. The sleeve was tighter compared to the first experimental run (MVR944_1). The difference of the diameter was ~0.18 mm.

5.3.8. Petrophysical properties

5.3.8.1. Elastic Properties

As described in Mngadi (2015), elastic properties such as Young's modulus and Poisson's ratio were computed from uniaxial compressive strengths (UCS) experiments using specimens from the remnant pillar in Cooke 4 mine. Ortlepp shears, when exhumed or sampled, provide critical information and evidence about the in-situ loading system during deformation. For instance, Ortlepp shears lacking the occurrence of a dynamic breakthrough rupture may indicate the origin from a stiff loading system; while Ortlepp shears with a breakthrough shear rupture and significant slip displacements may indicate a soft loading system (van Aswegen, 2013). This appreciation of the loading system such as soft and stiff is very important in understanding the complex process of the formation, physics and mechanism of these Ortlepp shears (van Aswegen, 2013).

Stiff rock mass tends to be associated with large values of Young's modulus (Perez, 2014). For instance, the quartzite rock mass, which comprise the remnant shaft pillar, is characterised by high Young's modulus and low Poisson's ratio (~0.13) (Mngadi, 2015). However, some weak soft lavas form part of the immediate hangingwall package, which constitute a soft loading system. Therefore, they may easily initiate the propagation of a dynamic breakthrough "unstable" rupture, resulting in large damaging seismic events. Young's modulus is a critical parameter that measures the ability of the rock mass to resisting permanent deformation or damage under applied stresses, and is related to the restoring force. Hooke's law states that deformation of the rock mass is directly proportional to the applied stress before exceeding the elastic limit and given by (Landau and Lifshitz, 1986; Sadd, 2005):

$$E = \frac{\sigma}{\varepsilon} \tag{4}$$

where E is Young's modulus (MPa),

σ is the stress (MPa), and

ε is the strain.

When the rock mass is under compressive loading, it will undergo extension in the orthogonal direction, and the ratio between the axial strain (ε_a) and the radial strain (ε_r) is called the Poisson's ratio (Lama and Vutukuri, 1978; Jaeger and Cook, 1979). The elastic limit for most materials including rock mass is between 0 - 0.5. The equation to compute the Poisson's ratio is given below:

$$v = \left|\frac{\varepsilon_r}{\varepsilon_a}\right| \tag{5}$$

where ε_a is the axial strain, and

ε_r is the radial strain.

5.3.8.2. Seismic velocities and density

To measure petrophysical properties of the rock mass such as the seismic wave velocities and densities, laboratory measurements were performed on core samples recovered from the remnant shaft pillar and geophysical borehole logging. These petrophysical properties are important for the estimation of the energy consumed from creating new fracture surface and energy radiated seismically (McGarr, 2000).

The study focuses on body waves (P-waves and S-waves). A very simple method to measure seismic velocities was used - a source and a receiver transducer pair. The source transmits seismic waves that travel through the rock mass to the receiver transducer. The traveltimes were recorded and measurements of the length of the sample were taken. The seismic velocity of the rock was then estimated (Mngadi, 2015). The P-waves are compressional and travel faster compared to S-waves. The P-wave velocity depends on bulk and shear moduli, defined by:

$$v_p = \sqrt{\frac{k+\frac{4}{3}G}{\rho}} \tag{6}$$

where G is shear modulus

ρ is the density, and

k is the bulk modulus

Contrary to P-wave velocity, the shear waves (S-waves) do not travel through liquids and depend on the shear modulus, defined by:

$$v_s = \sqrt{\frac{\mu}{\rho}} \tag{7}$$

5.3.9. Reflection seismic method

The earliest records of the application of seismic reflection technique in South Africa were in the mid-1960s. The method was used for exploration of hydrocarbons in the Karoo Basin (Fatti, 1987). In this regard, a former South African National Oil Company called Soekor (later merged with Mossgas to form now PetroSA) acquired more than ~13 000 km of 2-D seismic reflection data between 1966 and 1971 (Fatti, 1987; Scheiber-Enslin et al., 2014). Scheiber-Enslin et al. (2014) found that intrusive rocks (dolerite sills and dykes) produced strong reflections due to a significant acoustic impedance contrast between sills and the host rocks. These intrusive rocks were also intersected and confirmed by borehole information (e.g., sonic and geological logs).

The vertical resolution limit of ~ 70 m is larger than most dolerite sills and dykes thickness encountered in the Karoo Basin, which means the survey could not resolve the top and bottom boundary of individual sills thinner than 70 m. Consequently, a cluster of thin sills were treated as a thick sill zone. Furthermore, they reported that it is difficult to resolve the exact termination of individual sills due to the low quality of the data, and the effect of interference (Scheiber-Enslin et al., 2014). Nonetheless, Fatti (1970) described the lateral variations in reflected energy from dolerite sills ranging from low to high frequency resulting from thickness variations of the sill zones. In instances where dolerite sills occur at shallow depths (< 1 km), the signal-to-noise ratio becomes poor since most of the incident energy is reflected back to surface resulting in deeper reflectors being imaged poorly. In addition, sills tend to produce multiples, which may be difficult to distinguish from real geological reflectors (e.g., intrusive rocks) without constraining them with boreholes (Scheiber-Enslin et al., 2014).

In South Africa, the application of reflection seismic technique for mineral exploration began in the 1980s (Campbell and Peace, 1984; Durrheim, 1986). Reflection seismic technique was first used to conduct gold exploration in the hard rock environment (Malehmir, et al., 2012; Manzi et al., 2012a; Manzi et al., 2012b), which was later used to explore for platinum and base metals. Since then, reflection seismic technique has been a standard method deployed for mineral exploration and mine design in South Africa. Anglo American plc, during their exploration in the Kaapvaal Craton, acquired more than 16 000 km of 2-D reflection seismic surveys. This was subsequently followed by the acquisition of seven 3-D reflection seismic surveys to assist gold mine planning and development (Pretorius et al., 2003). In South Africa, one of the earliest well-known achievements of reflection seismic technique was the

delineation of the De Bron Fault. This fault is situated in the Joel Mine lease area, Free State Gold Fields (Campbell and Crotty, 1990). Since then seismic reflection has contributed immensely to the discovery of new deposits such as South Deep and ore bodies in the Bothaville Gap (Gray et al., 1994).

5.3.9.1. Acoustic impedance

Seismic reflection imaging offers undoubtedly one of the best subsurface geophysical image resolutions. However, the seismic image still has a resolution limit. When a source is set off near the surface, emitted elastic waves spread spherically in all directions from the source (Sheriff, 2002). Some elastic waves are transmitted into the subsurface and others are reflected back to surface when they encounter subsurface lithological contrast. The amount of energy reflected from the subsurface contrasts is approximately 0.1 - 10%. The energy is recorded using surface receivers/geophones. Times and amplitudes of these reflections are recorded and used to interpret the subsurface. As any geophysical method, seismic reflection imaging is sensitive to only a specific physical property of the rock. This property is called acoustic impedance, which is the product of the bulk density (ρ) and seismic wave velocity (V) (Herron, 2011).

$$Z = V * \rho \tag{8}$$

where V is the P-wave velocity and ρ is the density.

P-waves (V_p) are compressional (or longitudinal) and they travel at approximately twice the velocity of shear waves (S-waves). The acoustic velocity of elastic waves depends on the physical properties (elastic properties) of rocks, such as the bulk modulus and shear modulus, and on the bulk density of the rock (Simm and Bacon, 2014). Porous, weathered or fractured rocks will tend to have lower velocities than a fresh rock.

$$V_p = \sqrt{\frac{k+\frac{4}{3}\mu}{\rho}} \tag{9}$$

where V_p is the P-wave velocity, k is the bulk modulus and μ is the shear modulus (rigidity).

At the boundary/interface between two different media, energy is partitioned and that could be described using Zoeppritz equations (Shuey, 1985). There are two boundary conditions that must be met, tangential and normal components of displacement and stress at the interface must be continuous. The reflection coefficient and the transmission coefficient can be derived from acoustic impendence of two media. These coefficients are ratios of the amplitude at the incidence and the amplitude that is

reflected or transmitted. A reflection can be observed if there is a sufficient acoustic impedance contrast at the interface (Simm and Bacon, 2014). The required minimum reflection coefficient is 6% between two lithological units. This means high acoustic impedance contrast (≥ 6%) between two rock units will result in strong reflections, which makes the interpretation of the subsurface geology relatively easy as compared to low acoustic impedance contrast (< 6%), which results in weak reflections that are difficult to interpret (Bacon et al. 2003; Herron, 2011; Simm and Bacon, 2014).

$$R = \frac{A_R}{A_o} = \frac{V_2\rho_2 - V_1\rho_1}{V_2\rho_2 + V_1\rho_1} \tag{10}$$

where R is the reflection coefficient, A_o is the incidence amplitude, and A_R is the reflected amplitude.

Transmission coefficient:

$$T = \frac{A_T}{A_o} = \frac{2V_1\rho_1}{V_2\rho_2 + V_1\rho_1} \tag{11}$$

where T is the transmission coefficient, A_o is the incidence amplitude and A_T is the transmitted amplitude.

5.3.9.2. Seismic resolution

The temporal resolving power of the seismic data is commonly defined by the tuning thickness of data. It is a phenomenon of constructive or destructive interference of waves from closely spaced events or reflections. This is based on the fundamental wave equation. Vertical seismic resolution is the ability to distinguish between two closely spaced reflectors at depth. Seismic resolution depends on the bandwidth of the source pulse (Herron, 2011).

$$\lambda = \frac{V}{f} \tag{12}$$

where λ is the wavelength, *f* is the dominant frequency and V is the velocity. Frequencies decrease with depth because of the attenuation of seismic waves due to higher frequencies, and this also decreases the resolution at depth. Vertical resolution is estimated as $\delta \sim \lambda/4$ (Widess, 1973; Herron, 2011). Targets that are thinner than the quarter wavelength can still be detected, but their amplitude will be primarily dependent on the geometry of the target and not solely on the impedance contrast.

5.3.9.3. Fresnel zone

The spatial resolving power of seismic data is usually described in terms of the Fresnel zone. The Fresnel zone is the area on a reflector that returns energy to the receiver within half a cycle of the first reflection (Lindesay, 1989; Herron, 2011). The lateral extent of reflectors can only be accurately delineated if it is wider than the width of the Fresnel zone. The equation that defines the width of the first Fresnel zone (F_r) is given by:

$$F_r = \frac{V}{2}\left(\frac{TWT}{f}\right)^{\frac{1}{2}} \quad (13)$$

where F_r is the first Fresnel zone, TWT is the two way travel time to a reflector, V is the average propagation velocity and *f* is the dominant frequency of the seismic signal impinging on the reflector. Targets that are laterally shorter than Fresnel zone can also be detected, but the response may be a combination of reflections and diffractions (Malehmir, et al., 2013).

6. Summary of manuscripts

These manuscripts form the foundation of this PhD thesis. Therefore, in line with that view, this chapter provides summaries of the manuscripts. Here, the candidate will briefly describe the scientific ideas and key findings for each manuscript. The next chapters contain the manuscripts as submitted to various peer-reviewed journals. The manuscripts are the outcome of many efforts, engagements and hard work from SATREPS team to DSeis team members. Thus, the recognition is afforded correctly to my co-authors and co-workers, including laboratory technicians.

While the candidate did most of the work, it recognise that the quality of my research work was improved by the contributions of many co-authors. The candidate also recognise the efforts required to secure funding, install sensors and service the equipment, drill boreholes and curate the core to conduct complementary research. In Chapter 6, the candidate outlines his contribution clearly in each summary of the manuscript.

6.1. Geometry of brittle shear fractures occurring ahead of tabular mining stopes

The candidate performed the core logging, underground mapping, petrographic analyses, rock mechanics experiments and analysis of the high resolution microseismic data collected by the SATREPS team. The candidate didn't install seismic sensors or process the microseismic data, but rather interpreted the data and developed a fracture model. The candidate drafted the manuscript and prepared all the images.

The full version of manuscript 1 is presented in Chapter 7 of this PhD thesis in a journal format. The study used a multidisciplinary approach such as the (1) high-resolution microseismicity, (2) underground mapping, (3) petrographic analysis, and (4) rock mechanics to address the risks posed by fall of ground (FOG), rockbursts and seismicity to mine workers, infrastructure, mining operations and the public. The integration of multidisciplinary datasets allowed the team to develop the fracture model for different geotechnical zones such as weak (or soft) lava hangingwall and quartzite/conglomerate footwall.

In this manuscript, the study found that each rock type exhibits a specific rock mass response to loading. This is expressed by geotechnical zones where area-specific mining-induced fractures occur. The study found that more than ~90% of microseismic events are associated with fracturing ahead of the mining face, which delineated Ortlepp shears.

This study further shows that these fracture patterns are consistent with the fracture model proposed by Roberts and Schweitzer (1999) for the geotechnical zone characterised by weak/soft lava hangingwall and quartzite/conglomerate footwall (Figure 14; Manuscript 1). Underground microseismic monitoring and mapping were successfully used to delineate this weak geotechnical zone. This has important implications for the improvement of mine safety and the choice of mining methods and support, which will contribute to greater safety (zero harm).

6.2. Dynamic rupture propagation of brittle shear fractures

The candidate was trained in drilling workflow and terminologies; health, safety and environment; on-site management; sample handling and curation; downhole logging planning and execution; and data management by the ICDP Training Programme at the GeoZentrum KTB, Windischeschenbach, Germany. The candidate was part of the key personnel who worked with the drilling team for oversight and quality assurance (but did not necessarily conduct drilling). In addition, the candidate contributed to core curation for Cooke 4 mine, moving of the core from underground to surface, the University of the Witwatersrand and Council for Scientific and Industrial Research (CSIR).

The candidate performed core logging, petrographic analyses and fault gouge analysis. Experiment design, sample preparation and experiments were conducted by the candidate in Kyoto University, Japan. The candidate interpreted the results, and drafted the manuscript and prepared all the images.

The full version of the manuscript is presented in Chapter 8 in a journal format. This section discusses the rupture propagation and the weakening behaviour of underground shear fractures along shear zones. A multidisciplinary approach to research fundamental questions of the Earth Sciences were used – how do earthquakes propagate along shear zones, and what factors controls earthquake rupture propagation?

Mining at deep and high-stress levels induces stress fracturing around and ahead of the mining stope, with the Ortlepp shears occurring tens of metres ahead of the mining excavation (Moriya et al., 2015). These brittle shear fractures are particularly prone to large damaging seismic events (Mw 1-4). Moriya et al. (2015) and co-workers used acoustic emissions (AEs) to detect events down to Mw -5 to delineate these brittle shear fractures, and reveal that they resemble “Ortlepp shears”. The ICDP-DSeis

allowed us to drill and recover the ruptured rock mass and fault gouge from the remnant shaft pillar at 1 km depth, at Cooke 4 gold mine, South Africa.

We performed two types of friction experiments: one with a fault gouge layer between two sliding surfaces, and the other without a fault gouge layer 'rock-on-rock', both under room dry conditions at slip velocities ranging from ~1.0 mm/s to 1200 mm/s. These friction experiments revealed a remarkable difference in the frictional weakening behaviour, e.g., rock-on-rock friction experiments show weakening behaviour at lower slip velocity (~ 5 mm/s) and generally have lower frictional strength than those with the intervening fault gouge between sliding surfaces. This study shows that the presence of the fault gouge layer between sliding rock surfaces delays the onset of fault weakening.

It is proposed that flash heating may be the main active weakening mechanism within both our gouge and rock-on-rock experiments and provides a feasible account for the observed weakening. Here, we suggest that we may be able to describe brittle rupture propagation process along underground brittle shear zones by conducting low, intermediate and high slip velocity friction experiments with and without an intervening fault gouge between sliding rock surfaces. These findings should have important implications for the modelling of rupture propagation processes in underground shear zones, a phenomenon that influences the severity of rockbursts, and hence the safety of mine workers and mining operations.

6.3. Factors controlling the physics and mechanics of M5.5 rupture

Similar to the Cooke 4 mine drilling endeavour, the candidate was on-site and worked with the drilling team at Moab Khotsong mine, being responsible for oversight and quality assurance. Furthermore, the candidate contributed to core curation, logging and management, including moving the core from underground to surface and Council for Scientific and Industrial Research (CSIR).

The manuscript builds on the work of several co-workers in the ICDP-DSeis team, which are acknowledged through the citation of conference presentations, papers and theses. The candidate performed the core logging and petrographic analyses. In particular, a detailed study of 'core C', which penetrated the rupture zone. This was used to constrain the material properties and aid with the reprocessing of legacy seismic data. The candidate conducted forward modelling and re-interpreted reflection seismic data.

The candidate analysed reflection seismic data in conjunction with Hole C and the other two cores (Hole A and Hole B), and the location of microseismic events (which were studied by other members of the ICDP-Dseis team). The candidate conducted friction experiments to estimate the frictional properties of the recovered fault gouge. This was compared to Ortlepp shears occurring ahead of the stope face. The candidate drafted the manuscript.

The full version of manuscript 3 is presented in Chapter 9 of this PhD thesis in a journal format. This section discusses the structural architecture, the role of geology, physics and mechanics controlling the unusual large M5.5 strike-slip earthquake compared to the Ortlepp shear fractures (normal faults) occurring ahead of the stope at Cooke 4 mine with moment magnitudes of Mw 1-2.

The largest mining-related earthquake to date occurred in the Klerksdorp goldfields on 5 August 2014, hundreds of metres below the Moab Khotsong mine. The M5.5 earthquake had an 'unusual' strike-slip mechanism compared to common mining-induced ‘normal faults’ observed at Cooke 4 mine, which occur ahead of the mining excavation at mining levels. In a rare serendipitous case, the M5.5 earthquake occurred within an area traversed by legacy 2-D reflection seismic data acquired in 1992 for gold exploration. This legacy 2-D reflection seismic data was re-processed and re-interpreted using modern signal processing methods to identify geological structures that hosted the M5.5 earthquake.

Also, the earthquake was recorded by the underground in-mine seismic network near the source region. The DSeis team used the mine seismicity data to delineate spatially the M5.5 rupture, and drilled into this active seismogenic zone situated 3.5 km below the surface. To minimise drilling costs, the DSeis team used the Moab Khotsong mine infrastructure to access the drilling site situated ~ 2.9 km, a few hundred metres above the M5.5 earthquake rupture.

The DSeis team successfully drilled and recovered the fragile core, host rocks, rock breccia, dolerite sills and lamprophyre dyke. The drilling also intercepted hypersaline brine. The DSeis team used a specialised triple-tube drilling technique to maximise core recovery especially within tens of metres of the seismogenic zone characterised by a sandy fault gouge material and core-loss.

Reprocessing and re-interpreting the legacy 2-D reflection seismic data revealed that the geological structure that hosted the M5.5 earthquake crosscut the entire Witwatersrand Supergroup up to the Transvaal Supergroup, and potentially the base of the Karoo Basin (Figure 18 and Figure 19; Manuscript 3). Also, the reflection seismic data revealed several dolerite sills characterised by high seismic amplitudes.

The integration of the reflection seismic data and mine seismicity data including the DSeis drill core data such as geological core logging and geophysical borehole logging (gamma, density and velocity) allowed us to fully describe and make clear a near-vertical structure, striking NNW-SSE. The relatively younger and highly altered lamprophyre dyke intruded into this existing fault and older dolerite dykes. The fault was re-activated as a left-lateral strike-slip fault.

Using the recovered fault gouge material, we measured the particle size distribution of the gouge and performed the XRD analysis. The gouge minimum particle size approach ~ 10 μm and the fault gouge composition is predominantly talc and biotite minerals (> 40%). In addition, we performed friction experiments on the Moab Khotsong fault gouge sample at slip velocity of ~100 mm/s and normal stress of 2 MPa similar to friction experiments conditions conducted for Cooke 4 mine gouge samples.

Friction experiment results show that the peak friction coefficient of ~1.0 decreased exponentially to steady-state friction of ~0.66 over a slip weakening distance of ~9.1 m. The friction weakening behaviour and steady-state friction values are comparable with results obtained from normal faults occurring ahead of the mining stope at Cooke 4 mine. However, in this case, talc and biotite may be controlling the friction weakening mechanism, acting as a lubricant, whereas at Cook 4 mine friction weakening mechanism may be controlled by the frictional heating (flash heating).

The study found three active processes that influence the M5.5 earthquake seismogenic zone: (1) the complex structural architecture of the seismogenic zone (e.g., interception of fault, lamprophyre dykes and dolerite sills); (2), the mechanical process induced by tectonic and/or mining-related stresses and the weakness of lamprophyre dykes; and (3), the mechanical and chemical processes resulting from the water and rock interaction.

6.4. The energy budget of the mining-induced brittle shear fractures

The candidate performed triaxial compressive test experiments and density and seismic wave velocity measurements of the cores. The candidate further performed the particle size distribution measurements and analysis, computed energy budget and compared with Ortlepp shears. The candidate drafted the manuscript.

A highly stressed rock volume in deep mines (e.g., during mining of remnants shaft pillars) often increases the risks posed by normal-faulting earthquakes to mining operations. We present particle-size distribution analysis and the energy budget of the mining-induced ‘Ortlepp’ shear fractures during

seismic fault motion in Deep South African gold mines. In this unprecedented study, we directly probe seismogenic zones at great depths to better understand the controls of the seismogenic processes. To achieve this, we drilled (~41 m length) into the seismogenic zone at 1 km below the surface at Cooke 4 mine, using highly specialised triple-tube drilling with metal split spoons (common in scientific drilling).

We recovered host rocks, freshly fractured materials, newly formed fault gouge (commonly known as rock flour in South African gold mines) and Ortlepp shear fracture systems. This was compared to the frictional sliding experiments with confining stresses of up to ~20 MPa, comparable to the remnant pillar in-situ horizontal and vertical absolute stresses conditions at 1000 - 1200 m depth at Cooke 4 mine. Mining and experimentally induced fractures exhibit similar characteristics, such as the presence of the fault gouge and rough rupture surfaces. We computed the energy required to create a new fracture surface during an earthquake process.

These findings revealed extremely low surface energy values (0.15% and 0.56%) as a percentage of the total energy dissipated. These results suggest that only a small portion of the energy budget is required to create new fracture surfaces, which agrees with the expectations. When comparing to previous studies of seismic efficiency, the surface energy is in the same order of magnitude.

6.5. Detecting mining induced seismic sources in borehole core.

The candidate is the second author of this manuscript. The candidate worked at the core shed and was involved in core curation and transportation. The candidate performed the core logging, petrographic analyses, detailed fracture analysis and identification of the seismic source with the first author. The first author drafted the manuscript. However, the candidate contributed in expanding the introduction, analysis, discussion and added the abstract on the manuscript. In addition, the candidate added Figures 1 -4 and all Tables 1-4.

This manuscript was presented in the Appendix purely because I am the second author. This manuscript discusses and develops a criterion that may be used to identify shear fracture ruptures in drill core. At Cooke 4 mine, the DSeis team drilled the borehole especially to intersect and recover a series of shear ruptures delineated through acoustic emission (AE) monitoring and verified by underground observations.

Deep level mining requires knowledge of geological information, rock mechanics and mine seismology. Seismograms generally do not provide accurate hypocentre locations and merely reveals the location of rupture commencement. Big slip seismic events can span hundreds of square metres and the area of maximum displacement can be far away from the “location” as reflected in the seismic data. Mining-induced shear fractures may undergo ‘unstable’ dynamic rupture propagation that results in damaging seismic events under a soft loading system. Therefore, advance knowledge of their position in space (e.g., 3-D geometry) form an essential part of the structural model used as an input to mine and support design. Furthermore, precisely resolving the location of seismic sources and understanding their mechanical and physical characteristics is useful and enable workers to evacuate areas of potential seismicity and falls of ground. This mitigate the risks posed by these seismic sources to workers.

Here, we suggest that to identify seismic sources in drill core it is important to select the correct drilling technology such as the triple-tube core barrel. This is important for maximum core recovery and preservation such as the fragile fault gouge, rock breccia, shear rupture surfaces and soft slickensides along the rupture surface. It also requires a strict drilling protocol such as minimal core disturbance before core logging and detailed ultra-high-resolution imagery of the drill core. Detailed drill core observations revealed that the most important aspect of a shear ruptures is the presence of finely comminuted fault gouge. In addition, often associated with the preservation of soft slickensides and a cross fabric on shear rupture surfaces. The presence of fine rock fragments and fault gouge in the core tray may also indicate the presence of a shear fracture.

7. Geometry of brittle shear fractures occurring ahead of tabular mining stopes

The manuscript has been prepared in accordance with journal requirements.

Integration of underground mapping, petrology, and high-resolution microseismicity analysis to characterise weak geotechnical zones in deep South African gold mines

International Journal of Rock Mechanics and Mining Sciences, 114, 79-91

https://doi.org/10.1016/j.ijrmms.2018.10.003

Mngadi, SB[a,j,k], Durrheim, RJ[a,j,k], Manzi, MSD[a,j,k], Ogasawara, H[b,j,k], Yabe, Y[c,j,k], Yilmaz, H[d,j,k], Wechsler, N[e,k], Van aswegen, G[f,k], Roberts, D[g,k], Ward, AT[h], Naoi, M[i,j,k] , Moriya, H[c,j,k], Ishida, A[b,k], SATREPS team[h], ICDP DSeis team[i]

[a] School of Geosciences, University of the Witwatersrand Johannesburg, PO Bag 3, WITS, 2050, Republic of South Africa.

[b] College of Science and Engineering, Ritsumeikan University, 1-1-1 Noji Higashi, Kusatsu 525-8577, Japan.

[c] Graduate School of Engineering, Tohoku University, 6-3, Aza-Aoba, Aramaki, Aoba-ku, Sendai 980-8578, Japan.

[d] School of Mining Engineering, University of the Witwatersrand Johannesburg, PO Bag 3, WITS, 2050, Republic of South Africa.

[e] Department of Geosciences, Tel Aviv University, P.O. Box 39040, Israel

[f] Institute of Mine Seismology, 7129 Somerset West, Private Bag X15, Republic of South Africa

[g] Council for Scientific and Industrial Research, Centre for Mining Innovation, PO Box 395, Pretoria, Republic of South Africa.

[h] Cooke 4 Shaft, Sibanye Gold Limited, PO Box 82, Westonaria, Republic of South Africa.

[i] Earthquake Research Institute, The University of Tokyo, 1-1-1 Yayoi, Bunkyo-ku, Tokyo 113-0032, Japan.

[j] JST-JICA Science and Technology Research Partnership for Sustainable Development (SATREPS)

[k] The International Continental Scientific Drilling Program (ICDP) Dseis team

ABSTRACT

A highly-stressed shaft pillar is prone to large seismic events (Mw 1-4), fall of grounds and rockbursts, which may cause injuries and loss of production, especially in weak geotechnical zones. It is thus important to identify weak geotechnical zones in order to mitigate risks. In this study, we present integrated studies (underground mapping, petrology, rock mechanics and high-resolution microseismicity analysis) to understand the different geotechnical zones in the shaft pillar of Cooke 4 mine in South Africa. The footwall of the remnant shaft pillar comprises the Upper Elsburg reef of the Mondeor Formation, while the Ventersdorp Contact Reef (VCR) of the Venterspost Formation and soft/weak lavas of the Westonaria Formation form the hangingwall. Results from underground mapping and microscopic analysis show that the shaft pillar is composed of quartzites, pebbly quartzites, argillaceous quartzites and conglomerates. Underground mapping further shows that the shaft pillar is characterised by several discontinuities, which vary from minor to macro scale fractures. Laboratory uniaxial compressive strength (UCS) tests indicate that quartzite has the strongest strength, followed by pebbly quartzite, argillaceous quartzite and lastly, conglomerate. Analysis of high-resolution acoustic emissions (AEs) clusters indicates that the majority of AEs are associated with the mining stope faces. The clusters show the formation of Ortlepp shears ahead of the stope, which is caused by the excavation-induced stress field. Microseismic data further reveal that the fracture turning-point occurs in the soft strata (weak hangingwall lavas). The integration of these datasets has allowed us to develop the fracture model for different geotechnical zones, which concurs with previous models developed for the similar underground environment (i.e., weak/soft lava hangingwall and quartzite/conglomerate footwall). This has major implications for future mining, support, production and safety.

1. INTRODUCTION

Miners working in deep gold mines of South Africa face various hazards, including rockfalls and rockbursts associated with mining-induced fracturing and seismic events. Mining at deep levels in South African gold mines induces fracturing around an underground excavation, especially in highly stressed zones at depths greater than 1 km [1-3]. In this paper, we discuss the importance of integrating geological information (underground mapping and petrography), rock mechanical and microseismicity studies to address the risks posed by rockfalls and rockbursts to mine infrastructure, ore extraction operations and workers in deep and highly stressed mines in South Africa. The study area is situated

at Cooke 4 mine (previously known as Ezulwini mine), which is situated in the Witwatersrand Basin (Figure 1), famous for hosting one of the world's largest gold deposits.

Cooke 4 mine is an underground mine constructed in the 1960s with historical production of approximately 14 million pounds of uranium and 12 million ounces of gold. Historically, the mine exploited the Ventersdorp Contact Reef (VCR) of the Venterspost Formation. However, given the challenges encountered with support for the weak hangingwall of ~ 20 m thick zone of soft ultramafic lavas (48 – 138 MPa) of the Westonaria Formation (WAF), the mine ceased to exploit these reefs [4, 5]. The mine was put on care and maintenance in 2001 and re-opened in 2010 to exploit the orebody locally termed the Upper Elsburg reefs in the shaft pillar situated 1 – 1.2 km below surface (Figure 2). The Upper Elsburg reefs are made up of the Upper Elsburg Individuals (Waterpan Member) and the Upper Elsburg Massives (Modderfontein Member). The mine was closed again in 2017. The seismic catalogue used for this paper was collected from 2011 to 2012.

Primarily two types of fractures form around mine stopes viz., extension and shear. Two sets of extension fractures occur, one with a shallow dip, and the other forming parallel to the major principal stress (Figure 3). Extension fractures usually form close to the stope face. They are controlled by the shape of the stope face, and are easily observable in the hangingwall [2, 3]. Shear fractures are inclined to the major principal stress direction and they usually form ahead of the stope face [2, 6, 7]. These are referred to as Ortlepp shears [8], and are major sources of seismicity with moment magnitudes M_w 1-4, which pose risks to mining operations and mineworkers [8]. A local measurement of stress undertaken by Ogasawara et al. [9] at Cooke 4 shaft was 127 MPa, thus indicating the high levels of stress that make the rock surrounding the stope highly susceptible to stress fracturing.

In mining and earthquake seismology, it is important to understand the micromechanics of rocks [10], as it influences the formation of microcracks and how they coalesce to form shear fault planes, which often result in slip, causing microseismicity, depending on the magnitude of confining stress [11]. Microscopic observations have demonstrated that brittle rocks form (1) tensile microcracks that are parallel to the maximum stress direction when no confining stresses are applied; (2) tensile microcracks that interact and coalesce to form a macroscopic shear fault plane, especially in the presence of less-extreme confining stresses; and lastly (3) ductile flows in the presence of extreme confining stresses [12-14]. Furthermore, crack nucleation occurs at microscopic heterogeneities present in a rock. These usually occur at (1) the boundaries between different particles or materials, (2) pre-existing micro-

discontinuities, (3) cavities at grain boundaries, (4) matrix shearing caused by rotation, and (5) slip of hard mineral grains such as quartz [15, 16]. In brittle, porous rocks such as sandstones, shear localization often develops post peak stress. Most of the cracking that occurs prior to peak stress is intergranular [17], which is contrary to crystalline rocks where microcracking occurs in an intragranular fashion.

Previous mapping of underground fractures around the Witwatersrand Basin mining areas show that the mining-induced fracture pattern is largely influenced by the characteristics of the rock layers associated with the Ventersdorp Contact Reef (VCR) [2, 7, 18-24]. The turning (or inflection) point of the fractures occurs in the softer strata. In areas where the hangingwall comprises the soft lava, the turning point is positioned in the hangingwall; while in areas where the hangingwall comprises the hard lava, the turning point is positioned in the footwall (Figure 4) [24, 25].

Seismic waves emitted during fracturing were monitored using a dense state-of-the-art network of high sensitivity acoustic emission sensors near the mining area [26]. Most deep level gold mines in South Africa have in-mine seismic monitoring systems that record seismicity down to Mw -1. However, these systems are not capable of detecting very small seismic events down to Mw- 5. These small moment magnitudes can map the growth of macrofractures associated with underground excavations. However, a high sensitivity monitoring seismic network makes it possible to detect numerous weak microseismic events. Recently considerable attention has focused on the monitoring of the microseismic events associated with hydraulic fracturing and petroleum reservoir engineering. However, not much effort has been put in active deep mining operations to monitor seismicity with such high sensitivity seismic sensors. The Science and Technology Research Partnership for Sustainable Development (SATREPS) project deployed acoustics emission (AEs) sensors in underground operations to monitor and image these underground shear fractures around underground excavations [27, 28]. In this paper, we present the results from an integrated study taken to identify geotechnical zones defined by composition and fracture patterns in hangingwall and footwall rocks, using (1) high-resolution microseismicity, (2) underground mapping, and (3) petrographic analysis (core samples and microscopic analysis). This work is an attempt to close the gap between the rock engineering and geology. Most rock engineering studies tend to ignore the implications of the rock texture, macrostructures, microstructures and mineral assemblage (beside quartz) for rock strength, mechanical behaviour, fracture patterns and seismicity.

2. WITWATERSRAND BASIN

2.1. Regional Geology

The geology of the Archaean Witwatersrand Basin has been described by many authors (e.g., [29-31]) and the details are not repeated here. In summary, the Witwatersrand Basin formed over a period of 360 Ma (3.07- 2.71 Ga) and Dominion Group [31]. Witwatersrand Supergroup sediments were deposited on the Archaean Kaapvaal Craton (~3.6 - 3.2 Ga). The Witwatersrand Supergroup is subdivided into the (lower) West Rand and (upper) Central Rand groups [30, 33]. It is covered by the mostly volcanic rocks of the Ventersdorp Supergroup (2.72 - 2.63 Ga) [30]. The West Rand and Central Rand groups decrease in thickness towards the south-eastern margin of the basin. The West Rand Group is dominated by clastic sedimentary rocks and minor lavas [25]. Its average thickness is 4.6 km. The dominant rock types are fluvial quartzite, conglomerate and shale. The Central Rand Group, which hosts more than 70% of the gold bearing horizons, lies on top of the West Rand Group. The Central Rand Group consists of quartzite and conglomerate packages and minor shale and lava bands [34]. The group has an average thickness of 2.9 km.

The Witwatersrand Basin is structurally complex. The basin is characterized by major listric faults and their related drag folds, which are attributed to extensional tectonics that occurred during the deposition of the Ventersdorp Supergroup [35–38]. It is also intruded by dolerite sills and syenite dykes of four different ages: Karoo (~150 Ma), Pilanesberg (~1.30 Ga), Transvaal (~2.20 Ga), and Ventersdorp (~2.60 Ga). Many of these structures (joints, veins, fissures, dykes and faults) cut through reefs (conglomerates) and may cause loss of ore [39]. These structures may be associated with high stress instabilities that may result in failure and seismicity [40; 41].

2.2. Cooke 4 Shaft and Stratigraphy

Our study area in Cooke 4 mine is situated in the Mondeor Formation of the Turffontein Subgroup [42] at the top of the Central Rand Group. The shaft pillar is made up of the Upper Elsburg reefs of the Mondeor Formation (Figure 2). [42]. The Elsburg Individuals underlie the Elsburg Massives and consist of four well-defined conglomeratic units that are informally identified as the EA, EB, EC and ED. These conglomerate reefs display a general variation of lateral facies. The ED unit (a well-defined quartz wacke) separates the Upper Elsburg Individuals (Waterpan Member) from the overlying Upper Elsburg

Massives (Modderfontein Member). The Elsburg Massives reefs comprise three conglomerate packages, namely MA, MI and MB, which also vary in lateral facies [31]. The reefs that were mined were part of the MB to ED conglomerate reefs [39]. Dominant lithologies are alternating conglomerates and quartzites. The average dip of these rocks is 16°, south-east to south on average [4].

The Ventersdorp Contact Reef (VCR) is part of the Venterspost Formation, the basal unit of the Ventersdorp Supergroup [43], and overlies the Elsburg Massives. The Ventersdorp Supergroup is largely made up of volcanic rocks. Close to the base of the Ventersdorp lavas, a weak 20 m zone of rich ultramafic lavas of the Westonaria Formation (WAF) is encountered [5]. The WAF is made up of thick packages of ultramafic and tuffaceous lava, which are classified as soft (48 – 138 MPa) and medium to hard lava (42 – 313 MPa) (see Table 1) [4]. This diverges from the common Witwatersrand Supergroup orebodies, which have competent quartzite hangingwalls [24].

Underground mapping and reflection seismic data reveal that the area is characterized by major normal, dextral wrench and thrust faults. They all strike approximately northeast-southwest with throws that vary from 15 to 40 m. The most dominant of these are normal faults (e.g., the Roodepoort/Panvlakte Fault, Saxon Fault and the Doornkop Fault) with downthrows between 250 m and 550 m. Several other smaller scale faults have downthrows ranging from 20 m to 150 m [5].

3. METHODOLOGY

3.1. Petrography

In 2010, 29 boreholes were drilled underground at Cooke 4 mine, level 38 for the project ‘Observational studies in South African mines’ [40]. All boreholes were less than 100 m in length with a core diameter of 42 mm. These boreholes were drilled sub-parallel to the bedding planes. The cores were logged, and rock samples were selected for thin section analysis and rock mechanical testing. The core samples generally consisted of four rock types, viz. quartzite, pebbly quartzite, argillaceous quartzite and conglomerate. Description of these rocks included colour, composition (which is characterized by mineralogy) and texture (grain size, grain shape and grain framework). These properties (except colour) are known to influence the mechanical behavior of the rocks when subjected to stress [44, 45]. The petrographic analysis included the characterization of the metamorphic rocks forming the shaft pillar, using: (1) microscopic analysis with transmitted light, i.e., thin sections; (2) core/hand specimens; and (3) underground observations. Qualitative assessment of rock texture,

macrostructures, microstructures and mineral assemblage in a rock was done to provide an indication of rock strength, behaviour under stress, and the most likely failure mechanism.

3.2. Sample preparation

Sample preparation and testing was carried out in accordance with International Society for Rock Mechanics (ISRM) Standards, which can be obtained from the International Society for Rock Mechanics (ISRM) website: (http://www.isrm.net). Cylindrical samples were prepared, and three types of tests were conducted: Brazilian, triaxial and uniaxial tests. A total of 85 specimens were tested, 48 for triaxial tests, 16 for uniaxial compressive tests and 21 for Brazilian tests. Cutting the samples to ISRM accepted diameter was done using a diamond saw. The cores were cut to lengths that varied from 105 to 108 mm, which is 2.5 times greater than the diameter of the core. These were polished at both ends of the specimen to (1) ensure parallelism, (2) minimise errors during loading, and (3) ensure uniform distribution of load on the surface area. Lastly, the mass and length of each specimen were measured. The mass varied from 393.7 g to 401.5 g. These specimens were used for both triaxial and uniaxial compressive tests. Brazilian test samples were cut to the length of approximately half their diameter (~21 mm).

3.3. Rock mechanical testing

For uniaxial compressive strength measurements, four strain gauges were used on each specimen. Two of these were attached vertically (axial) and the other two were attached horizontally (circumferential). The specimen was compressed by the Amsler machine at a constant rate of 2-4 kN/sec until failure. The Brazilian test was conducted using the MTS machine (Exceed E45), which can handle tensional, compressional and shearing loads up to 300 kN. Pre-load was applied to all the specimens at a range of 80 – 90 N. For our measurements, the load was limited to 95 kN. For triaxial compressive tests, specimens were placed in a clean cell jacket to avoid oil leakage from the Hoek cell. The specimen was compressed using the Amsler machine at a constant rate of 2-4 kN/sec until failure. The confining pressures were calibrated on the hydraulic pump and the confining pressures used were 3, 8 and 15 MPa for all specimens. The drill cores we used had been drilled sub-parallel to the bedding planes, at different plunges and azimuths, to install seismic monitoring systems for the fault movement

monitoring and changes in elastic properties. This has implications for the rock strength anisotropy, i.e., the variation of the rock strength with the orientation of minerals, bedding planes and foresets.

3.4. Microseismicity

Mining-induced microseismicity ahead of an advancing excavation face at Cooke 4 mine, level 38, was monitored by a high-resolution underground array of acoustic emission (AE) sensors and accelerometers. The objective of the seismic array was to identify and map seismic sources and monitor localized damage accumulation and evolution. Six accelerometers and 28 acoustic emission (AE) sensors were used for seismic monitoring. Three accelerometers have a flat frequency response of up to 25 kHz and three have flat response of up to 10 kHz [46]. The sensors were Wilcoxon Research Inc. Model 736 and Wilcoxon Model 728, respectively. The AE sensors can record 65.5 ms worth of waveform data. The sampling rate on all channels is 500 kHz. The accelerometers act as a high-pass filter at 50 Hz and AE sensors act as a high-pass filter at 1000 Hz [46, 47]. The minimum event magnitude that was detected by these sensors was M_w –5.3. Often these AE sensors can record signals of up to 50 kHz with workable signal to noise ratio. This, however, largely relies on the input signal intensity [47]. The sensors were grouted inside boreholes. More than one sensor could be installed in one borehole, compared with previous studies which pressed sensors against the borehole wall using a spring [41]. The average spacing of the sensors was approximately 15 m. The sensor network was installed at 1 km below surface and spanned a volume that was approximately 100 m in diameter (Figure 5) [46]. The catalogue used for this study was collected over eight and–a-half months from 10 July 2011 (time: 7:21:6:39) to 25 March 2012 (time: 23:59). We used ~1.02 million seismic events. For finer details of the network, the recording system and the catalogue development procedure, the reader is referred to Naoi et al. [47].

4. RESULTS

4.1. Petrography

The original elastic rocks contain varying proportions of clay and quartz, with the quartz particles ranging from small grains to large pebbles. These rocks show signs of metamorphisms, and, due to alteration, unstable minerals may have reacted with fluid to form argillaceous quartzite, quartzite, pebbly quartzite and conglomerate, respectively. Quartzite, pebbly quartzite and conglomerate generally

exhibit sedimentary structures such as stratification or cross-stratification, which are commonly associated with pyrite. Quartzite is the predominant rock, while argillaceous quartzite only occurs in few centimetre-thick bands. Further inspection of the core indicates a breakage associated with the argillaceous quartzite contacts. Conglomerates and pebbly quartzites are both polymictic and oligomictic, which are characterized by scattered grits with yellow specks of lithic fragments.

Quartzite

Thin section analysis shows that quartz grains constitute approximately 92% of the quartzite sample. The quartzite samples consist mainly of sand-sized quartz grains [48], which are well sorted and have a continuous grain framework (Figure 6a) [49]. The quartz grains often show triple junction contact, which is an indication of compaction and interlocking nature (Figure 6b). Some of these quartz grains show polycrystalline texture. In between these grains there is an interstitial fine-grained matrix that is composed of phyllosilicate and clay minerals. This matrix is made up of silt-sized particles [48, 49] and constitutes approximately 8% of the rock, and is characterized by a prominent elongated matrix texture (Figure 6c).

Pebbly quartzite

The content of the quartz grains and labile mineral is approximately 90% of the whole sample. The rock has variable grain sizes, ranging from silt-sized grains to pebble gravel (4-8 mm). This rock is moderately sorted and displays a reasonably continuous grain framework [48, 49]. These sand-sized grains also show a high degree of fracturing and fragmentation (Figure 6d). Some of the gravel-sized pebbles are polycrystalline and the sand-sized grains show undulating extinction, which suggests that the mineral may have experienced deformation. The samples exhibits low matrix content, being approximately 10%. The matrix is composed of quartz and clay minerals.

Conglomerate

The conglomerate is clast supported and these clasts are mainly pebbles, with minor sand-sized fragments of angular-shaped quartz grains. These pebbles generally vary in size from 1 mm to 50 mm. The sample comprises of chert and quartz pebbles, which vary in colour from milky to smoky. Some of the quartz pebbles are polycrystalline (Figure 7a), characterized by fracturing that occurs across the

clasts associated with alteration (Figure 7b). The grain framework is discontinuous. The grain size of the whole sample ranges from coarse, poorly-sorted pebbles to fine-grained silt sized particles. The matrix is interstitial clay (phyllosilicate) that constitutes 10% of the whole sample. The matrix also contains elongated lenses with diagenetic features.

Argillaceous quartzite

The modal abundance of quartz grains is approximately 50%. The rock consists of quartz clasts that are medium sand-sized to gravel-sized particles, with 50% silt-sized matrix. Grains are massive, poorly sorted and randomly oriented, and show a discontinuous grain framework (Figure 7c). The gravel-sized quartz grains are rounded to sub-angular [50] and the sand-sized grains are fragmented and angular. The matrix is composed of both clay minerals and phyllosilicate (Figure 7d), possibly during metamorphism (pervasive alteration) of pre-cursor clay minerals to phyllosilicates.

4.2. Rock Strength

The uniaxial compressive strength (UCS) measurements indicate that quartzite has the highest UCS, followed by pebbly quartzite, argillaceous quartzite and lastly, conglomerate (Figure 8a). Triaxial compressive strength shows an increase in compressive strength with increasing confining stresses (Figure 9). Results from the Brazilian tests show that quartzite sample has the highest tensile strength and quartz vein has the least (Figure 8b), which indicates that the rock might be most likely to fail where veins occur. All specimens that were tested failed in a brittle manner, and in some instances, especially quartzite and pebbly quartzite, failure was explosive. These observations are in agreement with previous studies that shown that microseismicity tends to be more common in quartz-rich areas, and rarer in clay-rich areas when rocks are subjected to loading [51]. Therefore, this analysis suggests more seismicity may be expected to occur in quartzite and pebbly quartzite rocks.

4.3. Underground Mapping

The underground mapping at Cooke 4 shaft, level 38, included the mapping of the tunnel (walls, roof and face) and stope faces, and covered both structural (fractures, joints, faults, etc.) and sedimentological components. The underground mapping confirms that argillaceous quartzite mostly encases the conglomerate reef (Figure 10). Fractures observed in the stope can be correlated with the

model of fracturing around the stope (Figure 11). Extensive research has been conducted on these types of fractures [2, 7, 8; 24]. The fractures that form around the stope are characterised by shearing and dilation, which result in fault development or repeated formation and propagation of shear fractures. van Aswegen and Stander [8] named these shear fractures ‘‘Ortlepp shears’’ (see Figure 3). These fractures are the source of numerous seismic activities [52-53]. Therefore, it is expected that seismicity that represents the formation of these fractures should be detected using our high sensitivity underground acoustic emission sensor network.

4.4. Microseismicity

We studied microseismicity between 12 July 2011 and 10 October 2011. Acoustic emission clusters were successfully mapped. Three different clusters were identified: viz. cluster A, cluster B and cluster C (Figure 12a). More than 90% of microseismicity is associated with the mining front (cluster A). This suggests that these microseismic events are mainly controlled by the stress field ahead of the stope. Careful analysis of cluster A (i.e., clustering associated with the stope face) was conducted and the region marked with a rectangle (Figure 12b) was selected for analysis. Cluster A of AEs can be subdivided into five distinctive planar sub-clusters (1, 2, 3, 4 and 5). Generally, these planar microseismic sub-clusters strike sub-parallel to the mining front and dip steeply (~ 65^{o}) to the south except for planar cluster no.4, which dips to the north (Figure 12c-d). The development of these new planar sub-clusters and damage accumulation was carefully monitored in case a large seismic event should occur (Figure 13). Acoustic emission clusters were not accompanied by any violent or large seismic events. To confirm the spatial distribution of these planar sub-clusters, the relationship between the fractal dimensions (D) and b-value was computed [54]. The b-value was computed using least square analysis and maximum likelihood. Approximately D~2 and b~1 were obtained for no.1, 2 and 5 sub-clusters (Table 2). This confirms two-dimensional spatial distribution nature of these sub-clusters which, according to Moriya et al. [26], are associated with Ortlepp shear fractures forming ahead of the face. Guler [25] further showed that the mining-induced fracture pattern was mainly controlled by the characteristics of the rock type. The different types of rocks exhibit distinct attitudes of mining-induced fracturing. Roberts and Schweitzer [24] distinguished between fractures formed by weak and strong hangingwall rocks, defining them as different geotechnical zones. Mining-induced fractures identified in this study have the fracture turning points in the hangingwall. These fractures display geometric

characteristics of the weak hangingwall and competent footwall rocks (see Figure 14). This is probably due to the dominance of 'weak' or soft lava in the hangingwall and conglomerate-quartzite units in the footwall. These observations concur with a fracture model by Roberts and Schweitzer [24] for the geotechnical zone with soft lava in the hangingwall.

5. ANALYSIS AND DISCUSSION

5.1. Petrology

Petrological results show that the shaft pillar is made up of Upper Elsburg reefs of Mondeor Formation, which underlie the VCR (Venterspost Formation) and soft lavas (48 – 138 MPa) (Westonaria Formation) [4, 24, 53]. Core-logging and petrographic investigation results, confirmed by underground mapping, clearly show that there are four sedimentary rocks making up the shaft pillar at Cooke 4 shaft, level 38: quartzites, pebbly quartzites, argillaceous quartzite and conglomerates. The mineralogy includes argillaceous grains, phyllosilicates, clastic grains, clay and quartz. These rocks vary from each classified rock type from 50 % to 92 % quartz content. The matrix is composed of fine-grained clay minerals such as phyllosilicates in argillaceous quartzites. The abundance of these easily cleavable minerals (clay matrix), lower quartz content and absence of interlocking and continuous grain framework in rocks such as argillaceous quartzite and conglomerate is expected to result in the lower rock compressive strength [55]. An increase in quartz content and better interlocking and continuous grain framework in rocks, such as quartzite and pebbly quartzite, are expected to be the main cause for the increase in the rock strength [55]. This concurs with studies by Briggs [55], Shakoor and Bonelli [56] and Gunsallus and Kulhawy [57], which showed that the increase in quartz content results in an increase in the compressive strength. Furthermore, Fahy and Guccione [58] and Bell and Lindsay [59] showed that the grain contact plays a much bigger role in rock strength than the quartz content. Additionally, microscopic analysis showed that clasts in pebbly quartzite and conglomerates are pervasively microcracked. The microstructure of these rocks is expected to result in relatively high porosities and low compressive strengths. These microscopic analyses suggest that quartzite should have the highest compressive rock strength, followed by pebbly quartzite. However, based on our microscopic qualitative analysis, not much can be deduced regarding the order of strength of argillaceous quartzite and conglomerate, except that their compressive strengths are both lower than

quartzite and pebbly quartzite. Mechanical laboratory tests were conducted to substantiate these microscopic observations.

5.2. Rock Strength

5.2.1. Brazilian test

Andreev [60] showed that the Brazilian test is valid for materials that exhibit brittle failure. In our study all specimens that were tested using the Brazilian test failed in a brittle manner. The fractures were oriented sub-parallel to the loading direction [12]. The average tensile strength of quartzite is the highest (10.3 – 19.9 MPa), followed by conglomerates (10.5 – 13.3 MPa), and argillaceous quartzite (7.4 – 13.9 MPa), pebbly quartzite (7.3 – 7.1 MPa) and lastly, quartz veins (6.4 – 10.1 MPa). This suggests that quartzite would make a more reliable pillar based on its tensile strength, and rocks with quartz veins will fail more easily. This is supported by underground observation, where breakage was observed along the quartz vein in the stope face. The dominant rock failure mechanism is progressive slabbing and spalling, and one of the conditions for progressive spalling is a dilatant rock with localized regions of tension [61].

5.2.2. Uniaxial compressive and triaxial compressive strength

As the mining proceeds to greater depths or during the final stages of the remnant shaft pillar extraction, the stress concentrations and strain energy stored in the rock mass increase critically. The virgin stresses and induced stresses resulting from mining equal to the ‘absolute’ stresses in the rock mass around the mining excavation. When the magnitude of the stress exceeds the strength of the rock mass, stress fracturing occurs around the mining excavation [2]. Quartzite (143-202 MPa) and pebbly quartzite (96-173 MPa) both show large ranges of uniaxial and triaxial compressive strengths. Microscopic analysis show good sorting of grains, continuous grain framework, and less than 10% matrix. These may have largely contributed to the observed high rock strength. The possible mechanism for microcrack nucleation is the pre-existence of micro-discontinuities such as cavities at grain boundaries, or matrix shearing caused by quartz grain rotation or slip [15, 16]. The presence of macro-discontinuities such as sedimentary foresets and elongated lenses of matrix in the quartzite and drill core direction (sub-parallel to bedding plane) may have influenced the reduction of the quartzite uniaxial compressive strength, which ranged from 143 to 202 MPa, compared with other quartzite rocks

of the Witwatersrand Basin, which exhibit 200 - 300 MPa UCS (see Table 1 and Table 3) [4, 55]. Pebbly quartzite is mostly similar to quartzite in composition and texture. The UCS of pebbly quartzite (96-173 MPa) was slightly lower than quartzite (143-202 MPa). The presence of pebbles, with pre-existing fractures and highly fragmented (as observed on the thin sections) may have largely contributed to the lower pebbly quartzite UCS. The likely failure mechanism of pebbly quartzite is interpreted to be sliding along pre-existing planes of weakness [12, 13].

Conglomerate UCS values (76-153 MPa) overlap with pebbly quartzite UCS values (96-173 MPa). Under the microscope conglomerate showed poor sorting, an interstitial clay-phyllosilicate matrix, and fractures cutting through clasts (pre-existing planes of weakness). The presence of discontinuities in the rock is interpreted to have initiated the crack formation and failure. These results differ significantly from the UCS values found in a consultancy report for Cooke 4 mine [4], which reports UCS values ranging from 170 to 306 MPa (Table 1). This could be due to the direction of loading (anisotropy), which is sub-parallel to the bedding plane in this study. Loading parallel or sub-parallel to the bedding plane or mineral alignment is known to reduce the rock compressive strength [62]. The argillaceous quartzite showed overlapping UCS values, but with the lowest values (47-157 MPa). Under the microscope, argillaceous quartzite showed poorly sorted grains, a discontinuous grain framework and highly variable grain sizes (silt to gravel). The matrix was approximately 50% of the whole rock. The composition of the matrix includes both clay minerals and phyllosilicates (micas). The clays and micas are well known to be weak minerals, with cleavage. The presence of weak micas and cleavage reduces the rock strength. Therefore, shear rupture of the matrix as a result of rotation or slip of the quartz grains most likely caused microcrack nucleation and eventually the formation of a macro-shear plane [15, 16].

These rocks (quartzite, pebbly quartzite and conglomerate) generally have much stronger uniaxial compressive strength than the hangingwall volcanic rocks, soft tuffaceous lava (48 – 138 MPa) and argillaceous quartzite [4, 24]. The WAF is invariably weaker (<100 MPa) and often contains very weak zones, usually immediately above the VCR [5; 24] (see Table 3; Figure 15).

5.3. Microseismicity

In this paper we used in-stope mapping and advanced geotechnical monitoring to develop a practical fracture model and guide proactive interventions to mitigate the risk posed by seismicity and the fall of ground. Using our integrated approach, a fracture model was developed that characterises

the fragility of the hangingwall/footwall strata, which could be used during operations and prior to the entry of the mining crew in the stope [40]. Once the hangingwall vulnerability is identified through fracture modelling, appropriate support can be deployed or a crew could be evacuated from the stope to avoid potential falls of ground, rockburst or seismicity. The largest seismic event that was recorded by the Cooke 4 shaft 'in-mine' network is M_w 2.3, which occurred on 30 August 2009 [52]. In 2009, according to the mine seismicity report [52], 11 seismic events of magnitude > M_w 1.0 were reported. This report further determined the most likely maximum magnitudes to range from M_w 2.0 - 3.0. These events are often accompanied by 100 m rupture plane, while for M_w 0 the rupture plane can span 10 m [2]. Approximately 20% of the M_w 2 events result in fatalities or infrastructure damage, whereas an M_w 4 is almost certain to be accompanied by significant damage [2]. However, infrastructure damage and fatalities have been reported several times in Cooke 4 mine, and hence our deployment of high resolution seismic monitoring network [4-5, 52]. Contrary to initial mine reports, during our seismic monitoring period at Cooke 4 mine none of the AE clusters were accompanied by a large seismic event. The possible reason is that the resultant displacement is the consequence of the accumulation of numerous very small displacements, which occur as the stope face advances towards the shear fracture [2].

A detailed analysis of high-resolution acoustic emissions show that the majority of acoustic emissions are associated with the mining stope faces. The acoustic emission clusters delineate extension fractures and Ortlepp shears forming ahead of the stope caused by the excavation-induced stress field (Figure 14). Roberts and Schweitzer [24] observed that mining-induced extension fractures approximately dips at 60^o and 40^o towards each other, and indicated that the turning point of these fractures is in the weak strata. These extension fractures may coalesce and form shear fractures around the stope [2, 8, 24]. In this study, microseismicity data reveals that the turning point of these fractures is in the hangingwall (Figure 14). The hangingwall is largely composed of tuffaceous soft lavas from Westonaria Formation [4]. Underground mapping in the stope showed interlayered argillaceous quartzite and conglomerate reef, which were severely affected by several discontinuities, varying from minor faults to medium scale faults. Some of these discontinuities or fractures were attributed to shearing and dilation (Ortlepp shears) ahead and around the stope. The integration of these datasets has allowed us to develop the fracture model (Figure 14) for the geotechnical zone, which agrees with fracture model developed by Roberts and Schweitzer [24] for a similar underground environment (i.e.,

weak/soft lava hangingwall and quartzite/conglomerate footwall). Furthermore, our data show that microseismicity is also concentrated in the vicinity of service excavations such as tunnels (cluster B). This indicates high stress levels around the service excavation walls (tunnels) supported by core discing. More inspection on the data shows that Cluster C is further away from the excavations, which could be related to geological discontinuities. Naoi et al. [63] interpret cluster C to have been caused by an active fault zone consisting of multiple fault planes with thickness of 0.3 m.

6. CONCLUSIONS

The microscopic investigation and underground observations identified four rock types in the shaft pillar, viz. argillaceous quartzite, pebbly quartzite, quartzite, and conglomerate. The rock mineralogy includes argillaceous grains, clastic grains, phyllosilicates, clay and quartz, which have large influence on rock strength and hence fracture formation and the delineation of geotechnical zones. Underground mapping showed interbedded argillaceous quartzites and conglomerate reefs in the stope, which were cross-cut by several veins and strongly affected by numerous discontinuities. Discontinuities ranged from minor to medium-scale faults. Some of these discontinuities or fractures were attributed to shearing and dilation ahead and around the stope, viz. Ortlepp shears.

Different rock types exhibit specific rock mass response to loading. This is expressed by geotechnical zones where area-specific mining-induced fractures form. More than 90% of microseismicity is associated with the mining face, which delineated Ortlepp shears. This study further shows that these fracture patterns correlate positively with the fracture model proposed by Roberts and Schweitzer [24] for the geotechnical zone characterized by weak/soft lava hangingwall and quartzite/conglomerate footwall. Underground microseismic monitoring and mapping was successfully used to delineate this weak geotechnical zone. This has important implications for improvement of mine safety and the choice of mining methods and support, which will contribute to greater safety.

7. ACKNOWLEDGMENTS

Sibanye gold limited is acknowledged for providing permission to publish the results. The authors thank the School of Geosciences and the School of Mining Engineering at the University of the Witwatersrand, CIMERA, the CSIR Centre for Mining Innovation, JST-JICA, SATREPS team, and ICDP DSeis team for the use of their resources and facilities. RJD acknowledges the support of the South African Research Chairs Initiative of the Department of Science and Technology and National Research Foundation.

8. REFERENCES

[1] Ortlepp WD. Rockbursts in South African gold mines: a phenomenological view. In: Proceedings of the 1st International Congress of Rockburst and Seismicity in Mines. Johannesburg; 1984. p. 165-178.

[2] Jager AJ, Ryder JA. A Handbook on Rock Engineering for Tabular Hard Rock Mines. Braamfontein, Johannesburg: SIMRAC; 1999.

[3] Ryder JA, Jager AJ. A Textbook on Rock Mechanics for Tabular Hard Rock Mines. Braamfontein, Johannesburg: SIMRAC; 2002.

[4] Harvey F, Joughin W, Ortlepp DW. Design of Ezulwini Shaft Pillar Extraction. SRK Consulting Engineers and Scientists, Technical report; 2006; Report number: 346813

[5] Glasspool M, Ward AK. Ezulwini Mine: mandatory code of practice to combat rockburst and rockfall related accidents. SRK Consulting Engineers and Scientists; Technical report; 2010; Report number: DME16/3/2/1-A3

[6] Adams GR, Jager AJ. Petroscopic observations of rock fracturing ahead of stope faces in deep-level gold mines. J.S.A. Inst. Min. Metall. 1980; 80:204–209.

[7] Adams GR, Jager AJ, Roering C. Investigation of rock fracture around deep level gold mine stopes. In: Proceedings of the 22nd U.S. Rock Mechanics Symposium. M.I.T.; 1981. p. 159-185.

[8] van Aswegen G, Stander M. Origins of some fractures around tabular stopes in the deep Southern African mines. In: Proceedings of the 2nd Southern Hemisphere International Rock Mechanics Symposium (SHIRMS). Sun City; 2012. p. 63-78.

[9] Ogasawara H, Kato H, Hofmann G, Roberts D, Piper P, Clements T, Ward A. K, Yabe Y, Yilmaz H, Durrheim RJ. BX CCBO in-situ stress measurements at earthquake prone areas in South African gold mines - A summary of mini-workshop on 13 February 2014. In: Proceedings of the ARMA2014. Minneapolis, Minn.; 1-4 June 2014. Paper no. 14-7438.

[10] Hazzard JF, Maxwell SC, Young RP. Micromechanical modeling of cracking and failure in brittle rocks. J. Geophys. Res. 2000; 105: 683-697.

[11] Lockner DA. Rock failure. In: Rock Physics and Phase Relations, TJ Ahrens, editor. Washington D.C.: American: Geophy. Union; 1995. pp. 127-147.

[12] Griggs D, Handin J. Observations on fracture and hypothesis of earthquakes. In: Rock Deformation, D Griggs, J Handin, editor. Geological Society of America Memoirs, 1960. pp. 347-364.

[13] Fairhurst C, Cook NGW. The phenomenon of rock splitting parallel to the direction of maximum compression in the neighbourhood of a surface. In: Proceedings of the 1st International Congress on Rock Mechanics. Lisbon; 1966. p. 687-692.

[14] Horii H, Nemat-Nasser S. Compression-induced microcrack growth in brittle solids: Axial splitting and shear failure. J. Geophys. Res. 1985; 90: 3105-3125.

[15] Tapponnier, P. and Brace, W.F. Development of stress-induced microcracks in Westerly granite. Int. J. Rock Mech. Min. Geomech. Abstr. 1976; 13: 103-112.

[16] Sprunt ES, Brace WF. Direct observation of microcavities in crystalline rocks. Int. J. Rock Mech. Min. Sci. 1974; 11: 139-150.

[17] Wong T, David C, Zhu, W. The transition from brittle faulting to cataclastic flow in porous sandstones: Mechanical deformation. J. Geophys. Res. 1997; 102: 3009-3025.

[18] Brummer RK. Active methods to combat the rockburst hazard in South African gold mines. In: Proceedings of the 88th Conference on Applied Rock Engineering, (CARE). London; 1988. p. 35–43.

[19] Lenhardt WA. Seismic event characteristics in a deep level mining environment. In: Proceedings of the Rock at Great Depth Symposium. Balkema; 1989. p. 727-732.

[20] Gay NC. Mining in the vicinity of geological structures - an analysis of mining induced seismicity and associated rockbursts in two South African mines. In: Proceedings of the 3rd International Symposium on Rockbursts and Seismicity in Mines. Rotterdam; 1993. p. 57-62.

[21] Schweitzer JK, Kroener A. Geochemistry and petrogenesis of early Proterozoic intracratonic volcanic rocks of the Ventersdorp Supergroup, South Africa. Chem. Geol. 1985; 51: 265–288.

[22] Regional VCR Working Group. The multilateral VCR Working Group, 1990-1993. A review of activities and some regional findings. In: Proceedings of the 15th International Symposium on Congress of Mining and Metallurgical Institutions. Sun City; 1994a. p. 55–64.

[23] Regional VCR Working Group. Some regional characteristics of the Ventersdorp Contact Reef (VCR). S.A.J. Geol.1994b; 97: 385–386.

[24] Roberts MKC, Schweitzer JK. Geotechnical areas associated with the Ventersdorp Contact Reef, Witwatersrand Basin, South Africa. J.S.A. Inst. Min. Metall. 1999; 99: 157–166.

[25] Guler G. Analysis of the rock mass behaviour as associated with Ventersdorp Contact Reef stopes, South Africa. MSc Thesis. Univ. Witwatersrand, Johannesburg; 1998.

[26] Moriya H, Naoi M, Nakatani M, Murakami O, Kgarume T, Ward AK, Durrheim R, Philipp J, Yabe Y, Kawakata H, Ogasawara H. Delineation of large localized damage structures forming ahead of an active mining front by using advanced acoustic emission mapping techniques. Int. J. Rock. Mech. Min. Sci. 2015; 79: 157–165.

[27] Durrheim RJ, Ogasawara H, Nakatani M, Yabe Y, Kawakata H, Naoi M, Ward AK, Murphy S, Wienand J, Lenegan P, Milev AM, Murakami O, Yoshimitsu N, Kgarume T, Cichowicz A, JST-JICA SA research group. Establishment of SATREPS experimental sites in South African gold mines to monitor phenomena associated with earthquake nucleation and rupture. In: Proceedings of the 6th International Congress on Deep and High Stress Mining. Perth; 2012. p.173-187.

[28] Ogasawara H, Nakatani M, Durrheim RJ, Naoi M, Yabe Y, Moriya H, Hofmann GF, Stander C, Roberts DP, De Bruin P, Oelofse J, Kato H, Cichowicz A, Birch D, Ngobeni D, Milev A, Kgarume T, Satoh T, Horiuchi S, Kawakata H, Murakami O, Yoshimitsu N, Ward AK, Wienand J, Lenegan P, Yilmaz H, Mngadi S, Piper PS, Clements TN, Nakao S, Okubo M, Ishii H, Visser AV. Observational studies of the rock mass response to mining in highly stressed gold mines in South Africa In: Proceedings of the 7th International Congress on Deep and High Stress Mining. Perth; 2014. p. 123-137.

[29] McCarthy T, Rubidge B. The Story of Earth and Life. Cape Town: Struik Publishers; 2005.

[30] Dankert BT, Hein KAA. Evaluating the structural character and tectonic history of the Witwatersrand Basin. Precambrian Res. 2010; 177: 1-22.

[31] Robb LJ, Meyer FM. The Witwatersrand Basin, South Africa: Geological framework and mineralization processes. Ore Geol. Revs. 1995; 10: 67-94.

[32] Myers RE, McCarthy TS, Stanistreet IG. A tectono-sedimentary reconstruction of the development of the Witwatersrand Basin, with particular emphasis on the Central Rand Group. Econ. Geol. Res. Unit. 1989; 216: 497–540.

[33] McCarthy TS. The Witwatersrand Supergroup. In: The Geology of South Africa, MR Johnson, CR Anhaeusser, RJ Thomas, editor. Pretoria: Council for Geosciences; 2006. pp. 155–186.

[34] SACS (South African Committee for Stratigraphy), Stratigraphy of South Africa. Part 1 (Comp L.E. Kent). Lithostratigraphy of the Republic of South Africa, South West Africa/Namibia and the Republics of Bophuthatswana, Transkei and Venda. Pretoria: Geol. Surv. S. Afr.; 1980.

[35] Coward MP, Spencer RM, Spencer CE. Development of the Witwatersrand Basin, South Africa. In: Early Precambrian Processes, MP Coward, AC Ries, editor. London: Geological Society Special Publications; 1995; 95: 243–269.

[36] Vermaakt DT, Chunnet IE. Tectono-sedimentary processes which controlled the deposition of the Ventersdorp Contact Reef within the West Wits Line. In: Proceedings of the 15th International Symposium on Congress of Mining and Metallurgical Institutions. Sun City; 1994; 3: 117–130.

[37] Gibson MAS, Jolley SJ, Barnicoat AC. Interpretation of the Western Ultra Deep Levels 3D seismic survey. The Leading Edge. 2000; 19: 730–735.

[38] Beach A, Smith R. Structural geometry and development of the Witwatersrand Basin, South Africa. In: Early Precambrian Processes, AC Ries, RWH Butler, RH Graham, editor. London: Geological Society Special Publications; 2007; 272: 533–542.

[39] Ligege R. Cooke 4 shaft Geologist. Personal communication; 20 March 2013.

[40] Durrheim RJ, Ogasawara H, Nakatani M, Yabe Y, Naoi M, Moriya H, Cichowicz A, Takashi Satoh T, Hironori KH, Milev A, Kgarume T, Brink VZ., Ward AK, Ribeiro L, Manzi MSD., Mngadi S, the SATREPS Team. Observational Studies in South African Mines to Mitigate Seismic Risks: Challenges and Achievements. In: Proceedings of the AfriRock International Symposium. Cape Town; 3-5 October 2017.

[41] Ogasawara H, Durrheim RJ, Nakatani M, Yabe Y, Milev A, Cichowicz A, Kawakata H, Moriya H, JST-JICASA Research Group. A Japanese - South African Collaboration to Mitigate Seismic Risks in Deep Gold Mines. In: Proceedings of the 1st Hard Rock Safety Conference; Johannesburg; 2009; p.115-134.

[42] SACS (South African Committee for Stratigraphy), A revised stratigraphic framework for Witwatersrand Supergroup. Lithostratigraphy of the Republic of South Africa. Pretoria: Geol. Surv. S. Afr.; 2006.

[43] Johnson MR, Anhauesser CR, Thomas RJ. The Geology of South Africa. Pretoria; Council for Geoscience. 2006.

[44] Brace WF. Dependence of fracture strength of rocks on grain size. In: Proceedings of the 4th Rock Mechanics Symposium; Pennstate; 1961; p.99-103.

[45] Heap MJ, Vinciguerra S, Meredith PG. The evolution of elastic moduli with increasing crack damage during cyclic stressing of a basalt from Mt. Etna volcano. Tectonophysics. 2009; 471:153-160.

[46] Kgarume T, Spottiswoode S, Milev A, Nakatani M, Naoi M, Yabe Y, Philipp J, Durrheim R, Ogasawara H, Ward AT. Using acoustic emissions to study rock mass degradation due to stope fracturing. In: Proceedings of the 13th Biennial SAGA Conference; Kruger National Park; 6-9 October 2013.

[47] Naoi M, Nakatani M, Horiuchi S, Yabe Y, Philipp J, Kgarume T, Morema G, Khambule S, Masakale T, Ribeiro L, Miyakawa K, Watanabe A, Otsuki K, Moriya H, Murakami O, Kawakata H, Yoshimitsu N, Ward TA, Durrheim R, Ogasawara H. Frequency–magnitude distribution of -3.7 ≤ MW ≤ 1 mining-induced earthquakes around a mining front and b value invariance with post-blast time. Pure Appl. Geophys. 2013; 171: 2665-2684.

[48] Wentworth CK. A scale of grade and class terms for clastic sediments. J. Geol.; 1922; 30: 377-392.

[49] Folk RL. Petrology of Sedimentary Rocks. Texas: Hemphill Publication Co; 1974.

[50] Powers MC. A new roundness scale for sedimentary particles. J. Sediment Petrol. 1953; 23:117-119.

[51] Perez R, Marfurt K. Calibration of brittleness to elastic rock properties via mineralogy logs in unconventional reservoirs. In: Proceedings of the International Petroleum Technology Conference, Abstr.; Cartagena, Colombia; 8-11 September 2013.

[52] Joughin W. Review of the Ezulwini shaft pillar extraction. SRK Consulting Engineers and Scientists, Technical report; 2009; Report number: 394357/1

[53] Milev AM, Spottiswoode SM. Effect of the rock properties on the mining-induced seismicity around the Ventersdorp Contact Reef, Witwatersrand Basin, South Africa. Pure Appl. Geophys. 2002; 159:165–177.

[54] Kgarume TE, Spottiswoode SM, Durrheim RJ. Statistical properties of mine tremor aftershocks. Pure Appl. Geophys. 2009; 167:107-117.

[55] Briggs DJ. Mechanical properties of quartzites and associated rock types. Chamber of Mines South Africa Research Organization and Mining Technology Laboratory; 1982; Report number: 13/83

[56] Shakoor A and Bonelli RE. Relationship between petrographic characteristics, engineering index properties and mechanical properties of selected sandstones. Bull. Ass. Eng. Geol. 1991; 28: 55-71.

[57] Gunsallus KL. Kulhawy FH. A comparative evaluation of rock strength measures. Int. J. Rock Mech. Min. Sci. Geomech. Abstr. 1984; 21: 233-48.

[58] Fahy MP, Guccione MJ. Estimating strength of sandstone using petrographic thin-section data. Bull. Ass. Eng. Geol. 1979; 16: 67-85.

[59] Bell FG, Lindsay P. The petrographic and geochemical properties of some sandstones from the Newspaper Member of the Natal Group near Durban, South Africa. Eng. Geol. 1999; 53: 57-81.

[60] Andreev GE. A review of the Brazilian test for rock tensile strength determination. Part II: contact conditions. Min. Sci. Tech. 1991; 13: 457-465.

[61] Martin CD, Maybee WG. The strength of hard rock pillars. Int. J. Rock. Mech. Min. Sci. 2000; 37: 1239-1246.

[62] Kongkitkul W, Musika N, Tongnuapad C, Jongpradist P, Youwai S. Anisotropy in compressive strength and elastic stiffness of normal and polymer-modified asphalts. Soils Found. 2014; 54: 94-108.

[63] Naoi M, Nakatani M, Kgarume T, Khambule S, Masakale T, Ribeiro L, Philipp J, Horiuchi S, Otsuki K, Miyakawa K, Watanabe A, Moriya H, Murakami O, Yabe Y, Kawakata H, Yoshimitsu N, Ward A, Durrheim R, Ogasawara H. Quasi-static slip patch growth to 20 m on a geological fault inferred from acoustic emissions in a South African gold mine. J. Geophys. Res. 2015; 120: 1692–1707.

List of Figures

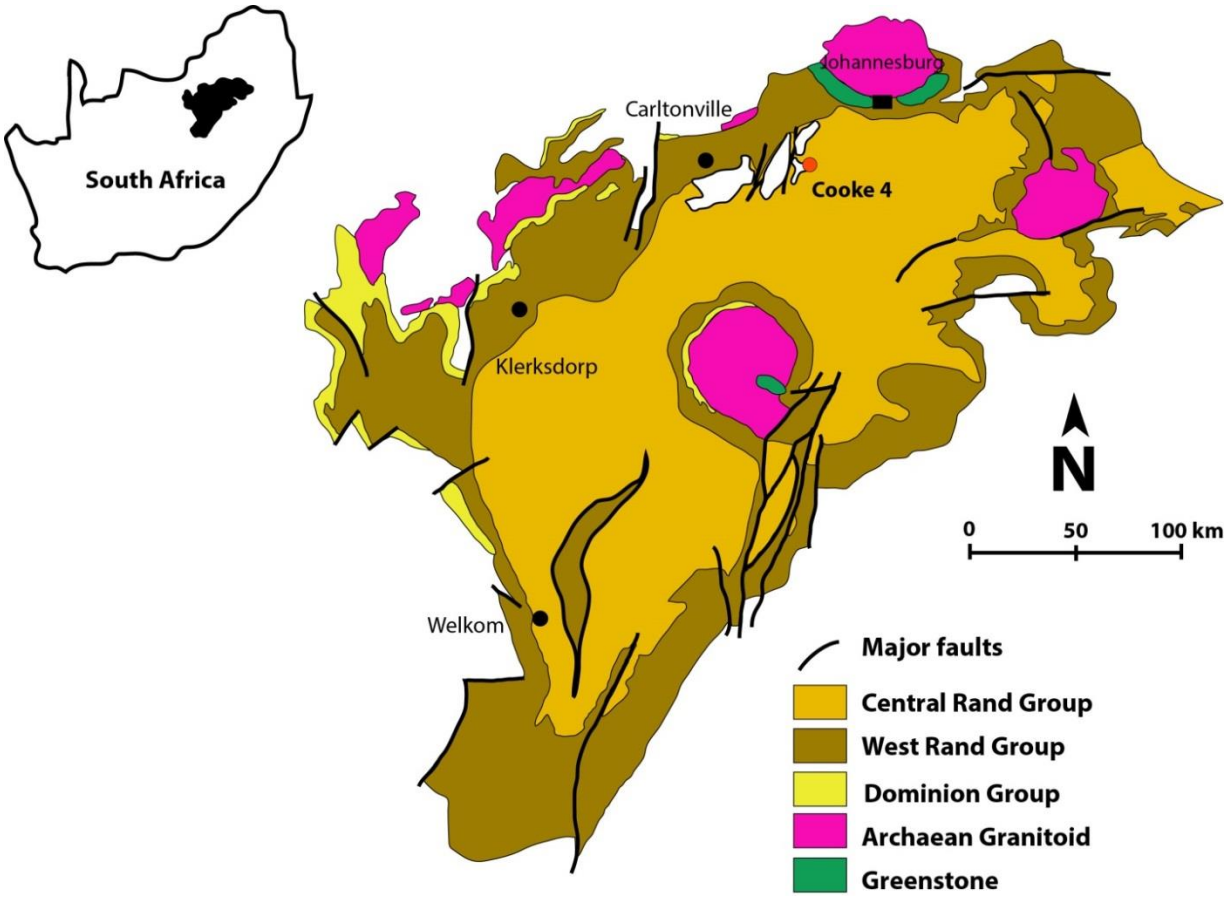


Figure 1: The Witwatersrand Basin map showing the general geology. The area of our study is located at Central Rand Group, Western areas, Cooke 4 (indicated in red) (modified from Dankert and Hein [30]).

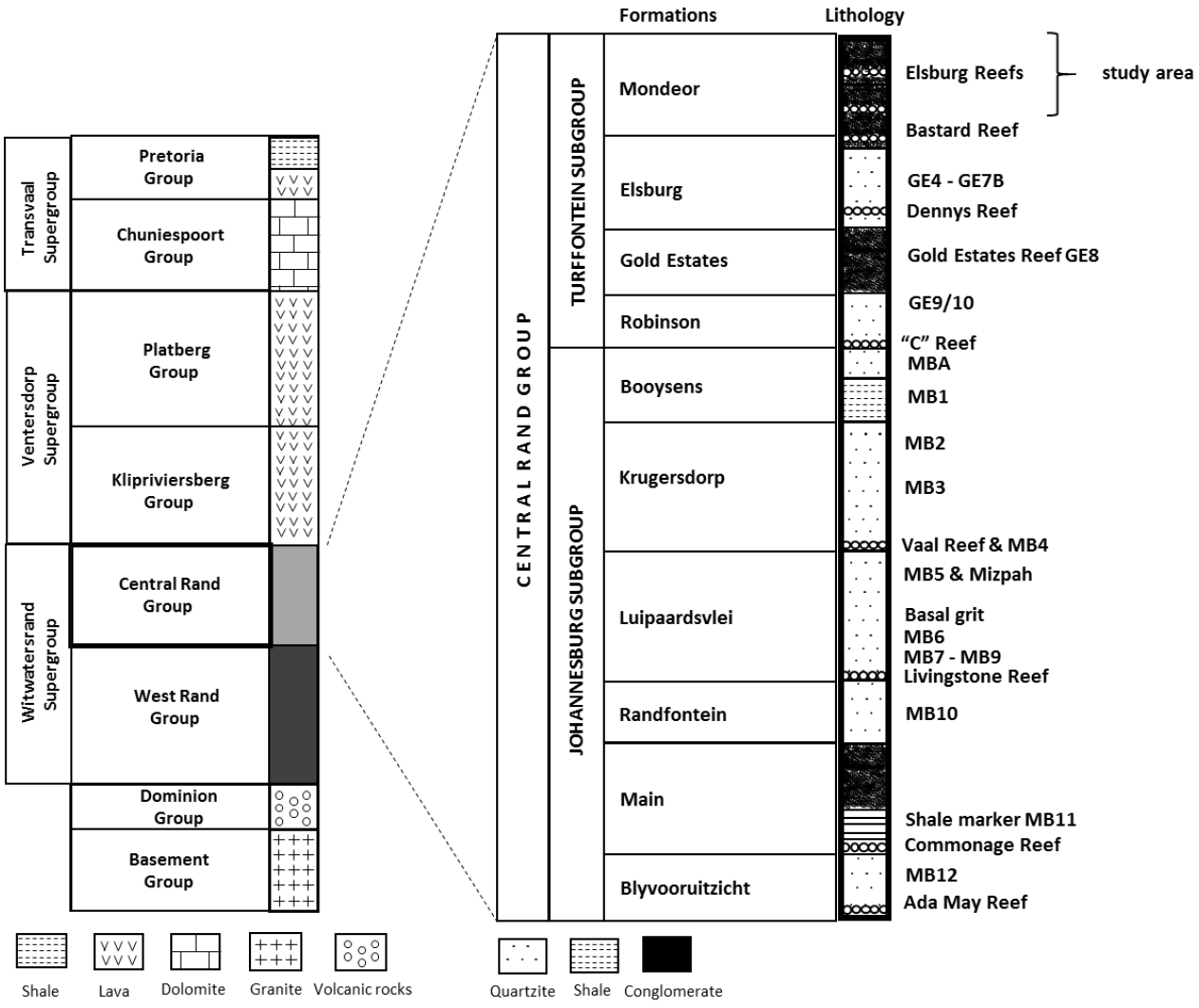


Figure 2: Generalized stratigraphy of the Witwatersrand Supergroup and Central Rand Group, showing the position of the Upper Elsburg Reef at the top of the Mondoer Formation [66].

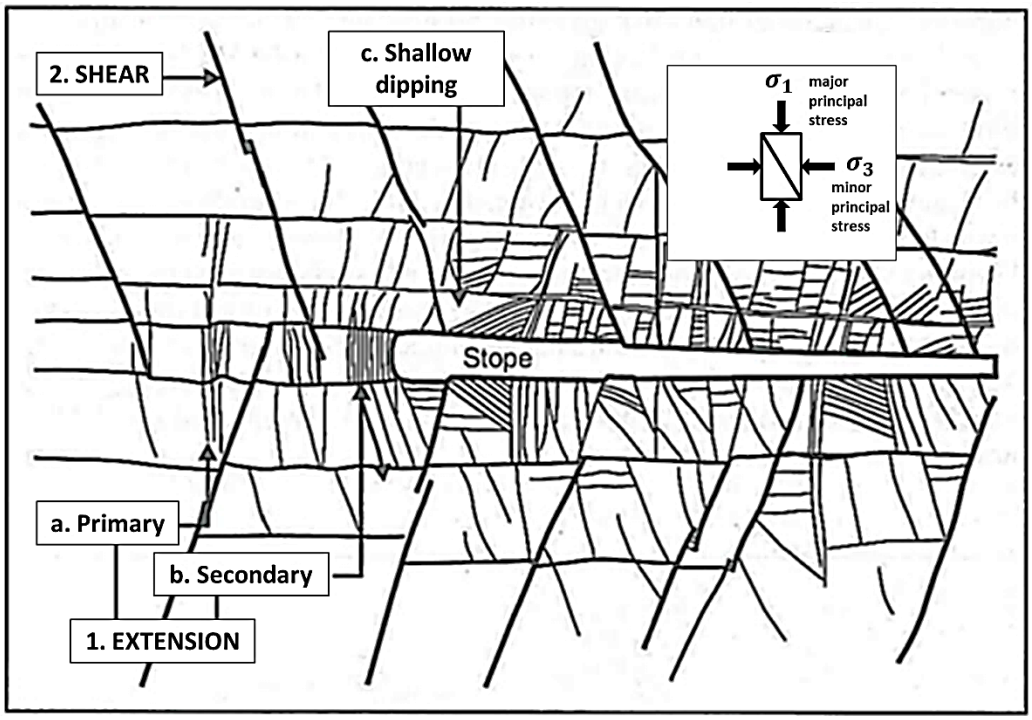


Figure 3: Schematic diagram showing [2] fractures around a stope: primary (1a), secondary (1b) and shallow dipping (1c) extension fractures and shear fractures (2).

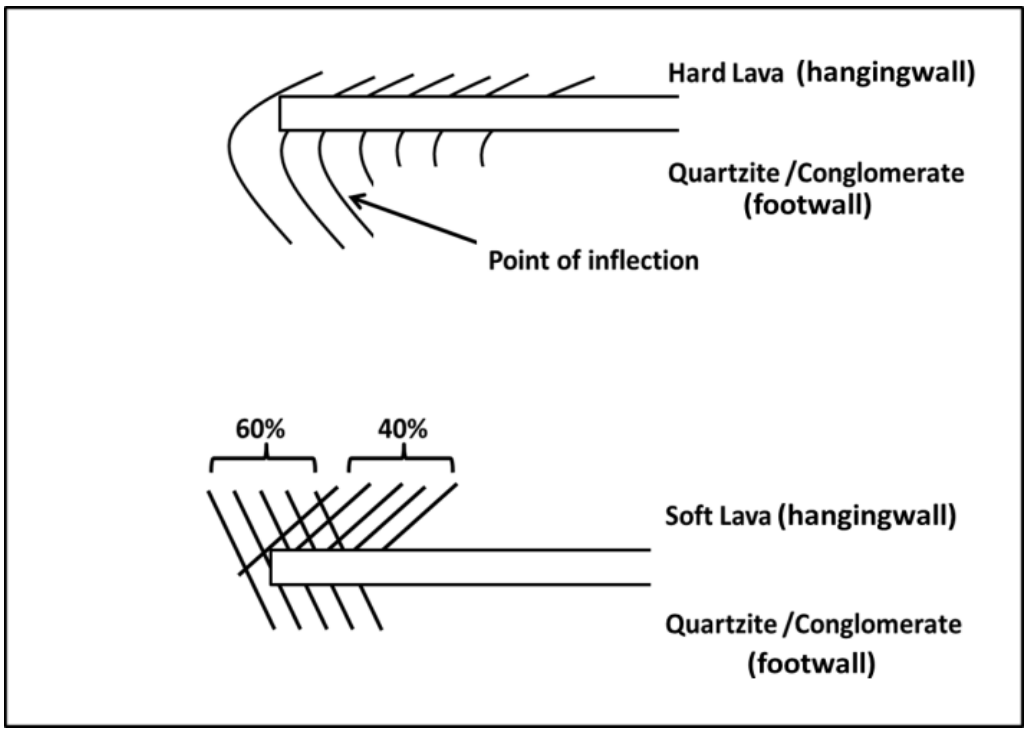


Figure 4: Mining-induced extension fractures controlled by the hard/soft lava hangingwall and conglomerate/quartzite footwall (after Roberts and Schweitzer [24]).

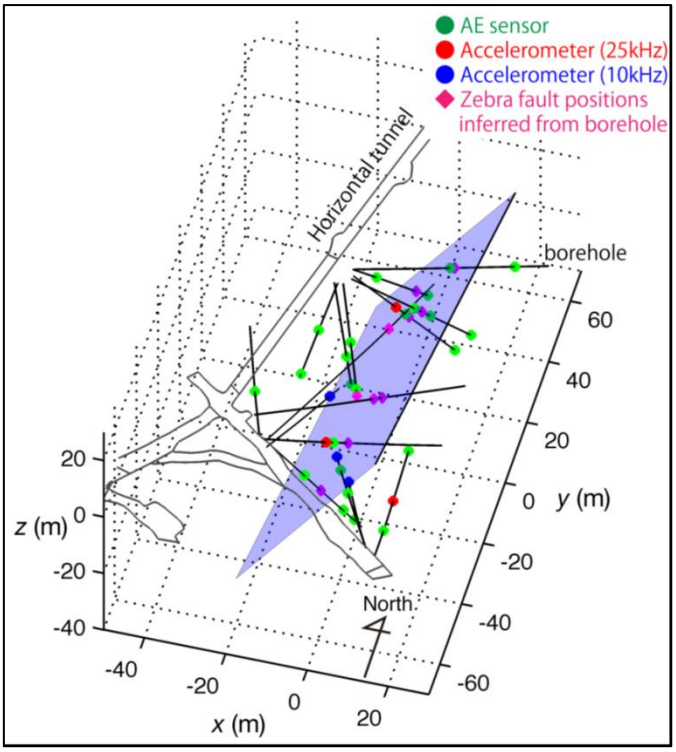


Figure 5: The sensor network deployed 1 km underground at Cooke 4 mine. It spanned a volume of approximately 100 m in diameter, with a spacing of roughly 15 m between sensors [48, 49].

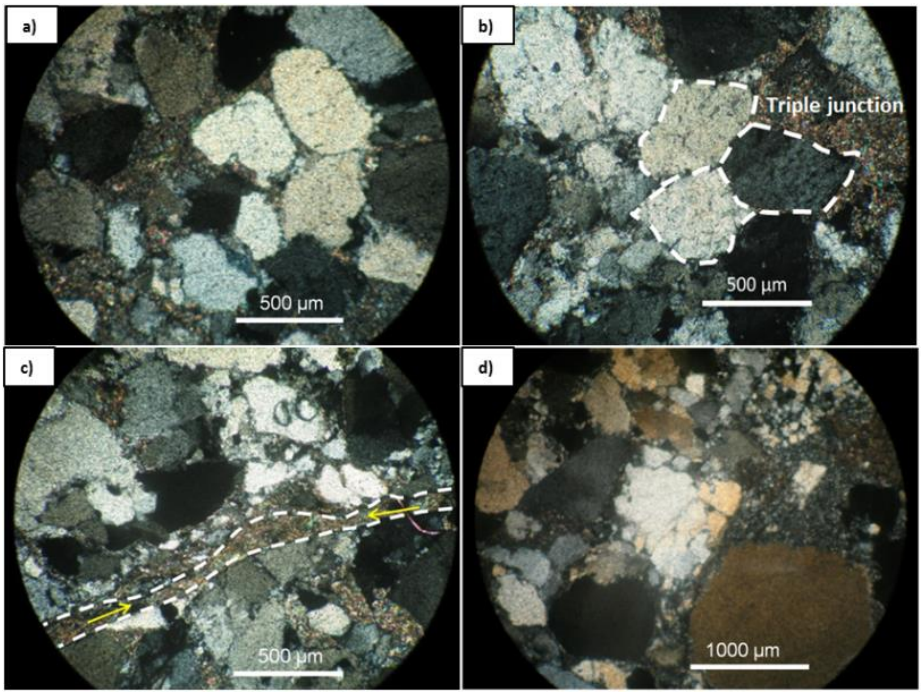


Figure 6: a) Continuous framework of quartz grains, which are well sorted, sand-sized, with minor interstitial matrix. The field of view is crossed-polarized light and 8/0.2 lens. b) The triple junction contact, which resulted from compaction of the rock mass. The field of view is crossed-polarized light and 8/0.2 lens. c) The elongated lens-like matrix, which cut across the thin section. The field of view is crossed-polarized light and 8/0.2 lens. d) Fracturing and fragmentation of quartz grains. This also shows a large variation in grain size from silt to coarse grain (1.5 mm).

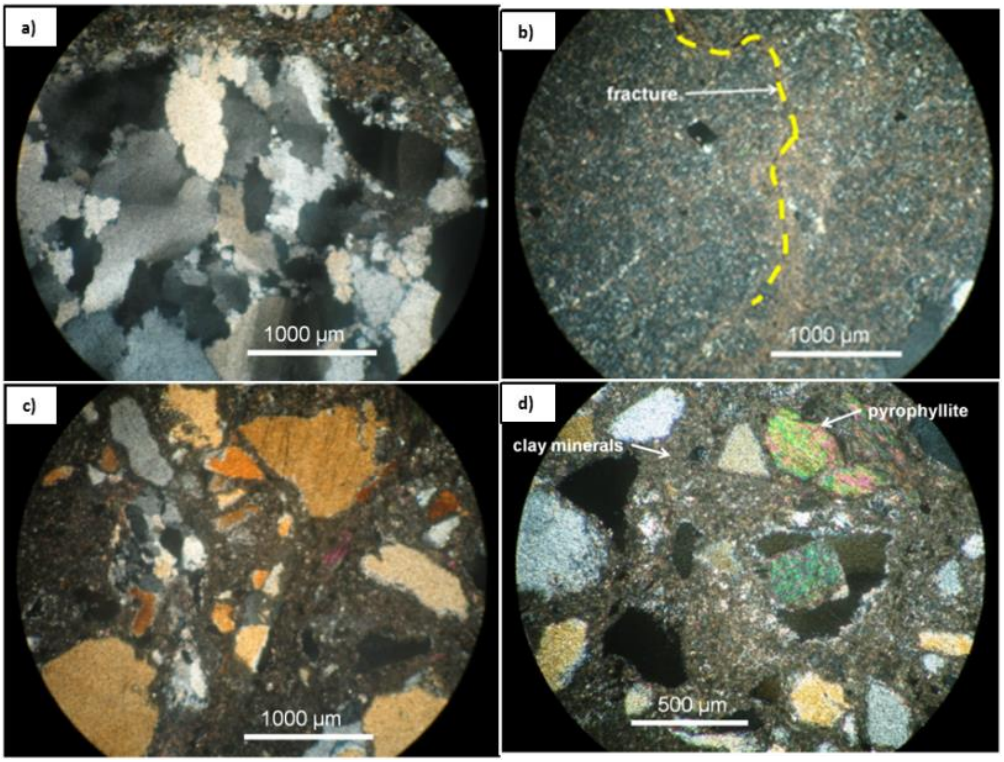


Figure 7: a) Polycrystalline quartz clast, which shows older deformation and alteration, not related to the microseismicity. The field of view is crossed-polarized light and 4/0.1 lens. b) Conglomerate shows fractures that are associated with alteration on the pebbles. The field of view is crossed-polarized light and 4/0.1 lens. c) The picture taken under the microscope showing poorly sorted grains and massive texture. The grain size varies from silt to gravel (according to Wentworth grain size scale [5]). The field of view is crossed-polarized light and 4/0.1 lens. d) Matrix composition is mostly phyllosilicate (mica) and clay minerals. The field of view is crossed-polarized light and 8/0.2 lens.

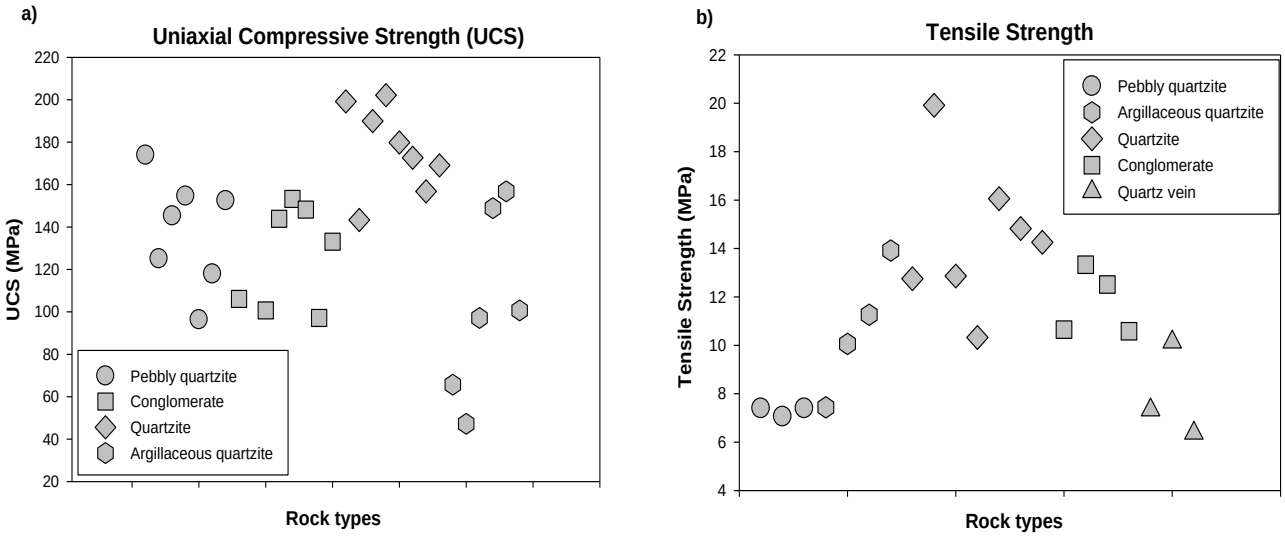


Figure 8: a) Uniaxial compressive strength test results for pebbly quartzite, quartzite, conglomerate and argillaceous quartzite. b) Results of the Brazilian tests, showing that quartzite has the highest tensile strength and quartz vein has the least.

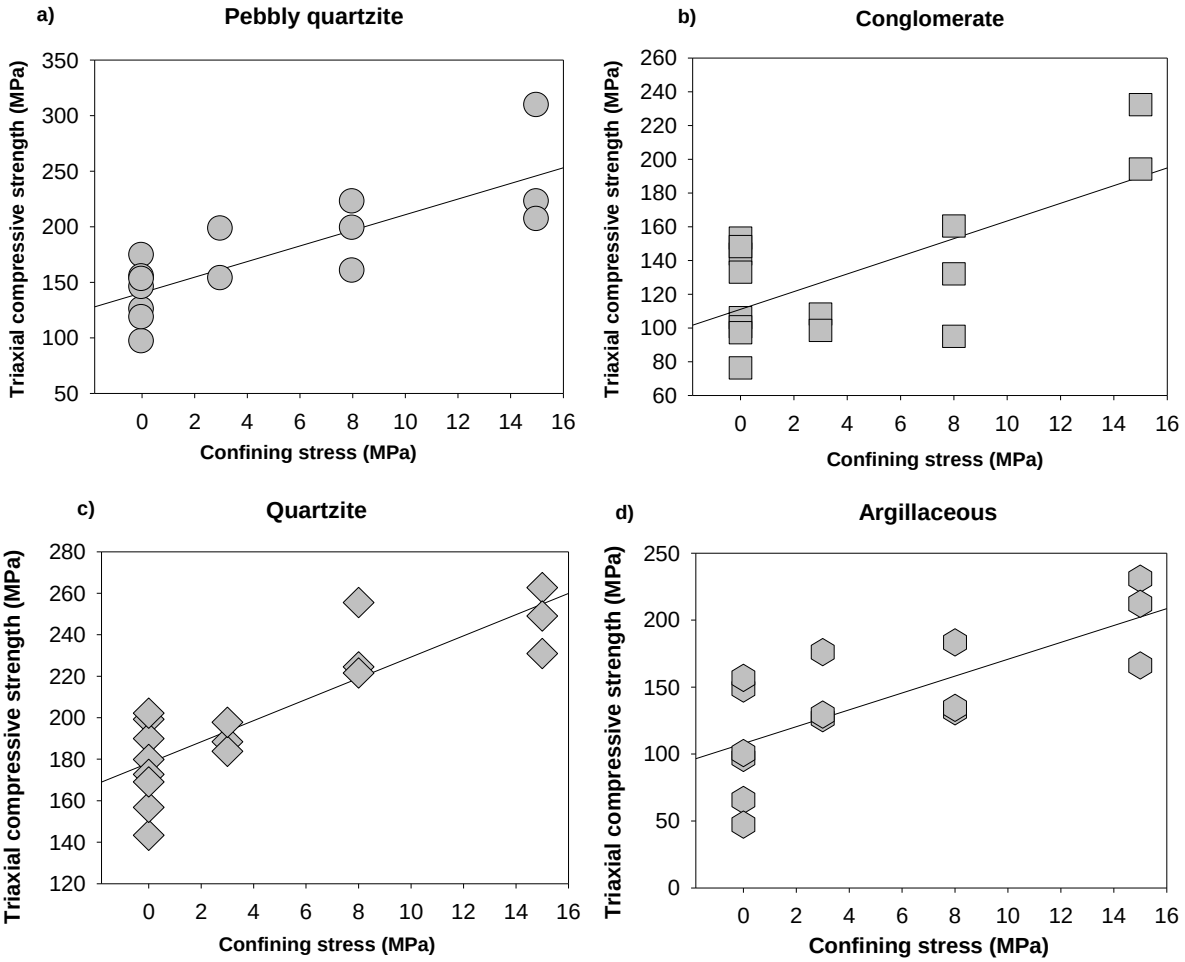


Figure 9: Triaxial compressive strength trend lines show an increase in compressive strength with increasing confinement. (a) Pebbly quartzite; (b) Conglomerate; (c) Quartzite; and (d) Argillaceous quartzite.

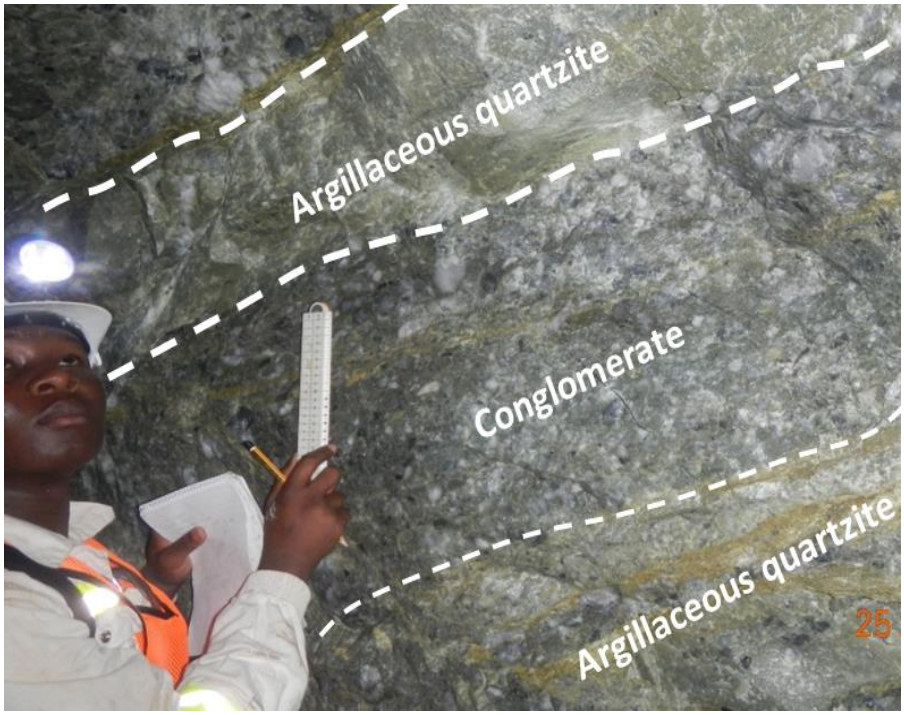


Figure 10: Interlayered conglomerate, argillaceous quartzite and pebbly quartzite in the stope.

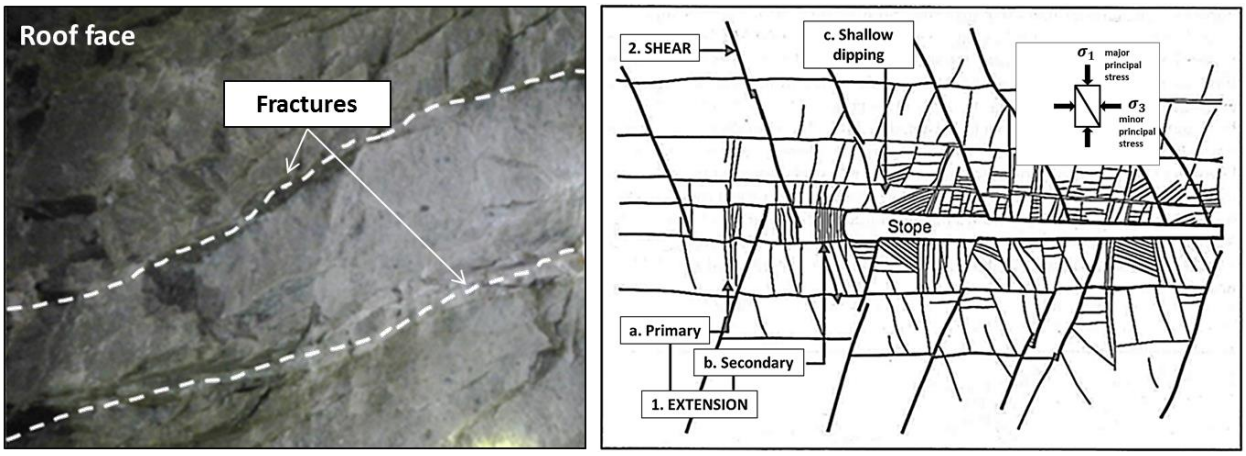


Figure 11: Observed underground fractures around the stope are correlated with the general model of fracturing around the stope face [3].

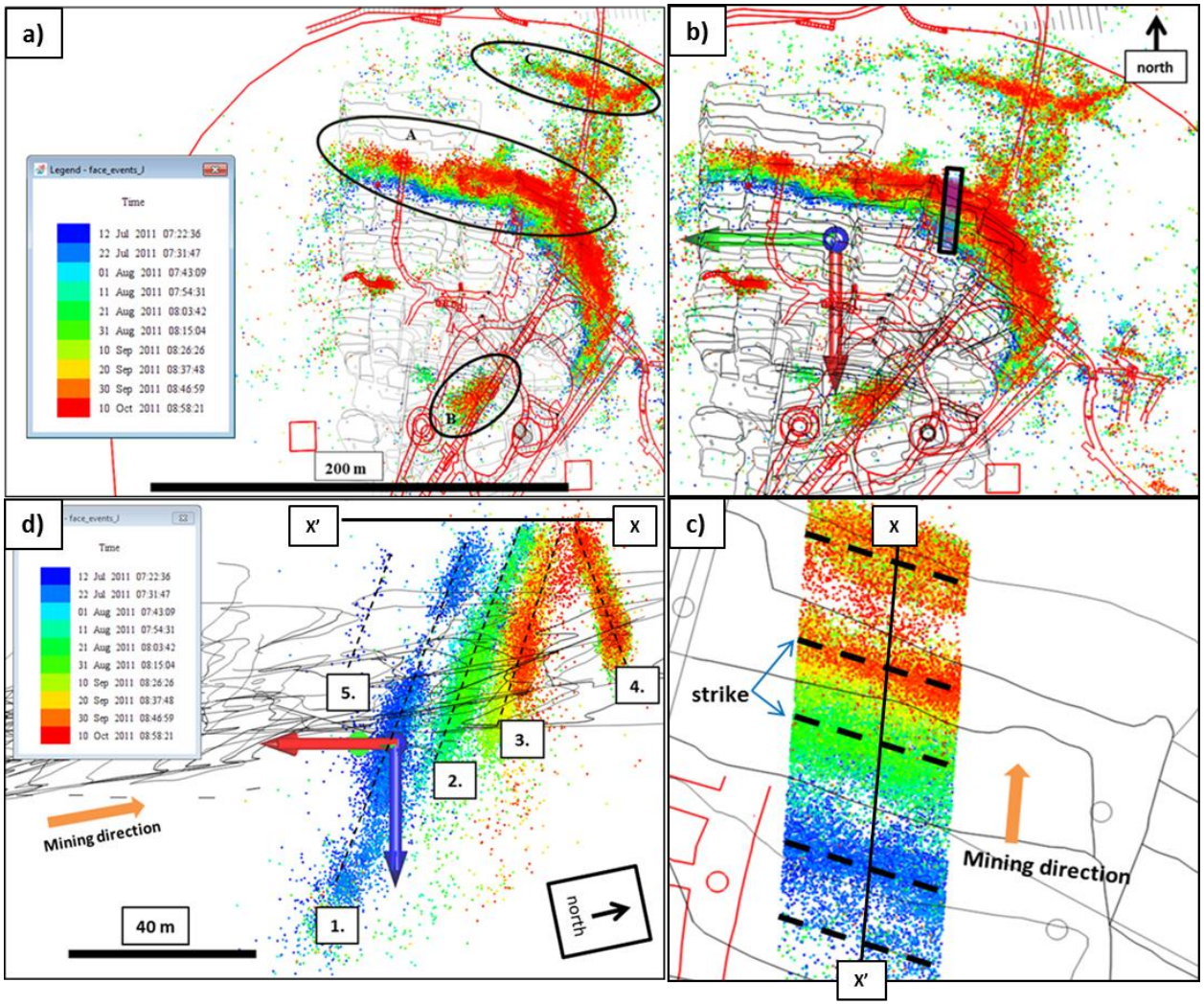


Figure 12: a) The hypocentre distribution of microseismicity in the mining area. b) The rectangle represents the region where seismic activities associated with the mining front were selected for analysis. c) The selected seismic activities region (top view). These events strike parallel to the mining front. d) Alignment of steeply dipping planar seismic events along the mining front (vertical section). Five planar sub-clusters can be clearly distinguished within cluster A.

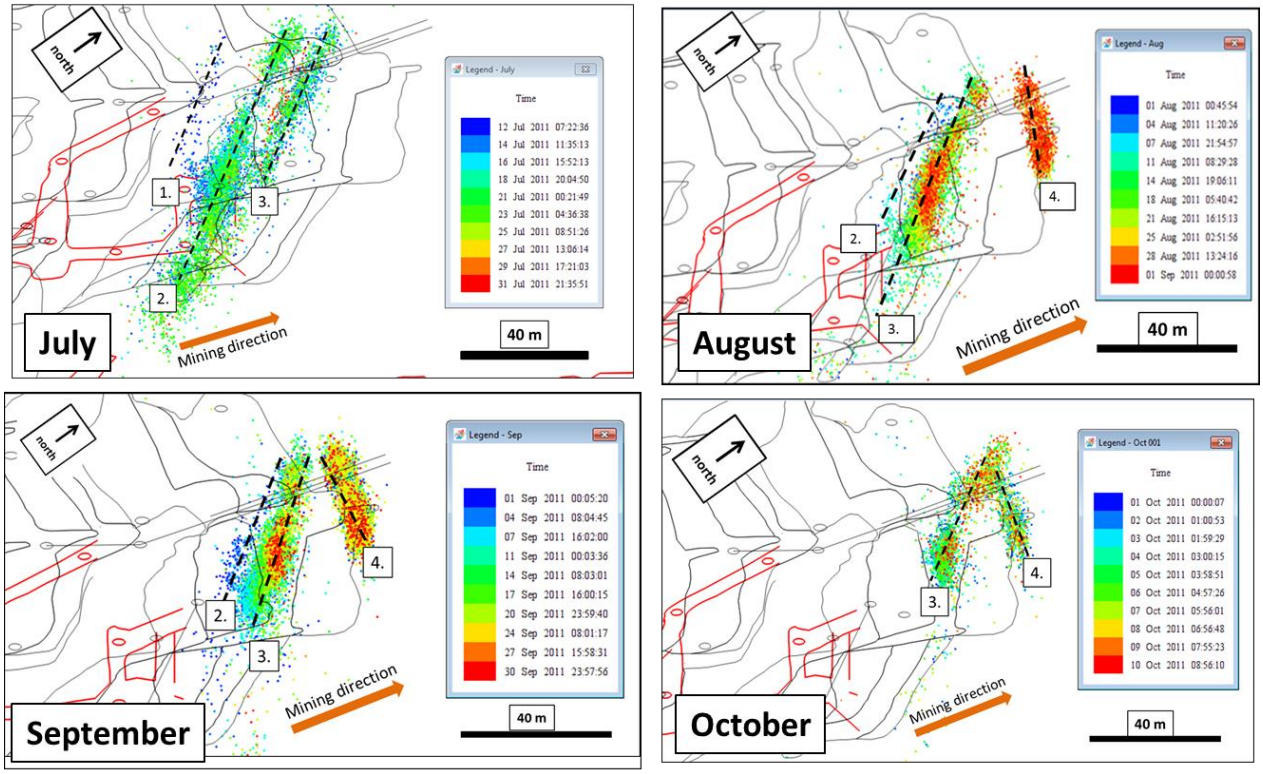


Figure 13: The evolution and growth of microseismicity from 12 July 2011 - 10 October 2011. AE clusters strike sub-parallel to the mining front and can clearly be subdivided into five distinctive planar clusters that dip very steeply. These fractures range in dip from 40º to 65º [24; 26]. The colours represent progression of time, the numbers 1 through 4 mark the order of fractures recorded by high-resolution seismic monitoring system as the mining advances (i.e. fracture 4 start to appear in August 2011 and fracture disappears).

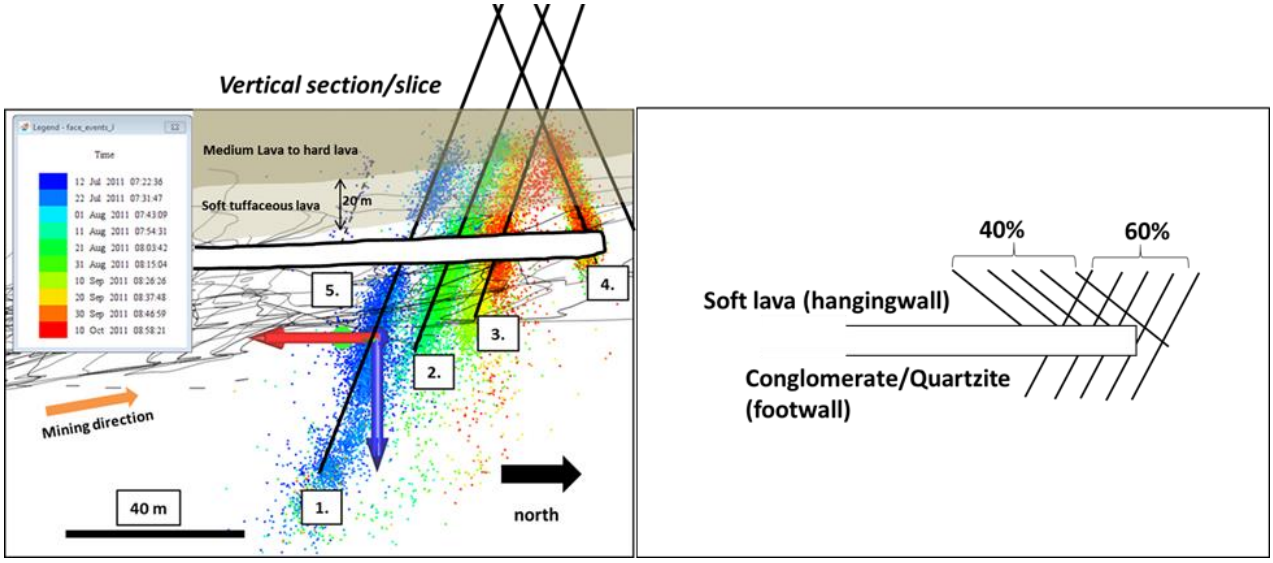


Figure 14: Roberts and Schweitzer [24] fracture model - weak/soft lava hangingwall and quartzite/conglomerate footwall correlated with microseismicity ahead and around the stope.

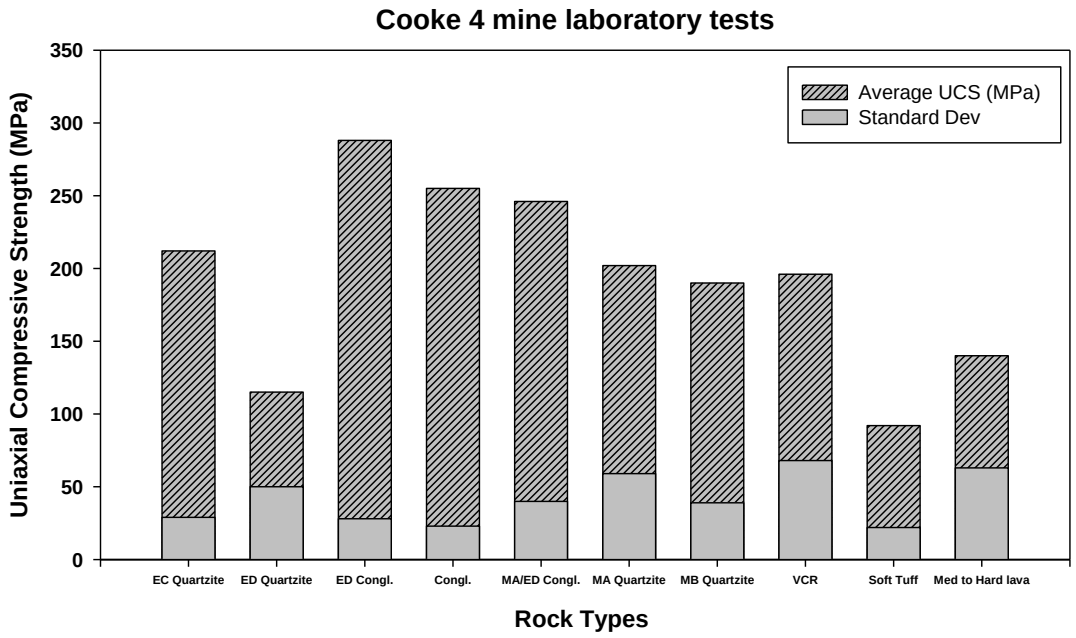


Figure 15: Summary of uniaxial compressive strength laboratory test results from Cooke 4 hangingwall volcanic rocks [24]. The hangingwall soft tuffaceous lava is weaker (<100 MPa) as compared to all other quartzite rocks tested.

List of Tables

Table 1: Laboratory tests from Cooke 4 mine [4].

		Rock type									
		EC Quartzite	ED Quartzite	ED Congl.	MA/ED Congl.	MA Congl.	MA Quartzite	MB Quartzite	VCR	Soft Tuff	Medium to Hard Lava
UCS (MPa)	Number of tests	4	3	4	3	10	8	10	7	21	35
	Min	169	59	250	229	170	116	146	62	48	42
	Max	233	153	317	273	306	263	287	264	138	313
	Average	212	115	288	255	246	202	190	196	92	140
	Std Dev	29	50	28	23	40	59	39	68	22	63

Table 2: The relationship between the fractal dimension and b-value of these planar sub-clusters.

Method	Parameter	Plane 1	Plane 2	Plane 5
Least squares	b-value	1.0	1.0	1.0
	D	2.0	2.0	2.0
Maximum likelihood	b-value	0.9	0.9	0.9
	D	1.7	1.7	1.7

Table 3: Laboratory tests results from Witwatersrand basin rocks [57].

Rock types	Confinement (MPa)	Stress at failure (MPa)
90 % Quartzite	0.0	289
	0.0	345
	3.4	369
	6.9	393
	13.8	477
	27.6	635
70 % Quartzite	0.0	198
	0.0	215
	3.4	225
	6.9	269
	13.8	336
	27.6	368

8. Dynamic rupture propagation of brittle shear fractures

The manuscript has been prepared in accordance with journal requirements.

The effect of a gouge layer on rupture propagation along brittle shear fractures in deep and high-stress mines

International J Rock Mechanics & Mining Sciences, available online from 1 December 2020.

https://doi.org/10.1016/j.ijrmms.2020.104454

Mngadi, SB[a,j,*], Tsutsumi, A[b], Onoe, Y[b], Manzi, MSD[a,j], Durrheim, RJ[a,j], Yabe, Y[c,j], Ogasawara, H[d,j], Kaneki, S[e,j], Wechsler, N[f,j], Ward, AK[g,j], Naoi, M[h], Moriya, H[c], Nakatani, M[i]. and the DSeis team[j]

[a] School of Geosciences, University of the Witwatersrand Johannesburg, PO Bag 3, WITS, 2050, Republic of South Africa.

[b] Graduate School of Science, Kyoto University, Kyoto, 606-8502, Japan

[c] Graduate School of Engineering, Tohoku University, 6-3, Aza-Aoba, Aramaki, Aoba-ku, Sendai 980-8578, Japan.

[d] College of Science and Engineering, Ritsumeikan University, 1-1-1 Noji Higashi, Kusatsu 525-8577, Japan.

[e] Disaster Prevention Research Institute, Kyoto University, Gokasho, Uji, Kyoto 611-0011, Japan.

[f] Department of Geosciences, Tel Aviv University, P.O. Box 39040, Israel.

[g] Cooke 4 Shaft, Sibanye Gold Limited, PO Box 82, Westonaria, Republic of South Africa.

[h] Graduate School of Engineering, Kyoto University, Nishikyo-ku, Kyoto, 615-8540, Japan.

[i] Earthquake Research Institute, The University of Tokyo, 1-1-1 Yayoi, Bunkyo-ku, Tokyo, 113-0032, Japan.

[j] The International Continental Scientific Drilling Program (ICDP) DSeis team.

ABSTRACT

The presence of fault gouge and the generation of wear material between two sliding rock surfaces plays a critical role in slip weakening and propagation of ruptures along underground brittle shear fractures forming ahead of tabular excavations in deep and high stress gold mining. We performed two types of friction experiments: one with a fault gouge layer between two sliding surfaces, and the other without a fault gouge layer 'rock-on-rock', both under room dry conditions at slip velocities ranging from ~1.0 mm/s to 1200 mm/s. These friction experiments revealed a remarkable difference in the frictional weakening behaviour, e.g., rock-on-rock friction experiments show weakening behaviour at lower slip velocity (~ 5 mm/s) and generally has lower frictional strength than those with the intervening fault gouge between sliding surfaces. This study shows that the existence of the fault gouge layer between sliding rock surfaces delays the onset of fault weakening (i.e., slip weakening displacement of gouge layer experiments is larger compared to rock-on-rock experiments). It is proposed that flash heating may be the main active weakening mechanism within both our gouge and rock-on-rock experiments, and provides a feasible account for the observed weakening. Here we suggest that we may be able to describe brittle shear fracture rupture propagation process along underground brittle shear zones by conducting low, intermediate and high slip velocity friction experiments with and without an intervening fault gouge between sliding rock surfaces. These findings should have important implications for the modelling of rupture propagation processes in underground shear zones, a phenomenon that influences the severity of rockbursts, and hence the safety of mine workers and mining operations.

1. INTRODUCTION

Drilling into seismogenic zones (or active faults) is one of the most important scientific approaches to address historical and new scientific questions concerning the physics and mechanics of earthquakes and faults [1-3]. One of the fundamental questions is: What controls earthquake rupture propagation along a shear zone? Deep mines provide unique opportunities to access focal areas and directly sample the fragile rock volume, fresh shear rupture surfaces and fault gouge through short, well-targeted and cost-effective drilling programs.

Deep gold mines are important for sustainable economic development, employment creation and poverty alleviation in South Africa. However, persistent seismicity, falls of ground, and rockbursts pose a serious risk to mining operations, the safety of mineworkers, infrastructure and people living near mining regions, and research continues into the cause and mitigation of mining-induced seismicity [4-6]. The ICDP-DSeis project “Drilling into Seismogenic zones of M2.0 to M5.5 earthquakes in deep South African gold mines” [3] recovered samples from the remnant pillar that remained after shaft pillar extraction at 1 km depth, at Cooke 4 gold mine (Figure 1) to study weakening behaviour and rupture propagation along shear zones. The remnant pillar was subjected to vertical stresses comparable to virgin stresses at depths of ~3-4 km (Figure 2). To minimise drilling-induced damage, we recovered the fractured rock mass after the mine had completed overstoping, relieving the stress in the rock mass almost entirely.

Deep and high-stress mining operations induce stress fracturing around and ahead of underground excavations, forming brittle shear fractures tens of metres ahead of a mining stope [7]. These brittle shear fractures sometimes de-stress the rock mass ahead of the mining stope, reducing the ability of the rock mass to store strain energy, which may mitigate the risk posed by large seismic events. However, some of these brittle shear fractures cause falls of ground, and are sometimes the source of large damaging seismic events M_w1-4 [8]. This has led to several studies of exhumed fault zones, notably the landmark paper “Anatomy of a mining-induced fault zone” [9].

Our work focuses on Ortlepp shears [10], which constitute a subset of dynamic brittle shears that form in deep and highly stressed mines (Figure 3). The genesis of Ortlepp shears is said to be similar to those of ‘conjugate shears’ forming under triaxial load in laboratory experiments and is characterised by normal displacement. They dip towards the stope face when in the hangingwall, and dip away from the stope face when in the footwall. Ortlepp shears primarily consist of two mechanical features, viz.

extension fractures and breakthrough shear ruptures [10]. Ortlepp [11-12] observed that most of these brittle shears exhibit the breakthrough shear ruptures. These shear fractures are also characterised by the formation of a fault gouge (known as 'rock flour' in South African gold mines, which is often found in exhumed seismic ruptures), which can be observed around the mining excavation once these fractures are exhumed through mining [13]. Reches and Dewers [14] proposed that the formation of this fault gouge is through dynamic rock pulverization during a fast propagating seismic event, occurring at the tip fracture due to stress intensity and strain rates. The model is based on analysis of the gouge material recovered from a new fault formed in a South African gold mine [15]. In this study, we sampled the fault gouge generated by these fresh shear ruptures to study slip weakening behaviour and rupture propagation along these shear zones.

However, one of the important questions is what magnitude earthquakes these recovered fresh shear ruptures experienced? We did not record any large seismic events (M_w 1-4) associated with these shear ruptures. Though to be noted, the limitation of acoustic emissions (AEs) sensors is that slightly larger seismic event will emit energy over a wide bandwidth, some of which will certainly be detected by AE sensors. However, the problem is the accurate determination of the moment. Furthermore, it is extremely challenging to measure the displacement in the recovered fragile drill core, unless one is extremely fortunate that the displacement is small and a particular marker happens to be within the recovered drill core. Nevertheless, some classic Ortlepp shears with displacements of up to 100 mm were mapped at different locations in stopes [16-17], which would suggest a Hanks-Kanamori moment magnitude (m_{HK}) of ~ 3.6 (see Table 1) [18]. In several cases the recorded seismic events were smaller by an order of magnitude and the large displacements attributed to the local softness of the loading system where the shear developed close to a stope [16].

Several factors influence fault stability, dynamic failure and weakening behaviour of fault rocks: for example, the mineral and chemical composition of the host rocks, the presence and type of fault gouge particles, contacts between sliding rock surfaces, roughness and the slip velocity [19-21]. Dieterich [19] described friction experiments with an intervening artificial gouge between two sliding rock surfaces. The results showed that parameters such as time, displacement and velocity influence rock friction, and that the strength of each of the contacting points (i.e., strength of the asperities) between sliding surfaces may control the frictional resistance. Marone et al. [22] reported frictional properties and stability of frictional sliding for artificial fault gouge between both rough steel surfaces

and Westerly granites in a triaxial apparatus under higher normal stress ≥ 50 MPa. They observed that friction experiments with an intervening gouge layer (composed of quartz sand) between sliding surfaces show friction coefficient increasing with slip velocity (a phenomenon called velocity strengthening), while rock-on-rock (bare granite surfaces) show friction coefficient decreasing with slip velocity (a phenomenon called velocity weakening). They further observed that velocity strengthening is directly proportional to the thickness of a gouge layer and surface roughness of sliding surfaces. Di Toro et al. [23] showed that increasing slip velocity to greater than 1 mm/s decreased frictional strength for quartz rocks. This frictional resistance was extrapolated to reduce to zero at high slip velocities, ~ 1000 mm/s, and was attributed to the formation of a thin 'silica gel' layer between sliding fault surfaces. Yao et al. [24] reported that flash heating controlled weakening behaviour, and that powder lubrication and the presence of nanoparticles may not be required for the dynamic weakening mechanism. Kanagawa et al. [25] also concluded that flash heating was responsible for the weakening of quartz rocks at sub-seismic slip velocities, and that silica gel may not be responsible for weakening.

Rowe et al. [26] conducted friction experiments on the novaculite rock type, which consists of euhedral quartz grains with traces of oxide minerals. Two cylinders (rock-on-rock) were sheared against each other at sub-seismic slip velocities of ~ 0.1 - 100 mm/s and normal stresses of ~ 2.5 MPa, with the total slip displacements between 3 and 30 m. Weakening was observed in every experiment, and most experiments achieved steady-state friction at slip displacements greater than 0.3 m. At slip velocities of ~ 0.1 mm/s, 1 mm/s, and 10 mm/s, the peak friction coefficient gradually decreased from ~0.7 to a steady-state value of ~0.45 – 0.6. At a slip velocity of ~ 100 mm/s, the friction coefficient reduced dramatically to less than 0.1. Importantly, they estimated the peak temperature (ΔT) at asperities during flash heating using the approach of Rice [27] and Violay et al. [28] for a range of slip velocities and asperity sizes. The results of temperature calculations are: at slip velocity of ~ 0.1 mm/s the ΔT is ~ 31 °C; at slip velocities of 1 mm/s the ΔT is ~ 100 °C; at slip velocities of 10 mm/s the ΔT is ~ 318 °C; and at slip velocities of 100 mm/s the ΔT is ~ 1006 °C. Kanagawa et al. [25] conducted friction experiments on intact agate and silica-gel gouge on quartz rocks showing weakening at sub-seismic slip rates of ~ 1–100 mm/s, and results indicated that the frictional strength is controlled by temperature, driven by frictional heating. At seismic slip velocities of ~ 1000 mm/s, they obtained ΔT ~2500 °C flash heating temperature at asperities.

As the slip velocity increases, the friction decreases exponentially from peak friction to a steady-state value [29]. The frictional resistance profile (or fault weakening behaviour) during seismic slip may affect the intensity and extent of the damage [23]. Reches and Lockner [20] suggested that researchers should focus more efforts in examining the mechanisms that govern a weakening process. To enhance our understanding of the shear rupture propagation of brittle shear fractures and provide insights on frictional weakening behaviour at seismogenic depths, we performed frictional experiments over a range of slip velocities (1.0 mm/s - 1200 mm/s) using rocks and fault gouge recovered from brittle shear fractures in deep and highly-stressed South African gold mines. We present physical observations of the host rock, recently-formed fragile rock breccia, shear rupture surfaces, fault gouge, and mineralogy. We also describe friction experiments conducted at low-to-high slip velocities typical of underground Ortlepp shears and tectonic earthquakes.

2. GEOLOGICAL SETTING AND COOKE 4 MINE

The study area is situated in Cooke 4 mine, one of the ICDP-DSeis drilling sites, which is located in the north section of the Witwatersrand Basin. The basin has an oval shape (NE-SW trending major axis ~ 300 km, minor axis ~ 150 km) [30]. The Dominion Group preceded the Witwatersrand Supergroup, and comprises of Archean volcano-sedimentary sequence [31-32]. The Witwatersrand Supergroup comprises interlayered conglomerate 'reefs' and quartzite rocks, and is overlain by the Ventersdorp Supergroup, which consists mostly of volcanic rocks [31].

The Witwatersrand Basin is made up of two groups [31, 33-34]. The (upper) Central Rand Group has an average thickness of ~2.9 km and hosts 70% of the gold deposits. The dominant rock types are fluvial quartzite, conglomerate and minor bands of shale. The (lower) West Rand Group is dominated by clastic sedimentary rocks and minor volcanic rocks. The average thickness of the West Rand Group is 4.6 km [35]. The basin is intruded by sills and dykes of four different generations: Karoo (150 Ma), Pilanesberg (1.30 Ga), Transvaal (2.20 Ga), and Ventersdorp (2.60 Ga). These structures are often associated with stress concentration instabilities and may result in failure and seismicity during mining activities [30].

The Cooke 4 mine was developed 60 years ago, and has since produced ~ 12 million ounces of gold and 14 million pounds of uranium. In 2001, the Cooke 4 mine was put on care and maintenance. In 2010, the shaft was re-opened to mine the remaining high-grade Upper Elsburg reef in the 1.0 – 1.2

km deep shaft pillar. The Cooke 4 shaft drilling targets “Ortlepp shears” occur in the Turffontein Subgroup in the Mondeor Formation at the top of the Central Rand Group [36]. The Mondeor Formation consists of alternating conglomerates and quartzite rocks that on average dip 16^{o} towards the south-east [37].

3. METHODOLOGY

At Cooke 4 mine, Naoi et al. [38-39] and the Science and Technology Research Partnership for Sustainable Development (SATREPS) team, under a 5-year collaboration project between South African and Japanese researchers "Observational studies in South African mines to mitigate seismic risks" used microseismic monitoring, capable of detecting seismicity down to M_w -5 to delineate both the temporal and spatial evolution of mining induced fractures around the stope. Moriya et al. [7] found that these fractures developed several tens of metres ahead of the mining front and with a geometry typical of Ortlepp shears. The ICDP-DSeis team drilled into a previously highly-stressed remnant of the shaft pillar situated 1.0 - 1.2 km below the surface to recover recently-formed fragile ruptures, rock breccia and fault gouge from seismogenic zones [40].

3.1. Triple-tube drilling, geological and geophysical logging

Drilling into deep and highly-stressed fractured seismogenic zones requires care and attention. Single- and double-tube core barrels are not suitable in such a fragile drilling environment. In the case of double-tube barrels, the tube sampler rotates (depending on a drilling system), which may shear the sample along weak planes; and the cored samples are subjected to erosion and disturbance by the drilling fluid. To achieve optimal core recovery, we deployed a triple-tube core barrel. The triple-tube barrel consists of a double core barrel sampler with a stationary liner (depending on a drilling system) that protects the cored samples during extraction. Fractured rock fractures were successfully recovered. The borehole was drilled from 1.2 km below the surface at Cooke 4 shaft, level 38. The borehole length is ~41.5 m, with a core diameter of 42 mm (azimuth: 30^{o}; plunge: 24^{o}; direction: NNE). The recovered host rocks form part of the lower Elsburg Individuals members. Geological logging of the core, true physical properties, and geophysical logging of the borehole (density and natural gamma) was conducted post drilling, and correlated with mapped shear fractures and host rock lithologies.

3.2. Rock and fault gouge composition

XRF and XRD were used for chemical and mineral analysis of rocks. The XRF analysis was used to identify major elements in our samples. For XRD analysis, the material was prepared using a back-loading preparation method. It was analysed with a Malvern Panalytical Aeris diffractometer with PIXcel detector and fixed slits with Fe filtered Co-Kα radiation. The phases were identified using X'Pert Highscore plus software. The relative phase amounts (weight %) were estimated using the Rietveld method. Major elements were determined using the Norrish Fusion [41] technique and Panalytical PW2404 X-ray fluorescence spectrometer. The results are presented in section 4.

3.3. Frictional sliding experiments

We conducted friction experiments at low-to-high velocities (~1.0 mm/s to 1200 mm/s), typical of underground Ortlepp shears and tectonic earthquakes [21]. A rotary-shear machine with the capability of low, intermediate and high-velocity friction testing was used [42-43], similar to the machine used by Tsutsumi et al. [43]. Two types of friction experiments were conducted: (a) with fault gouge 'rock flour' in between the quartzite rock cylinders, and (b) rock-on-rock friction experiments (experimental set-ups for (a) and (b) are both shown in Figure 4). We used cylindrical quartzite host rocks with a diameter of ~24 mm (+/-0.1mm) and a length of ~33 mm (+/-0.1 mm). Since there were limited natural gouge samples recovered from triple tube drilling, in addition to natural gouge samples, we used crushed and sieved artificial gouge collected from rock breccia from shear zones. The detailed description of the artificial and natural gouge is presented in section 4.3.

3.3.1. Fault gouge friction experiment procedure

We used manually-crushed and sieved samples as the gouges for the experiments from run number MVR918 to MVR923. In MVR925 and MVR926, we used the natural gouge samples from S (4) and S (3), respectively. A Polytetrafluoroethylene PTFE (Teflon) sleeve was used to confine and prevent the fault gouge from leaking during shearing or rotation. The sliding surfaces of our host blocks were roughened with 80# SiC abrasive powder to ensure even contact and prevent slippage along the interface [19, 24-25, 44-46]. According to Boulton et al. [46] this 80# SiC abrasive powder translate to 180 µm roughness. The gouge layer was in room dry conditions, with ~ 0.5 g gouge placed between a pair of quartzite cylinders, which translates to a thickness of approximately 0.5 mm (Figure 4 a-e). The

fault gouge was axially pre-loaded for 30 to 60 minutes (maximum) and then sheared under applied normal stress (~2 MPa). For MVR924, we conducted friction experiments on bare rock surfaces, without an intervening fault gouge and Teflon sleeve. We drilled a small 5 mm diameter hole at the center of quartzite cylinders and wrapped the tip with steel wire (with ~1 mm thickness) to avoid tensile failure during the experiments. We also ensured that rotating and stationary cylinder surfaces were parallel, making contact of the entire surface (Figure 4 f-j).

Because of the sample geometry, the slip rate varied as a function of distance from the center of the rotation axis. An equivalent slip velocity V_{eq} is defined such that $(\tau \cdot \mathrm{V_{eq}} \cdot S)$ is the rate of frictional work on the slipping surface area S, assuming that the shear stress τ is constant over the entire fault surface [42]. This velocity is given by:

$$\mathrm{V_{eq}} = \frac{4\pi}{3}\varphi \mathrm{R} \quad (1)$$

where R and φ are the radius of the sample and revolution rate, respectively.

3.3.2. Confinement: effect of PTFE (Teflon) sleeve

To estimate and correct for the effect of Teflon sleeve friction, we conducted experiments at a fixed equivalent slip velocity of 10 mm/s and varied the normal stress (2, 3, 4 and 5 MPa; MVR923). We also computed shear stress, and from these results, we could estimate the friction coefficient of the Teflon sleeve using the y-intercept of the shear stress and normal stress curve. The torque was unstable at high normal stress (~5 MPa), and the data were too noisy to be used.

Additionally, to investigate the effect of stress exerted by the Teflon sleeve on the measured friction (confinement), we conducted three runs of rock-on-rock experiments with and without the Teflon sleeve, and varied the size of the Teflon sleeve inner diameter to further investigate the relationship between the loose and tighter Teflon sleeves on measured friction, referred to as MVR944. For this, we used a fixed slip velocity of 10 mm/s and normal stress of 2 MPa. Similar to sample runs MVR924, we tested the parallelism of the rock-on-rock contact for the quartzite cylinders using pressure-sensitive paper. However, we did not use the wire to reinforce the samples, because we put a PTFE sleeve on the cylinders for this experiment. For the first run of the experiment (MVR944_1), we used a relatively large PTFE sleeve. The difference between the outer diameter of the stationary-side quartzite cylinder and an inner wall of the PTFE sleeve is about 0.05 mm. Note that this difference, i.e., the tightness of the sleeve, is approximately the same as that used for MVR918. The PTFE sleeve was removed to

conduct the next run (MVR944_2) for comparison under the same conditions. After removing the sleeve, we tried to remove the gouge powders formed on the fault surfaces with a vacuum cleaner. Then we applied the same normal stress on to the fault surfaces and restarted the experiment using the same slip rate. For the third run (MVR944_3), we stopped the motor, removed axial loading, and then inserted another PTFE sleeve. In this run, the sleeve used was tighter than the previous one; the difference of the diameter between the rock cylinder and the sleeve was about 0.18 mm.

3.3.3. Slip weakening distance (D_c) estimation

The friction tends to drastically decrease with increasing displacement at high slip velocities during sliding blocks (or rupture propagation). This phenomenon is called slip weakening behaviour. This slip weakening behaviour can be described by an exponential decay function [29, 47-48]:

$$\mu = \mu_s + (\mu_p - \mu_s)\, e^{\left(\frac{\ln(0.05)*d}{d_c}\right)} \quad (2)$$

where μ_p and μ_s are the peak friction coefficient and steady-state coefficient of friction, respectively. The fault displacement is characterised by an independent variable, d. The exponential decay curve decreases (friction coefficient) as d approaches infinity ($d \to \infty$), and therefore, we carefully define d_c as displacement where $(\mu_p - \mu_s)$ decreases to 5% of $(\mu_p - \mu_s)$ following Mizoguchi et al. [29]. We assume that newly defined d_c represents a critical slip displacement (D_c), over which the fault strength breaks down during rupture propagation [29].

3.4. The temperature increase through flash heating

We follow basically the calculation method given in Kanagawa et al. [25] to estimate the temperature increase at asperities by flash heating. The temperature increase ΔT (°C) caused by flash heating at an asperity contact is defined by [25-28]:

$$\Delta T = \frac{\sqrt{t_c}\mu_p S_i V}{\rho c_p \sqrt{\alpha\pi}} \quad (3)$$

where S_i (Pa) is the indentation strength, ρ (kg/m^3) is the density, α (m^2/s) is the thermal diffusivity and c_p (J/kg°C) is the heat capacity of the material, V (m/s) is the slip velocity and t_c (s) is contact time at an asperity. The contact time t_c (s) can be expressed as the asperity radius r (m) divided by slip velocity V (m/s):

$$t_c = \frac{2r}{V} \quad (4)$$

The indentation strength S_i (Pa) can be expressed by the normal force F (kg·m/s^2) divided by the contact area of a circular asperity experiencing plastic deformation:

$$S_i = \frac{F}{\pi r^2} \quad (5)$$

On the other hand, the normal force can be expressed as the normal stress σ (Pa) multiplied by the slip surface area A (m^2):

$$F = \sigma A \quad (6)$$

This means the temperature ΔT (°C) at an asperity contact can be given by:

$$\Delta T = \frac{\mu_p}{\rho c_p} \sqrt[4]{\frac{S_i^3 V^2 \sigma A}{\alpha^2 \pi^3}} \quad (7)$$

4. RESULTS

4.1 Host rock composition

Four main rock types were recovered viz. quartzite, pebbly quartzite, argillaceous quartzite, and conglomerate. In this study, core samples were further prepared for chemical and mineralogical analysis using XRF and XRD techniques. Table 2 shows the results of the XRF analysis of major elements and the loss on ignition (LOI). The most abundant major elements found are oxides: SiO_2 (>85%) and Al_2O_3 (>3%) and small amounts of F_2O_3, K_2O and TiO_2. The XRD results are shown in Table 3, and the main minerals found in all four host rocks are quartz and muscovite, consistent with the major elements. Quartzite consists of mostly quartz (~ 83-90 wt%) and muscovite (~9-16 wt%), pebbly quartzite consists primarily of quartz (~ 92-94 wt%) and muscovite (~ 5-7 wt%), argillaceous quartzite consists of quartz (~23-55 wt%) and muscovite (~41-74 wt%), and conglomerate largely consists of quartz (~75-95 wt%) and muscovite (~1-15 wt%). Minor minerals are microcline and pyrite. Microcline is predominantly found in argillaceous quartzite, and pyrite is largely associated with the conglomerate 'reefs'.

4.2. Mapping brittle shear fractures

Four main brittle shear fractures were recovered, mapped and analysed. These brittle shear fractures occur at different core depths, here referred to as S(1)~25.2 m; S(2)~ 27.4 m; S(3)~ 33.9 m and S(4)~ 39.9 m. These lithologies and brittle shear fractures were also delineated by geological and geophysical (natural gamma and density) logging of the core (Figure 5). The natural gamma and density logs correlate well with changes in lithology, lithological contacts and some shear fractures. The

observed brittle shear fractures are characterised by fault gouge (“rock flour”) and rock fragments (“rock breccia”) (Figure 6). Broken cm-scale rock fragments ("breccia") were observed in the core tray adjacent to the fractures, which further distinguished these brittle shear fractures from drilling-induced damage. Some fault gouge could be easily peeled off with a sharp object such as a knife (Figure 7a). Fracture rupture surfaces are characterised by rough angular surfaces (Figure 7b), contrary to drilling-induced fractures, which are characterised by smooth rupture surfaces. These rough surfaces occur at cm scale. Slickensides on the rupture slip surface are often weak and easily removed; these slickensides are referred to as "soft slickensides". For this reason, it is difficult to observe any 'clearly' preserved slickensides on these rupture slip surfaces. There was no observed mineralisation on these rough fracture surfaces, which suggests that these are recently formed fractures.

4.3. Fault gouge

4.3.1. Natural and artificial fault gouge composition

We sampled the recovered fault gouge material collected at various core depths (mapped locations) where these brittle shear fractures occur, e.g., 25.2 m; 27.4 m; 33.9 m, and 39.9 m. The recovered fault gouge was limited in volume, and it occurred mostly in quartzite and conglomerate rocks. We conducted XRD analysis of the natural gouge recovered from deep and high stress South African gold mines and ‘artificial’ gouge made up of crushed and sieved particles to examine the mineral phases before performing high velocity friction experiments (Table 4).

We further analysed selected wear particles generated and collected from the rock–on-rock experiments during sliding of quartzite rocks. The collected wear particles were fine enough to analyse directly with XRD without crushing. The wear gouge material was generated during sliding at 200 mm/s slip velocity and 2 MPa normal stress, room dry conditions (MVR924). The XRD results of this wear gouge material are shown in Table 4. We correlate the mineral phases of wear material with the host rocks, natural and artificial gouge. The natural gouge samples tend to have high quartz content, similar to recovered wear material post friction experiments at high slip velocities, while artificial gouge tends to have a lower content of quartz.

4.3.2. Fault gouge size distribution

4.3.2.1. Sieving particles

All fault gouge samples, natural and artificial, consist mainly of quartz and minor muscovite minerals (see above). They were sieved into bin sizes: (a) 1000 – 500 µm; (b) 500 – 250 µm ; (c) 250 – 125 µm ; and (d) to less than 125 µm. The fault gouge recovered from mining induced shear zones S(1) and S(2) were extremely limited and no friction experiments could be conducted on these natural gouge samples inconsequently, only gouge samples from shear fractures S(3) and S(4), and artificial gouge was used for friction experiments. The particle size distribution analysis of the natural gouge samples S (3) and S (4) from the sieving method are shown in Table 5. For artificial gouge, we crushed and sieved the samples using the same bin sizes (see Table 5) similar to the natural gouge samples. In general, for friction experiments, we used gouge particle sizes that are less than 125 µm, besides S (3) which did not have a minimum amount of weight sample required (~ 0.5 grams) to conduct friction experiments in our set up. We used a combination of two sieve bins (250 – 125 µm and less 125 µm) to produce 0.5 g required for sample S (3).

4.3.2.2. Laser diffraction particle size analyser

The laser diffraction particle size analyser method has been used in several particle size distribution studies for fault gouge analysis [14-15, 49-51]. We used the Malvern Mastersizer laser diffraction particle size analyser to examine the finer fraction of the gouge particle used, mostly less than 125 µm. The Malvern Mastersizer uses laser diffraction techniques to measure the size of particles. The particle size distribution of the artificial gouge approaches 1 µm to 500 nm (Figure 8a). Post friction experiments of bare rock surfaces, rock-on-rock, we collected gouge that fell from sliding surfaces and measured the particle size distribution of the wear material for MVR924 at slip velocity of 200 mm/s where gouge generation was visibly significant. The wear material grain size approaches ~ 1 µm to less (Figure 8b).

4.3.2.3. Scanning Electron Microscopy (SEM)

We further examined the texture of the limited gouge collected from mining induced shear fractures using the scanning electron microscopy (SEM), which could also be used to complement and verify the sieving and laser diffraction particle size analyser methods. For sample preparation, the fault gouge was glued to an SEM stub before application of the carbon coating (30 nm C). The coating was applied by heating to the carbon source until it evaporates, resulting in deposition of carbon material

onto specimens. This was done before being analysed under the SEM microscopy. The SEM observations of the experimental gouge material show that it does not contain any aggregated structure. It consists of ~ 0.3 - 80 μm angular to sub-angular clasts of quartz, pyrite and other oxides (Figure 9).

4.4. Friction experiments

We performed friction experiments at slip velocities of 1 – 1200 mm/s and normal stress of 2 MPa. The conditions of the experiments are summarized in Table 6, and results are shown in Table 7, Figure 10 and Figure 11. We compared manually-crushed and sieved artificial fault gouge with natural fault gouge recovered from drilling and rock-on-rock friction experiment results.

4.4.1. Artificial fault gouge and natural fault gouge

For manually-crushed and sieved gouge samples (Figure 10a) we found that at lower slip velocity of 10 mm/s and normal stress of 2 MPa, the peak friction of quartzite rocks is 0.86 and weakens to steady-state friction of 0.72 with a slip weakening distance of ~ 6.9 m. At higher slip velocities of 100 mm/s and 2 MPa normal stress, the peak friction is 0.97 and the weakening occurs to steady-state friction of 0.69, over a slip weakening displacement of ~9.6 m. At slip velocities of 200 – 1200 mm/s, we observed weakening over a slip weakening displacement of ~ 13.6 - 7.1 m with peak friction values of 1.02 – 0.91 decreasing to very low steady-state friction values of 0.26.

At slip velocity of 100 mm/s and normal stress of 2 MPa, the natural gouge sample S(3) had a peak friction of ~0.98, which weakened to steady-state friction of ~0.67 over a slip weakening displacement of ~12.8 m (Figure 10b; Table 7). With similar experimental conditions (slip velocity of 100 mm/s and normal stress of 2 MPa), the natural gouge sample S(4) revealed a peak friction of 0.92, and weakened to steady-state friction of 0.71 over a slip weakening displacement of ~6.1 m (Figure 10b; Table 7). These results show that the weakening behaviour of natural gouge samples is similar to the artificial fault gouge samples at similar slip velocities (~100 mm/s) (Table 7).

4.4.2. Rock-on-rock friction experiments

We conducted friction experiments on bare rock surfaces without any intervening fault gouge at slip velocities of 1 - 200 mm/s and constant normal stress of 2 MPa (Figure 11a-e). At low slip velocity (1.0 mm/s), no significant friction weakening was observed (i.e., friction remained very high), the peak

friction (0.76) weakened to steady-state friction of ~0.70. At slip velocity of 5 mm/s, we observed a weakening behaviour of peak friction of 0.81 to steady-state friction of 0.32 over a slip weakening displacement of 3.8 m. At slip velocities of ~ 10 - 200 mm/s, we observed short slip weakening distance of 0.5 – 2.9 m, with peak friction of 0.83 - 0.62 to steady-state friction of 0.32 – 0.20.

To help analyse the friction experiment results with a gouge layer (conducted with the Teflon sleeve around sliding surfaces inducing confinement which might have resulted in higher measured friction), we conducted rock-on-rock experiments with the Teflon sleeve (MVR944_1 and MVR944_3) and without the Teflon sleeve (MVR944_2) (see Table 6; Table 7 and Figure 11f). We observe that at slip velocity of 10 mm/s and normal stress of 2 MPa, the peak friction value for MVR944_1 is ~ 0.71; and weakened to steady-state friction of 0.29 over a slip weakening displacement of 1.8 m. For MVR944_3, with a tighter Teflon sleeve, at similar slip velocity and normal stress, the peak friction observed was 0.94, and weakened to steady-state friction of 0.31 over a slip weakening displacement of ~ 6.2 m. On the friction experiment performed without the Teflon sleeve (MVR944_2), we observed peak friction of 0.75; and steady-state friction of 0.23 over a slip weakening displacement of ~ 1.7 m. With a tighter Teflon sleeve (e.g., MVR944_3), we note that the weakening is 'delayed' (or rather the slip weakening displacement is lengthened) to ~ 6.2 m (Table 7 and Figure 11f).

It seems the results of MVR944 are not contradictory to the experiment performed in MVR924. The PTFE sleeve has only a small influence on the measured friction values if we use relatively loose-sized sleeves (MVR944_1). If we use more tight sleeves, the influence of the Teflon sleeve on measured friction increases slightly (MVR944_3). However, the increased friction values are still extremely low compared to friction measured on the gouge sample in MVR918. Also, we observed that MVR924 at slip velocity of 10 mm/s showed slightly higher steady-state friction coefficient even without Teflon sleeve compared to experiments performed with the Teflon sleeve (MVR944 tests).

We compare friction experiment results performed with the intervening gouge and on bare rock surfaces "rock on rock" (Figure 12, Table 7). With careful consideration of the effect of the Teflon sleeve on measured friction, the rock-to-rock sample weakens faster (i.e. short slip weakening displacement). In general, they tend to have lower frictional resistance at lower slip velocities compared to friction experiments with the intervening gouge layer. We also compare the mechanical behaviour of the natural and artificial gouge samples, we observed that the mechanical behaviour of the natural gouge is similar to that of the artificial gouge and has similar frictional strength (Figure 12).

4.4.3. Axial shortening data and wear material

We recorded the axial shortening during our friction experiments for both rock-on-rock and fault gouge. For friction experiments on bare rock sliding surfaces, weakening was observed in almost all the experiments. The peak friction decreases exponentially to steady-state friction. The corresponding axial shortening data are shown in Figure 11a-e. At high slip velocity of 200 mm/s, we observe no axial shortening up until ~ 1 m slip displacement, and then a decrease (Figure 11e). Since the sliding area between two bare rock surfaces was not confined by the Teflon sleeve during our rock-on-rock experiments, this was likely due to wear materials falling from the sliding surfaces leading to the shortening of specimens (Figure 13). Observations of rock-on-rock experiments at high slip velocity (200 mm/s) reveal that a large amount of gouge was generated, and the measured weight of the gouge material is 0.007 grams. The XRD and particle size distribution analysis were performed on the wear material (see section 4.3). The particle size distribution of the wear material has a minimum of ~ 1 µm (Figure 8b). In addition, at high velocities, damage and tiny mm-scale fractures were observed on the rock cylinder samples (Figure 13).

For gouge experiments, we measured axial shortening with corresponding frictional strength for selected artificial gouge experiments at 10 mm/s, 100 mm/s, 200 mm/s and 1200 mm/s slip velocities (Figure 14). Most samples showed a decrease in total sample length, which may be due to gouge thinning or compaction (Figure 14a-c). However, at the highest slip velocities (~ 1200 mm/s), we observed something different, there was initially an increase in axial length (i.e. dilation), followed by an abrupt shortening at a displacement just over 30 m accompanied by a gradual increase in friction.

5. DISCUSSION

5.1. Host rock and fault gouge composition

The mineral composition has a significant effect on the frictional properties of rocks, and therefore, many geological and engineering studies have been conducted on various silicate rocks [52-55]. The rock from Cooke 4 mine contains mainly quartz (SiO_2) and muscovite ($KAl_3Si_3O10(OH)_2$). In some instances, muscovite occurs in quantities much greater than 10 wt%. Mngadi et al. [17] studied these minerals in thin sections and conducted uniaxial compressive strength (UCS) tests: quartzite (143-202 MPa), pebbly quartzite (96–173 MPa), conglomerate (76–153 MPa) and argillaceous quartzite

(47–157 MPa). These rocks may be described as relatively competent and brittle; consequently, South African gold mines are generally described as a 'hard-rock' mining environment. The fault gouge material has a similar bulk composition to adjacent host rocks, which we interpret to indicate that it is fresh gouge material that has not undergone any alteration or notable weathering process or fluid interaction before sampling.

5.2. Friction experiments

We compare the results of our rock-on-rock and gouge friction experiments with the previously reported data (see Figure 15). Our results are consistent and follow the previously reported weakening trend of the quartz rocks very well. Di Toro et al. [21] used quartz sandstone, novaculite and other materials at normal stresses > 5MPa; Di Toro et al. [23] used novaculite at a normal stress of ~5 MPa; Kanagawa et al. [25] used intact agate and silica-gel gouge at a normal stress of ~1.5 MPa at sub-seismic to seismic velocities (1 - 1000 mm/s); Rowe et al. [26] used novaculite at a normal stress of ~ 2.5 MPa; Goldsby and Tullis [44] used novaculite and quartzite at normal stresses of ~28 MPa; and quartzite at normal stress ~112 MPa; and Hayashi and Tsutsumi [56] used chert at a normal stress of ~1.5 MPa.

Moore and Lockner [52] and Byerlee [57] conducted friction experiments using conventional triaxial deformation test rigs and found that frictional strength of a fault at slow slip rates (~μms^{-1}) may be dependent on the composition of the fault material if it contains phyllosilicates. In our experiments at lower slip velocities (both the gouge and rock-on-rock experiments used quartzite samples), the steady-state friction values were measured to be as high as ~0.8. This suggests that the experimental data from both gouge and rock-on-rock experiments on the quartzite samples obey Byerlee's law (i.e., friction ~0.8), even though the quartzite samples contain muscovite. Muscovite may have a weakening effect on the frictional strength of a fault at slow slip rates. However, our results suggest that the muscovite content in our samples had no such weakening effect. At higher slip velocities we recorded lower friction values (~0.2). These results show that the steady-state friction values of the quartzite rock-on-rock and the gouge samples have strong velocity dependence at higher slip velocities.

For comparison, we also conducted experiments with both confined samples (MVR944_1 and MVR944_3, both a with Teflon sleeve) and an unconfined sample (MVR944_2, without Teflon sleeve) and found that the experimental results for run MVR944 are similar to experiments performed without

a Teflon sleeve for rock-on-rock experiments. The Teflon sleeve has a small influence on the measured steady-state friction values ~0.29 (MVR944_1). If we use tighter Teflon sleeves, the measured steady-state friction increases slightly to 0.31 (MVR944_3). However, the slight increase is still very low compared to the steady-state friction of ~ 0.74 measured for the gouge sample in MVR918 experimental run. This means that the confining effect of the Teflon sleeve for gouge experiments didn't have a significant influence on the results of the measured friction and weakening behaviour, and that our results are valid.

In addition, at low to intermediate velocities (~10 mm/s), where the Teflon sleeve friction effects might be amplified, we conducted experiments to evaluate the effect of the Teflon sleeve friction (See section 3.3). We compute the PTFE Teflon sleeve friction (~ 0.24). Sawai et al. [58] used high-velocity peak friction and steady state-state friction experiments to determine the friction of the Teflon sleeve. Our results are comparable with the peak friction measurements on Nojima Breccia [58]. We computed the effect of Teflon sleeve friction and took it into account in our analysis. We conclude that the presence of gouge delays weakening and generally produces higher friction at low to high slip velocities (10 mm/s – 200 mm/s) compared to the rock-on-rock case, which has a faster weakening and a lower frictional strength.

5.2.1. Rock-on-rock experiments at low or sub-seismic slip velocities

Notably, on our rock-on-rock friction results, the observed weakening starts at a much lower slip velocity (~ 5 mm/s). Friction experiments conducted at lower slip velocities of 0.001 - 100 mm/s by Di Toro et al. [23] on bare rocks (Arkansas novaculite) also revealed a substantial reduction in the friction coefficient at a sliding velocity greater than 1 mm/s. The host rock (quartzite) used in our experiment has a lower quartz content than the novaculite used by Di Toro et al. [23] in their experiments at 5 MPa normal stress. Rowe et al. [26] also performed friction experiments on the novaculite at sub-seismic slip velocities of ~ 0.1 - 100 mm/s and normal stresses of 2.5 MPa. The weakening at low slip velocities were observed, and revealed that the peak friction coefficient reduced from ~0.7 to a steady-state value of ~0.45 – 0.6 at slip velocities of ~ 0.1 mm/s, 1 mm/s, and 10 mm/s. Kanagawa et al. [25] used agate for friction experiments with and without gouge at sub-seismic slip velocity (1 – 100 mm/s) and normal stress of 1.5 MPa. The agate host rock used by Kanagawa and co-workers is a rock comprising mainly cryptocrystalline silica, which is primarily chalcedony (intergrowths of quartz and moganite) with

alternating ‘microgranular’ quartz. The powder X-ray diffraction of the agate showed sharp peaks of quartz. Kanagawa et al. [25] reported that quartz rocks show weakening at slip velocities greater or equal to ~ 1 mm/s, whereas the weakening of other common rocks takes place at slip velocities greater or equal to ~ 100 mm/s. This is confirmed by our observations. We found that slip weakening occurred at slip velocities of ~ 5 mm/s at similar normal stresses (2 MPa vs 1.5 MPa).

Kanagawa et al. [25] argued that as density, heat capacity, thermal diffusivity and peak friction coefficient do not vary significantly in common rock-forming minerals, the temperature (ΔT) at an asperity contact is largely dependent on indentation strength (S_i). S_i can be correlated with the indentation hardness (H_i). The mineral quartz has a significantly greater H_i (~12 GPa) than other 'common' rock-forming minerals: micas 1 – 2 GPa; calcite 1.5 GPa; amphiboles 3.4 – 5 GPa; pyroxenes 3.4 – 6.5 GPa; feldspars 6 GPa; and olivine 6.5 – 8.4 GPa [59]. Therefore, with specified slip velocity (V), normal stress (σ) and area (A), the temperature (ΔT) at asperity contacts in quartz rocks will be greater than other common rock-forming minerals listed above, which means that greater frictional heat will be produced, which is likely accountable for weakening at lower slip velocities. We, therefore, estimated that at slip velocities of ~ 5 mm/s (using equation 7), for our quartz rocks the flash weakening temperature is approximate ~ 574 ^{0}C from the flash-heating model [27].

It should be noted that, before performing friction experiment at constant slip velocities of ~ 1 mm/s, 7 mm/s or 100 mm/s and normal stress of ~1.5 MPa, Kanagawa et al. [25] used carborundum abrasive (#80 SiC) on sliding surfaces to get even contacting and rough slip surfaces. This is precisely what we did for our bare rock on rock surfaces at slip velocities of ~1 mm/s, 5 mm/s, 10 mm/s, 100 mm/s and 200 mm/s and normal stress of 2 MPa. Therefore, comparisons can be confidently drawn.

It was also observed that steady-state friction measured in MVR944_2 is smaller than the friction value measured in MVR924 at 10 mm/s, both without Teflon sleeves. These differences in the steady-state friction could be as a result of sample condition such as the heterogeneous nature of rocks, including the presence of microcracks and the rock composition.

5.2.2. Wear rock material and physical observations of sliding surfaces

Rock wear is an important process for understanding fault gouge generation [60]. In our friction experiments on bare rock surfaces at low slip rates (~1 mm/s) no weakening was observed. However, at slip velocities of ~ 5 mm/s to 200 mm/s, slip weakening was observed. At high slip velocities of 200

mm/s, we observed a notable increase in axial shortening (i.e., when axial length or gouge thickness decreases, axial shortening increases) at greater than ~ 1 m slip displacement. This is indicative of high rock wear, which was confirmed by observations of the wear material that fell from sliding surfaces during friction experiments. At these slip velocities, we also observed sample damage at the edges of host rock cylinders (microfracturing) (Figure 13). In essence, these physical observations reveal that at high velocities both gouge generation and microcracking processes occur.

The observed damage on the quartzite rock cylinder specimens was likely caused partly by thermal fracturing, which is a product of 'high frictional heat', thus leading to the 'crack formation along grain boundary' between minerals due to their different thermal expansion rates [61]. The gouge generation is potentially due to thermal fracturing by frictional heat around sliding surfaces, even though the temperature on its own may not directly control the wear rate since 'different' wear rates were observed at similar temperatures and normal stress (~3 MPa) by Hirose et al. [60]. In addition to temperature and slip velocity, it is reported that surface roughness may also affect the wear behaviour. At high slip velocities, mechanical wearing processes, sintering and chemical processes influence the wear rate, in particular, for quartz or quartz-containing rocks [23, 44]. We also observed striations on the sliding surfaces which were parallel to the 'circumferential' slip direction. These sliding surfaces became shiny at high velocity and formed a continuous slickenside. The slickenside could be generated by sintering of wear particles by frictional heat. The sliding surface of the quartzite rock cylinders is covered by the wear material which fills surface pores (Figure 13), similar to Rowe et al. [26].

We examined the wear material produced by quartzite rocks using XRD and a particle size analyser. We compared the mineral phases of wear material with the host rocks, natural and artificial gouge. The wear material tends to have a high quartz content, similar to the natural gouge samples recovered from the deep and high stress Witwatersrand gold mines, while the artificial gouge has a relatively low quartz content. For wear material, this could be due to the quartz mineral's high indentation hardness compared to muscovite, which means more frictional heat is produced at asperity contacts - in this case, more wear material produced will be quartz. As for the artificial gouge, it could be the source rock composition, which is more argillaceous quartzite and any bias introduced by crushing and sieving. Also, the particle size distribution of wear material approaches ~ 1 μm to submicron size, comparable to the silica-gel powder used by Kanagawa et al. [25], which had particle sizes < 63 μm. Kanagawa et al. [25] contended that weakening of quartz rocks at sub-seismic slip

velocity is not as a result of lubrication by these 'wear materials' of hydrated amorphous silica or silica gel [23, 44], but that weakening was due to flash heating Yao et al. [24] in their experiments with brass host blocks, noted that 'nanoparticles' (with the particle size distribution of less than ~100 nm or 0.1 μm) were generally found scattered on the sliding slip surfaces. However, the measured frictional strength was still fairly high. These results reveal that the presence of nanoparticles on sliding surfaces is not adequate for the dynamic weakening of faults.

For friction experiments with an intervening gouge layer, we measured the axial shortening and friction at slip velocities of 10 mm/s, 100 mm/s, 200 mm/s and 1200 mm/s. In this case, at slip velocities (10 mm/s – 200 mm/s), experimental data reveals a decrease in the total length of the sample, which may be associated with gouge thinning or compaction. Han et al. [62] and Hirose et al. [60] observed a decrease in gouge layer thickness to a fraction of a millimetre, even for initially thicker gouge layers. Though, at seismic slip velocities (~ 1200 mm/s), we observed a continual increase in the total length of the sample (i.e., increase in gouge thickness), which may suggest that dilation is happening. This observation of dilation at seismic velocity might be due to thermal expansion.

5.2.3. The effect of fault gouge

The frictional behaviour of both the artificial and natural fault gouge sheared at a normal stress of 2 MPa is strongly dependent on slip velocity. For artificial gouge, we observed that the frictional strength at low slip velocity of ~10 mm/s remained relatively high, from peak friction of ~ 0.86 to steady-state of ~ 0.72 over a slip weakening displacement (D_c) of ~ 6.9 m. At sub-seismic slip velocities (100 mm/s), we observed weakening from peak friction of 0.97 to steady-state friction of ~0.69 over slip weakening displacement of ~9.6 m. At high 'seismic' slip velocities of 1200 mm/s, we observed 'dramatic' decrease in the frictional strength of the fault gouge from peak friction of ~0.91 to steady-state friction of ~ 0.26 over slip weakening displacement (D_c) of 7.1 m. This dramatic decrease followed the exponential trend [29].

The natural gouge collected from shear zones in deep and high stress South African gold mines was sheared at 'sub-seismic' slip velocities of 100 mm/s, and the frictional strength decreased dramatically from peak friction of ~0.92 – 0.98 to steady-state friction of ~0.67– 0.71 over a slip weakening displacement of ~ 6.1 – 12.8 m, similar to artificial gouge at sub-seismic velocities. There are differences in the slip weakening displacement (D_c) between fault gouge friction experiments

compared to the rock-on-rock. The fault gouge friction experiments tend to have larger slip weakening displacement, D_c, ranging from 6.9 – 13.6 m. While the slip weakening displacement (D_c) for rock-on-rock friction experiments is shorter and averages ~0.5 – 3.8 m.

Mizoguchi et al. [29] also described high velocity friction experiments on fault gouge collected from the Nojima fault. The coefficient of friction at slip velocities of 6 mm/s remained high at steady-state values of ~ 0.75, comparable with our results presented above (~0.72) at slip velocities of ~10 mm/s. At sub-seismic velocities (90 mm/s), they also observed an exponential decrease in friction from peak friction to steady-state friction, similar to our results above at slip velocities of 100 mm/s. This velocity threshold is far higher than the required slip velocity of ~3 mm/s to observe a dramatic weakening on novaculite bare rocks [23]. Di Toro et al. [23] revealed that the slip displacement over which weakening occurs depends on the sliding velocity, where slip displacement is D_c < 500 mm at 3 mm/s. It is important to note that the host rock (quartzite) we used in our experiment has a lower quartz content than the novaculite used by Di Toro et al. [23]. Similar to Di Toro et al. [23], we also observed dramatic weakening at lower 'threshold' slip velocities of 5 mm/s for friction experiment on bare rock surfaces (i.e. without gouge layer).

Yao et al. [24] performed friction experiments mostly on fault gouge collected from the Longmenshan fault in China, consisting primarily of illite-quartz-rich gouge (47% illite, 41% quartz) and pure-quartz gouge. The quartz-illite gouge has less quartz compared to our experiments, while the pure quartz gouge has more quartz compared to our friction experiments, which means our experiments falls in between these gouge compositions. All experiments were performed under normal stress of ~1.0 MPa. At slip velocities of 1000 mm/s for Illite-quartz gouge where the titanium alloy has a thermal conductivity comparable to gabbro (titanium alloy ~ 5.8 W/m/K and gabbro 3.25 W/m/K host blocks), which led to similar frictional behaviour from peak friction of ~ 0.55 – 0.6 to steady-state friction of ~0.2 at slip weakening displacement (~ 5 – 30 m). Compared with the illite-quartz gouge, the pure quartz gouge weakens more gradually, with larger values of slip weakening displacement (~ 10 – 30 m) and friction values for Ti alloy and gabbro host blocks, ~0.5 and 0.3, respectively. Yao et al. [24] concluded that the 'initial weakening velocity' values for fault gouge experiments are estimated to be larger than those observed for bare rock surfaces. These findings agree with models of fault strength decrease induced by changes at asperity contacts as a result of flash heating, which takes into account contact size distribution with displacement [27, 63].

When a gouge layer is present between sliding rock surfaces (sometimes referred to as 'non-cohesive rocks'), the strain is distributed within the gouge layer before being localized [22, 64]. The distributed strain results in a more ‘gradual’ temperature increase during slip, which delays the activation of flash heating weakening mechanisms [28]. In other words, the crucial effect of having a gouge layer is to delay flash heating since the number of 'contacts' that accommodate the sliding is more in a gouge, which lowers the average slip velocity per contact, and thus reduces the potential for activation of flash heating (see models by Yao et al. [24], Platt et al. [63]). This can be observed throughout our results, where the weakening distance for experiments with intervening gouge layer “non-cohesive rocks” is larger than rock on rock friction experiments, which tend to weaken over short slip displacement and lower slip velocities.

Modification of numerical models of traditional flash heating for sliding bare ‘rock-on-rock’ surfaces to accommodate an intervening gouge layer during sliding and deformation is challenging due to uncertainty mainly introduced by poorly quantified parameters such as contact dimension, thermal diffusivity and heat capacity, which change with slip displacement [65]. Recent work by Platt et al. [63] and Nielsen et al. [66] on high velocity friction experiments with an intervening gouge layer suggest that flash heating may induce slip weakening in granular materials due to (a) an increase in the bulk temperature of the material; and/or (b) localization of slip through thin slip surface or surfaces. The local temperature in a gouge is increased by both these mechanisms, which decreases the required critical velocity to induce flash weakening, though over larger slip displacements compared to bare-rock surfaces [24, 67].

Marone and Kilgore [68] performed gouge friction experiments using quartz sand to simulate granular gouge. They varied the initial thickness of the gouge layer and particle size to examine their effect on the slip weakening displacement D_c at slower slip velocities of 0.001 – 0.01 mm/s and normal stress of 25 MPa. The friction experiment results revealed that the slip weakening displacement D_c scales with shear strain in the gouge, and that it is influenced by the gouge thickness that contains the localized shear strain.

Our work shows that gouge contributes to the increase in slip weakening displacement (D_c), both at low and high slip velocities, in accord with the previous work on the simulated fault gouge [24, 28, 63]. The difference in D_c is more apparent when compared to slip weakening displacement of bare ‘rock-on-rock’ friction experiments as observed in our results. In friction experiments with a gouge layer,

at high slip velocities, the strain is distributed within the fault gouge layer, which increases temperature much more slowly during fault slip, delaying the initiation of the flash heating weakening mechanism [28], increasing the slip weakening displacement D_c and hence delaying accelerated slip [24, 63, 67]. At slower slip velocities, the gouge thickness may play a crucial role in delaying the slip weakening displacement [68].

Also, we observed that the weakening behaviour in the friction experiments with a 'tight-fitting' Teflon sleeve is delayed (i.e. it takes more displacement to reach low friction). Consistent with the explanation in other gouge friction experiments, the gouge could have been generated through the wear process (prevented by 'tight-fitting' Teflon sleeve from escaping) and forms a gouge layer which delays the activation of flash heating and slip weakening displacement. However, the minimum thickness of a gouge layer required to delay the slip weakening process remains uncertain. Another plausible explanation which could describe another active mechanism is that the tight PTFE Teflon sleeve is heated due to frictional heating, and the heating results in widening of the PTFE Teflon sleeve, reducing the frictional strength. The observed larger D_c could be attributed to the temperature-induced gradual expansion of the tight PTFE Teflon sleeve.

5.2.4. Temperature-induced and controlled weakening mechanism

Rice [27] developed a 'flash heating' theoretical model with adapted parameters from material science (tribology). The theoretical modelling of the mechanism was constrained by friction experiments conducted at high slip velocities. The results revealed that weakening mechanisms are controlled by temperature, driven by flash heating at extremely stressed frictional microcontacts during fast slip, decreasing the frictional strength. Using a flash heating equation (7), we computed ΔT with input parameters listed in Table 8. At slip velocities of ~100 mm/s and 1200 mm/s with the normal stress of ~2 MPa, we compute ΔT ~ 2568 °C and 3631 °C, respectively (Table 9). Our results are consistent with flash heating calculations of ~2500 °C conducted by Kanagawa et al. [25] at slip velocities of 100 mm/s and slightly smaller normal stress of ~1.5 MPa on quartz rocks. The computed temperature is greater than the melting temperature of quartz (~1700 °C), and could suggest that melting may have occurred in the course of these experiments [25]. Here we suggest that the weakening mechanism in our dry quartzite rocks, both with and without intervening gouge layer between sliding rock surfaces, are largely

induced and controlled by flash heating, which agrees with many researchers of quartz rocks showing weakening at sub-seismic to seismic slip velocities ~1-1000 mm/s [24-28, 45, 63].

Goldsby and Tullis [45] compared their experimental data with a theoretical model of flash heating. Specifically, they compared the friction experiments trends vs. velocity and reported that weakening of quartzite (~100% quartz from thin section analysis) and Arkansas novaculite (~100% quartz and minor calcite from thin section analysis) at slip velocities equal to or greater than 100 mm/s with the normal stress of 5 MPa fits well with the flash-heating model. They concluded that frictional heating at high slip velocities radically weakens faults, and induces shear localisation in principal deforming zones containing 'gouge'. They also observed that evident dramatic weakening behaviour happens even on dry bare 'rock-on-rock' surfaces because of flash heating at slip velocity larger than 100 mm/s. Contact shear strength is severely degraded above temperature ~1000°C. They concluded by positing that "flash heating is expected to be a dominant or contributing dynamic fault-weakening mechanism in many earthquakes". There are strong similarities with our experiment, such as a slip velocity of ~ 100 mm/s, and the rock types used (quartzite and novaculite, both quartz-rich rocks). We suggest that a credible explanation for the active weakening mechanism during a fault slip on our gouge experiments at high slip velocity, is flash heating.

Our suggestion of flash heating as the main active weakening mechanism during fault slip in our gouge experiments is further highlighted by Yao et al. [24], who similarly performed high-velocity friction experiments using a low- to high-velocity rotary shear apparatus. We have extensively highlighted similarities of our experiments above (see section 5.2.3) and we do not intend to repeat here. They examined the critical role of temperature increase in the dynamic weakening of fault gouge at seismic slip velocities using four different types of host block cylinders with thermal conductivity (watt per metre kelvin ($W.m^{-1}.K^{-1}$)): brass 123 $W.m^{-1}.K^{-1}$, stainless steel 15 $W.m^{-1}.K^{-1}$, titanium alloy 5.8 $W.m^{-1}.K^{-1}$ and gabbro 3.25 $W.m^{-1}.K^{-1}$, which means that absolute temperature values distributed within the gouges may be unrealistic compared to natural faults. Having said that, these experiments revealed that the prevailing weakening mechanism of their friction experiments of illite-quartz and pure-quartz gouges are most likely due to flash heating, and that the presence of gouge delays flash heating activation. Our results are consistent with these observations, the presence of the fault gouge is thought to be responsible for gradual rise in temperature in the gouge during the fault slip, and because of more contact in the gouge and reduction of the average slip velocity and therefore frictional heat, which delays

activation of flash heating through bulk temperature increase and/or shear localisation [24, 45-46]. As a result, the threshold of weakening velocity is higher compared to rock-on-rock experiments, which is in accord with our results.

In our study, we observed that rock-on-rock experiments weakened at far lower slip velocities (~ 5 mm/s), and that the slip weakening displacement is shorter averaging ~ 3.8 m compared to larger slip weakening displacement of ~ 6.9 – 13.6 m in gouge experiments. Here we suggest that a likely main weakening mechanism active in our friction experiments for our rock-on-rock friction experiments is flash heating [23, 26-27], and that due to indentation strength much more frictional heat is induced at lower slip velocities consequently, activating flash heating, an observation recently made by Kanagawa et al. [25]. This weakening at lower slip velocities is observed in various other quartz rocks [21, 23, 25-26, 44, 56]. For our gouge friction experiments we also attribute the main active weakening mechanism to flash heating driven by bulk temperature and/or shear localization. We think that the observed differences in slip weakening displacement may be explained through the presence of the gouge.

5.3. Implications for mining-induced shear zones

Our study compared 'crushed' and 'natural' fault gouge samples recovered from deep underground mines, and rock-on-rock friction results. We conclude that the natural fault gouge samples from the Cooke 4 mine shear fractures exhibit frictional strength behaviour similar to that of the crushed fault gouge. The resemblance between the crushed and natural fault gouge products, the mechanical behaviour, and the frictional strength results from these laboratory experiments suggest that it is reasonable to extrapolate experimental results to conditions typical of rupture propagation in deep mines, and possibly in tectonic earthquakes.

We found that friction-weakening occurs at relatively low slip velocities in quartzite, in accord with previous friction experiments on quartzite, novaculite, agate and chert rock types (i.e., quartz rocks) [21, 23, 25-26, 44, 56]. These studies suggest that weakening of quartz rocks generally occurs at lower slip velocities of ~ 1 – 5 mm/s, compared to several other common rock-forming minerals, where weakening occurs at higher slip velocities of ~ 100 mm/s and greater [25]. This difference may be attributable to much greater amounts of frictional heat produced at asperity contacts in quartz rocks than in other rocks, as recently proposed by Kanagawa et al. [25]. Another point is that the wear rate depends on the roughness of the surfaces. The roughness of the natural shear fractures is “on the cm-

scale", which is presumably much rougher than the experimental samples. This will have a huge effect on the wear rate and weakening. Weakening at lower slip rates in quartz rocks than in other rocks implies that dynamic weakening during faulting would preferentially occur in quartz rocks [25]. This is commonly seen in hard rock underground tabular-excavations in gold mines, where Ortlepp shears occur ahead of the mining front.

The D_c values obtained from gouge friction experiments for thermally-induced slip weakening tend to be large (i.e., 6.9 – 13.6 m) compared to values obtained from underground observations of brittle shear fractures occurring ahead of the mining tabular stope with a slip displacement of ~ 100 mm for Hanks-Kanamori moment magnitude (m_{HK}) of ~ 3.6. Mizoguchi et al. [29] showed that the D_c values attained through gouge friction experiments approach the same order of magnitude as seismological studies when normal stress is increased. Increasing normal stress results in increased stress at asperities, which in turn develops abrasive wear mechanism and increases frictional heating on asperities [69], which explains why thermally-induced weakening mechanisms are extra effective when increasing normal stress. This implies that in our gouge friction experiments, the D_c values at higher normal stresses can approach slip displacements observed on Ortlepp shears in deep and high-stress mines. This is possible because at deep (> 1000 m) and high-stress mining environment (vertical stress, σ_V ~127 MPa), normal stresses are extremely high.

The Di Toro et al. [23] rock-on-rock friction experiment results reveal a shorter slip weakening displacement of D_c < 500 mm at lower slip velocity of ~ 3 mm/s, which is lower than our rock-on-rock experiments, where weakening occurs at slip velocity of ~ 5 mm/s over a slip weakening displacement of 3.8 m. We think this is due to the higher normal stress of 5 MPa, which is more than twice our normal stress of 2 MPa. Also, these important results reveal the importance of normal stress in D_c scaling. In this regard, these results show that at higher normal stress D_c values obtained from laboratory experiments become the same order of magnitude and comparable to underground observations of mining-induced shear fractures with displacements of up to 100 mm. This means at deep levels where normal stress is high our results could be valid.

6. CONCLUSION

It has been long established that faults are lubricated when they are deformed at slip velocities typical of earthquakes, irrespective of the host rock type and weakening mechanism. This study reveals

that brittle shear fractures forming in deep and highly stressed underground mines hosted by interlayered bands of conglomerate ‘reefs’ and quartzite, characterised by rough rupture surfaces and fault gouge ‘rock flour’, show similar frictional mechanical behaviour to some of the previous high-velocity friction experiments conducted on quartz gouge samples and tectonic faults. Remarkably, our rock-on-rock friction experiments reveal a difference in weakening behaviour. They showed a dramatic weakening at a lower slip velocity than those during fault gouge friction experiments. We conclude that the likely main active weakening mechanism in our experiments is flash heating.

Here we show that we may be able to understand brittle shear fracture rupture propagation during a seismic event in deep mines by conducting friction experiments of both the gouge and rock-on-rock experiments. It is suggested that the presence gouge and the generation of gouge in an active rupture influences fault rupture propagation and may delay weakening, thereby reducing the likelihood of unstable rupture propagation, which often results in large damaging seismic events (M_w 1-4) in underground mines. These findings have important practical implications for understanding the factors that influence the severity of rockbursts in deep and high stress mines.

7. ACKNOWLEDGMENTS

We acknowledge the ICDP, JST-JICA SATREPS, JSPS Core-to-Core Program, JSPS - NRF Bilateral Research Program. Sibanye gold limited is acknowledged for providing permission to publish the results. The authors thank the Council for Geoscience, the Wits Seismic Research Centre, School of Geosciences, University of the Witwatersrand, Department of Geology and Mineralogy, Kyoto University, CIMERA and the CSIR Centre for Mining Innovation, for the use of their resources and facilities. This project was also funded by JSPS KAKENHI grants 21224012, 21246134, 26249137, the MEXT's Earthquake and Volcano Hazards Observation and Research Program, and the Earthquake Research Institute the University of Tokyo cooperative research program. RJD acknowledges the support of the South African Research Chairs Initiative of the Department of Science and Technology and the National Research Foundation.

8. REFERENCE

[1] Reches Z, and Ito H. Scientific Drilling of Active Faults: Past and Future. U Harms, C Koeberl, MD Zoback, editor. Continental Scientific Drilling, 2007. pp. 235-258.

[2] Mori J, Ellsworth W. Active fault and earthquakes. Unravelling the Workings of Planet Earth – Science Plan for 2014-2019. 2013. pp. 24-31.

[3] Ogasawara H, Durrheim RJ, Yabe Y, Ito T, van Aswegen G, Grobbelaar M, Funato A, Ishida A, Ogasawara H, Mngadi S, Manzi MSD, Ziegler M, Ward AK, Hofmann G, Moyer P, Boettcher M, Dight P, Ellsworth W, Liebenberg B, Wechsler N, Onstott T, Berset N, the DSeis Team. Drilling into Seismogenic Zones of M2.0 – M5.5 Earthquakes from Deep South African Gold Mines (DSeis): Establishment of Research Sites. In: Proceedings of the AfriRock International Symposium. Cape Town; 30 September–6 October 2017.

[4] Durrheim, RJ, Ogasawara H, Nakatani M, Yabe Y, Kawakata H, Naoi M, Ward A., Murphy S, Wienand J, Lenegan P, Milev AM, Murakami O, Yoshimitsu N, Kgarume T, Cichowicz A. JST-JICA SA research group. Establishment of SATREPS experimental sites in South African gold mines to monitor phenomena associated with earthquake nucleation and rupture. In: Proceedings of the 6th International Congress on Deep and High Stress Mining. Perth; 28–30 March 2012. p. 173-187.

[5] Durrheim RJ. Keynote: Has R&D contributed to improvements in safety and profitability of deep South African mines? In: Proceedings of the 7th International Congress on Deep and High Stress Mining, Sudbury; 16-18 September 2014.

[6] Ogasawara H, Nakatani M, Durrheim RJ, Naoi, M, Yabe Y, Moriya H, Hofmann GF, Stander C, Roberts DP, de Bruin P, Oelofse J, Kato H, Cichowicz A, Birch D, Ngobeni D, Milev A, Kgarume T, Satoh T, Horiuchi S, Kawakata H, Murakami O, Yoshimitsu N, Ward AK, Wienand J, Lenegan P, Yilmaz H, Mngadi S, Piper PS, Clements TN, Nakao S, Okubo M, Ishii H, Visser AV. Observational studies of the rock mass response to mining in highly stressed gold mines in South Africa. In: Proceedings of the 7th International Congress on Deep and High Stress Mining, Sudbury; 16-18 September 2014. p. 123-137.

[7] Moriya H, Naoi M, Nakatani M, Murakami O, Kgarume T, Ward AK, Durrheim R, Philipp J, Yabe Y, Kawakata H, Ogasawara H. Delineation of large localized damage structures forming ahead of an active mining front by using advanced acoustic emission mapping techniques. Int. J. Rock. Mech. Min. Sci. 2015; 79: 157–165.

[8] Ryder, J.A. and Jager, A.J. (2002). A textbook on rock mechanics for tabular hard rock mines. Braamfontein, Johannesburg: SIMRAC.

[9] Gay NC, Ortlepp WD. Anatomy of a mining induced fault zone. Geol. Soc. Am. Bull. Part 1, 1979; 90: 47-58.

[10] van Aswegen G. Ortlepp Shears – dynamic brittle shears of South African gold mines. In: Proceedings of the 1st Southern Hemisphere International Rock Mechanics Symposium. Perth; 6-19 September 2008. p. 111 – 120.

[11] Ortlepp WD. Rock fracture and rockbursts – An illustrative study. J. South. Afr. Inst. Min. Metall. 1997; 250.

[12] Ortlepp WD. A study of rockburst source mechanism. SIMRAC; 2000. Final Project Report, GAP 524.

[13] van Aswegen G, Stander M. Origins of some fractures around tabular stopes in the deep Southern African mines. In: Proceedings of the 2nd Southern Hemisphere International Rock Mechanics Symposium (SHIRMS). Sun City; 2012. p. 63-78.

[14] Reches Z, Dewers TA. Gouge formation by dynamic pulverization during earthquake rupture, Earth Planet. Sci. Lett. 2005; 235: 361–374.

[15] Wilson B, Dewers T, Reches Z, Brune J. Particle size and energetics of gouge from earthquake rupture zones, Nature. 2005; 434 (7034): 749-52.

[16] van Aswegen G. Geologist at Institute of Mine Seismology. Personal communication; 18 May 2020.

[17] Mngadi SB, Durrheim RJ, Manzi MSD, Ogasawara H, Yabe Y, Yilmaz H, Wechsler N, van Aswegen G, Roberts D, Ward AK, Naoi M, Moriya H, Nakatani M, Ishida A, SATREPS Team, ICDP DSeis Team. Integration of underground mapping, petrology, and high-resolution microseismicity analysis to characterise weak geotechnical zones in deep South African gold mines. Int. J. Rock Mech. Min. Sci 2019; 114: 79–91.

[18] Mendecki JA. Simple GMPE for underground mines. Acta Geophys. 2019; 67: 837–847.

[19] Dieterich JH. Modeling of rock friction. 1. Experimental results and constitutive equations. J. Geophys. Res. 1979; 84: 2161-2168.

[20] Reches Z, Lockner DA. Fault weakening and earthquake instability by powder lubrication, Nature. 2010; 467(7314): 452-455.

[21] Di Toro G, Han R, Hirose T, De Paola N, Nielsen S, Mizoguchi K, Ferri F, Cocco M. Shimamoto T. Fault lubrication during earthquakes. Nature. 2011; 471(7339): 494-498

[22] Marone C, Raleigh CB, Scholz, C. Frictional behavior and constitutive modelling of simulated fault gouge. J. Geophys. Res. 1990; 95: 7007–7025.

[23] Di Toro G, Goldsby DL, Tullis TE. Friction falls towards zero in quartz rock as slip velocity approaches seismic rates. Nature. 2004; 427: 436– 439.

[24] Yao L, Ma S, Platt JD, Niemeijer AR, Shimamoto T. The crucial role of temperature in high-velocity weakening of faults: Experiments on gouge using host blocks with different thermal conductivities. Geology. 2016; 44(1): 63–66.

[25] Kanagawa K, Murayama H, Sugita A, Takahashi M, Sawai M, Furukawa N, Hirose T. Weakening of quartz rocks at subseismic slip rates due to frictional heating, but not to lubrication by wear materials of hydrated amorphous silica or silica gel. Tectonophysics. 2020; 784: 228429. https://doi.org/10.1016/j.tecto.2020.228429.

[26] Rowe CD, Lamothe K, Rempe M, Andrews M, Mitchell TM, Di Toro G, White JC, Aretusini S, Earthquake lubrication and healing explained by amorphous nanosilica. Nature Com. 2019; 10: 320. doi.org/10.1038/s41467-018-08238-y.

[27] Rice JR. Heating and weakening of faults during earthquake slip. J. Geophys. Res. 2006; 111: B05311. doi.org/10.1029/2005JB004006.

[28] Violay M, Nielsen S, Gibert B, Spagnuolo E, Cavallo A, Azais P, Vinciguerra S, Di Toro G. Effect of water on the frictional behavior of cohesive rocks during earthquakes. Geology. 2014; 42: 27–30.

[29] Mizoguchi K, Hirose T, Shimamot, T, Fukuyama E. Reconstruction of seismic faulting by high-velocity friction experiments: An example of the 1995 Kobe earthquake. Geophys. Res. Lett. 2007; 34(1): L01308. doi:10.1029/2006gl027931.

[30] Jager AJ, Ryder JA. A Handbook on Rock Engineering for Tabular Hard Rock Mines. Braamfontein, Johannesburg: SIMRAC; 1999.

[31] Dankert BT, Hein KAA. Evaluating the structural character and tectonic history of the Witwatersrand Basin. Precambrian Res. 2010; 177: 1-22.

[32] McCarthy T, Rubidge B. The Story of Earth and Life. Cape Town: Struik Publishers; 2005.

[33] Robb LJ, Meyer FM. The Witwatersrand Basin, South Africa: Geological framework and mineralization processes. Ore Geol. Revs. 1995; 10: 67-94.

[34] McCarthy TS. The Witwatersrand Supergroup. In: The Geology of South Africa, MR Johnson, CR Anhaeusser, RJ Thomas, editor. Pretoria: Council for Geosciences; 2006. pp. 155–186.

[35] SACS (South African Committee for Stratigraphy), Stratigraphy of South Africa. Part 1 (Comp L.E. Kent). Lithostratigraphy of the Republic of South Africa, South West Africa/Namibia and the Republics of Boputhatswana, Transkei and Venda. Pretoria: Geol. Surv. S. Afr.; 1980.

[36] SACS (South African Committee for Stratigraphy), A revised stratigraphic framework for Witwatersrand Supergroup. Lithostratigraphy of the Republic of South Africa. Pretoria: Geol. Surv. S. Afr.; 2006.

[37] Harvey F, Joughin W, Ortlepp DW. Design of Ezulwini Shaft Pillar Extraction. SRK Consulting Engineers and Scientists, Technical report; 2006; Report number: 346813

[38] Naoi M, Nakatani M, Horiuchi S, Yabe Y, Philipp J, Kgarume T, Morema G, Khambule S, Masakale T, Ribeiro L, Miyakawa K, Watanabe A, Otsuki K, Moriya H, Murakami O, Kawakata H, Yoshimitsu N, Ward AK, Durrheim R, Ogasawara H. Frequency–magnitude distribution of -3.7 ≤ MW ≤ 1 mining-induced earthquakes around a mining front and b value invariance with post-blast time. Pure Appl. Geophys. 2014; 171: 2665-2684.

[39] Naoi M, Nakatani M, Kgarume T, Khambule S, Masakale T, Ribeiro L, Philipp J, Horiuchi S, Otsuki K, Miyakawa K, Watanabe A, Moriya H, Murakami O, Yabe Y, Kawakata H, Yoshimitsu N, Ward A, Durrheim R, Ogasawara H. Quasi-static slip patch growth to 20 m on a geological fault inferred from acoustic emissions in a South African gold mine. J. Geophys. Res. 2015; 120: 1692–1707.

[40] Ogasawara H, Liebenberg B, Yabe Y, Durrheim R, Ziegler M, Manzi MSD, Mngadi S, Onstott, T, Kaneki S, Yokoyama Y, the ICDP DSeis team. An overview of the completed ICDP project, Drilling into Seismogenic zones of M2.0-5.5 earthquakes in South African gold mines (DSeis). In: Proceedings of the EGU General Assembly. 7–12 April 2019; Geophys. Res. Abstr. 21: EGU2019-6503-1.

[41] Norrish K, Hutton JT. An accurate X-ray spectrographic method for the analysis of geologic samples. Geochim. Cosmochim. Acta. 1969; 33: 431-454.

[42] Shimamoto T, Tsutsumi A. A new rotary-shear high-velocity frictional testing machine: Its basic design and scope of research (in Japanese with English abstract). J. Struct. Geol. 1994; 39: 65– 78.

[43] Tsutsumi A, Fabbri O, Karpoff AM, Ujiie K, Tsujimoto A. Friction velocity dependence of clay-rich fault material along a megasplay fault in the Nankai subduction zone at intermediate to high velocities. Geophys. Res. Lett. 2011; 38: L19301. doi:10.1029/2011gl049314.

[44] Goldsby DL, Tullis TE. Low frictional strength of quartz rocks at sub-seismic slip rates. Geophys. Res. Lett. 2002; 29(17): 1844. doi:10.1029/2002GL015240.

[45] Goldsby DL, Tullis TE. Flash heating leads to low frictional strength of crustal rocks at earthquake slip rates: Science. 2011; 334: 216– 218. doi: 10.1126 /science .1207902.

[46] Boulton C, Yao L, Faulkner DR, Townend J, Toy VG, Sutherland R, Ma S, Shimamoto T. High-velocity frictional properties of Alpine Fault rocks: mechanical data, microstructural analysis, and implications for rupture propagation. J. Struct. Geol. 2017; 97: 71-92. doi.org/10.1016/j.jsg.2017.02.003.

[47] Hirose T, Shimamoto T. Growth of molten zone as a mechanism of slip weakening of simulated faults in gabbro during frictional melting. J. Geophys. Res. 2005; 110: B05202. doi.org/10.1029/2004JB003207.

[48] Brantut N, Schubnel A, Rouzaud JN, Brunet F, Shimamoto T. High-velocity frictional properties of a clay-bearing fault gouge and implications for earthquake mechanics. J. Geophys. Res. 2008; 113: B10401. doi.org/10.1029/2007JB005551.

[49] Chester JS, Chester FM, Kronenberg AK. Fracture surface energy of the Punchbowl fault, San Andreas system. Nature. 2005; 437(7055): 133-136.

[50] Keulen N, Heilbronner R, Stunitz H, Boullier AM, Ito H. Grain size distributions of fault rocks: A comparison between experimentally and naturally deformed granitoids. J. Struct. Geol. 2007; 29 (8): 1282-1300.

[51] Wechsler N, Allen E, Rockwell, TK, Girty G, Chester JS, Ben-Zion Y. Characterization of pulverized granitoids in a shallow core along the San Andreas Fault, Littlerock, CA. Geophys. J. Int. 2011; 186(2): 401-417.

[52] Moore DE, Lockner DA, Tanaka H, Iwata K. The coefficient of friction of chrysotile gouge at seismogenic depths. Int. Geol. Rev. 2004; 46: 385–398. doi:10.2747/0020-6814.46.5.385.

[53] Ikari MJ, Saffer DM, Marone C. Effect of hydration state on the frictional properties of montmorillonite-based fault gouge. J. Geophys. Res. 2007; 112: B06423, doi:10.1029/2006JB004748.

[54] Collettini C, Niemejer A, Viti C, Marone C. Fault zone fabric and fault weakness. Nature. 2009b; 462: 907 – 910. doi:10.1038/nature08585.

[55] Moore DE, Lockner DA. Talc friction in the temperature range 25 – 400 °C: Relevance for fault-zone weakening. Tectonophysics. 2008; 449: 120–132. doi:10.1016/j.tecto.2007.11.039.

[56] Hayashi N, Tsutsumi A. Deformation textures and mechanical behavior of a hydrated amorphous silica formed along an experimentally produced fault in chert. Geophys. Res. Lett. 2010; 37: L12305. doi.org/10.1029/2010GL042943.

[57] Byerlee JD. Friction of rocks. Pure Appl. Geophys. 1978; 116: 615–626.

[58] Sawai M, Shimamoto T, Togo, T. Reducation in BET surface area of Nojima gault gouge with seismic slip and its implication for fracture energy. J. Struct. Geol. 2012; 38: 117-138.

[59] Spray JG. Frictional melting processes in planetary materials: from hypervelocity impact to earthquakes. Annu. Rev. Earth Planet. Sci. 2010; 38: 221–254.

[60] Hirose T, Mizoguchi K, Shimamoto T. Wear processes in rocks at slow to high slip rates. J. Struct. Geol. 2012; 38: 102-116.

[61] Ohtomo Y, Shimamoto T. Significance of thermal fracturing in the generation of fault gouge during rapid fault motion: an experimental verification (in Japanese with English abstract). Struct. Geol. 1994; 39: 135-144.

[62] Han R, Hirose T, Shimamoto T. Strong velocity weakening and powder lubrication of simulated carbonate faults at seismic slip rates. J. Geophys. Res. 2010; 115: B03412.

[63] Platt J, Proctor B, Mitchell T, Hirth G, Goldsby D, Di Toro G, Beeler N, Tullis T. The role of gouge and temperature on flash heating and its hysteresis: American Geophysical Union. Fall Annual Meeting, abs. 2014; S11C-4360.

[64] Beeler, NM, Tullis TE, Blanpied ML, Weeks JD. Frictional behavior of large displacement experimental faults. J. Geophys. Res. 1996; 101: 8697–8715.

[65] Beeler, M, Tullis T, Goldsby D. Constitutive relationships and physical basis of fault strength due to flash heating. J. Geophys. Res. 2008; 113: B01401. doi: 10.1029/2007JB004988.

[66] Nielsen SB, Spagnuolo E, Violay M, Di Toro G. Friction at seismic slip rates: Testing thermal weakening models experimentally: American Geophysical Union, Fall Annual Meeting. San Francisco; 9–13 December 2013.

[67] Proctor BP, Mitchell TM, Hirth G, Goldsby DL, Zorzi F. Platt JD, Di Tor G., Dynamic weakening of serpentinite gouges and bare surfaces at seismic slip rates. J. Geophys. Res. 2014; 119: 8107–8131. doi: 10.1002 /2014JB011057.

[68] Marone C, Kilgore B. Scaling of the critical slip distance for seismic faulting with shear strain in fault zones. Nature. 1993; 362: 618–621.

[69] Scholz CH. The Mechanics of Earthquakes and Faulting, 2nd edition. Cambridge University Press, Cambridge; 2002.

[70] Ogasawara H, Kato H, Hofmann G, Roberts D, Piper P, Clements T, Yabe Y, Sakaguchi K. In-situ stress measurements to constrain stress and strength near seismic faults in deep level South African gold mines. In: Proceedings of the 6th International Symposium on In-Situ Rock Stress, Sendai; 20 - 22 August 2013.

[71] Adams GR, Jager AJ, Roering C. Investigation of rock fracture around deep level gold mine stopes. In: Proceedings of the 22nd U.S. Rock Mechanics Symposium. M.I.T.; 29 June -2 July 1981. p. 159-185.

[72] van Aswegan G. 2017. Unpublished Picture.

[73] Schon JH. Physical Properties of Rocks: Fundamentals and Principles of Petrophysics. Elsevier Science, Oxford; 1996.

[74] Stesky RM, Hannan SS. Growth of contact area between rough surfaces under normal stress. Geophys. Res. Lett. 1987; 14: 550–553.

List of Figures

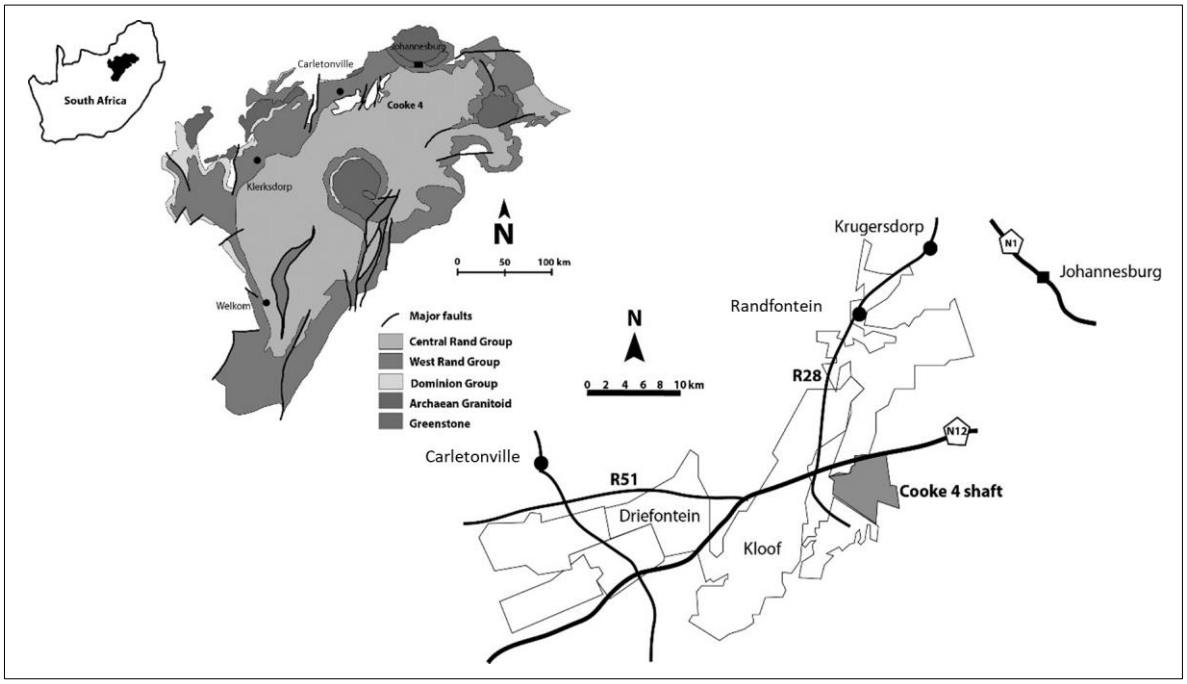


Figure 1: The study area is situated at Cooke 4 mine in the highly stressed remnant shaft pillar at 1000-1200m depth, Witwatersrand Basin (modified from [31]).

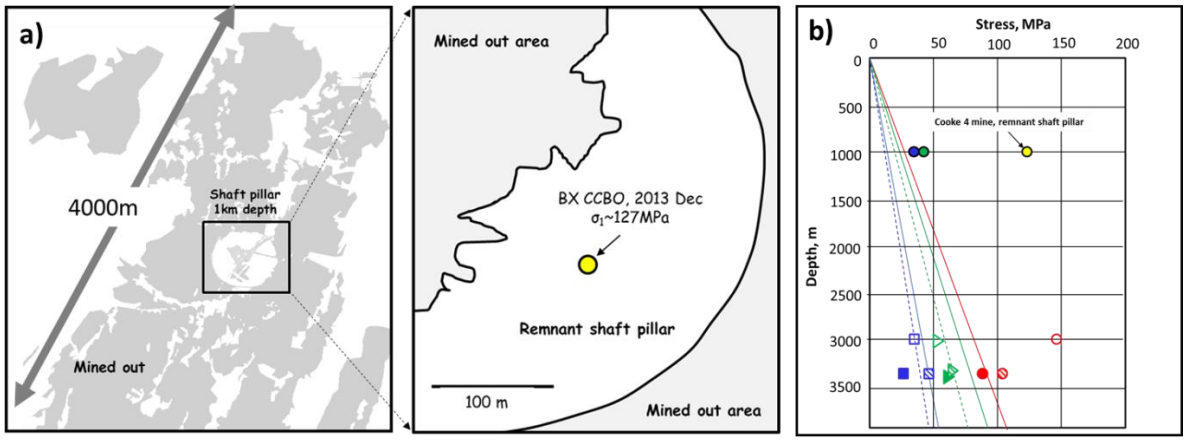


Figure 2: a) Cooke 4 mine remnant shaft pillar layout. The mined-out area is shown in grey and the white circle is the remnant shaft pillar. b) Vertical stress measurement (in yellow) in remnant pillar in December 2013 using an overcoring technique optimized for deep South African gold mines (Compact conical-ended borehole overcoring technique - CCBO) [70], and other previous measurements at equal and greater depths are shown for comparison (blue, red and green). The remnant pillar was subjected to vertical stress as large as those in virgin ground comparable at depths of ~3-3.5 km.

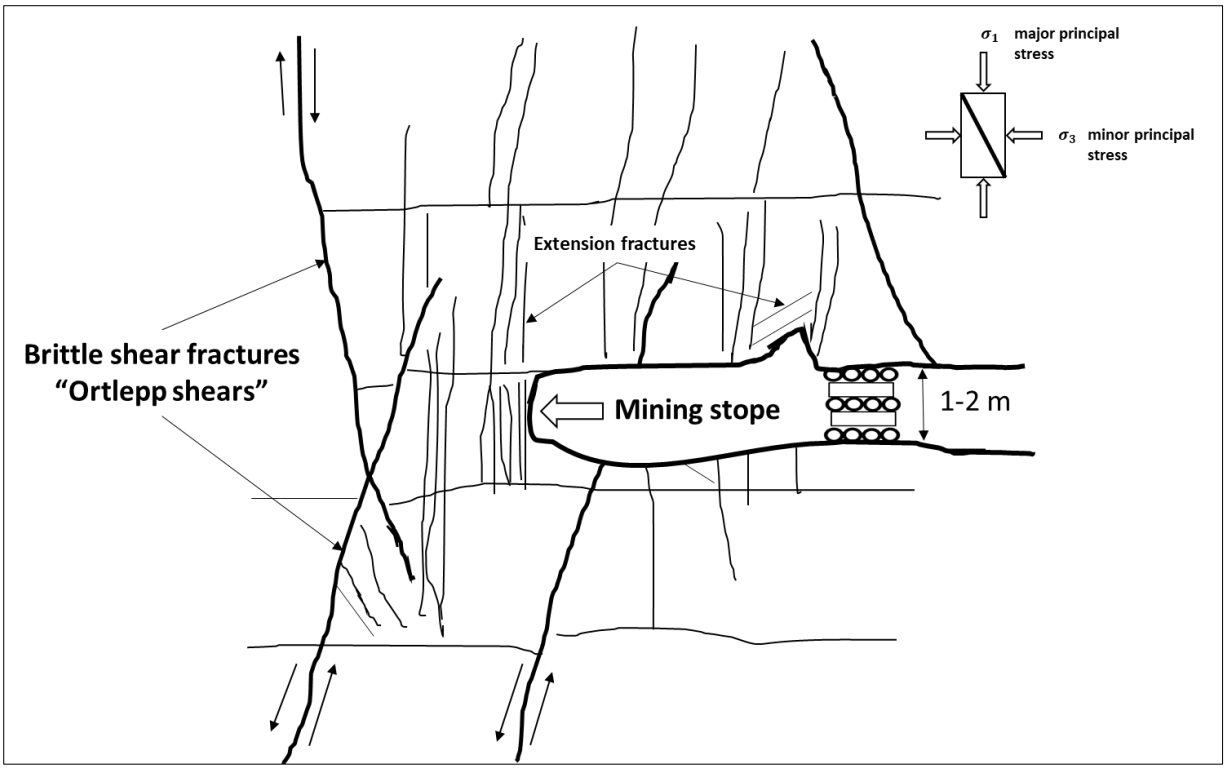


Figure 3: Ortlepp shears fractures are large brittle shear fractures often associated with large seismic events (Mw 1-4). Their origin is similar to 'conjugate shears' that form under triaxial tests [10]. They form ahead of the stope, are characterised by normal displacement (modified from [71]).

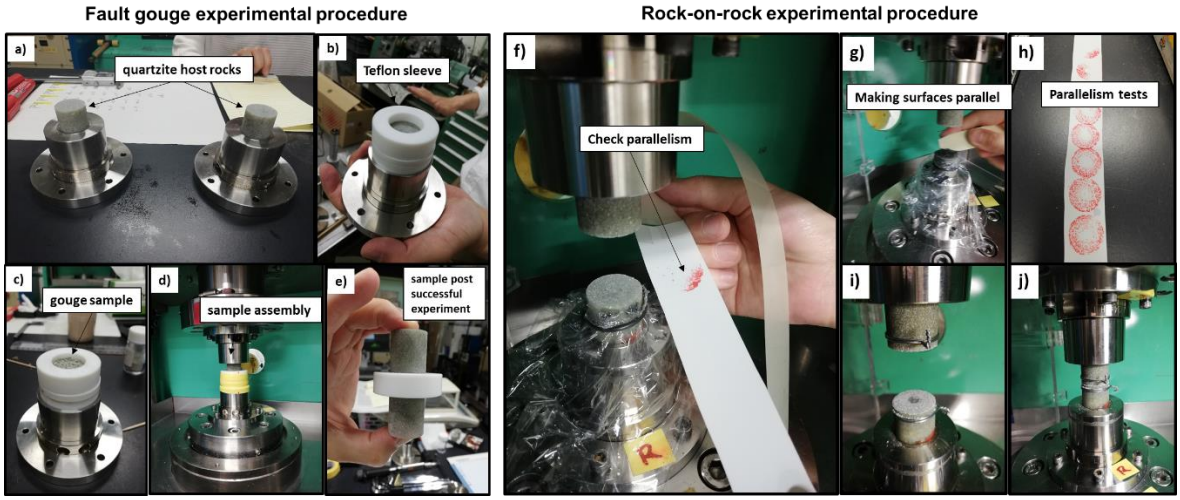


Figure 4. Friction experiments performed on the fault gouge and bare rock surfaces 'rock-on-rock'. a-e). We used manually-crushed and sieved samples as the artificial gouge for the experiments from run number MVR918 to MBR923. For experiments run MVR925 and MVR926, we used the natural gouge samples from shear fractures S (4) and S (3), respectively. (a) Prepared quartzite cylinders inserted in sample holders; (b) Teflon sleeve inserted around the quartzite cylinder; (c) gouge sample in the Teflon sleeve; (d) sample assembly; and (e) sample post successful experiment. f-j). We conducted friction experiments on bare rock surfaces, without an intervening fault gouge and Teflon sleeve, for run MVR924. (f) Sample assembly without the Teflon sleeve; (g) making sliding surfaces parallel; (h) using pressure sensitive paper to check parallelism; (i) quartz cylinders fastened with wire; and (j) experimental assembly.

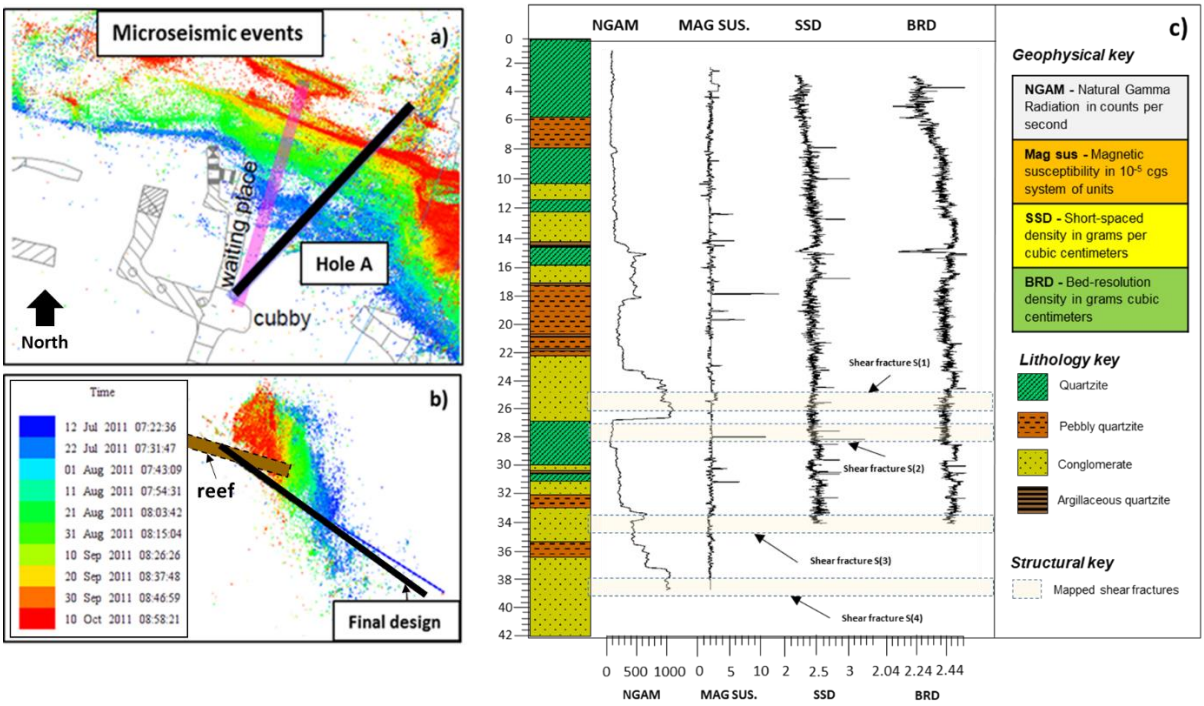


Figure 5: a) The hypocentre distribution of microseismicity associated with the mining front (top view). b) The vertical section of the mining-induced seismic events, which occur on steeply-dipping planar surfaces. c) Distance along borehole of mapped and recovered fragile mining-induced ruptures and host rocks.

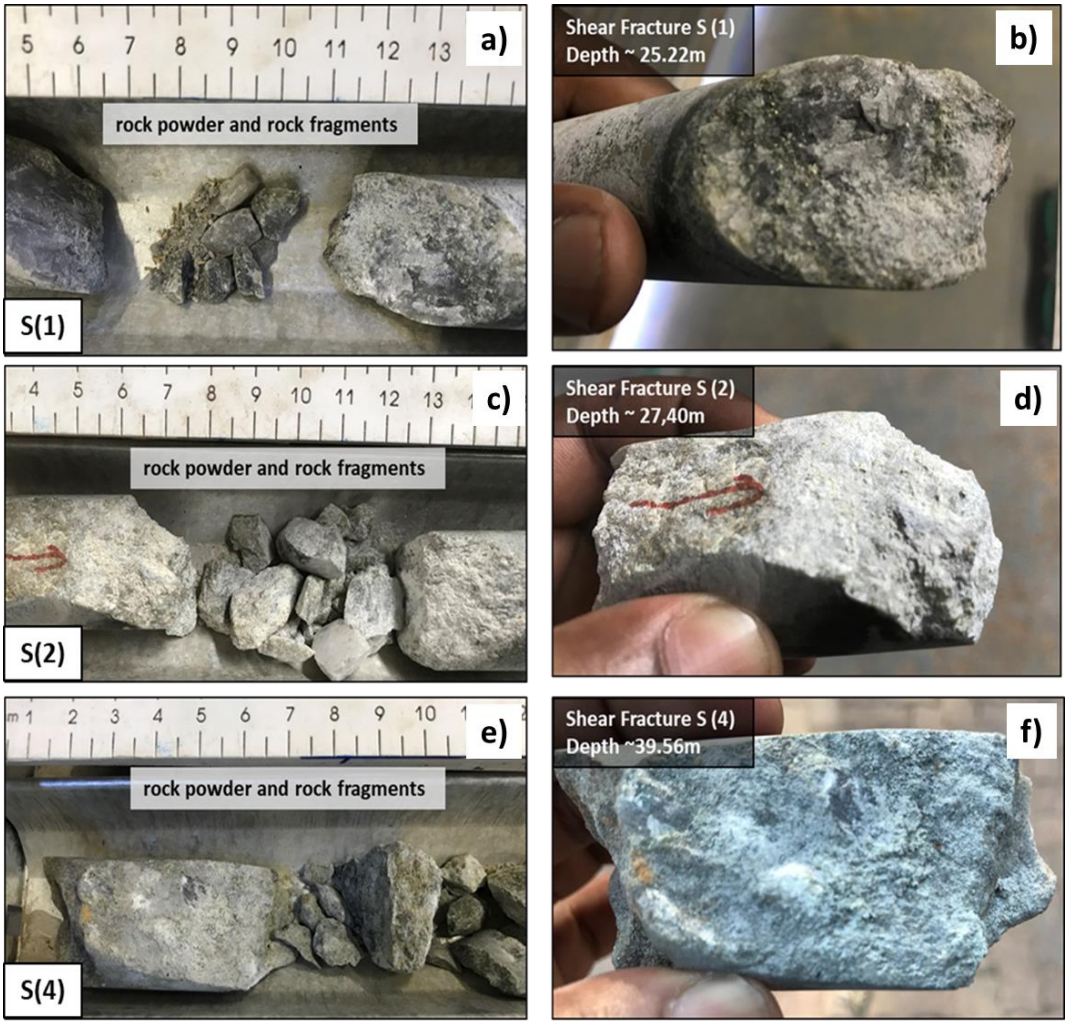


Figure 6: a, c, d).Ortlepp shears showing rock powder and rock fragments (broken rock fragments "breccia" in the range of cm-scale). b, d, f). Close up image of rough angular shear rupture planes.

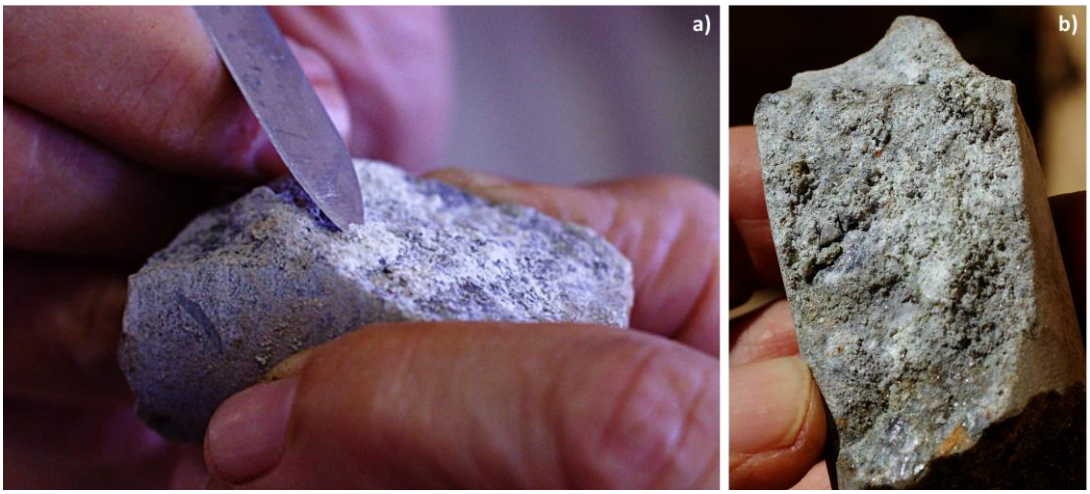


Figure 7: a) Some fault gouge "rock flour" could be easily peeled off with a sharp object such as knife. b) Rough angular shear rupture planes [72].

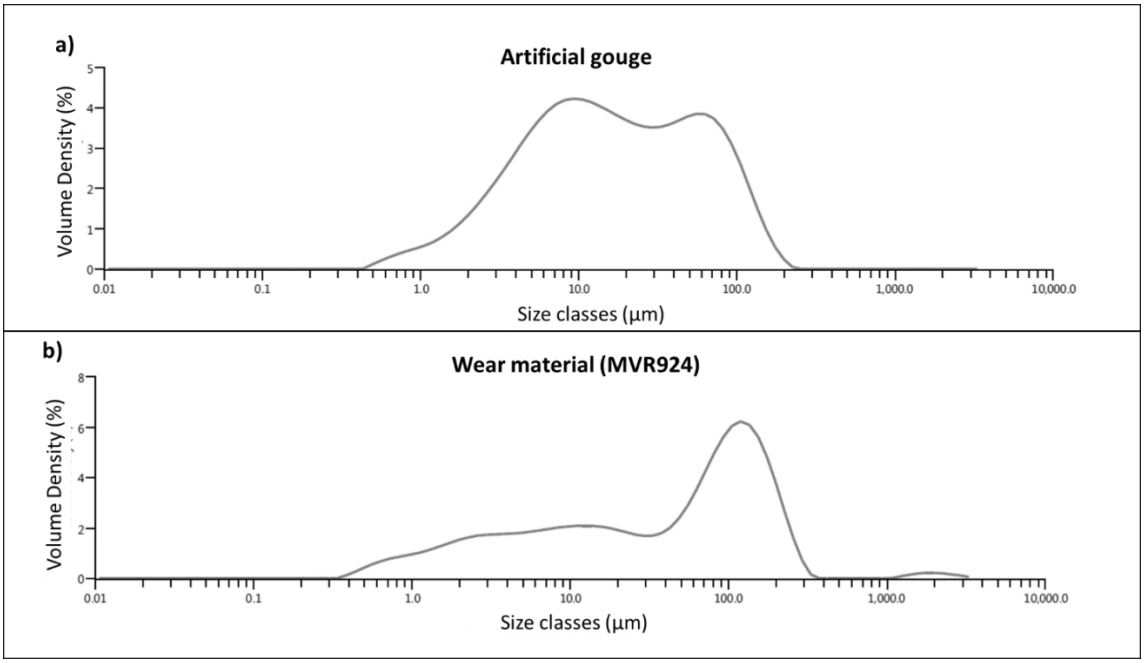


Figure 8: a) Particle size distribution of the artificial gouge; and b) particle size distribution of the wear material generated from MVR924 at 200 mm/s.

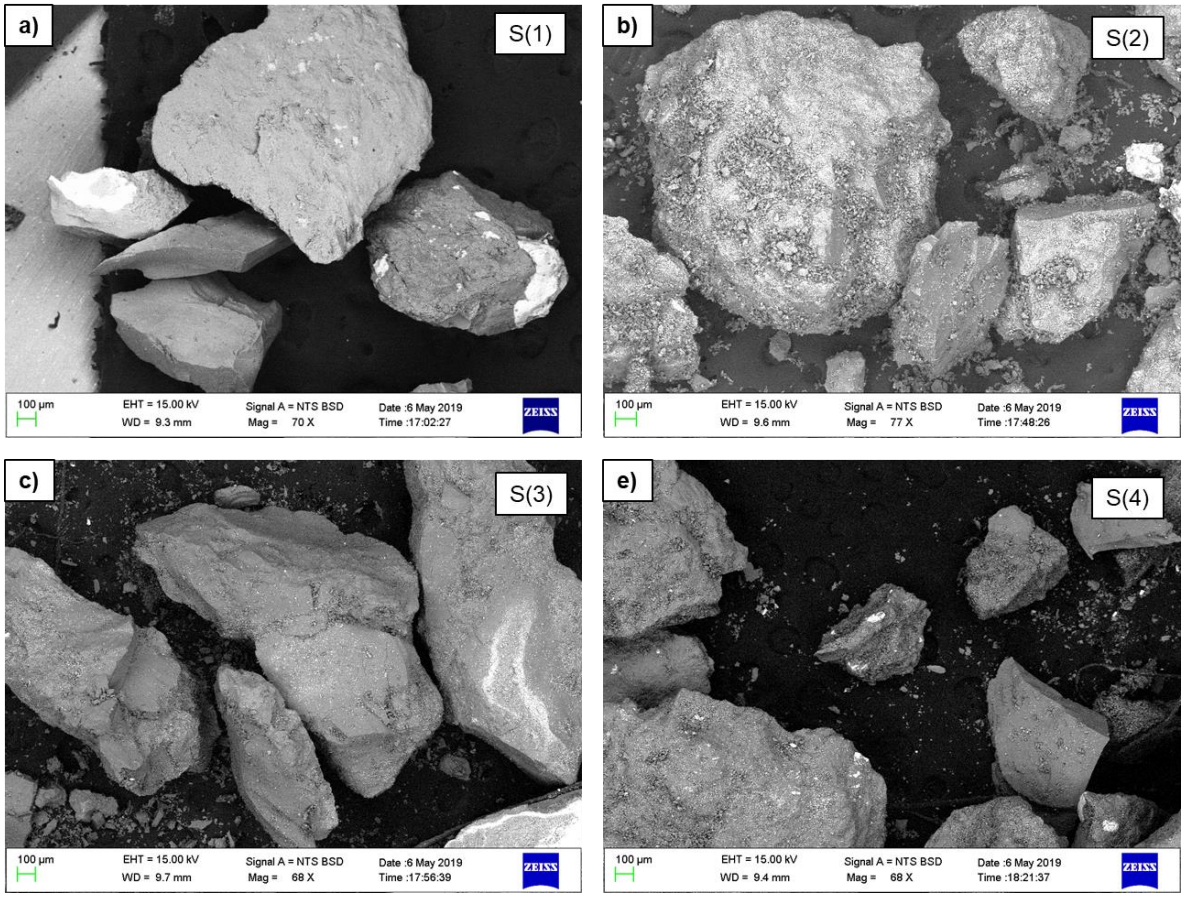


Figure 9: a-e) The scanning electron microscopy (SEM) images of gouge samples collected from the fresh rock fractures, no aggregated pattern is observed before performing high velocity friction experiments.

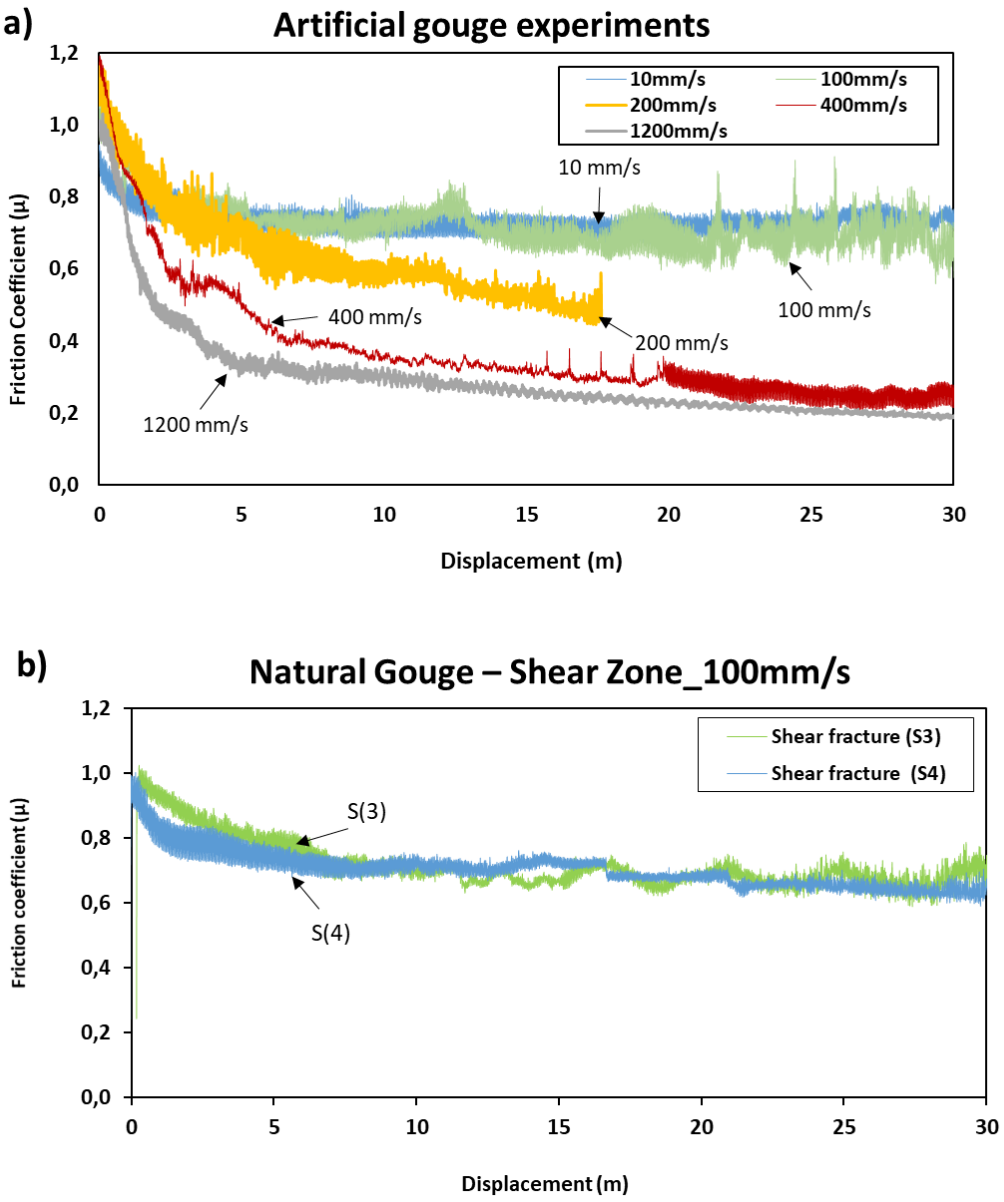


Figure 10: a) Friction experiments with gouge. We used manually-crushed and sieved samples as the gouges for the experiments from run number MVR918 to MVR923 (10 -1200 mm/s). These results for 'artificially prepared fault gouge' samples show the mechanical behaviours of gouge at intermediate to high slip velocities as a function of fault displacement. The curve shows a peak friction coefficient μ_p, which decreases exponentially to a steady-state friction coefficient μ_s. b). Natural gouge samples MVR925 and MVR926, we used the natural gouge samples recovered from underground shear fractures S (4) and S (3), respectively. These results for the natural gouge samples show the mechanical behaviors of gouge at slip velocities (100 mm/s) with fault displacement. For all natural gouge samples, the curve shows weakening, the peak friction coefficient μ_p decreases to a steady state friction coefficient μ_s.

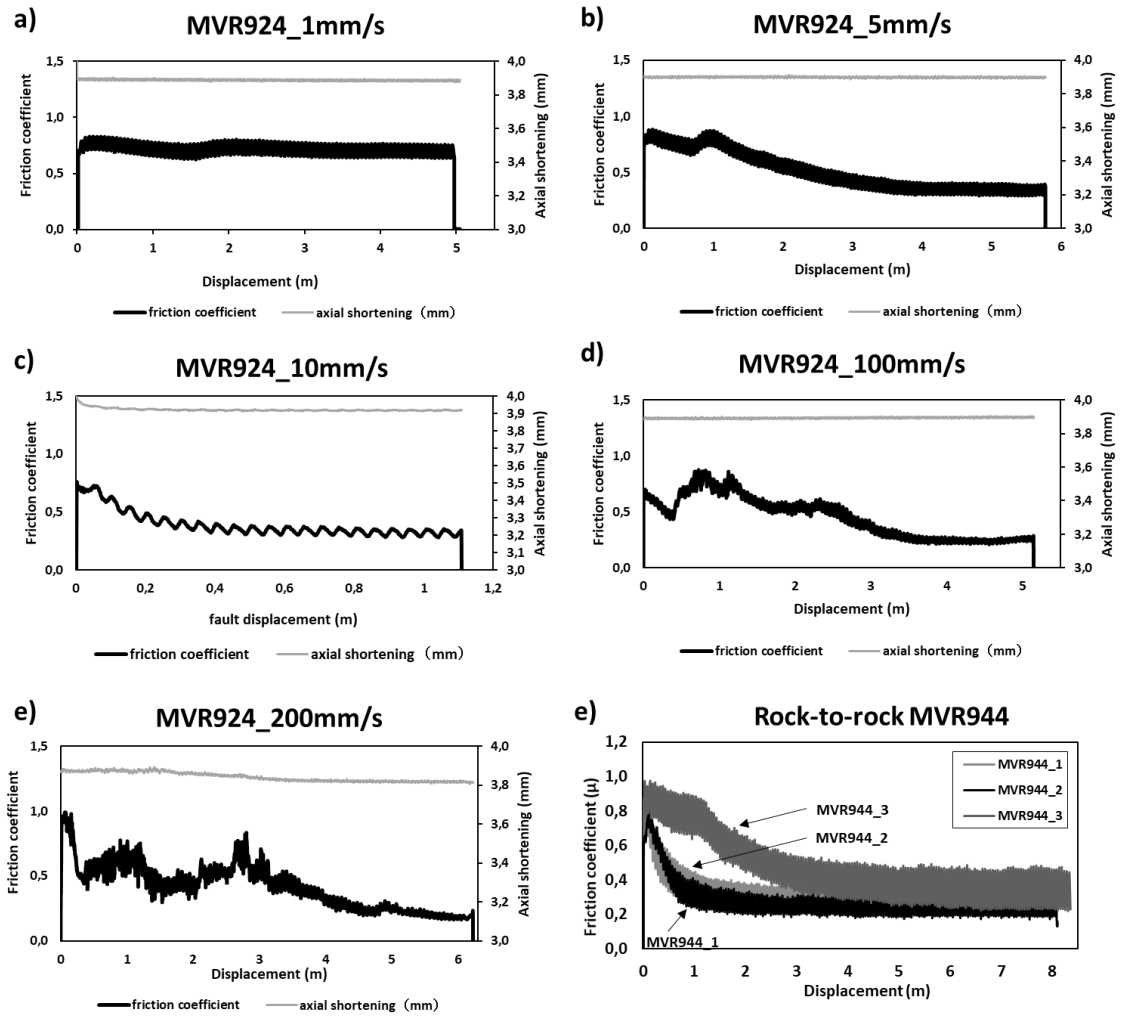


Figure 11: Friction experiments without gouge. a-e) For experimental runs of sample MVR924, we conducted friction experiments on bare rock surfaces, without an intervening fault gouge. These results for rock-to-rock samples show the mechanical frictional behaviour of gouge material and evolution of axial shortening from low, intermediate and high slip velocities with displacement. The curve shows no weakening at lower slip velocities (1.0 mm/s), and shows weakening behaviour for higher slip velocities 5.0 mm/s to 200 mm/s. For these slip velocities, the peak friction coefficient (μ_p) decreases exponentially to steady-state friction coefficient (μ_s). The corresponding axial shortening data for experimental run e) MVR924 at 200 mm/s shows no axial shortening until ~ 1 m slip displacement, and suddenly an increase indicating sample shortening. f). Three runs of rock-on-rock friction experiments (sliding surfaces on bare rock without an intervening gouge): MVR994_1 (d~0.05 mm) and MVR944_3 (d~0.18 mm) with Teflon Sleeve, and MVR944_2 without the Teflon Sleeve. This shows that the measured friction increases with the tighter Teflon Sleeve (MVR944_3). However, the increase is very small compared to gouge experiments measured friction at similar slip rates.

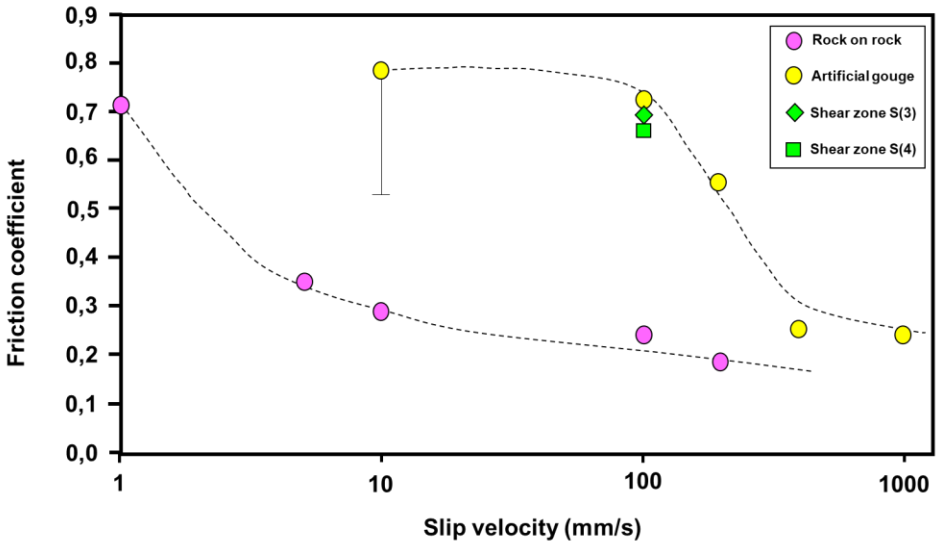


Figure 12. Comparison of gouge and rock on rock experimental results. After factoring in the effect of Teflon ring friction, we observed that rock-to-rock sample weakens quicker and generally have lower frictional strength at intermediate to high slip velocities compared to gouge samples. After our error analysis, we also compare the natural gouge samples from brittle shear fractures in deep underground mines and artificial gouge samples derived from shear fracture rock fragments of similar origin and bulk composition. We observed that the mechanical behaviour of the natural gouge is similar to that of the artificial gouge.

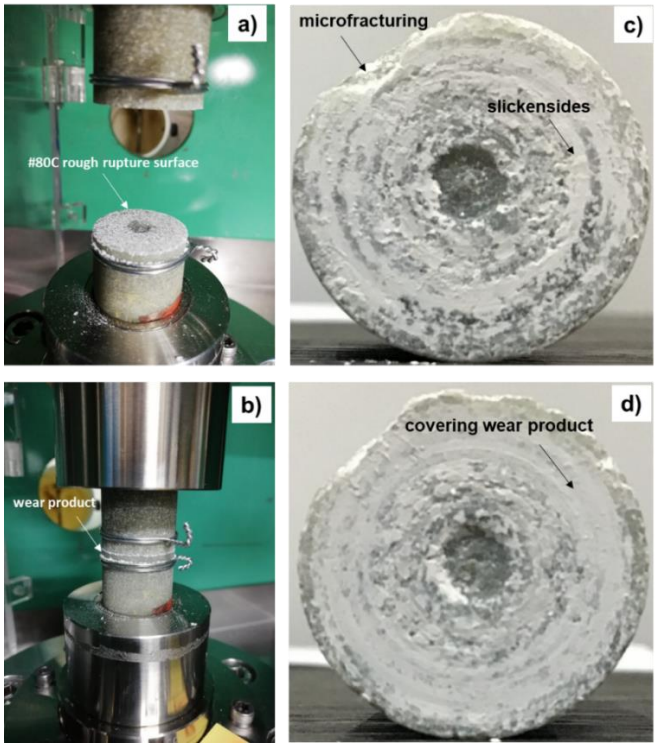


Figure 13: Photos of sliding surface of bare rock friction experiments at slip velocities of 200 mm/s. The sliding surfaces display concentric rings of powder on sample surfaces. The slickenside become more prominent with increasing velocity and wear material was dropped from sliding surfaces. The minimum size of wear particles approaches 10 µm.

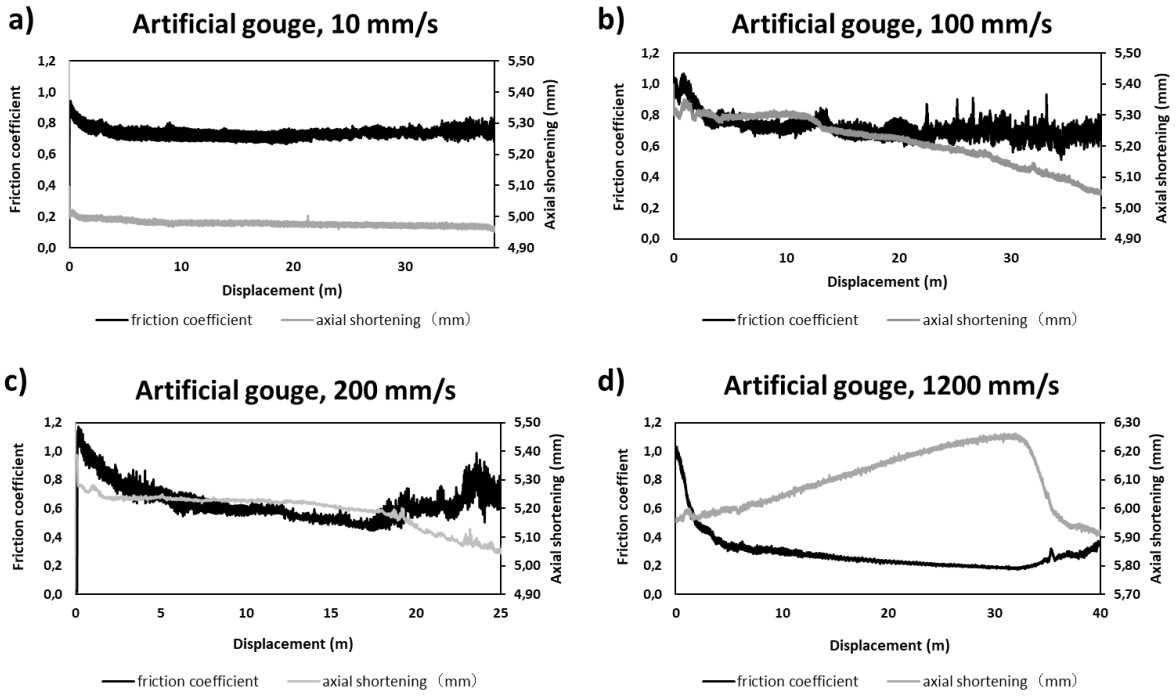
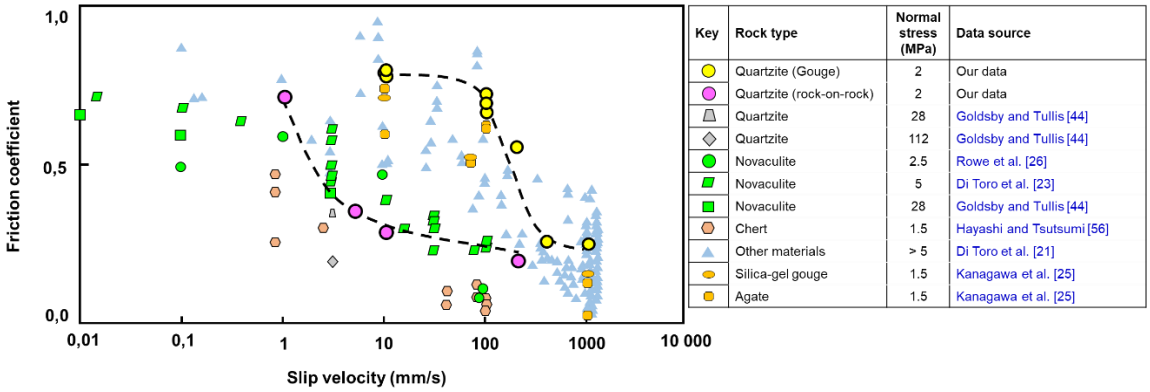


Figure 14: The evolution of axial shortening with corresponding frictional strength data of selected artificial gouge experiments at 10 mm/s, 100 mm/s, 200 mmm/s and 1200 mm/s slip velocities. a-c) Experimental runs tend to show increasing trend in axial shortening data. At high slip velocity (1200 mm/s), a sustained decrease in axial shortening data is observed and sudden increase at the end.



Key	Rock type	Normal stress (MPa)	Data source
	Quartzite (Gouge)	2	Our data
	Quartzite (rock-on-rock)	2	Our data
	Quartzite	28	Goldsby and Tullis [44]
	Quartzite	112	Goldsby and Tullis [44]
	Novaculite	2.5	Rowe et al. [26]
	Novaculite	5	Di Toro et al. [23]
	Novaculite	28	Goldsby and Tullis [44]
	Chert	1.5	Hayashi and Tsutsumi [56]
	Other materials	> 5	Di Toro et al. [21]
	Silica-gel gouge	1.5	Kanagawa et al. [25]
	Agate	1.5	Kanagawa et al. [25]

Figure 15: Our results are plotted with previously reported data on weakening behavior of quartz rocks at sub-seismic slip velocities and various normal stresses (Graph source: [25]).

List of Tables

Table 1: The Hanks–Kanamori moment magnitude (m_{HK}) for selected log P, average source sizes L(m) and displacement u_{max}(mm) (from [18]).

log P	-4.0	-3.0	-2.0	-1.0	0.0	1.0	2.0	3.0	4.0
Hanks–Kanamori (m_{HK})	− 1.72	− 1.05	− 0.38	0.28	0.95	1.62	2.28	2.95	3.62
Source size L(m)	0.9	1.9	4.1	8.9	19.1	41.2	89	191	412
u_{max} (mm)	0.23	0.49	0.1	0.02	0.49	10.5	22.6	48.6	104.8

Table 2: XRF results of the host rocks – quartzites, pebbly quartzites, argillaceous quartzites and conglomerates.

wt%	*SiO_2*	*Al_2O_3*	*F_2O_3*	*MnO*	*MgO*	*CaO*	*Na_2O*	*K_2O*	*TiO_2*	*P_2O_5*	*Cr_2O_3*	*NiO*	*LOI*	*TOTAL*
Conglomerate	85.70	3.40	6.22	0.01	0.04	0.04	0.01	0.56	0.20	0.04	0.02	0.03	3.49	99.76
Quartzite	89.12	6.99	0.41	0.00	0.04	0.03	0.08	1.62	0.11	0.02	0.02	0.00	1.06	99.50
Pebbly Quartzite	91.12	5.62	0.53	0.00	0.02	0.03	0.05	1.09	0.10	0.02	0.02	0.00	0.95	99.55
Argillaceous Quartzite	87.47	8.20	0.55	0.00	0.03	0.04	0.07	1.43	0.15	0.02	0.02	0.00	1.29	99.27

Table 3: XRD results for recovered host rock samples showing predominantly quartz and minor muscovite.

Lithology	*Sample no.*	*Depth (m)*	*Quartz (wt%)*	*Muscovite (wt%)*	*Pyrite (wt%)*	*Microcline (wt%)*	*TOTAL (wt%)*
Quartzite	H(1)	2.90	84.87	15.13	0.00	0.00	100.00
Pebbly Quartzite	H(2)	6.43	94.47	5.53	0.00	0.00	100.00
Quartzite	H(3)	9.14	90.71	9.29	0.00	0.00	100.00
Conglomerates	H(4)	10.35	90.95	5.60	3.45	0.00	100.00
Argillaceous. Quartzite	H(5)	14.30	23.10	75.11	0.69	1.09	99.99
Pebbly Quartzite	H(6)	18.95	92.91	7.09	0.00	0.00	100.00
Conglomerates	H(7)	23.17	87.79	5.43	4.85	1.93	100.00
Quartzite	H(8)	28.28	83.67	16.33	0.00	0.00	100.00
Argillaceous Quartzite	H(9)	30.00	55.15	41.88	1.30	1.34	99.67
Conglomerates	H(10)	32.83	75.17	14.72	6.74	3.37	100.00
Conglomerates	H(11)	37.75	94.53	1.33	4.14	0.00	100.00

Table 4: XRD results for recovered limited gouge samples of fragile dynamic shear fractures showing quartz and minor muscovite.

Sample no.	Depth (m)	Quartz (wt%)	Muscovite (wt%)	Pyrite (wt%)	Microcline (wt%)	TOTAL (wt%)
S(1)	25.22	96.21	2.94	0.85	0.00	100.00
S(2)	27.40	62.20	37.62	0.00	0.18	100.00
S(3)	33.95	90.07	9.93	0.00	0.00	100.00
S(4)	39.95	71.82	18.17	7.28	2.73	100.00
Artificial gouge	-	56.75	38.83	4.09	0.19	99.86
Wear material (MVR924)*	-	97.61	1.92	0.00	0.35	99,88

**The wear material of bare rock surface experiments (sample - MVR924) collected at 200 mm/s slip velocity.*

Table 5: The natural gouge was collected from shear zones, sieved and weighted before used in friction experiments. In addition, artificial gouge generated from crushing and sieving of rock fragments from shear zones were used.

Natural gouge S(3)		Natural gouge S(4)		Artificial gouge	
Sieve size (µm)	Weight (g)	Sieve size (µm)	Weight (g)	Sieve size (µm)	Weight (g)
< 125 µm	0.251 g	< 125 µm	0.504 g	< 125 µm	6.293 g
125 -250 µm	0.332 g	125 -250 µm	0.563 g	125 -250 µm	11.367 g
250 – 500 µm	0.362 g	250 – 500 µm	0.611 g	250 – 500 µm	12.499 g
500 -1000 µm	0.755 g	500 -1000 µm	0.940 g	500 -1000 µm	14.445 g

Table 6. Experimental conditions for natural, artificial gouge and rock-on-rock experimental runs.

Sample	Diameter (mm)	Diameter difference (Δ∅) (mm)	Gouge particle size (µm)	Normal stress (MPa)	V_{eq} (mm/s)
Artificial Gouge - MVR918	23.96	0.06	<125	2	10
Artificial Gouge - MVR919	23.95	0.09	<125	2	100
Artificial Gouge - MVR920	23.95	0.10	<125	2	1219
Artificial Gouge - MVR921	23.91	0.15	<125	2	199
Artificial Gouge - MVR922	23.91	0.18	<125	2	399
Artificial Gouge - MVR923*	23.94	0.19	<125	2, 3, 4 and 5	10
Rock-on-rock - MVR924	23.92	-	-	2	1
Rock-on-rock - MVR924	23.92	-	-	2	5
Rock-on-rock - MVR924	23.92	-	-	2	10
Rock-on-rock - MVR924	23.92	-	-	2	99
Rock-on-rock - MVR924	23.92	-	-	2	199
Natural Gouge - MVR925	23.94	0.18	<250	2	100
Natural Gouge - MVR926	23.96	0.17	<500	2	100
Rock on rock - MVR944_1 (with PTFE sleeve)	23.90	0.05	-	2	10
Rock on rock - MVR944_2 (without PTFE sleeve)	23.90	-	-	2	10
Rock on rock - MVR 944_3 (with PTFE sleeve)	23.90	0.18	-	2	10

**Experimental conditions were different and they were used to correct the Teflon friction from the results.*

Table 7. Friction experiments results for peak friction, steady-state friction and slip weakening displacement.

Sample	V_{eq} (mm/s)	Normal stress (MPa)	μ_p	μ_s	D_c (m)
Artificial Gouge - MVR918	10	2	0.86	0.72	6.9
Artificial Gouge - MVR919	100	2	0.97	0.69	9.6
Artificial Gouge - MVR921	199	2	1.02	0.51	13.6
Artificial Gouge - MVR922	399	2	1.06	0.26	11.9
Artificial Gouge - MVR920	1219	2	0.91	0.26	7.1
Rock-on-rock - MVR924	1	2	0.76	0.70	NA
Rock-on-rock - MVR924	5	2	0.81	0.32	3.8
Rock-on-rock - MVR924	10	2	0.77	0.32	0.5
Rock-on-rock - MVR924	99	2	0.62	0.20	2.9
Rock-on-rock - MVR924	199	2	0.83	0.36	2.1
Natural Gouge - MVR925 S(4)	100	2	0.92	0.71	6.1
Natural Gouge - MVR926 S(3)	100	2	0.98	0.67	12.8
MVR944_1 (with PTFE sleeve)	10	2	0.71	0.29	1.8
MVR944_2 (without PTFE sleeve)	10	2	0.75	0.23	1.7
MVR 944_3 (with PTFE sleeve)	10	2	0.94	0.31	6.2

Table 8. The input parameters used to calculate flash heating.

Density (kg/m^3)	2.69E+03	measured
Heat capacity(J/kg°C)	6.98E+02	quartz [73]
Peak Friction	0.8	this study
Thermal diffusivity (m^2/s)	4.16E-06	quartz [73]
Normal stress (Pa)	2.00E+06	this study
Slip-surface area (m^2)	4.49E-04	this study
Slip rate (m/s)	1.00E-01	this study
Indentation strength (Pa)	2.70E+09	quartzite [74]

Table 9. Temperature increase ΔT (°C) by flash heating at an asperity contact.

Sample	Diameter (mm)	Normal stress (MPa)	Veq (mm/s)	Temperature, ΔT (°C)
Rock-on-rock - MVR924	23.92	2	1	257
Rock-on-rock - MVR924	23.92	2	5	574
Rock-on-rock - MVR924	23.92	2	10	812
Rock-on-rock - MVR924	23.92	2	99	2568
Rock-on-rock - MVR924	23.92	2	199	3631

9. Factors controlling the physics and mechanics of M5.5 rupture

The manuscript has been prepared in accordance to general journal standards.

Identification of structures capable of hosting the M5.5 Orkney (South Africa) earthquake and factors controlling the physics and mechanics of rupture.

Mngadi, S.B.[a,e], Manzi, M.S.D.[a,e], Nkosi, N.Z. [b,e], Durrheim, R.J.[a,e], Ogasawara, Jr.H[c,e]., Noda, T. [c,e], Ogasawara, H.[c,e], Yabe, Y.[d,e] and DSeis team.

[a] School of Geosciences, University of the Witwatersrand Johannesburg, PO Bag 3, WITS, 2050, Republic of South Africa.

[b] Council for Scientific and Industrial Research, Centre for Mining Innovation, PO Box 395, Pretoria, Republic of South Africa.

[c] College of Science and Engineering, Ritsumeikan University, 1-1-1 Noji Higashi, Kusatsu 525-8577, Japan.

[d] Graduate School of Engineering, Tohoku University, 6-3, Aza-Aoba, Aramaki, Aoba-ku, Sendai 980-8578, Japan.

[e] The International Continental Scientific Drilling Program (ICDP) Dseis team.

ABSTRACT

On 5 August 2014, the largest mining related ML 5.5 earthquake occurred in the Klerksdorp goldfields, hundreds of metres below Moab Khotsong mine. The M5.5 earthquake had an 'unusual' strike-slip mechanism compared to common mining-induced ‘normal faults’ observed at Cooke 4 mine occurring ahead of the stope. In a rare case, the M5.5 earthquake occurred within the legacy 2-D reflection seismic data acquired in 1992 for gold exploration, which was re-processed and re-interpreted to delineate the architecture of geological structures that hosted the earthquake. In addition, the earthquake was recorded by the underground in-mine seismic network near the source region. The DSeis team used the mine seismicity data to locate the M5.5 rupture plane, and drilled into this active seismogenic zone situated 3.5 km below the surface. To minimise costs, the DSeis team used the Moab Khotsong mine infrastructure to access the drilling site (level 95) at ~ 2.9 km depth, a few hundred metres away from the M5.5 earthquake rupture. The DSeis team successfully drilled and recovered the fragile core, host rocks, rock breccia, dolerite sills and a lamprophyre dyke using specialised triple-tube drilling technique to maximise core recovery especially around the fault rupture zone characterised by the sandy gouge material and core-loss. Reprocessing and re-interpreting the legacy 2-D seismic data revealed that the geological structure that hosted the M5.5 earthquake crosscut the entire Witwatersrand Supergroup up to the Transvaal Supergroup, and potentially the base of the Karoo Basin. Also, the seismic reflection data revealed several dolerite sills characterised by high seismic amplitudes. The integration of the reflection seismic data and mine seismicity data including the DSeis drill core data such as geological core logging and geophysical borehole logging (gamma, density and velocity) allowed us to fully describe and make clear a near-vertical structure, striking NNW-SSE. The relatively younger and highly altered lamprophyre dyke intruded into this existing fault and older dolerite sills. The fault was reactivated as a left lateral strike-slip fault. Using the recovered fault gouge material, we measured particle size distribution of the gouge using laser diffraction particle size analyser and SEM analysis and performed XRD analysis. The gouge particle size, approach minimum of ~ 10 μm and composition is predominantly talc and biotite minerals (> 40%). We conducted friction experiments on the Moab Khotsong gouge sample at slip velocity of ~100 mm/s and normal stress of 2 MPa. The peak friction coefficient of ~1.0 decreased exponentially to steady-state friction of ~0.66 over a slip weakening distance of ~9.1 m. The friction weakening behaviour and steady-state friction values are comparable with results obtained from normal faults occurring ahead of the mining stope at similar slip

velocity and normal stress. However, in this case, talc and biotite may be controlling the friction weakening mechanism, acting as a lubricant. Here, we suggest that there are three active processes influencing the M5.5 earthquake seismogenic zone: first, the complex structural architecture of the seismogenic zone (e.g., intersection of fault, lamprophyre dykes and dolerite sills); second, the mechanical process induced by tectonic and/or mining related stresses; and third, the mechanical and chemical processes caused by the water and rock interaction.

1. INTRODUCTION

Mining at deep levels in highly stressed rock mass may induce earthquakes and pose risk to the life of workers, mine infrastructure, and the public. The study area is located in the Orkney mining district at the Moab Khotsong mine, Witwatersrand Basin (South Africa) (Figure 1). The focus of this study is at depths below mining levels, where the largest earthquake recorded in the mining region in South Africa occurred in 2014 with the local magnitude M_L 5.5. The vibrations of this mining related seismic event were 'felt' across South Africa and some neighbouring countries (e.g., Mozambique) with one recorded death. The assessed damage was valued at ~R130 million (US$ 8.6 million) (Midzi et al., 2015; Ogasawara et al., 2017). Even though these large seismic events may result in damage and loss of life, they also provide a rare opportunity to study the physics and mechanisms of earthquakes near source regions, which may enhance our understanding of seismic hazard and mitigation strategies (Nicolaysen 1992; Ogasawara et al. 2002; Nakatani et al., 2008; Reches et al., 2009; Durrheim, 2012; Ogasawara et al., 2014; Durrheim et al., 2017).

This M5.5 earthquake prompted seismologists, in particular, the ICDP-DSeis team to pose a few fundamental seismological questions relevant to this study: (1) what is the nature of fault rock that hosted the M5.5 earthquake?; (2) what is the role of geology?; and (3) is there a geological structure (fault or dyke) related to this earthquake? (Ogasawara et al., 2019). The International Continental Scientific Drilling Programme – Drilling into seismogenic zones of M2.0 - 5.5 earthquakes in deep South African gold mines team known as the ICDP - DSeis team drilled into a number of active faults. These seismogenic zones are situated in deep level and highly stressed rock mass in South African gold mines, including Moab Khotsong M_L 5.5 earthquake rupture and Cooke 4 mine shear fractures occurring ahead of the mining stope Mw 2. The Moab Khotsong M_L 5.5 seismic event occurred hundreds of metres below mining levels and the faulting mechanism was characterised by unusually strike-slip (Ogasawara et al., 2017; Manzunzu et al., 2017). This was distinct from the common 'normal faulting' mechanism associated with mining-induced events occurring at Cooke 4 mine. These two seismogenic zones also are characterised by distinctive geological signatures, fault material, damage extent and the earthquake scale, which may allow us to examine the influence these characteristics in the rupture generation and propagation process.

This study forms a small portion of a greater ICDP-DSeis project. The ICDP-DSeis project broader aims include the investigation of the extent of damage, the stress state around the fringes of

the earthquake, and the potential existence of living organisms associated with deep-level earthquakes. The ICDP-DSeis team comprises of international researchers from South Africa, Japan, Germany, Switzerland, the USA, Israel and India. The DSeis team completed drilling at Moab Khotsong to intercept the M_L 5.5 rupture and recover fragile fault rocks (Ogasawara et al., 2017). Here, we focus on investigating the fault rock composition, fault frictional properties and the architecture of the 'unusual' strike-slip fault in deep mines.

1.1. Mine seismicity

Mining in the Witwatersrand Basin extended a few hundred metres below the surface and seismicity began to be felt and reported in the towns close to goldfields (Riemer and Durrheim, 2012). It is worth noting that earthquake seismology in South Africa predates mining related seismicity, the earliest event in the South African catalogue is dated in the 1690s (Durrheim, 2015). One of the largest recorded mining related earthquakes occurred in Welkom on 8 December 1976 with local magnitude M_L 5.1. This event caused a collapse of apartments (Durrheim, 2015). Subsequent to that, on 9 March 2005 in Stilfontein town in the Klerksdorp region a seismic event with a local magnitude of M_L 5.3 occurred (Durrheim et al., 2006). On 5 August 2014, in the town of Orkney in the Klerksdorp goldfields the largest earthquake recorded in the mining region occurred with a local magnitude of M_L 5.5.

Unique to this study, the M_L 5.5 earthquake was recorded with dense and high resolution in-mine seismic network. The in-mine seismic network consisted of 46 triaxial geophones with a frequency of 4.5 Hz and a sampling rate of 6 kHz. The geophones were located near the M_L 5.5 earthquake at mining levels between 2000 m and 3500 m depth (Imanishi et al., 2017). Using this dense in-mine seismic network located near the source region, more than 2000 foreshocks and aftershocks were recorded from 4 August 2014 to 31 October 2014, which included the mainshock (M5.5 earthquake). The velocity structure used to process and locate these seismic events – also routinely used at Moab Khotsong mine is the P-wave velocity of ~5960 m/s, and the S-wave velocity of ~3610 m/s. The depth of the mainshock was located at ~ 4780 m. The delineated aftershock distribution spanned ~ 8000 m in strike length and ~3000 m in dip length (Imanishi et al., 2017). The distribution of these aftershocks revealed that the M_L 5.5 rupture plane dips near vertical and strike NNW-SSE, with the prevailing strike-slip mechanism (Imanishi et al., 2017; Ogasawara et al., 2018).

Imanishi et al. (2017) reported that the M_L 5.5 earthquake triggered seismicity at the mining levels. However, to the authors' knowledge, no seismic rupture was observed or mapped in the mining levels. This could mean that the main rupture did not propagate to the mining levels. Therefore, the geological structure responsible for M_L 5.5 earthquake remains elusive and not clearly understood. In addition, the aftershock plane when projected to the mining levels did not match any known fault or geological structures that could have hosted the M_L 5.5 earthquake (Ogasawara et al., 2018).

1.2. Legacy reflection seismic data

Coincidentally, the M_L5.5 seismic event occurred in mining regions well covered by the 2-D seismic reflection data originally acquired for mineral exploration. These 2-D seismic reflection data can be examined using new advanced technologies to re-process (where original raw data files exist) and re-interpret (with new visualisation techniques) to make clear the geological structures that hosted the M_L 5.5 event. This is a rare and unique opportunity, which should help researchers attempt to answer why the M_L 5.5 earthquake occurred and stopped. With the 2-D seismic reflection data made available by the mines, several efforts have been made to examine and characterise the geological structure that hosted the Orkney earthquake M_L 5.5 (Ogasawara Jr. et al., 2017; Manzi et al., 2018). Ogasawara Jr. et al. (2017) re-interpreted one of the 2-D seismic reflection data that intersected the aftershocks that delineated the M_L 5.5 rupture. In addition to 2-D seismic reflection data, more work was conducted on the 3-D seismic reflection data acquired in 1996, which covered a much wider area (Linzer et al., 2018; Manzi et al., 2018; Ogasawara et al., 2020; Noda et al., 2020). The 3-D seismic reflection data revealed strong reflectors, which were correlated with mapped sills recovered from the DSeis drill core.

Recent technological advances in reflection seismic data processing and interpretation techniques (or visualisation) have made extracting new information from legacy reflection seismic data possible such as the pre-stack algorithms and post-stack seismic attributes (Manzi et al., 2012a and b; Rutherford and Williams, 1989; Tsuru et al., 2005). In this study, the 2-D legacy reflection seismic data were reprocessed and interpreted using latest algorithms to improve the structural interpretation of the data.

2. GEOLOGY OF MOAB KHOTSONG MINE

2.1. Witwatersrand Supergroup

The geology of the Archaean Witwatersrand Basin has been described in detail by several researchers since the gold rush in 1886 (Robb and Meyer, 1995; McCarthy and Rubidge, 2005; Dankert and Hein, 2010). Here, we do not intend to repeat those details. However, we highlight critical tectonic events that shaped the Witwatersrand Basin and key stratigraphic markers relevant to the reflection seismic interpretation of the Witwatersrand Basin. The Witwatersrand Basin was formed over a period of ~360 Ma (3.07 - 2.71 Ga) (Robb and Meyer, 1995). The Witwatersrand Supergroup was deposited unconformably on top of the basement granitoids and volcano-clastic sedimentary rocks of the Dominion Group. The basement granite terrains and greenstone belts were eroded by multiple streams, allowing sediments to be deposited into the inland sea. The deposition occurred during the collision of the Archaean Kaapvaal Craton and the Zimbabwe Craton (Robb and Meyer 1995) and was terminated by episodes of thrust folding (McCarthy and Rubidge, 2005; Dankert and Hein, 2010). The volcanic rocks of the Ventersdorp Supergroup (2.7 - 2.6 Ga) overlie the Witwatersrand Supergroup, dolomites of the Transvaal Supergroup (2.3 - 2.6 Ga) which were intruded by the Bushveld Complex (largest platinum deposit in the world), followed by the deposition of the Karoo Basin (Dankert and Hein, 2010) (Figure 1).

The Witwatersrand Supergroup comprises two groups, viz. the West Rand Group and the Central Rand Group (Myers et al., 1989; Robb and Meyer, 1995; McCarthy, 2006; Dankert and Hein, 2010). The West Rand and Central Rand groups tend to decrease in thickness towards the south-eastern edges of the basin. The average thickness of the basin is ~ 4.6 km. The West Rand Group is dominated by clastic sedimentary rocks such as quartzites and shales with a ratio of about 1:1, and conglomerate ‘primarily mined for gold’. The Central Rand Group hosts more than 70% of the gold-bearing ‘conglomerates’ horizons, and lies on top of the West Rand Group. The Central Rand Group also consists of quartzite and conglomerate packages, and minor bands of shale and lavas (Kent, 1980; SACS, 1980 and 1990). The Vaal Reef is the major gold-bearing conglomerate exploited at Moab Khotsong mine and neighbouring mines such as Kopanong and Great Nolingwa.

2.2. Faulting

The Witwatersrand Basin is structurally complex and has been affected by neotectonic activities. The basin can largely be described by major listric faults and their related drag folds that are ascribed to the extensional tectonic regime during the deposition of the Ventersdorp Supergroup (Vermaakt and

Chunnet, 1994; Coward et al., 1995; Gibson et al., 2000; Beach and Smith, 2007). Watts (2005) conducted a detailed mapping of faults with vertical displacements in excess of 10 m at the neighbouring Kopanong mine. These faults tend to be mostly reactivated. They can be grouped into two main categories (1) Zuiping-type faults, and (2) Jersey-type faults (Figure 2). Watts (2005) concluded that most of these faults are Platberg age. The Platberg volcanism occurred at 2754-2709 Ma (Gumsley et al., 2020).

The Zuiping-type faults tend to strike parallel to the edges of the Witwatersrand Basin and dip north-west; while, the Jersey-type faults also tend to strike parallel to the basin edges (similar to Zuiping-type faults), but distinguishably dips southeast (Watts, 2005). The trend of NE – SW fault strike direction is mainly due to the old pre-existing zones of weakness. It is also evident from surface drilling and seismic reflection data that the Vaal Reef was overlain by ~ 2 km of sediments and lava during the Platberg period, which means that it was shallow enough to allow faults to be reactivated. In addition, smaller Zuiping type faults have been thrust by the reverse faults, which may indicate that the thrusting is post-Platberg in age (Watts, 2005). A classic Jersey fault would typically be characterised by more than one fault, where smaller faults occur ahead of a major fault zone (Watts, 2005).

2.3. Dykes and sills

Our study area is characterised by numerous sills and dykes that intruded at different geological ages and have been subjected to several damaging brittle seismic events (Yabe et al., 2019). The sills and dykes are of different ages, such as known post-Karoo dykes of pre-Cretaceous and Cretaceous age (145 - 66 Ma), Karoo dykes (150 Ma), Pilanesberg (1.30 Ga), Transvaal (2.20 Ga), and Ventersdorp (2.60 Ga). These intrusive rocks often host large damaging seismic events (M3.0-3.9) (van der Heever, 1982) and therefore, are important to understand for mine design and during mining operations (Ogasawara et al., 2019; Yabe et al., 2019).

In the first half of the 1960s, Wilson and colleagues presented a comprehensive study of numerous intrusive rocks occurring in the Klerksdorp Goldfields (Wilson et al., 1964). This was followed by Joughin (1966)'s research work, which provided a detailed petrological analysis and description, and seismicity assessment, which revealed that these intrusive rocks are associated with large damaging seismic events. Jaffery (1975) noticed that larger dykes were associated with seismicity and rockburst, and that they affect seismicity distribution in the mining regions. van der Heever (1982) conducted a

detailed study on the influence of the geological structures on seismicity and rockbursts in the Klerksdorp Goldfields. The study examined the influence of dykes (Lamprophyre dykes, Karoo dolerite dykes, etc.) on seismicity. The study revealed that seismic events were associated with dykes. They also reported that the regions where dykes and sills 'intersect' are often characterised by high seismicity and large events (M3.0-3.9) (van der Heever, 1982).

Watts (2005) conducted a detailed work on dykes and sills at the neighbouring mine (Kopanang mine). The study examined the structural relationship between numerous faults and intrusive rocks. In addition, the geometry of these structures were linked to the regional structural evolution. Numerous faults and dykes are characterised by normal displacement and some exhibit strike-slip displacement.

The intrusion of these dykes and sills occurred during periods of crustal extension, post the termination of sediment deposition in the basin. These dykes and sills are important for relative age constraint between them and other structures. Majority of these intrusive rocks are similar to the Buffer dykes, which characteristically strike ESE-WSW to SSE-NNW and show dip direction to the south and north with minor vertical movement, which means they are likely of Klipriviersberg age.

The Diagonal dykes strike E-W to ENW-WSW, dipping at 50° to 70° to the north. These dykes exhibit substantial vertical and horizontal displacements on the reef. The DW dykes strike NE-SW and dip vertical to sub-vertical. The Popeye dykes are younger dykes. They tend to strike N-S and dip sub-vertical. Most dykes, including the Popeye dykes are very sporadic. The ages of these dykes range from early-Ventersdorp to pre-Cretaceous (Watts, 2005). The lamprophyre dykes are the most uninterrupted intrusive rocks (van der Heever, 1982). They tend to be transgressive and are thought to be post-Karoo in age (van der Heever, 1982). Wilson et al. (1964) classified these dykes as kimberlites of Cretaceous age.

3. MOAB KHOTSONG MINE DRILLING: HOLE A, B AND BRANCH HOLE C.

The ICDP-DSeis team drilled into the M5.5 earthquake rupture delineated by the in-mine seismic network located close to the source region (Figure 3a). Before drilling could take place, the ICDP-DSeis team excavated drilling site ~2900 m below surface, with dimensions of 6 m x 6 m x 6 m. The mine safety regulations did not allow larger excavation dimensions. However, the ICDP-DSeis team could successfully drill and recover fragile ruptured core and fault gouge material. The drilling plunged at 35º–45º downward from the excavated drilling site. The NQ diameter drilling was selected since it is the

minimum diameter required to conduct geophysical borehole logging. Initially, the DSeis team used a 3 m long double-tube core barrel to drill Hole A and B (Ogasawara et al., 2020).

Drilling of Hole A was extremely challenging, severe deviation from the initially planned drilling path occurred, which resulted in the drilling direction being almost sub-parallel to the rupture plane hosting the M5.5 earthquake. In Hole A, we, therefore, did not intercept the M5.5 rupture zone, which led to the termination of drilling activity at ~ 817 m distance from the collar (Figure 3b). However, the core and borehole were still extremely useful for analysis of the geological formation and structures surrounding the fault zone.

The deviation of Hole A led to the drilling of Hole B. This took into consideration the lessons learnt from the drilling of Hole A such as deflection, and the drilling angle was modified by 15º (Figure 3b) (Ogasawara et al., 2020). The Hole B intersected the uppermost part of the M5.5 rupture zone, and we experienced a '3 m core-loss zone' using a double tube core barrel. The drilling was terminated at 700 m from the collar after intercepting the rupture zone and encountering core-loss. Because the important part of the core was lost, i.e., core samples at the dyke location adjacent to the core-loss zone, we drilled a branch hole ('Hole C') using a 1.5 m 'triple tube' core barrel compared to 3 m 'double tube' core barrel used initially in Hole B. The 1.5 m triple tube core barrel drilling technique successfully recovered core samples and fragile fault gouge material. The Hole C was drilled with a deviation of ~2º - 3º at 545 m distance from the borehole collar of Hole B (Figure 4). Hole C was very short and terminated at ~96 m (i.e., equivalent to 641 m distance from the borehole collar of Hole B) (Babrosco quartzite). Holes B and C intersected an altered lamprophyre dyke and the subsequent core-loss zone (Figure 4).

The Hole B intersected matching geological formations with Hole A such as the Roodepoort Formation, Crown Formation and Babrosco Formation. In general, lithologies comprise of quartzite, metasiltstone, basalt and altered dolerite dykes and sills (Figure 4) (Rickenbacher, 2018; Ziegler et al., 2018). In Hole B, notably, we intersected a different intrusive rock (lamprophyre dyke), which was not observed in Hole A, this dyke was immediately followed by ~3 m length of the core-loss zone at 612 m depth from the collar. The location of the dyke and core-loss zone in the drill core corresponds to the location of the aftershock plane, which was delineated from M5.5 earthquake. This suggests that the dyke might be the geological structure that hosted the M5.5 rupture.

The drilling programme was immediately followed by detailed core logging and downhole geophysical borehole logging of Hole A. The geophysical borehole logging included density and seismic

velocity measurements, which showed high seismic velocities coinciding with intrusive rocks compared to other rocks (Figure 5). This suggests that intrusive rocks should have higher acoustic impendence contract relative to the country rocks. The ICDP-DSeis team scanned the recovered core using unrolled and rolled optical images with a DMT CoreScan3 optical scanner provided by ICDP for all the 1.6 km core length (Hole A, Hole B and Hole C) at CSIR Mandela Mining Precinct. For recovered core from Hole A, Yabe et al. (2019) performed non-destructive stress measurements and analysis on the core, and revealed that stress concentration coincided with the intrusive rock at ~440 m from the borehole collar (Figure 5). A different zone of stress concentration was observed, which coincided with the depth or location of the upper part of the aftershock plane. The core was sampled at selected lithological units for XRD and thin section micrographs analysis.

4. PHYSICAL PROPERTIES AND SEISMIC RESPONSE

4.1. Physical properties

The acoustic impedance contrast is the product of the physical properties of the dykes, sills, discontinuities and the surrounding host rocks. The previous work suggests that the lamprophyre dykes and dolerite sills would have larger acoustic impedance contrast relative to metasedimentary host rocks such as quartzite and metasiltstone (Rickenbacher, 2018). In addition, volcanic rocks such as the basaltic lavas found in our study area would produce high acoustic impendence with the clastic metasedimentary rocks. In our study area, the physical properties of the drill core samples recovered from Moab Khotsong drilling endeavour were measured through geophysical borehole logging and laboratory testing for compressional velocity (V_p) and density (ρ) (Rickenbacher, 2018).

Rickenbacher (2018) measured density of drill core samples recovered from DSeis drilling endeavour, and found that for metasedimentary rocks the density values are between 2.70 and 2.86 g/cm^3; and for intrusive rocks the density values range between 2.90 and 3.07 g/cm^3. These results were compared to geophysical borehole logging of the short-spaced density measurements obtained from full-wave sonic geophysical borehole logging of Hole A (Figure 5), which showed consistency. Rickenbacher (2018) measured the P-wave velocity (V_p), and revealed that the P-wave velocity for metasedimentary rocks are between 5.50 and 5.90 km/s. For the Crown metabasalt the average P-wave velocity is ~5.99 km/s; while for intrusive rocks it is between 6.48 and 6.53 km/s. These laboratory

results agree with the geophysical borehole logging results conducted by DSeis team shown in Figure 5.

4.2. Forward modelling

To appropriately image dykes (thin structure) at depth using reflection seismic method is complex. This endeavour requires acoustic impedance contrast between the target 'dykes' and the surrounding host rocks to be large enough, in that, sufficient energy is reflected back to the receivers (Simm and Bacon, 2014; Hammer et al., 2014). This also means higher frequencies are needed to detect a thin structure of ~1 – 3 m thickness. However, high frequencies are often attenuated quickly with depth, which creates a challenge for imaging thin structures at great depths. To investigate this problem, forward modelling was performed to examine the seismic response of the host rocks and intrusive rocks. This was used to guide the interpretation of the 2-D reflection seismic data (acquired in 1992 by AngloGold Ashanti for gold exploration).

We conducted forward modelling using geological logging information of Hole A, lithologies and their corresponding physical properties measured in the laboratory (Table 1). In addition, geophysical borehole logging data was used to constrain the forward modelling (Figure 5). In Hole A, six intrusive rocks with the apparent thicknesses of 16.2 m, 43.1 m, 38.7 m, 2.0 m, 3.4 m and 68.2 m were mapped and measured initially by Rickenbacher (2018). In Hole B, four intrusive rocks with the apparent thicknesses of 15.2 m, 38.5 m, 44.9 m (similar to Hole A), and unique lamprophyre dyke, which is adjacent to the core loss zone, were mapped, measured and documented (Rickenbacher, 2018). The geological model was based on litholgies recovered in Hole A (Figure 6).

4.2.1. Key findings

We used 2-D finite-difference method (Tesseral software package) to compute forward modelling with parameters: Wavelet - 2D Acoustic Ricker wavelet of 65 Hz; Receiver Interval - 25 m; Source Interval: 50 m. To better image the subsurface, the horizontal length of the model was set to 1900 m and the vertical length (depth) was set to 3500 m. After creating synthetic shot gathers, ray paths and a velocity model from the synthetic data (Figure 7a and Figure 7b), Pre-Stack Time Migration (PSTM) approach was used to process the data. The geological model is shown in Figure 8a and the synthetic PSTM seismic section is shown in Figure 8b.

The PSTM seismic section revealed that the lithological boundaries in the study could be resolved with the reflection seismic methods. For example, the strong reflections observed in the model correspond to sills (at the top of the West Rand Group), Black Reef Formation (boundary between the dolostone of the Transvaal Supergroup and Ventersdorp Lavas), Ventersdop Contact Reef (boundary between Central Rand Group quartzites and Ventersdorp lavas). The model has the contact between the dolomite and lava at ca. 600 m, while the migrated section shows it at 400 m. Similarly for the Lava/Quartzite contact: ca. 1300 m on the model, but 700 m on the migrated section. This difference in depths may be attributed to the velocity model used for time-to-depth conversion of the migrated section (Figure 8).

To investigate if the near-vertical fault could be imaged by seismic method, we created a fault in the geological model (Figure 8a). It is clear from the PSTM section that the fault is well imaged and it associated with some zones of amplitude attenuation. These results provided some confidence that the reprocessing of the legacy profile could allow us to image sills and near-vertical structures that might be responsible for M5.5 earthquake. Summarily, modelling work shows that dyke thickness is unlikely to be imaged directly, unless it is associated with a near-vertical fault zone.

Furthermore, the structural complexities of the subsurface in our study area include a series of deformation, metamorphism, extensive faulting and several sills and dyke intrusions have a potential of generating complex reflected seismic wavefields that may hide the targeted reflections from the structures of interest (Hammer et al., 2014). With the survey that was originally designed for gold exploration, small variations in the geometry of the individual dykes will be difficult to image, however, the reprocessing of the data may enhance the continuity of some geological features.

5. DATA ACQUISITION AND PROCESSING

5.1. Data acquisition parameters

The 2-D seismic reflection data acquisition layout was originally designed for mineral exploration (gold), with the primary focus on the Ventersdorp Contact Reef (VCR) at Moab Khotsong mine. The VCR is targeted because it occurs few metres above the seismically transparent Vaal Reef horizon, which is the most economic horizon in the study area. The 2-D seismic reflection profile (AV01) was selected for reprocessing and reinterpretation (Figure 2). The reflection seismic data were acquired by AngloGold Ashanti more than 2 decades ago, in 1992 (Figure 2 and Figure 9). The selected 2-D seismic

profile (AV01) intercept the M5.5 aftershocks nearly perpendicularly. Acquisition parameters are presented in Table 2. The survey was conducted on land using 4 vibrators as energy sources. For seismic profile line AV01, the total survey length is 11 km in E-W direction. Data were recorded by 440 channel array with 10 Hz geophone, the receiver spacing of 25 m and sampling rate of 4 ms.

5.2. Processing of the legacy data

Processing of the 2-D reflection seismic data was performed using a modern processing flow. However, to improve the likelihoods of imaging the thin target, substantial efforts were undertaken in particular with focus on static corrections, especially residual statics (see Hammer et al., 2014). The preliminary processing steps involved geometry, quality control such as editing and muting traces and picking of first-breaks. Pre-stack processing involved residual statics, band-pass filtering, normal moveout (NMO) and deconvolution. The raw shot gathers are shown before reprocessing is performed in Figure 10, while Figure 11 shows after re-processing is performed on raw shot gathers. The difference is demonstrated by Figure 12, which illustrates the reflections being enhanced by the application of the bandpass filter, which makes clear the structure hosting the M5.5 earthquake. Figure 12 shows a good correlation between the reprocessed seismic section and the modelled seismic section, which demonstrates that the parameters used for in modelling exercise provided some first-pass guidance on the reprocessing parameters of the legacy seismic data.

6. ROCK MINERALOGY AND CHEMISTRY

6.1. Core sampling

Post DSeis drilling endeavour, recovered fragile core samples were logged in detail, scanned and documented through an ICDP digital logging system and high-resolution optical scanner. Daily news were posted online, comprising of core logging information and scanning updates, which were available immediately to all the members of the ICDP-DSeis all over the world. Three boreholes (Hole A, B and branch Hole C) were drilled at 2.9 km below the surface at Moab Khotsong gold mine. The ICDP-DSeis team recovered siltstones, shales, quartzites, intrusions, basaltic lava and gouge material as described above in detail (Rickenbacher, 2018). Sampling for our study focused on branch Hole C, in particular, the intrusions, basalts and fault gouge near the M5.5 rupture zone. The sampling was conducted between 596 m and 612 m from the borehole collar of Hole B (Table 3).

6.2. XRF analysis

Lamprophyre dyke: The major elements comprising the lamprophyre dyke are presented in Table 4: SiO_2 (46.14 - 45.31 wt%), Fe_2O_3 (15.52 - 15.93 wt%), MgO (16.63 - 18.74 wt%) and K_2O (3.14 - 2.37 wt%). The lamprophyre dyke comprise of high iron, magnesium and potassium, and relatively lesser silica.

Basalt: The major elements comprising the basalt rocks are also shown in Table 4**:** SiO_2 (52.46 - 62.55 wt%), Al2O3 (11.74 - 12.81 wt%), Fe_2O_3 (10.44 - 11.77 wt%), MgO (0.80 - 7.53 wt%), K_2O (1.12 - 4.15 wt%) and Na_2O (2.41 - 6.06 wt%). These basalts contain high aluminium and iron, less magnesium and potassium.

6.3. XRD analysis

Lamprophyre dykes: The dominant minerals found in the intrusive rock (lamprophyre dykes), which is thought to host the M5.5 earthquake are biotite (25.06 – 29.62 wt%), talc (22.60 – 37.05 wt%), actinolite (16.79 – 23.11 wt%), diopside (4.04 – 14.43 wt%), chlorite (5.00 – 7.46 wt%), kaolinite (3.40 – 4.77 wt%), calcite (1.02 – 4.30 wt%) and quartz (0.37 – 0.83 wt%) (Table 5).

Fault gouge: The gouge material was sampled at 63 m (branch Hole C) (i.e., equivalent to 608 m distance from the borehole collar of Hole B) (see Figure 4), around the core loss zone. Approximately, 3 – 4 grams of the gouge material was sampled for XRD analysis. The XRD results of the gouge material from Moab Khotsong are shown below (Table 6). Our XRD results of the gouge material show biotite (20.06 – 20.09 wt%), talc (20.86 – 22.03 wt%), actinolite (32.57 – 33.97 wt%), calcite (11.98 – 13.31 wt%), chlorite (9.77 – 11.33 wt%), quartz (1.56 – 1.76 wt%) and sepiolite (0.27 – 0.44 wt%).

Basalt rocks: The samples were prepared for XRD analysis and the results are shown in Table 5. The basalt rocks generally comprises of major mineral components, plagioclase (23.81 - 47.78 wt%), quartz (24.72 – 37.29 wt%), microcline (2.89 – 27.06 wt%), sepiolite (8.13 – 15.94 wt%), and minor mineral components, biotite (1.47 – 3.15 wt%), calcite (1.63 – 3.94 wt%), chlorite (1.04 – 2.16 wt%),

dolomite (0.05 – 1.00 wt%), diopside (2.54 – 4.00 wt%), epidote (0.19 – 1.58 wt%) and kaolinite (0.00 – 6.11 wt%).

6.4. Thin section micrographs

In addition to detailed geological core logging and geophysical borehole logging, we performed thin section analysis of the recovered fragile core samples to further fully describe the surrounding host rocks and fault rocks. We analysed the mineralogy, grain size distribution and texture of the rocks using photomicrograph.

Lamprophyre dyke: Thin section micrographs show that lamprophyre dyke mainly comprises of micas (i.e., biotite and talc as indicated by XRD above), which are brownish in colour. The thin section micrographs are shown in plane polarised light (PPL) and cross-polarised light (XPL) (Figure 13). The lamprophyre dyke displays 'circular' structures that are defined by dark rims.

Basalts: Thin section micrographs of the Crown Formation are shown in plane polarised light (PPL) and cross-polarised light (XPL) (Figure 14). The thin section micrographs show a very fine-grained glassy matrix, which is altered. In addition, the thin section display amygdales and elongated structure such as veins.

6.5. Fault gouge material

6.5.1. Laser diffraction particle size analyser

To measure the particle sizes of the fault gouge material recovered from M5.5 earthquake. We used laser diffraction particle size analyser (Spectris plc. 2005). The instrument has a detection limit of submicron (0.02 µm – 2000 µm) (Spectris plc. 2005). This method has been widely used in several particle size distribution analysis of the fault gouge material and other engineering materials (Chester et al., 2005; Wilson et al., 2005; Keulen et al., 2007; Wechsler et al., 2011). The graph shows the relative volumes of material as a function of particle size. The measured fault gouge particle sizes approach ~ 10 µm (Figure 15).

6.5.2. SEM analysis of gouge samples

In addition to laser diffraction particle size analysis, the scanning electron microscopy (SEM) was used to analyse the fault gouge particles (Sammis et al., 1987; Shao and Zou, 1996). It must be noted

that we did not sieve the Moab Khotsong mine gouge samples. The fault gouge was glued to an SEM stub and coated with the carbon (30 nm C). The grains are generally well rounded and the particle size approaches ~ 11 µm lower limit, and ~1.2 mm upper limit (Figure 16).

Furthermore, to determine the chemical composition of the gouge particles, the energy-dispersive x-ray spectroscopy (EDS) was used. The EDS detector splits the distinctive X-rays signature of different elements into an energy spectrum (Figure 17). The elements identified are: SiO2 (38.36 - 62.33 wt %), Fe (19.53 - 45.61 wt %), MgO (1.84 – 7.60 wt %), CaCO3 (2.89 - 6.26 wt %) and Al2O3 (0.69 - 2.97 wt %) (Table 7).

6.5.3. Friction experiment results

The fault gouge sampled from the Moab Khotsong mine reached a peak friction coefficient of ~1.0 that decreased to steady-state friction of ~0.66 at ~ 100 mm /s slip velocities. This weakening occurred over a slip weakening distance of ~9.1 m (Figure 21; Table 8).

7. INTEGRATION OF REFLECTION SEISMIC DATA AND SEISMICITY

7.1. Reflection seismic profile at Moab Khotsong mine

We carefully selected 2-D seismic reflection profile (AV01), which was re-processed and re-interpreted (Figure 18). The reason behind the selecting of this 2-D seismic profile, in particular, is that it cross-cut the aftershock plane perpendicular which delineates the M5.5 rupture plane. Here, we interpret the 2-D seismic data with the focus on regional structural geology and the structure that hosts the M_L 5.5 earthquake. The seismic reflection data interpretation is often ambiguous mainly because of complex structural geology in the area characterised by dykes of several ages and extensive faulting. To minimise that, we used existing geological data from the mine and published literature. In addition, we used the geological core logging and geophysical borehole logging data from the Moab Khotsong mine drilled by the ICDP-DSeis team (specifically drilled to intercept the M_L 5.5 rupture). These data were integrated and used to constrain the reflection seismic data interpretation and improve confidence.

Imperative to the study, critical stratigraphic markers such as the base of the Karoo Basin were identified. This boundary was previously resolved through borehole observations and 3-D reflection seismic data interpretation by Watts (2005). We could also detect the Transvaal Supergroup (2.6 Ga) and Ventersdorp Supergroup (2.7 Ga) boundary due to the acoustic impendence contrast between

dolomites and Archaean volcano-sedimentary rocks. Most significantly, the Witwatersrand Supergroup comprising of the Central Rand and the West Rand Group was resolved due to the acoustic impendence between the Ventersdorp Supergroup lavas and the Central Rand Group clastic sedimentary rocks.

Structurally, the area is extremely disturbed with multiple sub-vertical faults that tend to branch (Figure 18). The fault branching may be caused by pre-existing geological inhomogeneities or by the release of stored strain energy. We also observe high amplitude reflectors that tend to die down laterally as we track the seismic reflector (Figure 18). These may be attributed to the presence of sills. There seems to also exist low amplitude vertical structures, which are not necessarily associated with displacement (Figure 18). These may be associated with intrusion of dykes.

The faulting regime seems to be dominated by strike-slip faulting where no vertical displacement is observed. However, there seems to be another regime of faulting that show vertical displacement – predominately reverse faulting (thrusting) which are widely reported in the Witwatersrand Basin literature, and some minor areas of normal faulting (Figure 18). With the closer examination of the aftershock plane and their cut-off, we observe strong reflectors, which could be sills (Figure 19). These sills may be responsible for the sharp termination of the aftershocks.

8. ANALYSIS AND DISCUSSION

8.1. Host rocks, intrusives and fault gouge: mineralogy and chemistry

The drill core recovered from the ICDP-DSeis Hole A and B form part of the Jeppestown Subgroup of the West Rand Group. Both these drill core of Hole A and Hole B showed strong similarities and are described in detail by Rickenbacher (2018). They intercepted the Roodepoort Formation, Crown Formation and Babrosco Formation of the Jeppestown Subgroup (Rickenbacher, 2018), which are characterised by metasedimentary rocks, basalts and various intrusive rocks, including dykes and sills (Armstrong et al., 1991; Ogasawara et al., 2017; Manzi et al., 2018; Rickenbacher, 2018). The petrological analysis by Rickenbacher (2018) was limited to hand specimens and thin section analysis. Nonetheless, the studies revealed that intrusive rocks were largely similar in mineral composition with variations in the extent of alteration (Rickenbacher, 2018). These analyses were focused on Hole A and B, at that time the Hole C was not yet drilled.

Our detailed examination of petrology focused on Hole C (branch), which included the XRD, XRF and thin section micrographs analysis. We found that the basalt rocks major mineral components are

plagioclase and quartz, and minor mineral components are biotite, calcite, chlorite, dolomite, diopside, epidote and kaolinite. These basalts belong to the Crown Formation (Armstrong et al., 1991; Dankert and Hein, 2010; Rickenbacher, 2018). The intrusive rock recovered in Hole C found near to the core-loss zone (adjacent to the M5.5 rupture zone) was identified as the lamprophyre dyke, which is thought to host the M5.5 earthquake. The mineral composition of the lamprophyre dyke revealed major mineral components to be biotite and talc with a combined modal abundance of ~25 – 66 wt%, and minor mineral components comprise of actinolite, diopside, chlorite, kaolinite, calcite and quartz. Presently, the nomenclature and classification are not well-defined (Daya, 2019), and we don't intend to discuss it here. The lamprophyres are characterised as alkaline rocks that comprise of shiny plates of biotite (or phlogopite), amphibole, pyroxene, within an altered groundmass and interstitial calcite (Rock, 1977; Rock, 1987; Mitchell, 1994).

This largely agrees with the initial work conducted by Rickenbacher (2018) on Hole B (mother hole), where he found metabasalt of the Crown Formation and a unique 'dark grey' intrusive rock identified as a lamprophyre dyke. He found that this intrusive rock 'adjacent' to the fault differs significantly 'optically' with other intrusive rocks (dolerite dykes and sills). The reason for the grey to black colour in the lamprophyre dyke was explained by the presence of high mica content, which he observed under thin section micrographs (Rickenbacher, 2018). On thin sections, Rickenbacher (2018) identified these micas as sericite, which appeared brownish, laminated and very fine-grained. However, Ogasawara (pers comm.) noted that Rickenbacher (2018) microscopic observations of the lamprophyre dyke were similar to those described by Hrouda et al. (2019). Yet, Rickenbacher (2018) identified the mica as sericite instead of talc, which was revealed by our XRD results (lamprophyre dyke).

In Hole C (branch) at a distance of 63 m (i.e., ~608 m from the borehole collar of Hole B), we also conducted the XRD analysis of recovered and mapped fault gouge material occurring next to the lamprophyre dyke and results are shown above. This material was also observed in Hole B, which was equivalent to the gouge material observed at borehole depth of ~ 612 m (Rickenbacher, 2018). The fault gouge samples from Moab Khotsong mine contain talc and biotite (>40 wt%) occurring as predominant minerals. The XRD results of the gouge material show calcite, quartz, biotite, actinolite, chlorite, talc and sepiolite. This agrees with findings by Kaneki et al (2018), where XRD analysis of the fault gouge material revealed the existence of talc mineral (Kaneki et al., 2018). Talc and biotite minerals have low friction and often characterise seismogenic processes (Moore and Lockner, 2004; Moore and

Michael, 2007; Ogasawara et al., 2019). In this study, talc and biotite's combined modal abundance is generally greater than 40 wt%. However, detailed analysis seems to suggest that the concentration of talc and biotite is greater in the lamprophyre dyke than in the the gouge material.

8.1.1. Lamprophyre dykes

In South Africa, lamprophyre dykes have not been studied extensively compared to kimberlites, which host diamonds. Their composition, size distribution and ages have not been widely reported. The oldest reported lamprophyre dykes in the Kaapvaal Craton are found in the Johannesburg Dome situated ~180 km northeast of the Klerksdorp goldfields (Anhaeusser, 1999; Prevec et al., 2004). Recently, lamprophyre dykes have also been reported in the Western Limb of the Bushveld Complex in deep platinum mines, which are located ~170 km north of the Klerksdorp goldfields. The Bushveld Complex is known for its world-class platinum deposits. In the Bushveld Complex, these lamprophyre dykes are associated with underground gas outbursts and rock failure, which pose a risk to mineworkers and damage to infrastructure. These gas outbursts are attributed to sudden 'depressurisation' induced by mining activities (Daya, 2019). In addition, these lamprophyre dykes when exhumed during mining operations decompose very quickly (~24 - 48 hours), resulting in falls of ground (FOG) and seismicity of variable magnitudes.

Daya (2019) conducted a detailed study of the lamprophyre dykes that intruded the Bushveld Complex. The study revealed that these dykes tend to form as irregular or anastomosing sets of hundreds of sub-parallel dyke swarms and often bifurcate at depths of ~1000 to 3000 m. These are similar depth ranges to the ICDP-DSeis drilling programme of ~ 2900 m below surface. The dykes are nearly vertical (dip > 80°) and strike between WNW and ESE, with the strike length extending ~50 km (Daya, 2019; Hughes et al., in prep.). The DSeis mine seismicity data revealed that the lamprophyre dykes strike NNW-SSE, which are comparable in terms of strike directions. The measured apparent thickness varies between ~ 0.1 and 20 m, with the true thickness of ~0.5 to 3 m. This is similar to the thickness measured in the DSeis drill core of the lamprophyre dykes, and the near-vertical dip delineated by our mine seismicity data and the re-processed reflection seismic data. Hughes et al. (in prep.) conducted geological age dating of these lamprophyre dykes, which revealed that the dykes are between 177.2 and 131.8 Ma (Jurassic-Cretaceous). This age data agrees with the structural relationship observed from reflection seismic data where we suggest that lamprophyre dykes intruded

into an existing fault which cross-cuts the entire Witwatersrand Basin. In addition, these lamprophyre dykes were reported by Watts (2005) in the Klerksdorp goldfields at mining levels in adjacent mine, Kopanong mine.

8.1.2. Dolerite dykes and sills

Important to this study, in Hole A and Hole B, Rickenbacher (2018) mapped several 'thick' intrusive rocks, which intruded metasedimentary rocks. In particular, Hole A revealed several intrusive rocks with a variable apparent thickness between ~ 2.0 m and 68.2 m. In Hole B, the apparent thickness of intrusive rocks varied between 15.2 and 44.9 m. This excludes the lamprophyre dyke identified and discussed above, which is optically unique - dark grey to black and medium-grained. These intrusive rocks were correlated in Hole A and B, and display similar appearances such as colour, thickness and textures. Majority of these mapped intrusive rocks both in Hole A and B show parallel bedding and were identified as dolerite sills (Rickenbacher, 2018).

Geophysical investigations including electrical methods and 2-D seismic reflection legacy data in the Karoo Basin have greatly improved the understanding of the Karoo dolerite dykes and sill complex (van Zijl, 2006; Scheiber-Enslin et al., 2014). These geophysical studies have enabled researchers to characterise the dolerite complex into three zones: (a) the first dolerite zone comprises of widespread regular sills spanning ~30 km and inclined sheets forming at the edges (Cole et al., 2011). (b) The second dolerite zone comprises of more abundant intrusions that are typically saucer-shaped (Du Toit, 1920). These intrusions tend to occur within the Upper Ecca Group and Beaufort Group, and occasionally in the upper formations. (c) The third dolerite zone comprises of smaller amount dolerite intrusions compared to zone one and two. This zone is characterised mainly by dykes that are understood to feed the lavas that intruded the Stormberg Group (Chevallier et al., 2001). In the Karoo, the typical thickness of dykes is between ~2 m and 10 m. These dolerite dykes can be traced for 30 km to 80 km (Duncan and Marsh, 2006).

The geometry and mechanisms controlling the formation of these sills, inclined sheets and dykes have been reported (Burchardt, 2008; Scheiber-Enslin et al., 2014). Burchardt (2008) reported that sills often intrude between lithologies of varying mechanical properties due to a difference in the stress field. For instance, in the study area, these sills form between metasedimentary rocks and basaltic lava. This can be mapped on the recovered core samples, and physical properties measured using the

geophysical borehole logging of density and velocity. The Karoo field observations suggest that dykes may grow into inclined sheets that may form into inner and outer sill (Chevallier and Woodford, 1999). Furthermore, numerical modelling has also shown that a sill emplacement may result in doming of the overlying sediments and when the edges of a dome reach a critical angle the stress induces the formation of the inclined sheet that cross-cut the host rocks. These inclined sheets may continue up until the magma pressure drops which results in the intrusion following the bedding again. This process may carry on again to form an outer sill at an upper stratigraphic location (Malthe Sørenssen et al., 2004).

8.2. Reflection seismic and seismicity

8.2.1. Klerksdorp goldfield regional tectonics

Using re-processed reflection seismic data with an improved resolution, we re-interpreted the data and we successfully delineated key stratigraphic markers of the Witwatersrand Basin, which are also reported above and in the literature (Figure 17). Specifically, the re-processed and improved high-resolution reflection seismic data revealed the boundary between the West Rand Group and Central Rand Group of the Witwatersrand Supergroup. The West Rand Group and Central Rand Group reflection seismic boundary is approximated through the strong reflection of the Crown Lavas of the West Rand Group with surrounding conglomerates and quartzites. Rickenbacher (2018) measured the P-wave velocity. The tests showed that P-wave velocities for metasedimentary rocks (quartzite and conglomerate) are ~5.50 - 5.90 km/s and Crown metabasalt are ~5.99 km/s. This stratigraphic marker observed in our reflection seismic data agrees with previous 2-D and 3-D reflection seismic interpretation studies, where several authors throughout the Witwatersrand Basin delineated this stratigraphic marker (Watts, 2005; Manzi et al., 2012a and b; Nkosi, 2016; Ogasawara Jr. et al., 2018; Noda, 2020). This is also consistent with the geology described in the literature – giving our data more confidence to interpret other related geological structures such as faults and dykes.

We could delineate the seismic reflector between the Central Rand Group of the Witwatersrand Supergroup and the Ventersdorp Supergroup. This reflector is a result of the difference in acoustic impendence contrast between underlying conglomerates and quartzite rocks and lavas of the Ventersdorp Supergroup. This agrees with the detailed work conducted by Nkosi et al. (2016), where they identified this seismic marker as the Ventersdorp Contact Reef (VCR), a boundary between the

top of the Central Rand Group and the base of the Ventersdorp Supergroup. Nkosi et al. (2016) reported that the VCR reflector's high amplitude is due to the strong contrast in acoustic impendence between Klipriviersberg Group lavas (velocity ~6.40 km/s and density ~2.90 g/cm^3) of the Ventersdorp Supergroup and quartzites (velocity ~5.70 km/s and density ~2.67 g/cm^3) of the Central Rand Group (Nkosi et al., 2016). These density and velocity values are consistent with the laboratory measurements conducted by Rickenbacher (2018) and geophysical borehole logging conducted by the DSeis team. The VCR is very important in the Witwatersrand Supergroup because it is exploited in various mines for gold such as the Cooke 4 mine (Nkosi et al., 2016; Mngadi et al., 2019).

In this study, we also detected the boundary between the Transvaal Supergroup and the Ventersdorp Supergroup. This is due to the acoustic impendence contrast between the overlying dolomites and underlying volcano-sedimentary rocks of the Transvaal Supergroup and the Ventersdorp Supergroup, respectively. This is consistent with the BLR is imaged as a strong reflector by Nkosi et al. (2016). Similar to our study, the strong acoustic impedance contrast was attributed to the dolomites (velocity ~6.7 km/s and density ~2.84 g/cm^3) of the Transvaal Supergroup and the Klipriviersberg Group lavas of the Ventersdorp Supergroup (velocity ~6.40 km/s and density ~2.90 g/cm^3) (Nkosi et al., 2016). In economic terms, this boundary is linked with the Black Reef (BLR), which is also exploited for gold (Nkosi et al., 2016).

Additionally, through borehole data Watts (2005) correlated with the reflection seismic data, we identified the base of the Karoo Basin. This marker is important for our study because we can assess the chronology of critical geological events and intrusions related to the M5.5 Orkney earthquake.

8.2.2. Structure of Moab Khotsong mine

Structurally, the reflection seismic section shows that the study area is extremely disturbed by multiple sub-vertical features that tend to branch. These near-vertical features are associated with attenuation of seismic amplitudes (or low amplitude near-vertical structures) (Figure 18 and Figure 19). There seems to be no significant displacement associated with the majority of these features characterised by the low seismic amplitudes. We interpreted these features as a combination of faults and dykes. No significant displacement may suggest that these faults are strike-slip. These dykes may have intruded into pre-existing faults. The combination of faults and dykes are interpreted, however, it is extremely difficult to distinguish between the two on the seismic section without any displacement or

off-set. Therefore, we used the DSeis drilled core from Holes A, B and C to constrain these observations. The lamprophyre dyke was mapped adjacent to the fault and fault gouge material. In addition, the drill cores indicate the extensive degree of alteration and fracturing adjacent to the lamprophyre dyke.

We also observe high amplitude reflectors that tend to die down laterally as we track the reflector. We interpreted these high amplitude lateral structures as sills. Again, as stated above, these were mapped on the recovered drilled core by the DSeis team. These seismic reflectors are due to high P-wave velocity (6.7 - 6.5 km/s) and density (2.99 – 3.06 g/cm^3) contrast between intrusive rocks and surrounding metasedimentary rocks P-waves (5.9 - 5.5 g/cm^3) and density (2.71 - 2.86 g/cm^3). The re-processed 2-D seismic data indicates the presence of numerous dykes and sills in the West Rand Group. It is reported that these sills, in particular, may represent intrusions that have used the older thrust faults as zones of weakness along which they have intruded (Watts, 2005).

Here, we could successfully detect thin dykes to depths exceeding 2.9 km. However, as predicted by numerical modelling above, throughout the seismic section the thickness of these dykes is not resolved. In addition, sills show lateral variation in seismic amplitudes which eventually die down. Interpreting amplitude variation of reflectors is complex. This is because many factors may contribute to amplitude various such as thickness or/and composition. Evidence from Hole A and B, show numerous intrusive rocks with variable apparent thickness between ~ 2.0 m and 68.2 m; and 15.2 and 44.9 m, respectively. This may suggest that the variations in amplitude may be caused by thickness deviation since the composition is largely similar for sampled dolerite sills as shown above (Rickenbacher, 2018). On the seismic data, these sills extend for kilometres, however, it is difficult to determine where they terminate. This agrees with various authors, findings suggesting similar sills in the Witwatersrand Basin and Karoo Basin (Watts, 2005; Duncan and Marsh, 2006; Cole et al., 2011; Scheiber-Enslin et al., 2014).

The lamprophyre dyke is thought to have later intruded into the fault structure associated with M5.5 earthquake. As discussed above, the lamprophyre observed in the Witwatersrand Basin is similar to those observed in the Bushveld Complex, which are Jurassic-Cretaceous in age. Important to this study, the re-processed and enhanced seismic data delineated the fault structure clearly, which cut through the West Rand Group and Central Rand Group near vertically (here we name it *F1*). These observations agree with the previous work conducted by various researchers, which identified the near-

vertical fault structure, which is 'potentially' responsible for the M5.5 earthquake (Ogasawara et al., 2017; Manzi et al., 2017). Ogasawara Jr. et al. (2018) specifically re-interpreted 2-D seismic reflection data and delineated the near-vertical geological structure occurring below the mining levels at Moab Khotsong mine.

Furthermore, the integration of reflection seismic data and seismicity data reveals that the aftershocks strike NNW-SSE in a planar structure and fit very well with the fault structure (F1) delineated by reflection seismic data, which is near vertical (Figure 19). The seismicity recorded by the mine seismic network, however, reveals an interesting termination of the aftershocks just below the mining levels. This termination of aftershocks is inconsistent with the fault structure, which extends beyond mining levels and cuts across the West Rand and Central Rand Group, and possibly the base of Karoo Basin. The cut-off of the aftershocks occurs at the depth where the lamprophyre dyke intersects the sill. Watts (2005) conducted detailed underground observations in the neighbouring Kopanong mine in the Klerksdorp goldfields to determine the age relationship of these intrusive rocks. This classification was based on cross-cutting relationships; chilled margins; inclusions and veining; alteration; and deformation. The study revealed that: Early N-S and Buffer dykes are of Klipriviersberg age; followed by Zuiping faults of early Platberg age; the Diagonal and DW dykes of late Ventersdorp (to be noted is that there seems to be a level of uncertainty); the Jersey fault (also to be noted is that there seems to be a level of uncertainty); and the Popeye Dykes which are Post Karoo. The Popeye Dykes are identified to spread through to the base of the Karoo Basin on seismic data (Watts, 2005). The Popeye dykes described above are similar to the lamprophyre dykes hosting the M5.5 earthquake under light microscopy (e.g., thin section analysis). This may suggest that the lamprophyre dykes, which are age dated younger in the Bushveld Complex, may be members of the Popeye dyke suite or related to it (Watts, 2005; Hughes et al., in prep.).

Detailed examination of the influence of the geological structures on seismicity and rockbursts in the Klerksdorp Goldfields was performed by van der Heever (1982). The study examined the influence of lamprophyre dykes and Karoo dolerite dykes relevant to this study, and various other dykes on seismicity. They could show that about 42% of seismic events occurred in proximity to dykes (in the region of ~ 60 m from a known dyke), while about 16% occurred along with a known dyke location. In addition, these studies revealed that the region where dykes and sill 'intersect' are often characterised by the formation of large damaging seismic events (van der Heever, 1982). Sill meandering is often

encountered, which sometimes assume local transgressive attitudes towards the country rocks and are truncated by these lamprophyre dykes (Wilson et al., 1964; van der Heever, 1982). This relationship and geometry of these intrusive rocks are similar to our study area situated in the West Rand Group, below the Moab Khotsong mine. The intersection of lamprophyre dykes and dolerite sills may have been a critical factor in the nucleation of the M5.5 earthquake, similar to large damaging seismic events associated with these intersections reported by van der Heever (1982).

8.3. Factors controlling M5.5 earthquake

Dykes often intrude fault planes over lengths of up to several kilometres, e.g., 15-16 km (van der Heever, 1982). Here, we found that the lamprophyre dykes are the youngest generation of igneous intrusive rocks in the Klerksdorp goldfields (Watts, 2005; Hughes et al., in prep.; van der Heever, 1982). These dykes are often water- and methane-bearing and are associated with seismicity which poses a risk to the mining operation. These dykes are soft, incoherent and do not form strong, rigid transgressive bodies (van der Heever, 1982). The dykes are characterised by variable thicknesses of ~1 m to greater than 3 m, strike northerly and dip near vertical (van der Heever, 1982). These geometric attributes are consistent with those observed on the reprocessed 2-D seismic section data where the imaged dyke (possibly the lamprophyre dyke) observed in the fault zone is interpreted to host the M5.5 earthquake.

van der Heever (1982) reported that the Vaal Reef was not vertically displaced at mining levels, and typical near-horizontal slickensides along fault contacts characterise these dykes (van der Heever, 1982). This observation is difficult to confirm with seismic because the Vaal Reef cannot be imaged by seismic since it occurs at the interface between the Central Rand Group quartzite units. van der Heever (1982)'s observations, however, agree with the aftershock data, which revealed that the M5.5 earthquake fault mechanism is strike-slip (Imanishi et al., 2017). Furthermore, with the integration of the DSeis drill core and reflection seismic data, this study revealed that the M5.5 earthquake is characterised by two structural elements - horizontal dolerite sill that produced high amplitude reflections and the near-vertical lamprophyre dyke, and faults that are characterized by a zone of low amplitudes. These structural elements may mark the termination of the aftershocks associated with the M5.5 rupture.

We also conducted high slip velocity (100 mm/s) friction experiments on the M5.5 fault gouge recovered from deep drilling at Moab Khotsong mine. The fault gouge was sheared at an applied normal

stress of ~2 MPa. The fault gouge sample (weight of ~1 grams, equivalent to ~1 mm gouge thickness) was used as an intervening layer between two sliding rock surfaces (Figure 20). The sliding rock quartzite cylinders and a Teflon sleeve were used to prevent the fault gouge from leaking during shearing. The friction experiments were conducted under room-dry conditions. We found that the frictional resistance weakens exponentially with increasing slip displacement during rupture propagation viz. slip weakening behaviour. The slip weakening behaviour is described by the exponential decay equation (Mizoguchi et al., 2007):

$$\mu = \mu_r + (\mu_i - \mu_r)\, e^{\left(\frac{\ln(0.05)*d}{d_c}\right)} \quad (1)$$

where, μ_i is the peak friction coefficient (frictional resistance), μ_r is the steady-state friction coefficient, d is displacement. The exponential decay equation decrease friction to a constant value, as displacement approaches infinity, thus, we define d_c as a displacement where $(\mu_i - \mu_r)$ decreases to ~5% of $(\mu_i - \mu_r)$, and let d_c represent D_c. This means d_c represents a critical slip displacement (D_c), which is defined as the weakening of the frictional resistance over slip weakening displacement during rupture propagation (Mizoguchi et al., 2007).

At slip velocities of ~100 mm/s, the Moab Khotsong gouge sample had the peak friction coefficient of ~1.0, which decreases to steady-state friction of ~0.66 over a slip weakening distance of ~9.1 m (Figure 21; Table 8). These results are very high for samples with considerable amount of micas. This may be as a result of the dependence of friction on gouge layer thickness. Experiments from Ortlepp shears contained thin gouge layers (~0.5 mm), while the thickness of gouge layers for Moab Khotsong samples was thicker (~1 mm). However, this is comparable with the values obtained from Ortlepp shear fractures - at slip velocity of 100 mm/s and normal stress of 2 MPa, the natural gouge sample S(3) had peak friction of ~0.98, which weakened to steady-state friction of ~0.67 over a slip weakening displacement of ~12.8 m (Mngadi et al., 2020). With similar experimental conditions (slip velocity of 100 mm/s and normal stress of 2 MPa), the natural gouge sample S(4) revealed peak friction of 0.92 and weakened to steady-state friction of 0.71, over a slip weakening displacement of ~6.1 m. These results show that the weakening behaviour of natural gouge samples is comparable at similar slip velocities (~100 mm/s) (Table 8) (Mngadi et al., 2020).

It has been reported in the Bushveld Complex that these lamprophyre dykes are associated with rock failure through decomposing and gas outbursts, also that when dykes and sills intersect large damaging seismic events tend to occur, which is similar to the geometry (or architecture) of geology in

our study area. Naturally, dykes intrude mechanically weak zones such as faults, and therefore, tend to be associated with stress concentration over time, which exceed the fault strength and cause reactivation of faults. This is supported by work conducted by Yabe et al. (2019a) and Yabe et al. (2019b), which measured the stress variations in the drill core successfully using the diametrical core deformation analysis (DCDA) stress-measurement method (Funato and Ito, 2017). The measurements revealed the localisation of stress in specific locations adjacent to (a) the M5.5 rupture in Hole B; (b) the upper edge of the aftershock region; and (c) the hypersaline brine fissure in Hole A (Yabe et al., 2019b). The composition of the fault gouge material and lamprophyre dykes reveal that talc and biotite are dominant minerals, which agrees with the findings in Hole B and Hole C (branch) that the fault gouge material contains more than 20% of the talc mineral (Kaneki et al., 2018; Hirono et al., 2019). The presence of brine may have contributed to the dissolution of lamprophyre dykes, which is also reported in the Bushveld Complex. Additionally, it was observed that these lamprophyre dykes are characterised by extensive alteration (Rickenbacher, 2018). The mineralogy may also suggest that the dynamic rupture propagation is controlled by gouge material with the dominant mineral composition such as talc and biotite, acting like a powder lubricant. This is similar to findings of talc from the San Andreas Fault, a transform plate boundary with subduction of paleo-ridge-structure (Zoback et al., 2011).

Here, we suggest that three critical processes control the M_L 5.5 earthquake seismogenic zone: (a) intersection of lamprophyre dykes and dolerite sills creating natural zones of weakness, (b) mechano-physical damage induced by tectonic and/or mining related stresses; and (c) mechano-chemical processes due to water and rock interaction (Nisson et al., 2019; Wiersberg et al., 2019; Ogasawara et al., 2019). Compared to Cooke 4 mine seismogenic zone forming ahead of the mining face in the Archean quartzite formation of the Witwatersrand Supergroup, the seismogenic zone is controlled by mechanical damage induced by mining-related stresses (Mngadi et al., 2019; Mngadi et al., 2020). To understand the effect of geology associated with these mining induced ‘normal faults’ or earthquakes forming ahead of the stope at Cooke 4 mine, Mngadi et al. (2019) used integration of underground mapping and microseismic data, which reveal that the fracture turning-point occurs in the soft strata (weak hangingwall lavas). This is relevant in this study because lamprophyre dykes constitute a soft strata. Furthermore, Mngadi et al. (2020) performed several friction experiments with and without the intervening gouge layer recovered from similar DSeis drilling endeavour in deep and high stress

Cooke 4 mine seismogenic zone. These friction experiments exposed ‘characteristics’ that may be responsible for aseismic evolution of ‘normal faults’ occurring ahead of the stope.

9. CONCLUSION

Mining induced seismicity is associated with magnitudes of Mw 1 - 4 at mining levels, which are typically normal faults occurring ahead of the stope (van Aswegen, 2008). The M5.5 Orkney earthquake was different, as it ruptured below the mining levels with a strike-slip faulting mechanism striking NNW-SSE. The DSeis team drilled into the Roodepoort Formation, Crown Formation and Babrasco Formation of the West Rand Group, the country rocks that host the M5.5 earthquake rupture. This was followed by the geophysical borehole (density and velocity) logging and geological core logging. The core logging and petrographic analysis revealed metasiltstone, metashale, metaquartzite and metabasalts, intruded by highly altered dolerite sills and lamprophyre dykes. The lamprophyre dyke was adjacent to the core-loss zone and fault gouge material that is characterised by talc and biotite minerals. The intrusive rocks were correlated to high seismic velocity and density in the geophysical borehole logs.

The newly re-processed reflection seismic data revealed the fault ‘architecture’ (*F1*), which is interpreted to cut across the entire Witwatersrand Supergroup. Integrating reflection seismic data and the aftershocks data recorded by the in mine seismic network, the dataset revealed a strike-slip faulting mechanism that strike NNW-SSE. In addition, friction experiments with an intervening gouge layer recovered from M_L 5.5 earthquake rupture revealed that at high slip velocity of ~100 mm/s and normal stress ~ 2 MPa, similar ‘friction weakening behaviour’ is observed compared to Cooke 4 mine ruptures that occur ahead of the mine stope. Equipped with the scientific evidence, we suggest that three critical processes mainly control the M_L 5.5 earthquake seismogenic zone: (1) the architecture of the fault zone (e.g., intersection of lamprophyre dykes and dolerite sills); (2) stress accumulation induced by tectonic and/or mining related activities; and (3) water and rock interaction. This is different compared to the Cooke 4 mine seismogenic zone, where ‘normal faults’ occur ahead of the mining front in the quartzite formation of the Central Group with no influence of intrusive rocks and mechano-chemical process. The Cooke 4 mine seismogenic zone is largely controlled by mechanical damage induced by mining-related stresses.

10. ACKNOWLEDGMENTS

We acknowledge the ICDP, JST-JICA SATREPS, JSPS Core-to-Core Program, JSPS - NRF Bilateral Research Program. Sibanye gold limited is acknowledged for providing permission to publish the results. The authors thank the Council for Geoscience, the Wits Seismic Research Centre, School of Geosciences, University of the Witwatersrand, Department of Geology and Mineralogy, Kyoto University, CIMERA and the CSIR Centre for Mining Innovation, for the use of their resources and facilities. This project was also funded by JSPS KAKENHI grants 21224012, 21246134, 26249137, the MEXT's Earthquake and Volcano Hazards Observation and Research Program, and the Earthquake Research Institute the University of Tokyo cooperative research program. RJD acknowledges the support of the South African Research Chairs Initiative of the Department of Science and Technology and the National Research Foundation.

11. REFERENCES:

Anhaeusser, C. (1999). Archaean crustal evolution of the central Kaapvaal Craton, South Africa: evidence from the Johannesburg Dome. South African Journal of Geology, 102, 303–322.

Armstrong, R.A., Compston, W., Retief, E.A., Williams, I.S., Welke, H.J., 1991. Zircon ion microprobe studies bearing on the age and evolution of the Witwatersrand triad. Precambrian Research, 53, 243–266.

Bacon, M., Simm, R. and Redshaw, T. (2003). 3-D Seismic Interpretation. Cambridge University Press.

Barnes, A.E. (1996). Theory of 2-D complex seismic trace analysis. Geophysics, 61, 264–272.

Bucholz, E.W., Zhao, X., Sinnott, S.B. and Scott S. (2012). Perry friction and wear of pyrophyllite on the atomic scale. Tribology Letters, 46, 159 – 165.

Byerlee, J.D. (1978). Friction of rocks. Pure Applied Geophysics, 116, 615–626.

Beach, A. and Smith, R. (2007). Structural geometry and development of the Witwatersrand Basin, South Africa. In: Early Precambrian Processes, AC Ries, RWH Butler, RH Graham, editor. London: Geological Society Special Publications, 272, 533–542.

Burchardt, S. (2008). New insights into the mechanics of sill emplacement provided by field observations of the Njardvik Sill, Northest Iceland. Journal of Volcanology and Geothermal Research, 173, 280-288.

Campbell, G. and Crotty, J.H. (1990). 3-D seismic mapping for mine planning purposes at the South Deep Prospect. In: Ross-Watt, D.A.J., Robison, P.D.K. (Eds.). Proceedings of the International Deep Mining Conference. The Southern African Institute of Mining and Metallurgy Symposium Series, 10, 569-597.

Campbell, G. and Peace, D.G. (1984). Seismic reflection experiment for gold exploration, Wits Basin, Republic of South Africa. Paper presented at the 46th Annual Meeting of the European Association of Exploration Geophysicists (EAEG), London, England.

Camden-Smith, P.M. (1980). The sedimentology, geochemistry and diagenesis of West Rand Group sediments in the Heidelberg area, Transvaal. Thesis submitted in fulfilment of the requirements for the degree of Master of Science at the University of Cape Town.

Chester, J.S., Chester, F.M. and Kronenberg, A.K. (2005). Fracture surface energy of the Punchbowl fault, San Andreas system. Nature, 437, 133–136.

Chevallier, L. and Woodford, A. (1999). Morpho-tectonics and mechanism of emplacement of the dolerite rings and sills of the western Karoo, South Africa. South African Journal of Geology, 102, 43-56.

Chevallier, L., Goedhart M. and Woodford, A. (2001). The Influence of Dolerite Sill and Ring Complexes on the Occurrence of Groundwater in Karoo Fractured Aquifers: A Morpho-Tectonic Approach. Water Research Commission Report. 937/1/01.

Cole, D.I., Robey, K. Chevallier, L. and Viljoen, J. (2011). The geology of shales with a gas potential in the Main Karoo Basin of South Africa and impact of hydraulic fracturing on groundwater. Council for Geoscience Report 2011-0142. Council for Geoscience Western Cape Regional Office, Bellville, pp. 43.

Collettini, C., Niemeijer, A., Viti, C. and Marone, C. (2009). Fault zone fabric and fault weakness. Nature 462, 907–910.

Coward, M.P., Spencer, R.M. and Spencer, C.E. (1995). Development of the Witwatersrand Basin, South Africa. In: Coward, M.P., Ries, A.C. (Eds.). Early Precambrian Processes: Geological Society, London, Special Publications, 95, 243–269.

Dankert, B.T. and Hein, K.A.A. (2010). Evaluating the structural character and tectonic history of the Witwatersrand Basin. Precambrian Research, 177, 1-22.

Daya, P. (2019). The petrology and petrogenesis of lamprophyric dykes in the Bushveld Complex, and their possible role in causing gas outbursts. Master of Science Thesis. University of the Witwatersrand, Johannesburg.

De Kiewiet. C.W. (1941). A History of South Africa, Social and Economic. New York: Oxford University Press, pp. 292.

Di, H. and Gao, D. (2014). A new algorithm for evaluating 3D curvature and curvature gradient for improved fracture detection. Computers & Geosciences, 70, 15–25.

Dienwiebel, M., Verhoeven, G.S., Pradeep, N., Frenken, J.W.M., Heimberg, J.A. and Zandbergen, H.W. (2004). Superlubricity of graphite. Physical Review Letters, 92, 126101.

Duncan, A. R. and Marsh, J. S. (2006). The Karoo Igneous Province. In: M. R. Johnson, C. R. Anhaeusser and R. J. Thomas (Eds.). The Geology of South Africa. Geological Society of South Africa and Council for Geoscience, 461-499.

Durrheim, R.J., Anderson, R.L., Cichowicz, A., Ebrahim-Trollope, R., Hubert, G., Kijko, A., McGarr, A., Ortlepp, W.D. and Van der Merwe, N. (2006). Investigation into the risks to miners, mines and the public associated with large seismic events in gold mining districts. Department of Minerals and Energy, Pretoria, South Africa.

Durrheim, R.J., Ogasawara, H., Nakatani, M., Yabe, Y., Milev, A., Cichowicz, A., Kawakata, H., Moriya, H. and the JST-JICA SA research group. (2010). Observational Study to Mitigate Seismic Risks in Mines: a new Japanese–South African collaborative project. Proceeding of the 5th International Seminar on Deep and High Stress Mining. (ed. Van Sint Jan and Yves Potvin), Australian Centre for Geomechanics, Perth, Australia, 215–225.

Durrheim, R.J., Ogasawara, H., Nakatani, M., Yabe, Y., Kawakata, H., Naoi, M., Ward, A.K., Murphy, S., Wienand, J., Lenegan, P., Milev, A.M., Murakami, O., Yoshimitsu, N., Kgarume, T., Cichowicz, A. and JST-JICA SA research group. (2012). Establishment of SATREPS experimental sites in South African gold mines to monitor phenomena associated with earthquake nucleation and rupture. In: Proceedings of the 6th International Congress on Deep and High Stress Mining. Perth, pp.173-187.

Durrheim, R.J. (2015). Geophysical laboratories in deep gold mines: earthquakes, neutrinos, extremophiles and the origin of the Earth's magnetic field. The History of Geophysics in Southern Africa. J.H. de Beer (ed.). SUN MeDIA, Stellenbosch, pp. 116–138.

Du Toit, A.I. (1920). The Karoo Dolerites. Transactions, Geological Society of South Africa, 33, 1-42.

Fatti, J. (1987). Reflection seismic surveys in the Karoo Basin by Soekor. South African Geophysical Association Yearbook, pp. 22-30.

Funato, A. and Ito, T. (2017). A new method of diametrical core deformation analysis for in-situ stress measurements, International Journal of Rock Mechanics and Mining Sciences, 91, 112-118.

Galerne, C.Y., Galland, O., Neumann E.R. and Planke, S. (2011). 3D relationships between sills and their feeders: evidence from the Golden Valley Sill Complex (Karoo Basin) and experimental modelling. Journal of Volcanology and Geothermal Research, 202, 189-199.

Gibson, M.A.S., Jolley, S.J. and Barnicoat, A.C. (2000). Interpretation of the Western Ultra Deep Levels 3D seismic survey. The Leading Edge, 19, 730–735.

Gray, N.K, Tucker, R.E. and Kershaw, D.J. (1994). The Sun Project-I. Discovery of a major new Witwatersrand goldfield. In: Anhaeusser, C.R. (Eds.). Proceedings of the 15th Congress for Council of Mining and Metallurgical Institutions, Symposium Series, 14, 95-102.

Gumsley, A., Stamsnijder, J., Larsson, E., Söderlund, U., Naeraa, T., de Kock, M., Sałacińska, A., Gawęda, A., Fabien Humbert, F. and Ernst, R. (2020). Neoarchean large igneous provinces on the Kaapvaal Craton in southern Africa re-define the formation of the Ventersdorp Supergroup and its temporal equivalents. Geological Society of America Bulletin 132(9-10). DOI: 10.1130/B35237.1

Hammer, P.T.C., Clowes, R.M. and Ramachandran, K. (2014). Seismic reflection imaging of thin, kimberlite dykes and sills: exploration and deposit characterization of the Snap Lake dyke, Canada. Lithos, 76, 359– 367.

Hansen, D.M., Cartwright, J.A. and Thomas, D. (2004). 3D Seismic Analysis of the Geometry of Igneous Sills and Sill Junction Relationships. Geological society, London, Memoirs, 29, 199-209.

Hirano, M., Shinjo, K., Kaneko, R. and Murata, Y. (1991). Anisotropy of frictional forces in muscovite mica. Physical Review Letters, 67, 2642– 2645.

Hirono, T., Asayama, S., Kaneki, S. and Ito, A. (2016). Preservation of amorphous ultrafine material: A proposed proxy for slip during recent earthquakes on active faults. Scientific Reports, 6, 36536.

Herron, A.D. (2011). First step in seismic interpretation. Geophysical monograph series number 16. Tulsa, Oklahoma. Society of Exploration Geophysicists. The international society of applied geophysics.

Hrouda, F., Faryad, S.W., Kubínová, S., Verner, K. and Chlupáˇcová, M. (2019). Simultaneous free flow and forcefully driven movement of magma in lamprophyre dykes as indicated by magnetic anisotropy: case study from the Central Bohemian dyke swarm, Czech Republic. Geosciences, 9, 104.

Hughes, H.S.R., Kinnaird, J.A., Mcdonald, I., Kramers, J.D. and Nex, P.A.M. (In preparation). A major swarm of orangeite dykes exposed in platinum mines across the Western Bushveld Complex, South Africa.

Imanishi, K., Ogasawara, H., Yabe, Y., Horiuchi, S., Okubo, M. and Murakami, O. (2017). Source parameters of the 2014 M5.5 Orkney earthquake sequence, South Africa, estimated by using

near-field underground seismic arrays in gold mines. IAG-IASPEI 2017. S02. Anthropogenic seismicity. 31 July 31, 2017.

International Institute of Earthquake Engineering and Seismology (IIEES). (2004). Sumatra, Indonesia Earthquake of 26 December 2004, Mw=9.1. http://www.iiees.ac.ir/en/sumatra-indonesia-earthquake-of-26-december-2004-mw9-1/. (Accessed: 05 February 2018).

Jeffery, D.C. (1975). Structural discontinuity in the Witwatersrand Group on the ERPM Mine: their geology, geochemistry and rock mechanics behaviour. Unpublished MSc thesis, University of the Witwatersrand, Johannesburg, South Africa, pp.184.

Joughin, N.C. (1966).The Measurement and Analysis of Earth Motion Resulting from Underground Rock Failure. Ph.D. Thesis, University of the Witwatersrand.

Kaneki, S., Yokoyama, Y., Hirono, T., Yabe, Y. and Ogasawara, H. (2018). Mineralogical characteristics of fault rocks recovered from aftershock zone of the M5.5 Orkney earthquake in South Africa (ICDP DSeis project). Seismological Society of Japan Fall Meeting, Abstracts.

Keulen, N., Heilbronner, R., Stunitz, H., Boullier, A.M. and Ito. H. (2007). Grain size distributions of fault rocks: A comparison between experimentally and naturally deformed granitoids. Journal of Structural Geology, 29, 1282-1300.

Kikuchi, M., Nakamura, M. and Yoshikawa, K. (2003). Source rupture processes of the 1944 Tonankai earthquake and the 1945 Mikawa earthquake derived from low-gain seismograms. Earth Planets Space, 55, 159–172.

Lindesay, J.P. (1989). The Fresnel zone and its interpretive significance. The Leading Edge of Exploration, 8, 33–39.

Malehmir, A., Koivisto, E., Manzi, M.S.D., Cheraghi, S., Durrheim, R.J., Bellefleur, G., Wijns, C., Hein, K.A.A. and King, N. (2013). A review of reflection seismic investigations in three major metallogenic regions: The Kevitsa Ni–Cu–PGE district (Finland), Witwatersrand goldfields (South Africa), and the Bathurst Mining Camp (Canada). Ore Geology Reviews, 56, 423-441.

Malthe-Sørenssen, A., Planke, S., Svensen, H. and Jamtveit, B. (2004). Formation of saucershaped sills. In: C. Breitkreuz and N. Petford (Eds.). Physical Geology of High-Level Magmatic Systems. Geological Society, London, Special Publication, London, 234, 215-227.

Manzi, M.S.D., Gibson, M.A.S., Hein, K.A.A., King, N. and Durrheim, R.J. (2012a). Application of 3D seismic techniques to evaluate ore resources in the West Wits line Goldfield and portions of the West Rand Goldfield, South Africa. Geophysics, 77, WC163-WC171.

Manzi, M.S.D., Durrheim, R.J., Hein, A.A. and King, N. (2012b). 3D edge detection seismic attributes used to map potential conduits for water and methane in deep gold mines in the Witwatersrand Basin, South Africa. Geophysics, 77, WC133-WC147

Manzunzu, B., Midzi, V., Mulabisana, T.F., Zulu, B., Pule, T., Myendeki, S. and Rathod. G.W. (2018). Seismotectonics of South Africa. Journal of African Earth Sciences, 149, 271-279.

Marfurt, K.J. (2006). Robust estimates of 3D reflector dip. Geophysics, 71, 29-40.

McCarthy, T.S. (2006). The Witwatersrand Supergroup. In: The Geology of South Africa, MR Johnson, CR Anhaeusser, RJ Thomas, editor. Pretoria: Council for Geosciences, pp. 155–186.

McCarthy, T.S. and Rubidge, B. (2005). The Story of Earth and Life. Cape Town: Struik Publishers.

Midzi, V., Pule, T., Manzunzu, B., Mulabisana, T., Zulu, B.S. and Myendeki, S. (2020). Improved earthquake location in the gold mining regions of South Africa using new velocity models. South African Journal of Geology, 123, 35–58.

Mitchell, R.H. (1994). The lamprophyre facies. Mineralogy and Petrology, 51, 137–146.

Mizoguchi, K., Hirose, T., Shimamot, T. and Fukuyama, E. (2007). Reconstruction of seismic faulting by high-velocity friction experiments: An example of the 1995 Kobe earthquake. Geophysical Research Letters, 34, L01308. doi: 10.1029/2006gl027931.

Moore, D.E., Lockner, D.A., Tanaka, H. and Iwata, K. (2004). The coefficient of friction of chrysotile gouge at seismogenic depths. International Geology Review, 46, 385–398.

Moore, D.E. and Lockner, D.A. (2008). Talc friction in the temperature range 25°–400°C: Relevance for fault-zone weakening. Tectonophysics, 449, 120–132.

Myers, R.E., McCarthy, T.S. and Stanistreet, I.G. (1989). A tectono-sedimentary reconstruction of the development of the Witwatersrand Basin, with particular emphasis on the Central Rand Group. Economic Geology Research Unit, 216, 497–540.

Nkosi, Z.N. (2016). Seismological and mineralogical studies of the world's deepest gold-bearing horizon, the Carbon Leader Reef, West Wits Line goldfields (South Africa): Implications for its poor seismic reflective character. MSc Thesis. University of the Witwatersrand, Johannesburg.

Ogasawara, H., Nakatani, M., Durrheim, R.J., Naoi, M., Yabe, Y., Moriya, H., Hofmann, G.F., Stander, C., Roberts, D.P., de Bruin, P., Oelofse, J., Kato, H., Cichowicz, A., Birch, D., Ngobeni, D., Milev, A., Kgarume, T., Satoh, T., Horiuchi, S., Kawakata, H., Murakami, O., Yoshimitsu, N., Ward, A.K., Wienand, J., Lenegan, P., Yilmaz, H., Mngadi, S.B., Piper, P.S, Clements, T.N, Nakao, S., Okubo, M., Ishii, H., Visser, A.V. (2014). Observational studies of the rock mass response to mining in highly stressed gold mines in South Africa. In: Proceedings of the 7th International Congress on Deep and High Stress Mining. 16-18 September 2014. p. 123-137. Sudbury, Australia.

Ogasawara, H., Durrheim, R.J., Yabe, Y., Ito, T., van Aswegen, G., Grobbelaar, M., Funato, A., Ishida, A., Ogasawara, Jr. H., Mngadi, S.B., Manzi, M.S.D., Ziegler, M., Ward, A.K., Hofmann, G., Moyer, P., Boettcher, M., Dight, P., Ellsworth, W., Liebenberg, B., Wechsler, N., Onstott, T., Berset, N. and the DSeis Team. (2017). Drilling into Seismogenic Zones of M2.0 – M5.5 Earthquakes from Deep South African Gold Mines (DSeis): Establishment of Research Sites. In: Proceedings of the AfriRock International Symposium. 30 September 2017 – 6 October 2017, Cape Town, South Africa.

Ogasawara, Jr. H., Manzi, M.S.D., Durrheim, R.J. and Ogasawara, Snr. H. (2017). Calibration of the seismic velocity structure and understanding of the fault formation in the environs of the Orkney M5.5 earthquake, South Africa. In: Proceedings of the AGU Fall Meeting, 11 -15 December 2017, Abstracts S51A-0570, New Orleans, Louisiana.

Ogasawara, Jr., H., Manzi, M.S.D., Durrheim, R.J., Ogasawara, Snr. H., and SATREPS. (2018). A capable geological structure of the Orkney M5.5 earthquake of 5 August 2014 by re-processing seismic reflection data. In: Proceedings of the European Geosciences Union (EGU) General Assembly, 8–13 April 2019, Vienna, Austria.

Ogasawara, H, Liebenberg B, Yabe Y, Durrheim R, Ziegler M, Manzi MSD, Mngadi S, Onstott, T, Kaneki S, Yokoyama Y, the ICDP DSeis team. An overview of the completed ICDP project, Drilling into Seismogenic zones of M2.0-5.5 earthquakes in South African gold mines (DSeis). In: Proceedings of the EGU General Assembly. 7–12 April 2019; Abstracts 21: EGU2019-6503-1. Vienna, Austria.

Ogasawara, Snr. H. (2020). Personal Communication.

Ogasawara, Snr. H., Noda, T., Manzi, M.S.D., Durrheim, R.J., Yabe, Y., Hirono, T., Yamamoto, Y., Matsuzaki, T., Higashi, M., Yoshida, S., Yokoyama, Y., Suzuki, K., Ligaraba, D., Masondo, N., Nkosi, Z., Mngadi, S.B., Liebenberg, B., van Heerden Esterhuizen. (2020). ICDP DSeis: an altered lamprophyre dike identified at the M5.5 seismogenic zone by the analyses of the 3D reflection data and drilled core at Kochi Core Center. JpGU-AGU Joint Meeting. [SSS15-01]. Makuhari, Japan.

Pawlak, Z., Pai, R., Bayraktar, E., Kaldonski, T. and Oloyede, A. (2008). Lamellar lubrication in vivo and vitro: friction testing of hexagonal boron nitride. Biosystems, 94, 202–208.

Pretorius, C.C., Muller, M.R., Larroque, M., and Wilkins, C. (2003). A Review of 16 years of Hardrock Seismics on the Kaapvaal Craton. (In: D.W. Eaton, B. Milkereit, M.H. Salisbury, eds.). Hardrock seismic exploration, Geophysical Developments No.10, Society of Exploration Geophysicists.

Prevec, S.A., Anhaeusser, C.R., Poujol, M. (2004). Evidence for Archaean lamprophyre from the Kaapvaal Craton, South Africa. South African Journal of Science, 100, 549–555.

Reches, Z. and Ito, H. (2007). Scientific Drilling of Active Faults: Past and Future. In: Harms U., Koeberl C., Zoback M.D. (eds) Continental Scientific Drilling. Springer, Berlin, Heidelberg. pp. 235-258. https://doi.org/10.1007/978-3-540-68778-8_6

Reddy, P.R. (2012). Historical development of seismic imaging technique – An Overview. The Journal of Indian Geophysical Union, 16, 71-86.

Rickenbacher, M. (2018). Geological and Geotechnical Rock Mass Model from two deep DSEIS boreholes drilled at Moab Khotsong, Swiss Federal Institute of Technology Zurich, MSc Thesis.

Rock, N.M.S. (1987). The nature and origin of lamprophyres: an overview. Geological Society, London, Special Publications, 30, 191–226.

Rock, N.M.S. (1977). The nature and origin of lamprophyres: some definitions, distinctions, and derivations. Earth Science Reviews, 13, 123–169.

Robb, L.J. and Meyer, F.M. (1995). The Witwatersrand Basin, South Africa: Geological framework and mineralization processes. Ore Geology Reviews, 10, 67-94.

Roberts, A. (2001). Curvature attributes and their application to 3-D interpreted horizons: First Break, 19, 85-100.

Rutherford, S.R. and Williams, R.H. (1989). Amplitude-versus-offset variations in gas sands, Geophysics, 54, 680–688.

SACS (South African Committee for Stratigraphy). (1980). Stratigraphy of South Africa. Part 1 (Comp L.E. Kent). Lithostratigraphy of the Republic of South Africa, South West Africa/Namibia and the Republics of Bophuthatswana, Transkei and Venda. Pretoria: Geological Survey of South Africa.

SACS (South African Committee for Stratigraphy). (1990). South African Stratigraphy. (Kent, comp.). Lithostratigraphy of the Republic of South Africa, South West Africa/Namibia, and the Republics of Bophuthatswana, Transkei and Venda. Handbook, Geology of South Africa, p. 690.

Sammis, C., Osborne, R., Anderson, J., Banerdt, M. and White, P. (1987). Self-similar cataclasis in the formation of fault gouge. Pure and Applied Geophysics, 124, 1-2, 53-78.

Simm, R. and Bacon, M. (2014). Seismic Amplitude. An Interpreters Handbook. Cambridge University Press, New York.

Scheiber-Enslin, S., Ebbing, J. and Webb, S. (2014). Geophysically plumbing the main Karoo Basin, South Africa. South African Journal of Geology, 117, 275-300.

Sherrif, R.E. (2002). Encyclopedic Dictionary of Applied Geophysics (4th ed.): Society of Exploration Geophysicists, Geophysical Reference series No. 13.

Spectris plc. (2005). Malvern Instruments: Instruction manual. Enigma Business Park (www.malvern.co.uk).

Tamura, H., Tsujimichi, K., Yamano, H., Shiota, K., Kubo, M., Fahmi, A. and Miyamoto, A. (1997). Molecular dynamics simulation of the friction between talc (001) surfaces. Applied Surface Science, 119, 335–340.

Taner, M.T., Koehler, F. and Sheriff, R. (1979). Complex seismic trace analysis. Geophysics, 44, 1041–1063.

Tanioka, Y. and Satake, K. (2001). Detailed coseismic slip distribution of the 1944 Tonankai earthquake estimated from tsunami waveforms. Geophysical Research Letters, 28, 1075– 1078.

Tsuru, T., Miura, S., Park, J.O., Ito, A., Fujie, G., Kaneda, Y., No, T., Katayama, T. and Kasahara J. (2005). Variation of physical properties beneath a fault observed by a two-ship seismic survey off southwest Japan. Journal of Geophysical Research, 110, doi: 10.1029/2004JB003036.

van der Heever, P. (1982). The Influence of Geological Structures on Seismicity and Rockburst in the Klerksdorp goldfields. MSc (Geology). University of Johannesburg. Retrieved from: https://ujdigispace.uj.ac.za/ (Access date: 19 July 2020).

van Zijl, J.S.V. (2006). Physical characteristics of the Karoo sediments and mode of emplacement of the dolerites. South African Journal of Geology, 109, 329-334.

Vermaakt, D.T. and Chunnet, I.E. (1994). Tectono-sedimentary processes which controlled the deposition of the Ventersdorp Contact Reef within the West Wits Line. In: Anhaeusser, C.R. (Eds.). Proceedings of the 15th Congress of the Council for Mining and Metallurgical Institutions, 3, 117–130.

Yabe, Y., Abe, S., Ito, T., Ishida, A., Sugimura, K., Kanematsu, M., Higashi, M., Tadokoro, R., Ogasawara, H., Funato, A., Kato, H., Watson, B., Mngadi, S.B., Durrheim, R.J., Hofmann, G. and Scheepers, L. (2019). In-situ stress around source faults of seismic events in and beneath South African deep gold mines', in W Joughin (ed.), Proceedings of the Ninth International Conference on Deep and High Stress Mining. The Southern African Institute of Mining and Metallurgy, Johannesburg, 399-411.

Watts, M. (2005). Mark Watts Project. Anglo Gold Ashanti, pp. 104.

Webpage. https://doi.org/10.2204/iodp.sd.11.02.2011. (2011). This page contains the latest international trade data for South Africa, including service trade data, and tariffs. [Accessed: 31/10/2020] (e-mail: support@oec.world).

Wechsler, N., Allen, E., Rockwell, T.K., Girty, G., Chester, J.S. and Ben-Zion, Y. (2011). Characterization of pulverized granitoids in a shallow core along the San Andreas Fault, Littlerock, CA. Geophysical Journal International, 186, 401-417.

Wiersberg, T., Zimmer, M., Kujawa, C., Liebenberg, B., Ogasawara, H., Onstott, T.C., Cason, E., Vermeulen, Jan-G. and van Heerden, E. (2019). Investigations on fault zone gases in South African gold mines. Abstract EGU2019-5670. 7-12 April 2019, Vienna, Austria.

Wilson, B., Dewers, T., Reches, Z. and Brune, J.N. (2005). Particle size and energetics of gouge from earthquake rupture zones. Nature, 434, 749– 752.

Wilson, N.L., Toens, P.D. and Van der Schyff, D.B., (1964). The geology of the Vaal Reef Basin in the Klerksdorp area. In: Haughton, S.H. (Ed.), The Geology of Some Ore Deposits in Southern Africa. Geological Society of South Africa, Johannesburg, 399–416.

Ziegler, M., Rickenbacher, M., Berset, N., Liebenberg, B., Ishida, A., Sugimura, K., Noda, T., Ogasawara, H., Mngadi, S., Durrheim, R., Ito, T., Funato, A. and the ICDP DSeis team. (2018). Core and borehole logging and stress measurements of a 817 m long borehole drilled from 2.9

km depth toward the Moab Khotsong 2014 M5.5 aftershock zone (ICDP DSeis project in South Africa). Abstract EGU2018-10377. 9-13 April 2018, Vienna, Austria.

Zoback, M., Hickman, S., Ellsworth, W., and the SAFOD Science Team. (2011). Scientific Drilling Into the San Andreas Fault Zone – An Overview of SAFOD's First Five Years. Scientific Drilling, 11, 14–28.

List of Figures

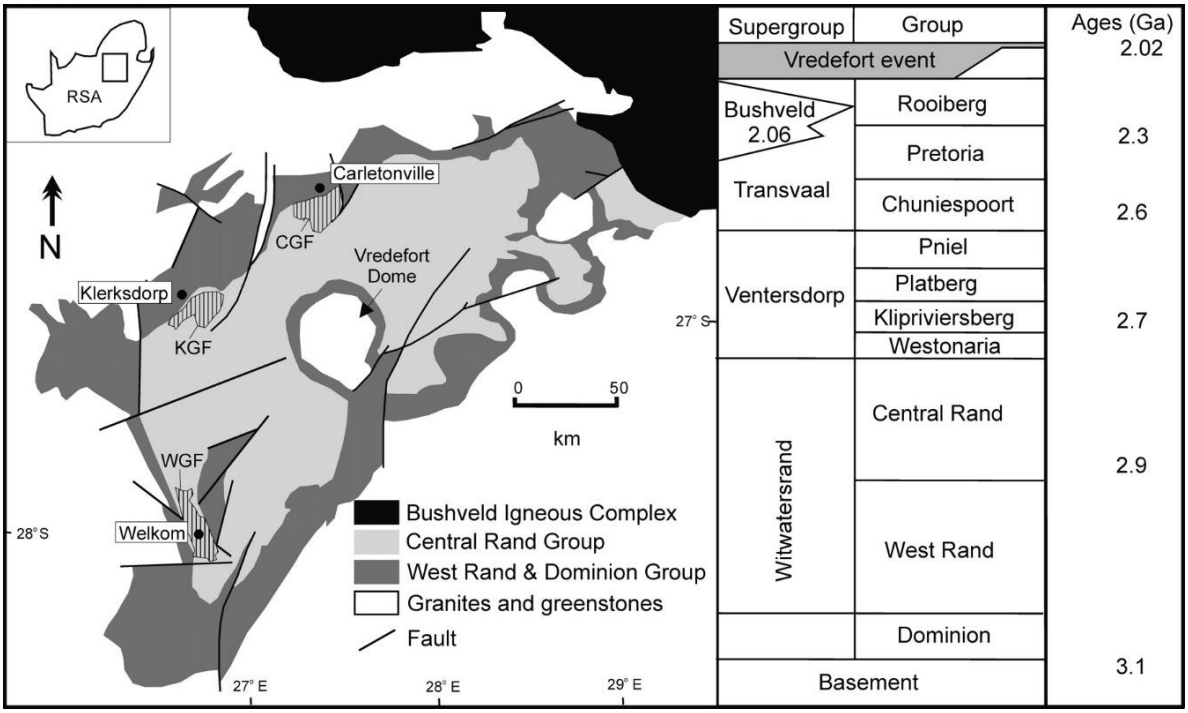


Figure 1: The Witwatersrand Basin showing all the goldfields including our study area – Klerksdorp goldfields, Moab Khotsong mine. In addition, the Stratigraphy and geology of the Witwatersrand Basin (modified after Frimmel, 1997; Dankert and Hein, 2010).

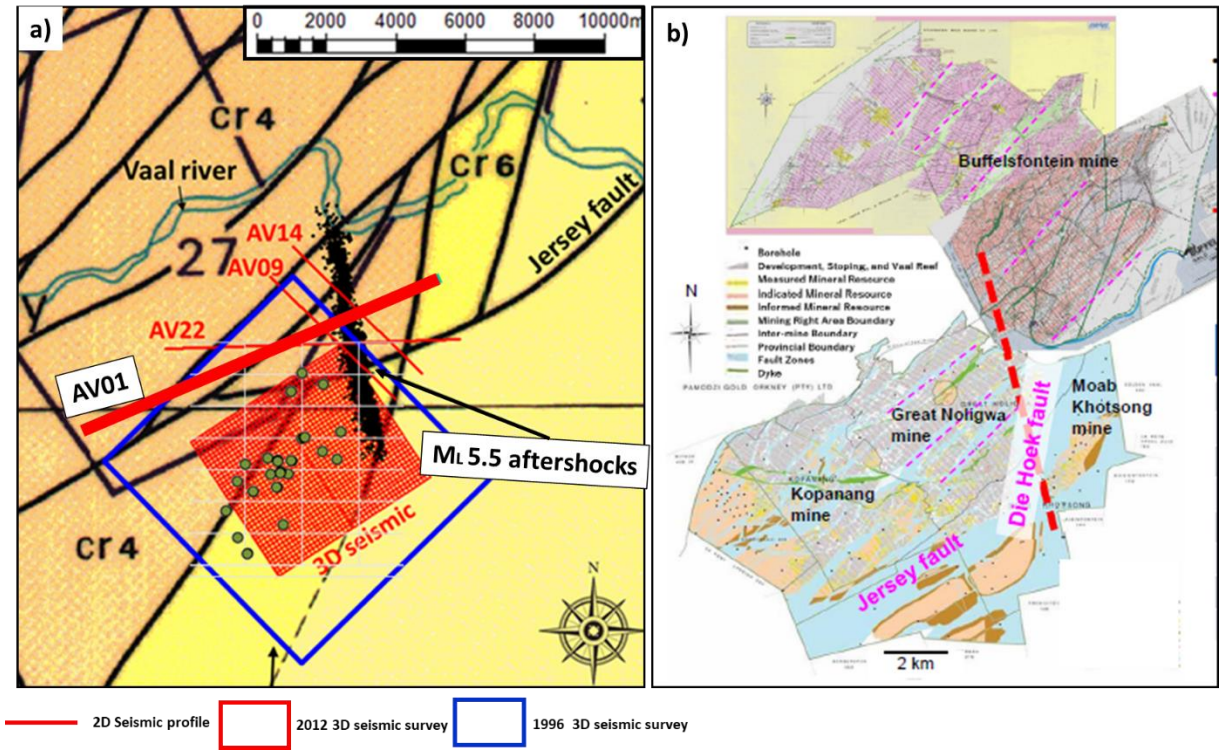


Figure 2: Selected 2-D seismic reflection profile (AV01) in relation to geology, aftershocks, structures, boreholes, 1996 3-D survey (blue) and 2012 3-D survey (red) (Modified from Ogasawara Jr. et al., 2018).

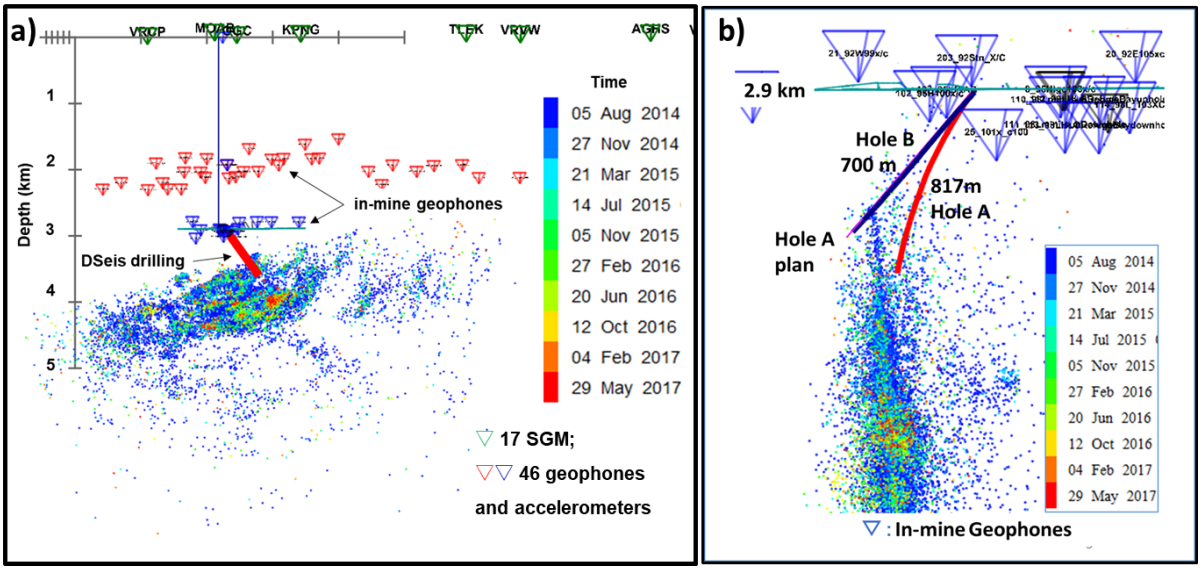


Figure 3: a) Location of aftershocks generated by M5.5 earthquake delineating the rupture plane. b) Location of Hole A and Hole B, where Hole B intercepted the rupture and intrusive rock potentially responsible for M_L 5.5 event (Ogasawara et al., 2019).

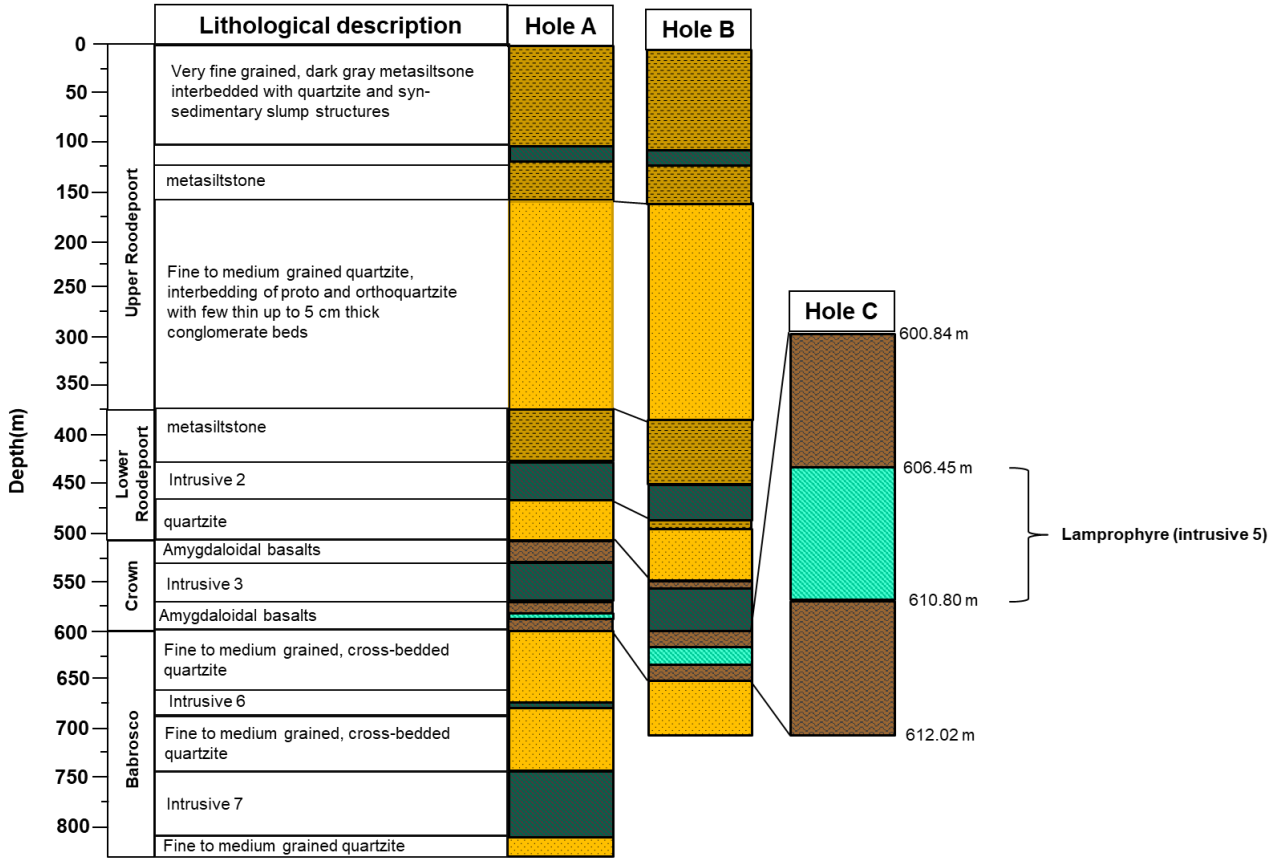


Figure 4: Ziegler et al. (2018) compiled core logging descriptions of recovered fragile core from the ICDP-DSeis drilling programme – Hole A, B and we added the branch Hole C (not shown to scale) which is the main focus of this study (modified from Rickenbacher, 2018).

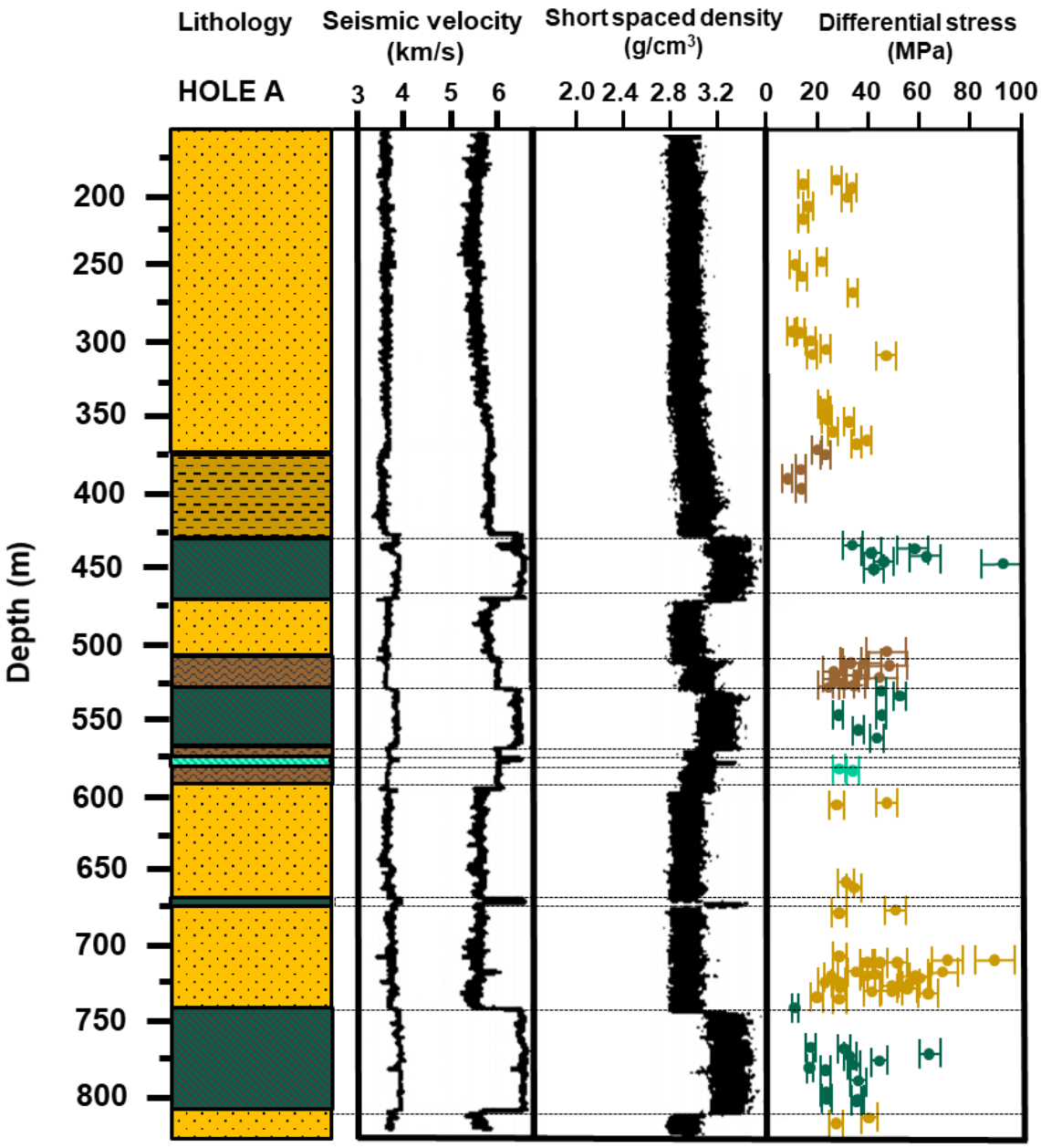


Figure 5: The lithological units described from core logging and geophysical borehole logging (Rickenbacher, 2018). Yabe et al. (2019) used Diametrical Core Deformation Analysis (DCDA) to measure in-situ rock differential stress.

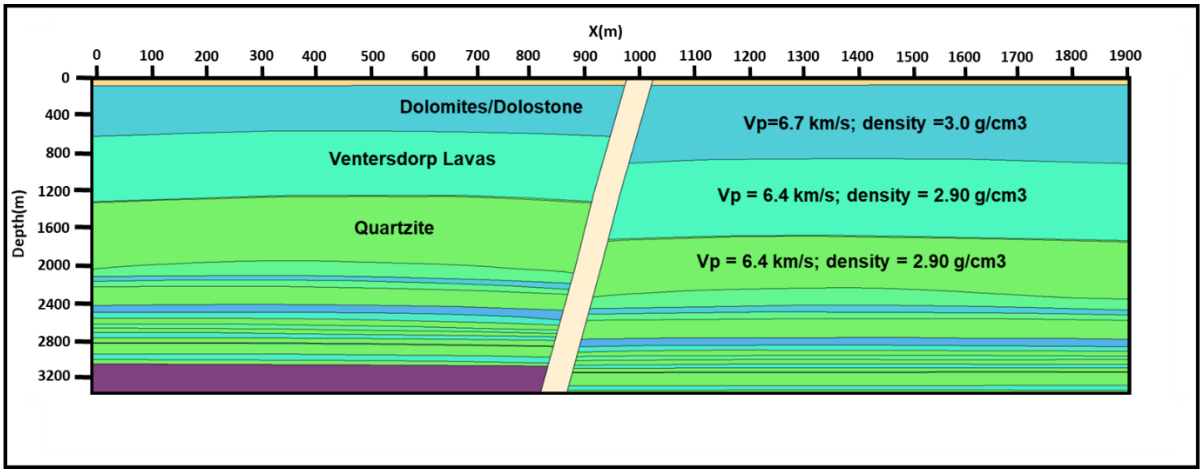


Figure 6: A geological model of the West Rand Group based on the Hole A (lithological units) recovered from ICDP-DSeis drilling programme.

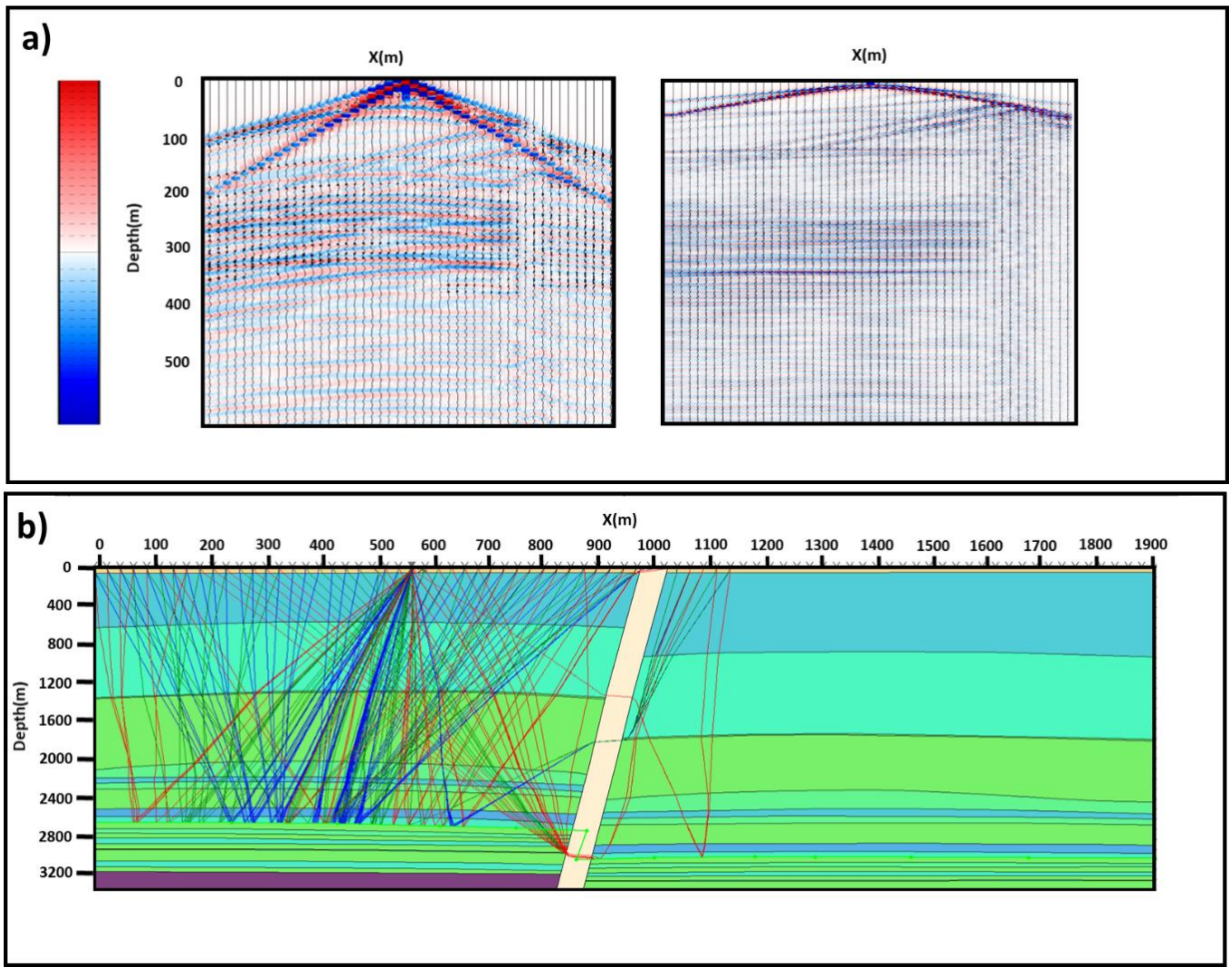


Figure 7: a) The illustration of the synthetic shot gathers; and (b) ray paths (red and blue) of seismic waves shown on the geological model. Please note that ray path colours have no specific meaning.

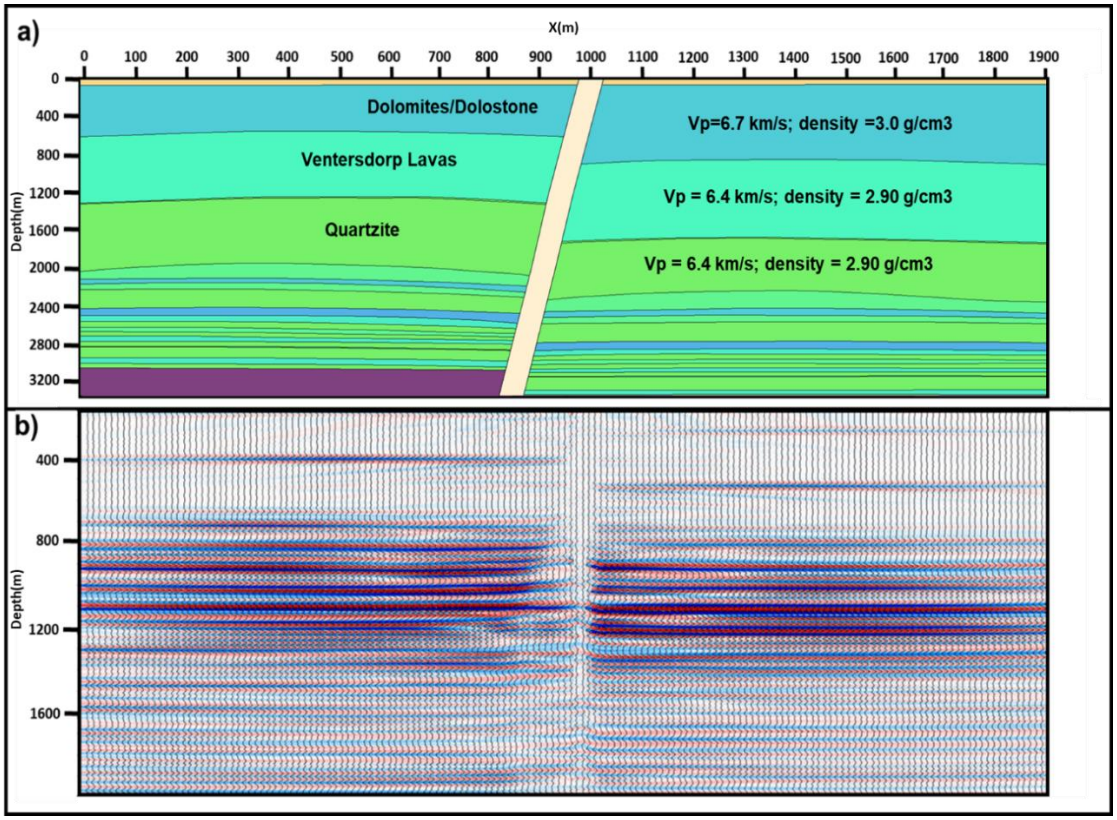


Figure 8: a) A geological model based on the Hole A. b) The corresponding pre-stack time migration 2-D seismic model showing the expected theoretical seismic response. The model has the contact between the dolomite and lava at ca. 600m, while the migrated section shows it at 400 m. Similarly for the Lava/Quartzite contact: ca. 1300 m on the model, but 700 m on the migrated section. The velocity model used for time-to-depth conversion of the migrated section might have caused the shift.

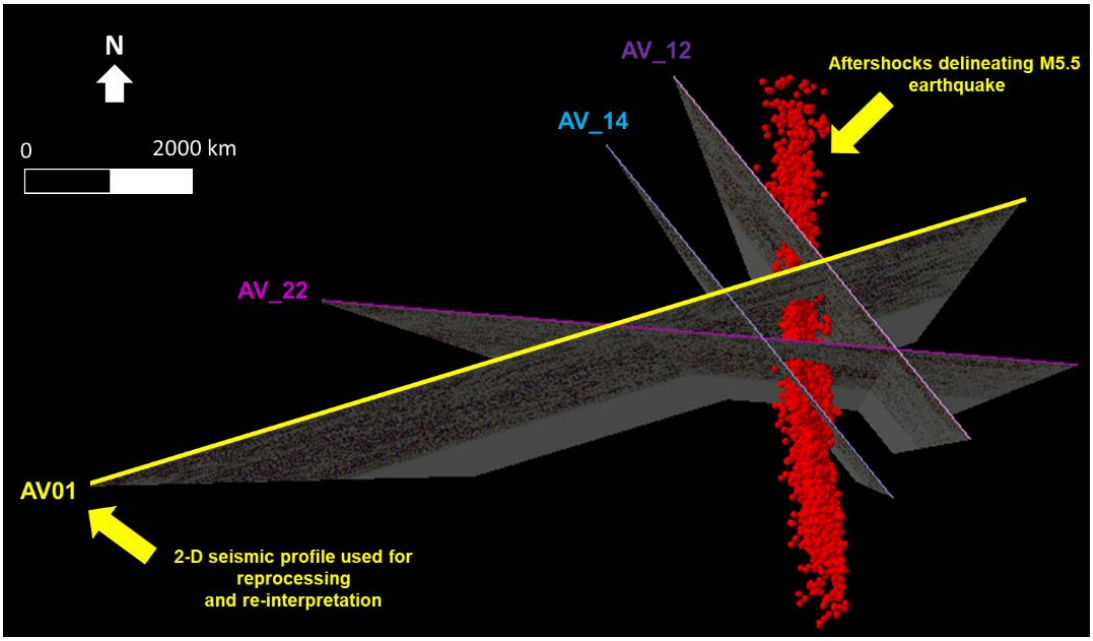


Figure 9: The selected legacy 2-D reflection seismic profile (AV01) to be re-processed and re-interpreted. This reflection seismic profile is almost perpendicular to the aftershock plane that delineates the M5.5 earthquake rupture (modified from Ogasawara Jr. et al., 2018).

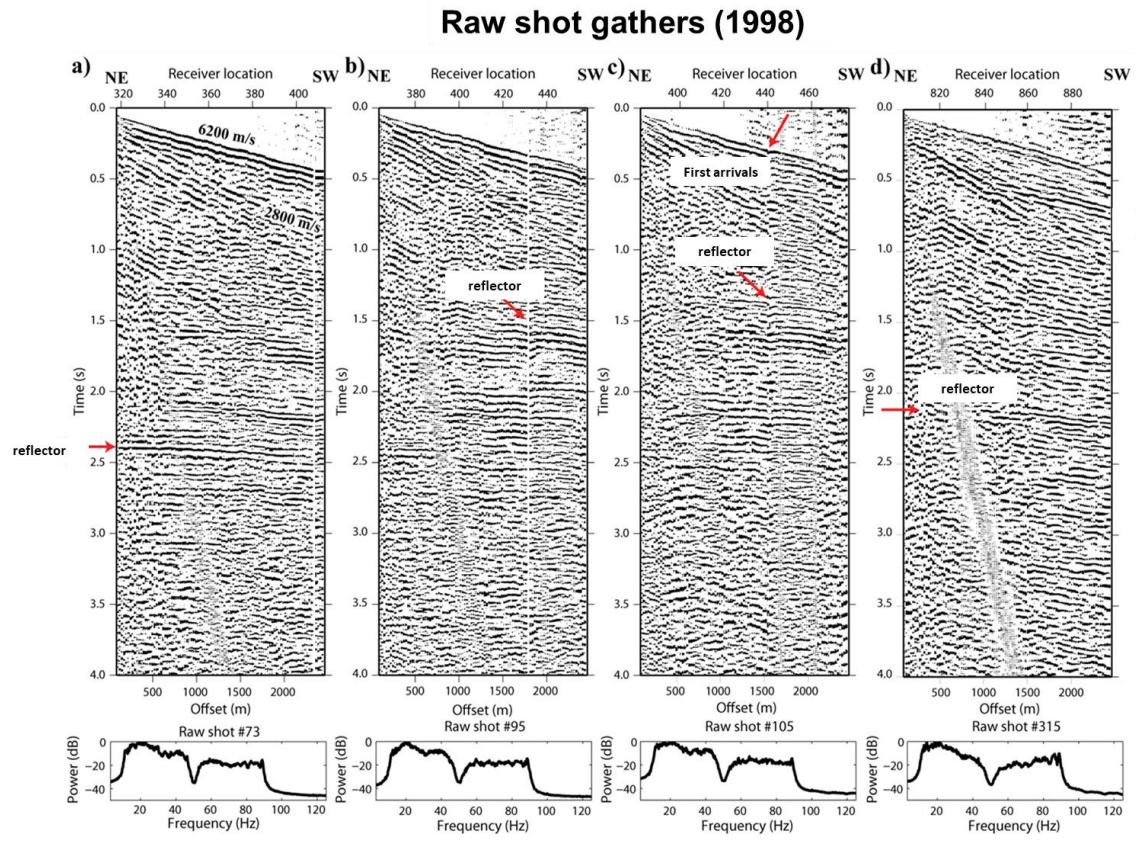


Figure 10: The raw shot gathers are shown before the re-processing of the reflection seismic data to make clear M5.5 earthquake rupture.

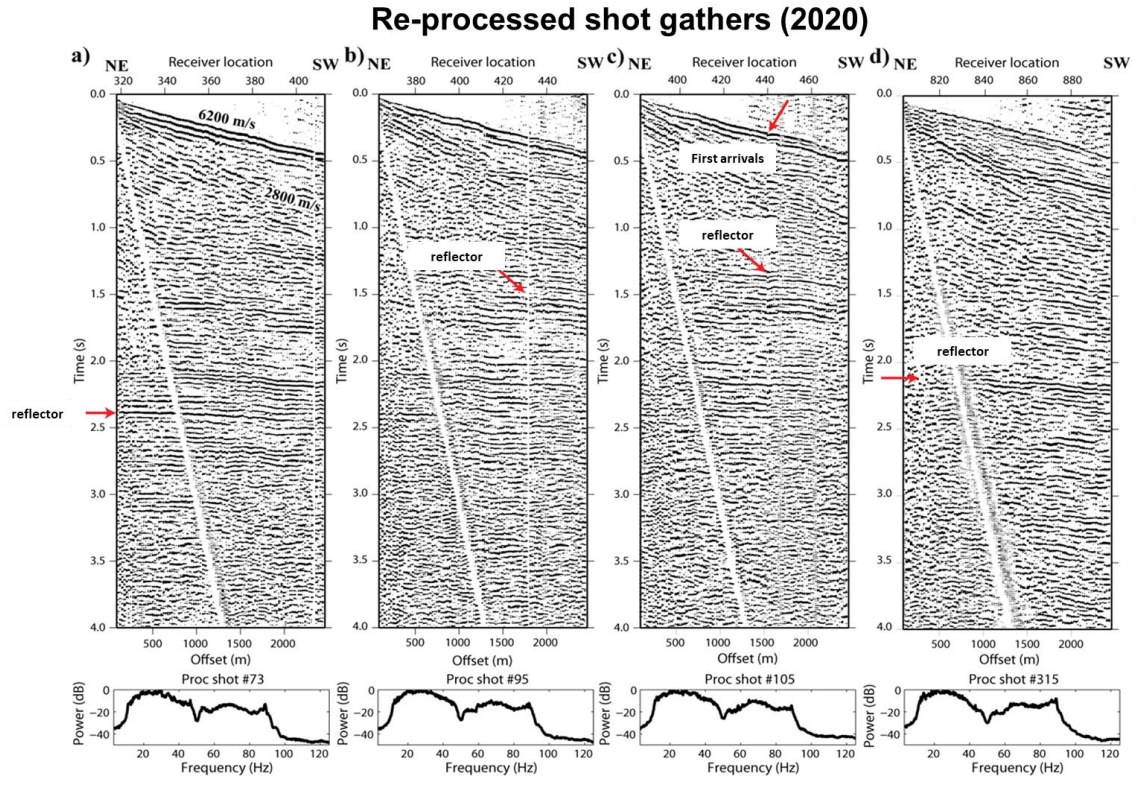


Figure 11: The re-processed shot gathers showing the effects of the bandpass filter, attenuation of airwaves and various other processing steps.

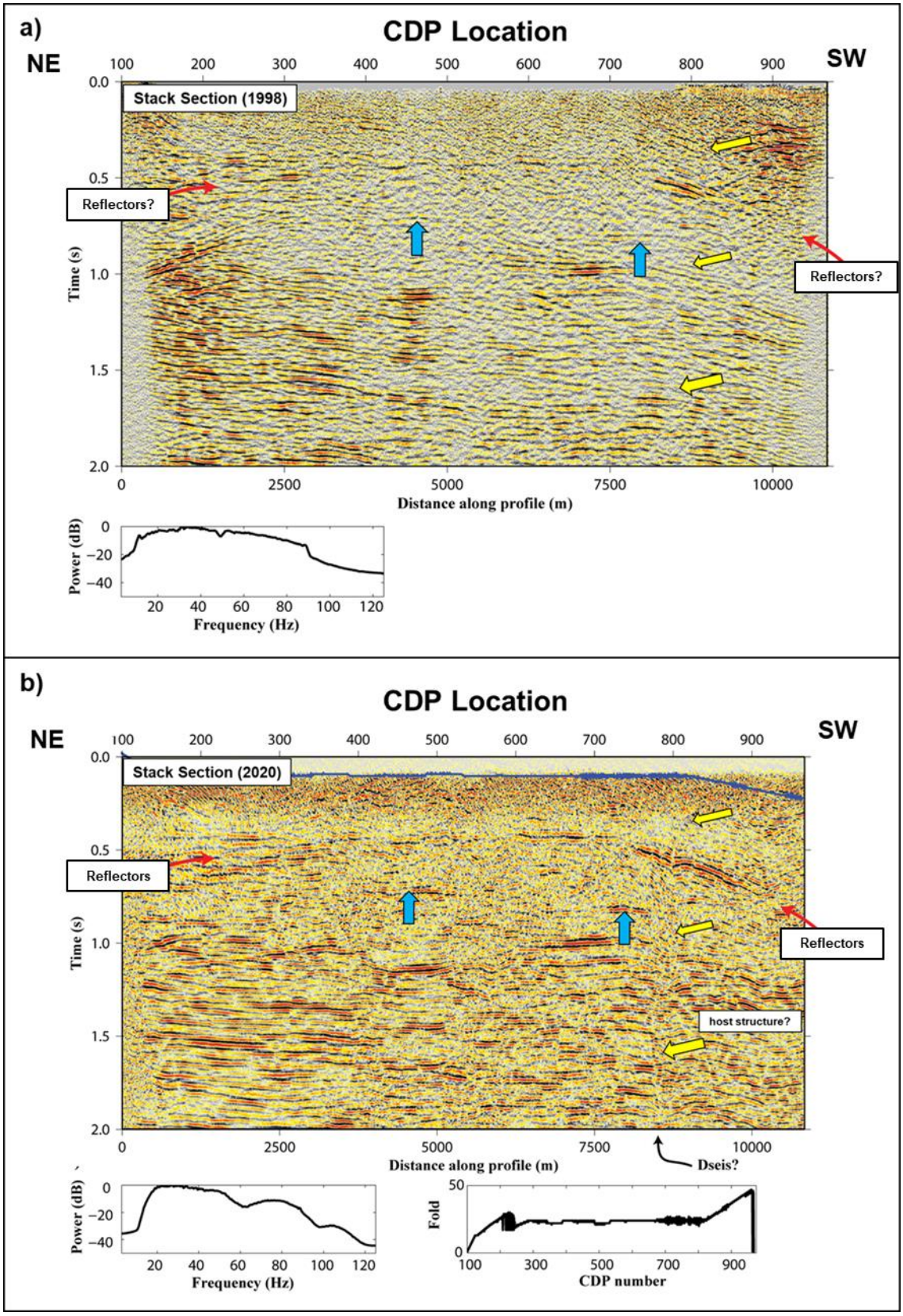


Figure 12: a) The legacy 2-D reflection seismic data (AV01) before re-processing. b) The re-processed 2-D legacy 2-D reflection seismic data showing the improved resolution of structures and reflectors.

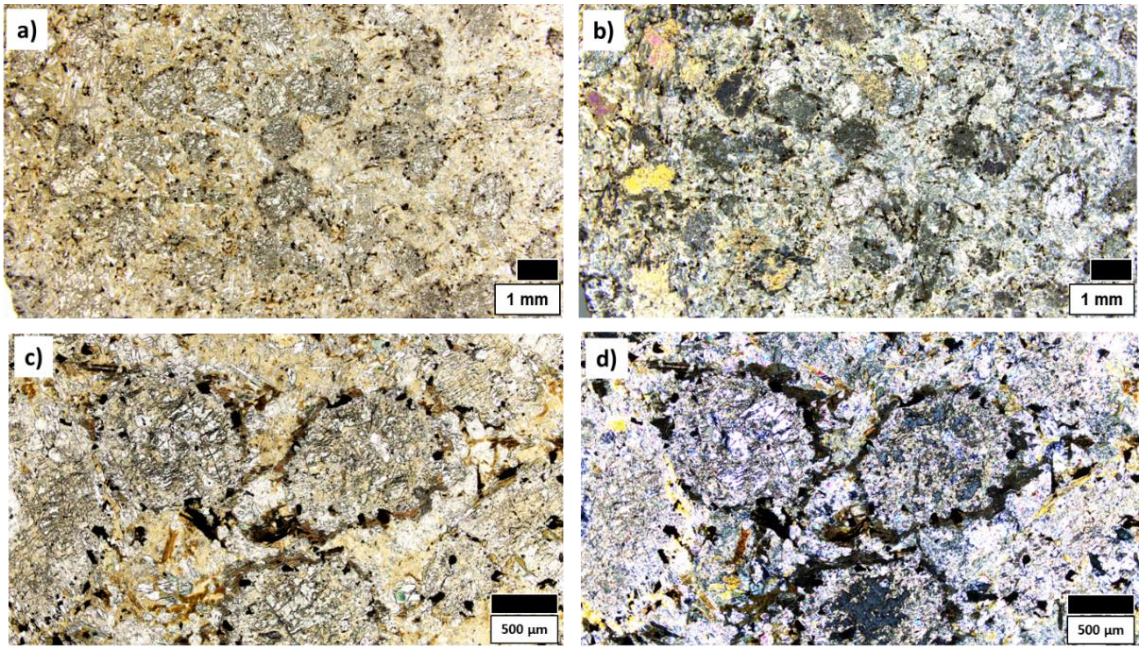


Figure 13: Thin section of the lamprophyre dykes are shown in PPL (a, c) and XPL (b, d). The lamprophyre dyke shows circular structures that are characterised by dark rims.

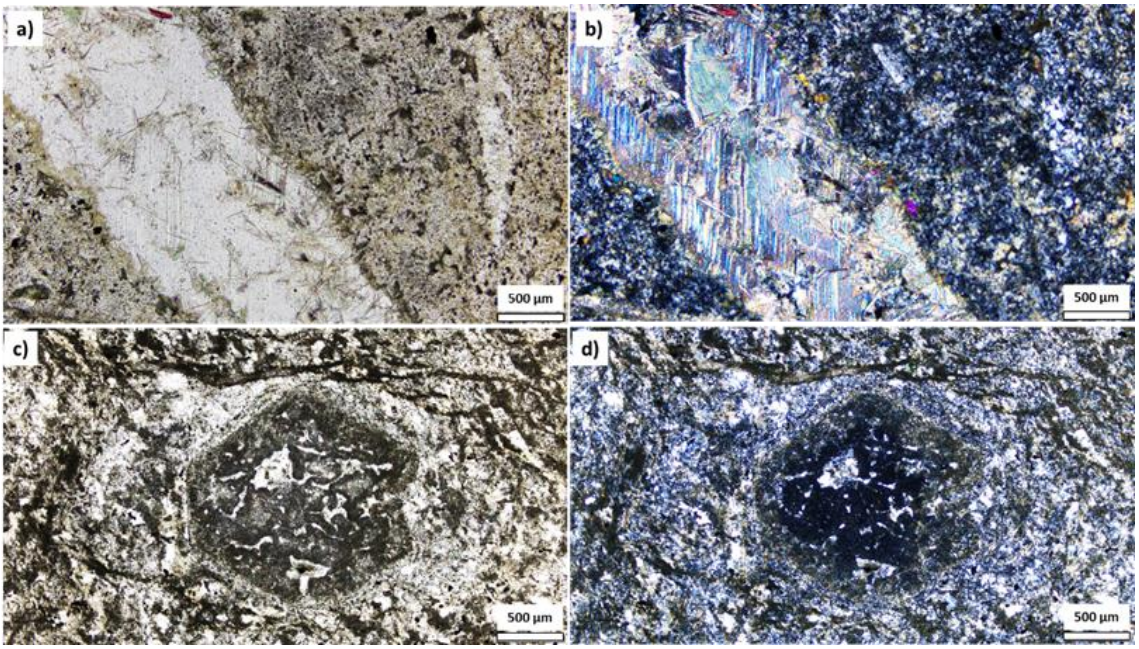


Figure 14: Thin section analysis of basalt rocks of the Crown Formation are shown in PPL (a, c) and XPL (b, d). The basalts show very fine grained matrix and consist of veins and amygdales filled with calcite and quartz.

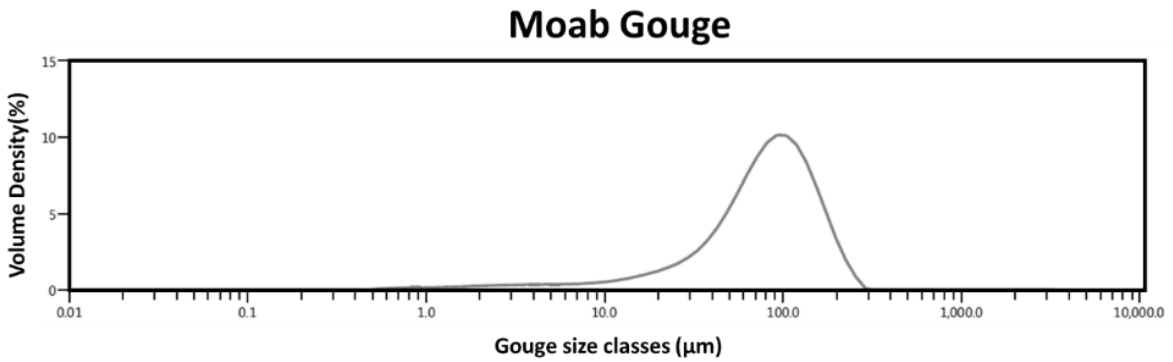


Figure 15: Particle size distribution of the Moab Khotsong mine gouge material recovered from the M5.5 earthquake rupture. We used the Malvern Mastersizer laser diffraction particle size analyser to examine the finer fraction of the gouge.

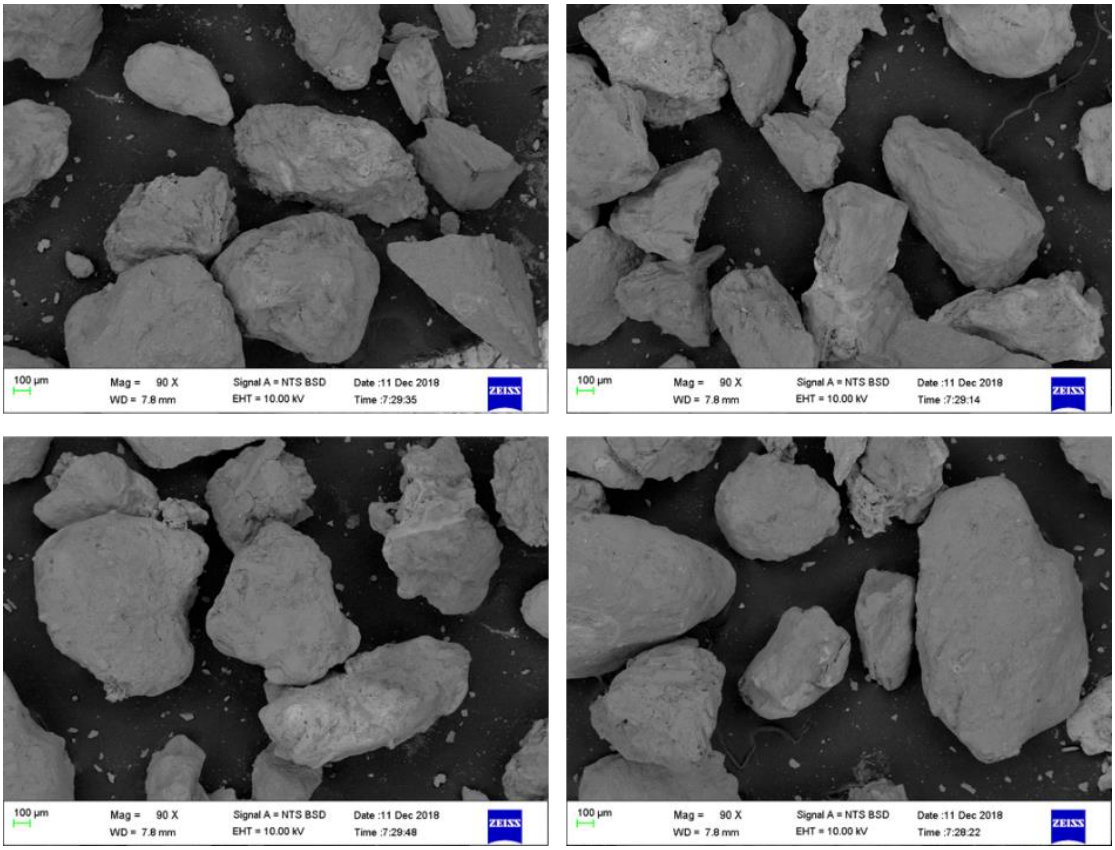


Figure 16: The scanning electron microscopy (SEM) images of gouge samples collected from the Moab Khotsong mine, no aggregated pattern is observed. SEM analysis showing particles greater than 200 µm.

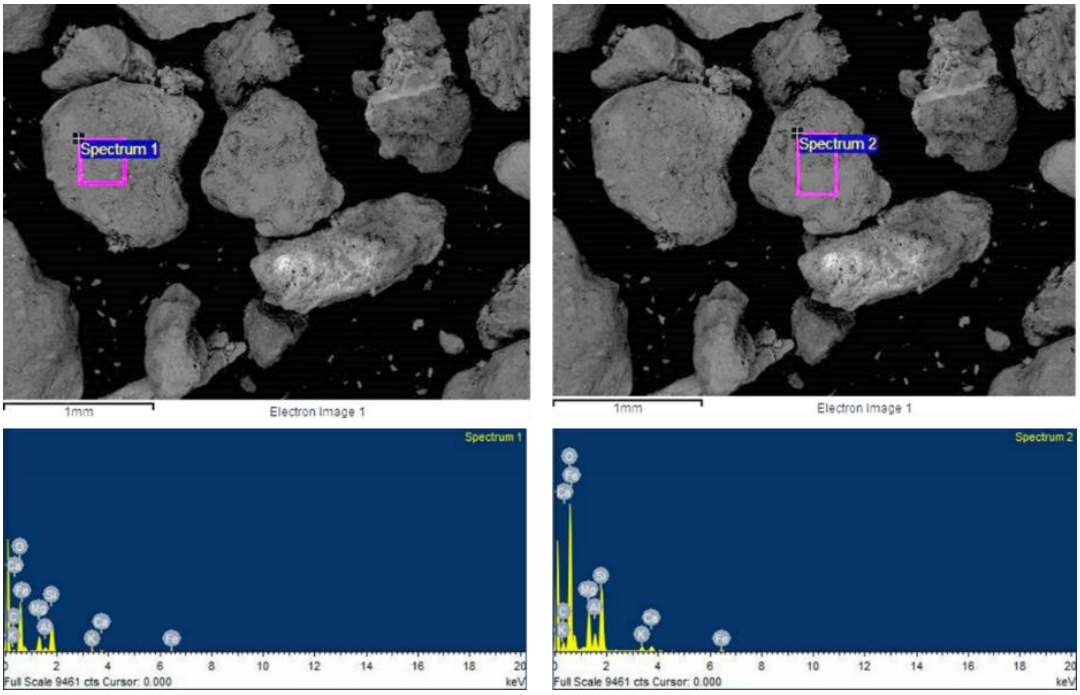


Figure 17: Chemistry of the gouge particles using the energy-dispersive x-ray spectroscopy (EDS).

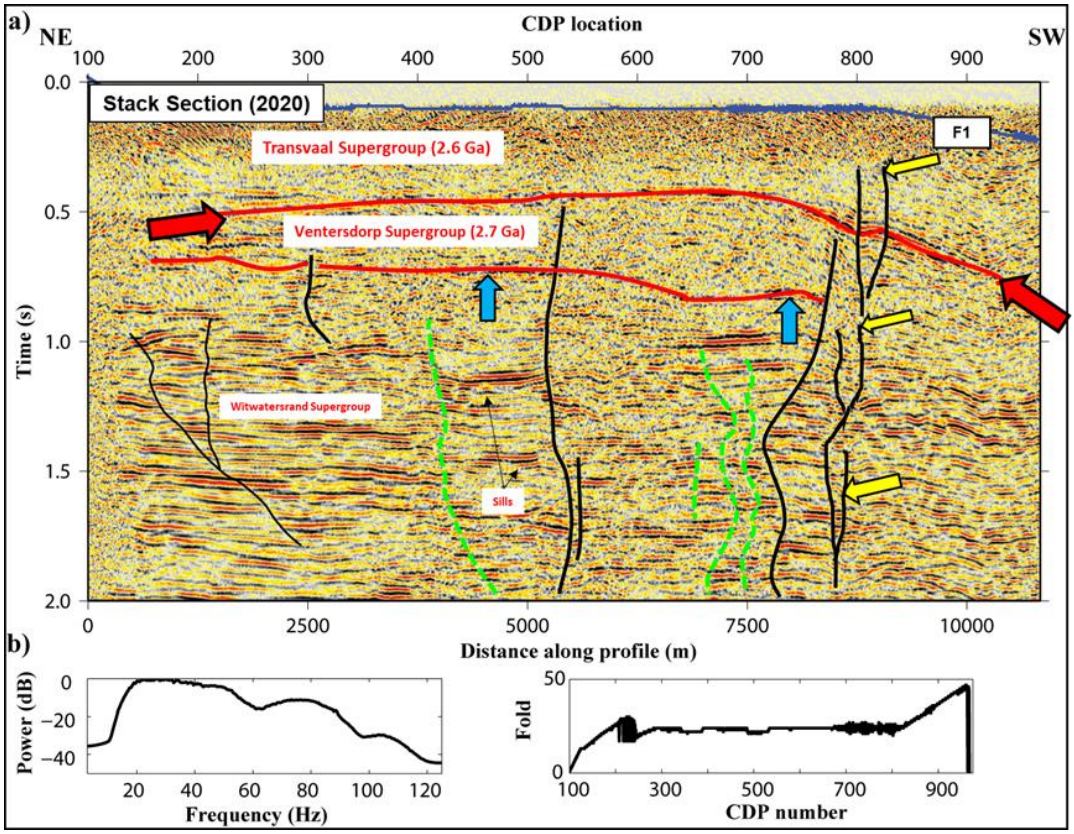


Figure 18: The re-processed legacy 2-D reflection seismic data (AV01) showing stratigraphic markers such as the Transvaal Supergroup, Ventersdorp Supergroup and Witwatersrand Supergroup. The structures are mapped clearly, and faults are shown in black while dykes are shown in green. The fault hosting the M_L 5.5 earthquake is indicated by F1.

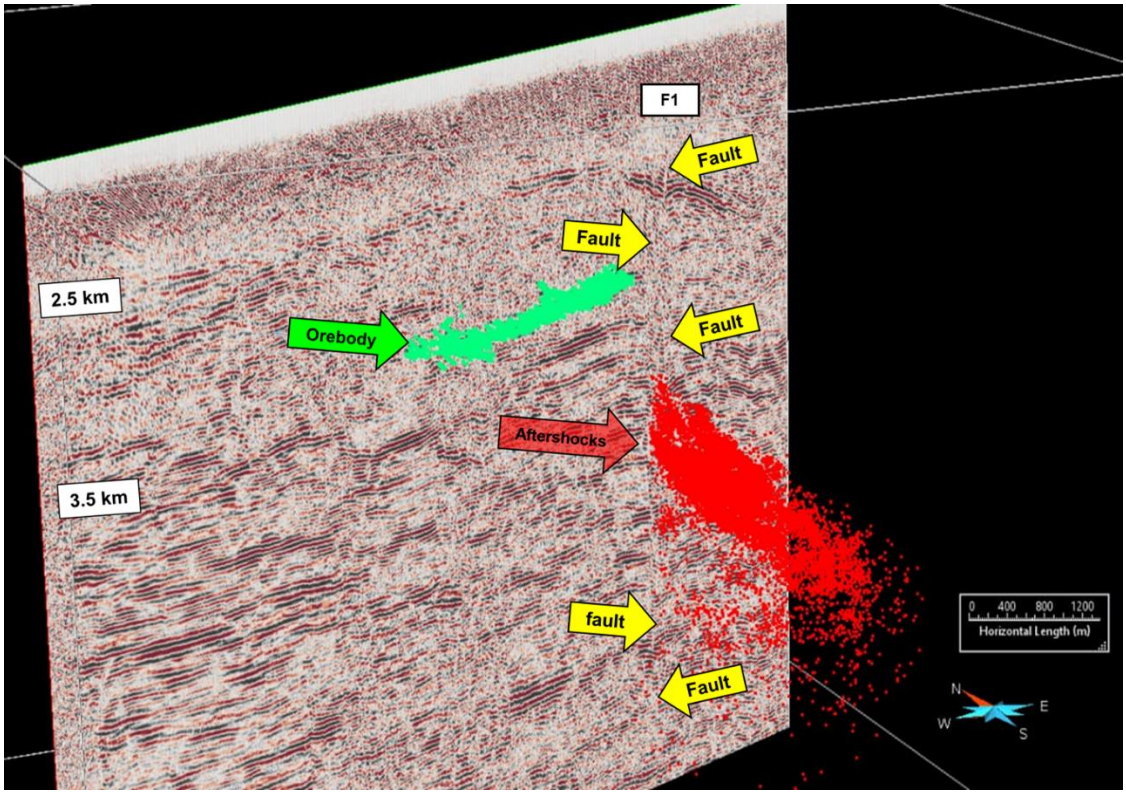


Figure 19: The seismic section extracted from the legacy 3-D reflection seismic data shows the mining stopes (green), fault structure (namely F1) that hosted the M5.5 earthquake and seismicity data (red) (aftershocks).

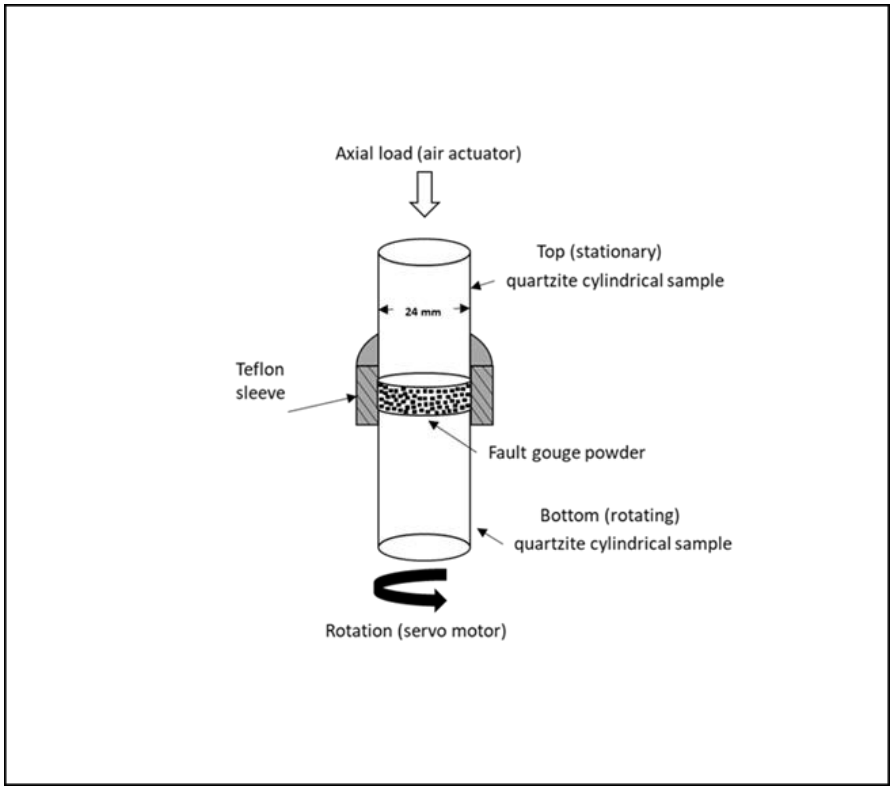


Figure 20: A graphic illustration of the sample assembly for high-velocity friction experiments conducted with an intervening gouge material recovered from M5.5 earthquake (Mngadi et al., 2020).

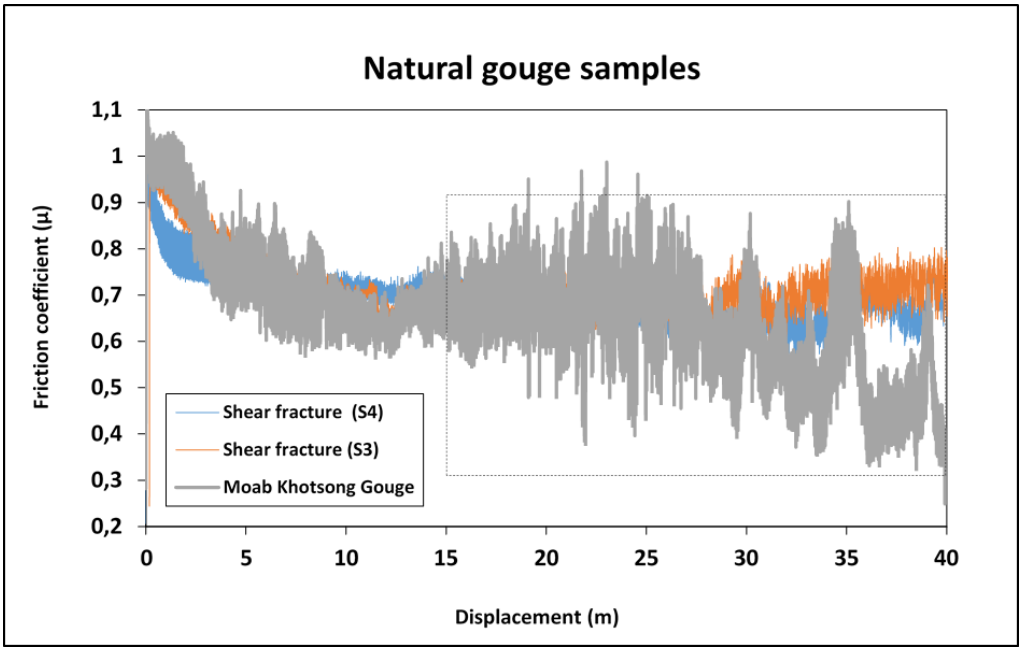


Figure 21: The friction weakening behaviour of the Moab Khotsong mine fault gouge, in comparison with the fault gouge samples recovered from the normal faults (Mw 2) occurring ahead of the stope at Cooke 4 mine, versus the strike-slip fault characterised by the lamprophyre dykes and dolerite sills.

List of Tables

Table 1: Parameters used for seismic reflection finite difference modelling shows lithology, physical properties (velocity and density) and the thickness of rock layers.

Lithology	Thickness (m)	Density (g/cm^3)	Vp (km/s)
metasiltstone	100	2.86	5.9
intrusive	40	3.06	6.7
metasiltstone	60	2.86	5.9
quartzite	200	2.71	5.5
metasiltstone	75	2.86	5.9
intrusive	50	3.06	6.5
quartzite	50	2.71	5.5
basalt	40	2.8	5.9
intrusive	50	2.99	6.5
basalt	40	2.8	5.9
quartzite	60	2.71	5.5
intrusive	5	3.06	6.5
quartzite	60	2.71	5.5
intrusive	50	2.99	6.5
quartzite	20	2.71	5.5

Table 2: The legacy 2-D reflection seismic data acquisition parameters of the line (AV01).

2-D Seismic Reflection Survey - Acquisition Parameters	
Type of survey	2-D seismic profile
Year	1992
Total survey length	11 km
Line direction	E-W
Spread	2975-25-X-25-2975 (m)
Nominal fold	50
Recording System	
Recording	SN 338
Sampling rate	4 ms
Recording length	6 s
Sweep length	16 s
Sweep	15 – 17 Hz
Source Information	
Source spacing	50 m
Energy source	4 vibrators (Pelton Mk Ⅱ) in a line. linear pattern
Receiver Information	
Receiver spacing	25 m
Receiver/trace	6
Geophone type	10 Hz (SM4U)GG

Table 3: Sampling of Hole C beginning at 596 m (distance from borehole collar of Hole B) to 612 m.

Core Sampling					
	Sample no.	**Depth (m)**	**Length (cm)**	**Box No.**	**Slot No.**
Basaltic	B(1.1)	596.3	2.0	7	2
Intrusive	I(1)	598.3	0.8	7	3
Basaltic	B(2.1)	600.8	2.0	7	5
Basaltic	B(2.2)	601.7	2.0	8	2
Intrusive	I(5.1)	606.4	2.0	9	6
Intrusive	I(5.2)	607.6	half piece	7	2
Intrusive	I(5.3)	608.2	2.0	10	2
Basaltic	B(3.1)	610.8	2.0	10	5
Basaltic	B(3.2)	611.4	2.0	11	2
Basaltic	B(3.3)	612.0	1.0	11	2

Table 4: XRF analysis of the intrusive rocks, basaltic lavas and lamprophyre dykes.

wt%	**SiO_2**	**Al_2O_3**	**Fe_2O_3**	**MnO**	**MgO**	**CaO**	**Na_2O**	**K_2O**	**TiO_2**	**P_2O_5**	**Cr_2O_3**	**NiO**	**LOI**	**Total**
Basaltic	52.46	12.81	11.09	0.18	7.53	8.52	2.41	2.25	0.61	0.08	0.07	0.03	2.15	100.18
Intrusive	63.32	12.33	9.64	0.15	0.91	3.32	4.81	2.02	1.00	0.49	0.01	0.00	2.25	100.24
Basaltic	60.94	12.04	10.97	0.16	0.90	3.74	3.16	4.15	0.97	0.48	0.01	0.00	2.38	99.89
Basaltic	61.31	12.17	10.2	0.19	2.01	2.45	6.06	1.48	0.91	0.46	0.01	0.00	2.59	99.84
Intrusive	46.14	5.26	15.52	0.22	16.63	7.51	0.52	3.14	1.88	0.19	0.17	0.14	2.63	99.94
Intrusive	45.31	4.81	15.93	0.22	18.74	5.25	0.46	2.37	1.8	0.17	0.19	0.17	4.79	100.19
Intrusive	61.94	11.95	11.77	0.10	1.04	3.13	2.98	4.21	0.95	0.47	0.01	0.00	1.63	100.17
Basaltic	62.26	12.45	10.44	0.18	0.80	3.00	5.79	1.12	0.99	0.51	0.01	0.00	2.46	100.00
Basaltic	62.55	11.74	11.03	0.19	0.88	3.49	4.73	1.55	0.97	0.50	0.00	0.00	2.59	100.22

Table 5: XRD analysis of host rocks from Moab Khotsong mine. Hole C (Branch Hole that intercepted the rupture zone).

Sample no.	Depth (m)	Calcite	Actinolite	Chlorite	Talc	Dolomite	Quartz	Plagioclase	Diopside	Epidote	Microcline	Sepiolite	Biotite	Kaolinite
I(1)	598.3	0.39	29.76	14.81	0.00	1.53	4.55	24.95	4.86	4.89	9.50	0.00	0.40	4.38
B(2.1)	600.8	2.22	0.00	1.04	0.00	0.05	27.04	35.33	2.72	1.58	10.76	11.61	1.56	6.11
B(2.2)	601.7	3.94	0.00	1.05	0.00	0.78	26.37	23.81	2.54	0.95	27.06	12.03	1.47	0.00
I(5.1)	606.4	2.84	5.56	0.00	0.00	0.00	14.23	58.94	2.24	0.00	3.22	11.81	1.02	0.14
I(5.2)	607.6	1.02	23.11	5.00	22.60	0.00	0.83	0.00	14.43	0.00	0.00	0.00	29.62	3.40
I(5.3)	608.2	4.30	16.79	7.46	37.05	0.00	0.37	0.00	4.04	0.00	0.16	0.00	25.06	4.77
B(3.1)	610.8	1.63	1.30	2.16	0.00	0.69	37.29	26.24	4.00	0.19	13.89	8.13	3.15	1.33
B(3.2)	611.4	2.92	0.00	1.21	0.00	0.25	24.72	47.78	3.08	0.57	2.89	15.06	1.52	0.00
B(3.3)	612.0	3.10	0.00	1.34	0.00	1.00	28.81	34.32	3.53	1.33	4.90	15.94	1.89	3.85

Table 6: XRD analysis of recovered Moab fault gouge from Orkney M 5.5 event (Hole C. Branch depth 608 m).

Sample no.	Calcite	Quartz	Biotite	Actinolite	Chlorite	Talc	Sepiolite	Total (wt%)
Moab fault (1)	13.31	1.76	20.06	33.97	9.77	20.86	0.27	
Moab fault (2)	11.98	1.56	20.09	32.57	11.33	22.03	0.44	

Table 7: The energy dispersive x-ray spectroscopy (EDS) elements analysis.

Sample no.	$CaCO_3$	SiO2	MgO	Al_2O_3	Feldspar	Wollastonite	Fe	Tungsten	Albite	Total
Spectrum 1	2.89	61.93	7.60	1.96	1.80	2.02	21.80	0	0	
Spectrum 2	3.99	57.42	6.83	2.97	2.40	2.88	23.51	0	0	
Spectrum 3	6.26	38.36	1.84	0.69	0	2.01	45.61	5.24	0	
Spectrum 4	5.65	51.75	5.12	1.68	1.17	5.18	29.44	0	0	
Spectrum 5	4.98	62.33	7.27	1.49	0.84	2.76	19.53	0	0.81	

Table 8: The peak (μ_p) and steady (μ_s) state friction coefficient of the Orkney M5.5 earthquake compared to Ortlepp shear fractures at 100 mm/s slip velocities (V_{eq}) and 2 MPa normal stress over defined slip weakening distance D_c.

	V_{eq} (mm/s)	Normal stress (MPa)	μ_p	μ_s	D_c (m)
Moab Gouge	100	2	1.0	0.66	9.15
Shear fracture S(3)	100	2	0.92	0.71	6.1
Shear fracture S(4)	100	2	0.98	0.67	12.8
Artificial Gouge	100	2	0.97	0.69	9.6

10. The energy budget of the mining-induced brittle shear fractures

This draft manuscript may still need some work before submission to the journal.

The energy budget of the mining-induced brittle shear fractures in deep and high stress mines inferred from laboratory experiments

Mngadi, SB[a,f], Manzi, MSD[a,f], Durrheim, RJ[a,f], Yabe, Y[b,f], Ogasawara, H[c,f], Wechsler, N[d,f], Ward, AT[e,f] and ICDP DSeis team[f]

[a] School of Geosciences, University of the Witwatersrand Johannesburg, PO Bag 3, WITS, 2050, Republic of South Africa.

[b] College of Science and Engineering, Ritsumeikan University, 1-1-1 Noji Higashi, Kusatsu 525-8577, Japan.

[c] Graduate School of Engineering, Tohoku University, 6-3, Aza-Aoba, Aramaki, Aoba-ku, Sendai 980-8578, Japan.

[e] Department of Geosciences, Tel Aviv University, P.O. Box 39040, Israel

[f] Institute of Mine Seismology, 7129 Somerset West, Private Bag X15, Republic of South Africa

[h] Cooke 4 Shaft, Sibanye Gold Limited, PO Box 82, Westonaria, Republic of South Africa.

[k] The International Continental Scientific Drilling Program (ICDP) Dseis team

ABSTRACT

Larger seismic events generally occur on pre-existing fault systems with gouge present from previous ruptures, while Ortlepp shears are produced by the fracturing of relatively intact rocks. Therefore, the energy budget could differ. Extremely stressed rocks in deep mines (especially during mining of remnant shaft pillar) often increase the risks posed by mining induced seismicity (e.g., normal faulting occurring ahead of the face creating new fracture surfaces). The study compared mining induced shear fracture surfaces formed ahead of the mining face and fracture surfaces created by triaxial compressive strength laboratory tests conducted at confining stresses up to 20 MPa, which is comparable to deep underground mining conditions. We observed robust physical similarities such as the presence of the fault gouge material and rough rupture surfaces between shear ruptures produced by triaxial compressive strength laboratory experiments and the mining induced shear ruptures developing ahead of the stope in deep South African gold mines. Additionally, we measured the particle size distribution of the comminuted fault gouge material generated from several laboratory experiments runs. The specific surface area (0.163 - 0.246 m^2/g) and density (2.72 g/cm^3) measurements were used to compute the surface energy, defined as the energy consumed in creating a new fracture surface during the earthquake process. These findings revealed very low values of surface energy as compared to the total energy ranging between 0.15% and 0.56%. These findings give a strong indication that a small share of the energy budget is required to create new fracture surfaces. When comparing to previous studies of seismic efficiency, surface energy is in the same order of magnitude.

1. INTRODUCTION

1.1. Overview

In this study, recently-formed brittle normal faults that occur in the relatively undisturbed ground in deep underground mines were targeted. This targeted approach eliminates many limitations of fault gouge material recovered from mature, altered and extensively weathered fault rocks, often from multiple seismic events – which are not a true reflection of a "seismic event". A fault damage zone is a product of many processes acting on a fault during the seismic cycle or process (Savage and Brodsky, 2011). Efforts to quantitatively determine and constrain dissipated energy from the formation of new fracture surfaces within the fault damage zones led to some important debates, such as whether the fracture surface energy constitutes a significant portion of the overall energy budget of earthquakes (Chester et al., 2005; Rockwell et al., 2009; Reches and Dewers, 2005; Wilson et al., 2005). The fracture surface energy is one of the critical parameters that influence rupture propagation and therefore, an important consideration for assessment of seismic risk and falls of ground in deep mines.

To make a meaningful contribution to the understanding of fracture surface energy, faulting and earthquake processes require direct and near-field observations. Deep South African gold mines may be the solution. Mining-related earthquakes were found to resemble natural tectonic earthquakes in some ways (Richardson and Jordan, 2002). This study focuses on freshly formed 'mining-induced' normal faults occurring tens of metres ahead of the mining stope (known as Ortlepp shear fractures) in deep and high stress remnant shaft pillar at Cooke 4 mine (Figure 1).

Due to the extensive mining history dating back to 1960s, several closures and reopening of the mine operations at these depths, the absolute stress conditions in the remnant shaft pillar are extremely elevated compared to virgin stresses. The virgin stresses (prior to mining activities) in South African gold mining regions can be computed from the equation below (Jager and Ryder, 1999):

$$\sigma_v = 0.027 * h \quad (1)$$

where (h in metres) is the depth and (σ_v in MPa) is the vertical component of the virgin stress. Therefore, the vertical component of the virgin stress in our study area ($h \sim$ 1000 m - 1200 m) is estimated to be ~ 27 MPa - 32 MPa. Therefore, to measure in-situ absolute stress conditions during mining activities, the Compact Conical-ended Borehole Overcoring (CCBO) technique has been used (Ogasawara et al., 2013; Sakaguchi et al., 1992; Sugawara and Obara, 1999). Elastic properties required as input parameters to compute the absolute stress are obtained from the drill core samples

recovered from overcoring.

Ogasawara and colleagues conducted the CCBO stress measurements in remnant shaft pillar at Cooke 4 mine. The measured major principal stress components were σ_1~ 123 MPa – 136 MPa and minor stress components were σ_3~ 28 MPa – 35 MPa, shown in Table 1 (Ogasawara et al. 2014b). The orientation of the measured major principal stress is almost vertical, and the minor principal stress is almost horizontal. From these stress measurements we could compute the average k-ratio, which is defined as the horizontal stress (σ_h) divided by the vertical stress (σ_v):

$$k = \frac{\sigma_h}{\sigma_v} \quad (2)$$

We found that in the remnant shaft pillar the prevailing average k-ratio is ~ 0.3. It is well understood that the formation of Ortlepp shears is analogous to 'conjugate shears' occurring under triaxial compressive stresses in laboratory experiments, and are characterised by normal displacement (van Aswegen, 2007). Spottiswoode (1978) conducted triaxial compressive tests using East Rand Proprietary Mines (ERPM) quartzite at confining stresses of ~ 13 MPa – 28 MPa, which is equivalent to ~ 1000 - 2000 m depths, respectively, to examine energy required to produce new free surfaces during failure. Similar to Spottiswood (1978), this study conducted triaxial compressive tests to try recreate comparable underground stress conditions such as confining stresses up to 20 MPa. Triaxial compressive tests were conducted on drill core samples recovered near these underground mining-induced normal faults.

It was thought that a comparision of triaxial compressive tests with mining-induced normal faults may reveal the scale-dependency of fracturing. At Cooke 4 mine, the stope height is generally ~1 – 2 m (Figure 2a), with an average length of ~ 20 m – 30 m (Figure 2b). The mining stope face advances ~ 10 m per month on average (Moriya et al. 2015). These mining activities induce differential stresses that often exceed the in-situ rock strength and form Ortlepp shear fractures, which are associated with M_w 2 seismic events. Statistically, magnitudes such as M_w 4 are virtually certain to cause damage (Jager and Ryder, 1999). During normal faulting occurring ahead of the stope face, stored strain energy is dissipated. There are three main energy distributions: (a) frictional heat, (b) seismic waves, and (c) fracture energy (including both the early extension fractures and the later shear fractures) (Olgaard and Brace, 1983). The fracture energy may be estimated by particle size distribution (PSD) analysis of fault rocks.

There are many debates on the energy budget of earthquakes, some estimates of the fracture energy range from 1% or less (Chester et al., 2005; Olgaard and Brace, 1983; Rockwell et al., 2009; Wechsler et al., 2011; Yshioka, 1986) to as much as 50% (Barber and Griffith, 2017; Reches and Dewers, 2005; Wilson et al., 2005). Critical to the disagreements, are the methods used to analyse the particle size distribution in clay-rich minerals and matured 'weathered' fault zones.

1.2. Mining induced normal faults 'Ortlepp shear fractures'

In early 1970s, there was a historic study linked to an accidental finding of two remarkable shear zones during mining of remnant pillar at the East Rand Proprietary Mines (ERPM), South Africa. This historic discovery resulted in the excavation of inclined tunnels to exhume and examine in details these two shear fractures. The examination of these shear zones showed: (a) normal fault displacement; (b) rupture nucleating and propagating through previously intact rock mass; (c) micro- to macro scale complex fault zone structures; (d) average displacement between 0.05 to 0.06 m with the maximum slip displacement of ~ 0.1 m; (e) a gouge largely developed along the main shear fracture forming a layer with a thickness of ~ 0.01 – 0.05 m; and (f) further examination of the fault gouge material by Spottiswoode (1978) through laboratory investigation indicated that the fault slip was produced by an average shear stress of ~ 40 MPa (Ortlepp, 1978; Gay and Ortlepp, 1979; McGarr et al., 1979; Spottiswoode, 1980; McGarr, 2016). In addition, in situ stress measurements from overcoring strain-relief by Gay (1972; 1975); and McGarr et al (1979) revealed an average shear stress of ~ 70 MPa.

These brittle shear zones have been since described in detail by various researchers (Gay and Ortlepp, 1979; McGarr et al, 1979; Brummer, 1987; Ortlepp, 1997; Bosman and van Aswegen, 2003; van Aswegen, 2013; Mngadi et al., 2019). However, as first noted by van Aswegen (2007), over the years various terminology has been used to describe these shear fractures. Terms such as – mining induced fault zone; shear zone; shear fracture; burst fracture; shear rupture; dynamic rockburst rupture; and dynamic brittle shear has been used (Gay and Ortlepp, 1978; McGarr et al., 1979; Brummer, 1987; Ortlepp, 1997; Bosman and van Aswegen, 2003). Ortlepp shear fractures are characterised by two mechanical features - en echelon extension fractures and breakthrough shear ruptures (see p. 43 of Ortlepp, 1997; van Aswegen, 2007; Figure 11; Manuscript 5). Although, in some instances Ortlepp shear fractures may occur without breakthrough shear ruptures, which may be indicative of a 'stiff loading system' (van Aswegen, 2007). They tend to dip steeply away from the stope face in the footwall

and dip towards the stope face when in the hangingwall (Figure 2a) and strike sub-parallel to the stope face (Figure 2b) (van Aswegen, 2007).

The underground mapping through excavated tunnels revealed that the fractures systems dip dimensions were at least 20 - 30 m. The fracture zones span an area of ~ 500 - 600 m^2 (Gay and Ortlepp, 1979; Ortlepp, 1978; Spottiswoode, 1978). Recently, in our study area, Moriya et al. (2015) used high frequency 28 acoustic emission (AE) sensors and 6 accelerometers to delineate AE clusters that strike parallel to the face; they are steeply dipping (~65°) with dip dimension of ~ 10 – 30 m, typical for Ortlepp shear fractures.

1.3. Fault gouge

In deep and high stress South African gold mines seismic events occur on a daily bases. They generate fresh fault gouge which can be collected straightaway after the seismic event and importantly, with no alteration and weathering preceding gouge recovery. The host rock is dry quartzites (predominantly quartz and minor muscovite) with negligible porosity (McGarr et al., 1979; Olgaard and Brace, 1983).

In particular, aspects that influence the amount of gouge generated in a fault zone such as: (a) intact rock strength; (b) maximum slip displacement; (c) in situ stress state; (d) initial fault gouge before rupture propagation; and (e) displacement field at fracture tip (sliding mode).

Also, previous laboratory experiments studies revealed that the presence of the fault gouge, mineral composition, gouge particle size distribution (PSD) and gouge thickness influences the fracture energy and fault rupture propagation (Biegel et al., 1989; Mngadi et al., 2020). Moreover, some studies of the fault gouge have examined the relationships between confining stresses and the amount of gouge generated (Engelder, 1974; Olgaard and Brace, 1983; Sammis et al., 1987).

1.4. Particle-size distributions

In brittle faults of all scales, fault gouge formation and grain size reduction consistently occur (Scholz, 2002). Particle size reduction occurs either by crushing, grinding, cutting, vibrating, or other processes is called comminution (Kanda and Kotake, 2007). The particle size distribution (PSD) is considered as one of the most critical factors used to quantitatively describe the fault gouge (Chester et al., 2005; Keulen et al., 2007; Wechsler et al., 2011; Wilson et al., 2005). Therefore, several methods

that measure the particle size distribution of fault rocks emerged (Table 2) (Kato et al., 2003; Keulen et al, 2007). The traditional method used is sieving, which comes from sedimentology (Sammis et al., 1987). Optical microscopy on thin sections is also used (Monzawa and Otsuki, 2003); while some researchers use the laser diffraction particle size analyser (Wechsler et al., 2011; Wilson et al., 2005).

The particle size distribution may be expressed by means of a power-law relationship for "self-similar" distributions, and the gradient of the distribution is referred to as the fractal dimension (D-value) (Turcotte, 1992). The fractal dimension is often used as a parameter that enables comparison of the particle size distribution of naturally occurring seismic events to experimentally induced shear fractures (Marone and Scholz, 1989). On average, the fractal dimensions of several published datasets on the particle size distribution of fault rocks ranges from 1.4 to 2.6. Often, high fractal dimensions (D-values) are associated with fresh fractures. Also, there seems to exist a relationship between the fault rock (particle shape and size distribution), with the mechanical behaviour of faults. Therefore, preserved fault rocks may provide critical evidence and hints of faults mechanical behaviour.

Here, the focus is on the particle size distribution of mining-induced normal faults and frictional sliding experiment faults of the Witwatersrand Basin, which are predominantly quartzite with an average grain size of about 0.5 mm (McGarr et al., 1979; Olgaard and Brace, 1983). In this paper, we examine the influence of experimental conditions such as confining stresses on the fault rock microstructure and particle size distribution, and compare the results to mining-induced normal fault rock cored from a recently active Ortlepp shear fractures occurring ahead of the mining front in deep and high stress South African gold mines.

1.5. Energy budget

A number of investigations of exhumed fault zones have attempted to quantify the surface area of the fault gouge in the principal slip zone (PSZ), as well as off-fault brittle damage, to estimate the surface energy (Chester et al., 2005; Keulen et al., 2007; Olgaard and Brace, 1983; Rockwell et al., 2009; Wechsler et al., 2011; Wilson et al., 2005). Several challenges exist for this practice. For mature faults, estimating the number of seismic events which have contributed to the damage measured can be difficult (e.g., not all generated damage is seismic). Moreover, damage distribution along faults is heterogeneous, and the choice of representative elementary volume of rock to subsample can drastically change the resulting surface area estimates.

These field-based estimates are usually contextualised in terms of theoretical predictions from dynamic rupture models (Reches and Lockner, 1994) as well as laboratory analogs such as dynamic loading experiments (Doan and Gary, 2009; Yuan et al., 2011). New surfaces are the principal defects produced at shallow crustal depths; therefore the 'defect' energy will be mostly surface energy. Energy flux as heat or seismic radiation is known to an order of magnitude, but estimates of surface energy range over several orders of magnitude. The surface energy is given by (Olgaard and Brace, 1983):

$$E_A = S_T \gamma \quad (3)$$

where S_T is the total surface area created during faulting, and

γ is the specific surface energy.

For most common minerals, e.g., quartz, specific surface energy γ is ~ 0.7. A reasonable estimate of E_A will therefore, depend on the accuracy of the measurement of S_T (Olgaard and Brace, 1983). To find a fault gouge in its original condition, unspoilt and fresh is extremely rare. Often the fault gouge found exposed on a surface may have undergone several episodes of alteration and lithification, which changes the original nature of the fault zone (Olgaard and Brace, 1983). Therefore, the fault gouge found exposed on rupture zone surfaces may not reflect the mechanical conditions at focal the depth or during seismic event. In addition, rupture zones are usually inaccessible at seismogenic depths (Wilson et al., 2005; Ogasawara et al., 2019).

To make an accurate estimate of S_T, fault gouge is needed from the site of a very recent earthquake. Most earthquakes emanate from depths of several kilometres or more. Thus, only deep drilling or mining (Olgaard and Brace, 1983) can allow sampling. In deep and high-stress South African gold mines, mining-induced faults produce fresh fault gouge that can be sampled almost immediately following the seismic event. In order to characterise S_T, we examine selected fault gouge specimens by thin section micrographs; mechanical sieving; scanning electron microscopy (SEM); and laser diffraction particle size analyser. Additionally, the fault gouge and discontinuity surface roughness often reveals the history of faulting. Therefore, studying the variations in the fault gouge and discontinuity surface roughness in mining-induced normal faults and frictional sliding experiments could be critical for examining the earthquake source mechanism (Yoshioka, 1985).

2. GEOLOGY OF THE COOKE 4 MINE

The Cooke 4 mine is situated in the Witwatersrand Basin, which comprises largely of the Archaean quartzites (2.98 – 2.84 Ga). The Basin thickness averages ~ 4.6 km, and consists of two groups: the Central Rand Group and the West Rand Group (Robb and Meyer, 1995; McCarthy, 2006; Dankert and Hein, 2010). The basin is elongated with the long axis ~3 km and the minor axis ~1.5 km (Ryder and Jager, 2002). The NW rim of the Basin on average dips 16^{o}, to the southeast (Harvey et al., 2006). Comprehensive work on various mining methods and standards in deep and high stress South African gold mines are provided by Jager and Ryder (1999) and Ryder and Jager, (2002). The Central Rand Group is located on top of the West Rand Group. The Central Rand Group dominant lithologies are alternating conglomerate “reef” and quartzite. The West Rand Group mainly consists of clastic sedimentary rocks with minor lavas (SACS, 1980 and 2006).

3. METHODS

After spatial-temporal delineation of mining induced normal faults forming ahead of the mining front, to relieve the high stresses from the remnant shaft pillar before drilling, the mine conducted overstoping to reduce on-reef stress concentrations that might cause rockbursts. The DSeis team drilled into fragile mining-induced normal faults with the aim to recover the host rocks, rock breccia and fault gouge. The team used a specialised 1.5 m triple-tube core barrel with metal split spoons and tin foil to maximise core recovery. The conventional single and double-tube core barrels are not suitable for such highly-stressed drilling environments characterised by intense fracturing. The single and double tube sampler rotates and often shears core samples along rock mass discontinuities. Also, drilling fluids cause erosion and disturbance of core samples.

The triple-tube core barrel produced a better quality of recovered core samples compared to the single and double tube core barrels. The borehole length was ~41.5 m, with the core diameter of 42 mm. Detailed fractures, rock breccia and fault gouge were recovered in the core despite core loss (associated with the fault gouge zone) in some areas. The recovered lithologies are from the Mondeor formation. The rock samples were selected for rock frictional sliding experiments and particle size analysis. The core samples generally consisted of four different types of rocks, viz. quartzite, pebbly quartzite, argillaceous quartzite and conglomerate.

We compared freshly recovered ruptures to experimentally-induced ruptures (confining stresses 5, 10, 15 and 20 MPa). Gouge generated from experimentally-induced ruptures were collected, sieved

and analysed using the Malvern Mastersizer 2000 laser diffraction particle size analyser and scanning electron microscope (SEM). We estimate the fracture energy using grain-size analysis of gouge from experimentally-induced fractures. The methods used for the analysis were thin section, scanning electron microscope (SEM), and laser diffraction particle size analysis (Keulen et al., 2007).

3.1. Frictional sliding experiments

Frictional sliding experiments under triaxial load were conducted and analysed, including post-failure gouge particle size analysis. Sample preparation and testing were carried out following the International Society for Rock Mechanics (ISRM) Standards (http://www.isrm.net). Cylindrical samples were prepared with a dimension of length greater than twice the diameter (42 mm) for triaxial compressive tests. Specimens were placed in a clean cell jacket to avoid oil leakage from the Hoek cell. The confining pressures used were: 5, 10, 15 and 20 MPa. The jackets were removed and the fault gouge along the sliding surfaces was carefully collected with a brush. The specimen was compressed at a constant rate of 2-4 kN/sec. The amount of the fault gouge varied from sample to sample; analysis and measurements were made of the amount of gouge volume with increasing confining stresses.

3.2. Particle Size Distribution

3.2.1. Thin-section micrographs

Using thin-section microscopic analysis (2D) we can constrain the grain size or particle size distribution (PSD) of the host rocks, before conducting frictional sliding experiments, which gives the estimated average original particle size distribution. One of the pitfalls of using thin section micrographs is that the minimum size of measurable grains is ~2 µm (Keulen et al., 2007).

3.2.2. Sieving particles

Fault gouge comprises mainly of quartz and muscovite (see Mngadi et al., 2020), and sieving bins used for size distribution range are: (a) 1000 – 500 µm; (b) 500 – 250 µm ; (c) 250 – 125 µm ; (d) to less than 125 µm. The fault gouge volume recovered was very limited. Therefore, only shear fractures: S (3) and S (4) were sampled for particle size distribution analysis (see Table 3).

3.2.3. Scanning Electron Microscopy (SEM)

To complement the sieving and thin section micrographs methods, the scanning electron microscopy (SEM) is often used to measure the particle sizes, especially if there are gouge particles that are less than 2 µm (Sammis et al., 1987). For sample preparation, the fault gouge was glued to an SEM stub and a 30 nm thick carbon coating was applied. The coating was applied by heating the carbon source until it evaporates, resulting to deposition of carbon material onto specimens. The data collected were analysed for particle size distribution. In addition, to determine the chemical composition of the gouge particles measured, energy dispersive x-ray spectroscopy (EDS) was used.

3.2.4. Laser diffraction particle size analyser

Recently, this method has been used in several particle size distribution analysis studies for fault gouge analysis (Chester et al., 2005; Keulen et al., 2007; Wechsler et al., 2011; Wilson et al., 2005), and other engineering studies. We also used the Malvern Mastersizer 2000 laser diffraction particle size analyser to compare and complement the methods described above. This was done to ensure that the systematic limitation inherent in each method is mitigated. The instrument provides detection limits or measurement size range from submicron to millimetre (0.02 µm – 2000 µm) of wet or dry materials such as the fault gouge particles (or ceramics powder) of milligram quantities (Spectris plc., 2005).

The fault gouges produced by triaxial compressive strength tests were collected at the laboratory and stored in plastic bags. The fault gouge were separated into different grain sizes using sieves, for powder greater than 1.00 mm and less than 1.00 mm. The weight of the fault gouge samples greater and less than 1.00 mm were measured to account for every powder collected. However, the experiment analysed the fault gouge particle samples that were less than 1.00 mm, and in micron scale due to the instrument resolution detection limit.

The fault gouge was mixed with distilled water and stirred to minimise aggregation of fault gouge particles. Further, to minimise aggregation a sample vibrator was used to separate the particles into individual gouge particles. The sample was gradually added to 800 ml of distilled water. Once the sample reached obscuration range the measurement is started. The laser particle analysis cannot distinguish between agglomerates and individual gouge particles. This is mitigated in fresh rock fractures and fault gouge comprising of non-clay minerals. The clay grains often stick together causing agglomerates.

3.2.5. Seismic velocity and density measurements

The measurement method uses two transducers, where one is used as a source of seismic waves, while the other is used as a receiver. The source is used to transmit seismic waves that travel through the specimen to the receiver. The travel time is recorded and the length of the specimen is measured. To compute the seismic wave velocity of the specimen, the value of the measured length of the specimen is divided by the recorded travel time.

4. RESULTS

4.1. Thin-section micrographs

Previous petrographic studies revealed four rock types viz. quartzites, pebbly quartzite, argillaceous quartzite and conglomerates, which are characterised mainly by abundance of quartz and minor muscovite (Mngadi et al., 2019). Thin-section micrographs confirm that the host rocks consist mainly of sand-sized quartz grains. The grain size distribution is estimated to be an average of 500 µm and up to 2 mm (Figure 3 a–d). We did not account for the cement that fills the gaps between grains, which could likely create small particles when the rock mass fragments.

4.2. Mining-induced fractures

Here, key characteristics of these brittle shear fractures are outlined – the presence of the fault gouge, known as ‘rock flour’ in South African gold mines and rough rupture surfaces that occur in mm to cm scale shown in Figure 4a and Figure 4b (see Mngadi et al., 2020).

4.3. Frictional sliding experiments

We present frictional sliding experimental results performed under triaxial compressive strength tests. The triaxial compressive strength tests were conducted at confining stresses of up to 20 MPa, higher than previous experiments (see Mngadi et al., 2019), which is closer to horizontal stresses experienced in situ (~28 – 40 MPa) in deep underground mines such as Cooke 4 mine.

The experimentally-induced fractures, which are characterised by the gouge material “rock flour” and rough rupture surfaces (Figure 4c and Figure 4d), very similar to ‘mining-induced’ shear fractures recovered from the DSeis triple-tube drilling (van Aswegen et al. in prep; Mngadi et al., 2020).

From a study of the experimentally-induced ruptures, it was found that seismic slip created gouge particles. The gouge particles generated from the experiments were sieved and weighed for particle size distribution analysis. Generally, conglomerate and quartzite 'rock types' generated a greater proportion of 'large' particles (weight > 2.1 grams) for sieve size of < 1.0 mm, compared to argillaceous quartzite and pebbly quartzites (weight > 0.496 grams) for sieve size of < 1.0 mm (see Table 3). This suggests that gouge generation (<1.00 mm) is dependant on rock type (e.g., mineralogy).

There is a general increase in the compressive strength of these rocks under increased confining stresses (Figure 5). No clear relationship could be observed between the amounts of fault gouge generated and confining stresses (Figure 6). This suggests that the generation of the fault gouge is not simply dependent on confining stresses.

Under uniaxial load, the elastic behaviour of the stress-strain curve is described by Young's modulus (E) and Poisson's ratio (v). The Young's modulus of the host rock is between 60 GPa and 77 GPa. The Poisson's ratio for the rock types is between 0.14 and 0.24 (Table 4).

4.4. Density and seismic wave velocities

The density and seismic velocities were measured. The P-wave velocities range between 5253 m/s and 5711 m/s, and the S-waves velocities range between 2717 m/s and 3430 m/s (Table 5). The density tends to increase with seismic velocities (P-wave and S-wave).

4.5. Damage characterisation and particle size analysis

4.5.1. Sieved 'rock flour' particles

Mining-induced fault gouge: The fault gouge commonly referred to as "rock flour" in South African deep mines, was recovered from mining-induced brittle shear fractures during our DSeis drilling endeavour. The fault gouge recovered from mining-induced shear zones was very limited in volume and particle size distribution was measured using the traditional sieving method. The particle size distribution sieving bins used were: (a) 1000 – 500 µm; (b) 500 – 250 µm; (c) 250 – 125 µm; and (d) to less than 125 µm.

Most mining-induced fault gouge particles (36%) are concentrated between 1000 – 500 µm, and 19% are less than 125 µm. The fault gouge particle size distribution from mining-induced shear zones,

S (4) showed fault gouge generation of 0.504 g (weight) and S (3) showed fault gouge 0.251 g for sieve size < 125 µm (Table 6 and Figure 7).

4.5.2. Scanning Electron Microscopy Analysis

We used the SEM to analyse the fault gouge generated by frictional sliding experiments and found that smaller particles are sub-rounded, and bigger particles are angular and flaky (Figure 8a & b). Also, the SEM micrographs analysis for the fault gouge generated by the mining-induced shear fractures showed irregular, sub-rounded to angular particles (Figure 8c & d). In comparison, these fault gouge textures are similar, both comprising a mixture of sub-rounded and angular particles.

The Energy Dispersive X-ray Spectroscopy (EDS) was used to determine the chemical composition of the fault gouge materials. The EDS spectrum results for experimentally-induced fault gouge samples are shown as a plot of X-ray counts vs. energy (keV). The EDS examination on fault gouge particles revealed Si, O, Al and Mg (Figure 9). In addition, the EDS of some samples revealed a substantial quantity of ore minerals such as pyrite – Fe, Ti, S, O, Al and S (Figure 9).

4.5.3. Laser diffraction particle size analyser

The frictional sliding experiments under confining stresses up to 20 MPa were conducted on intact rock samples under dry conditions at room temperature. The fault gouge particle size distribution approach submicron size (~1.9 µm) (Figure 10). The particle size distribution clearly shows two populations of the fault gouge particle distribution. At confining stresses of 20 MPa there seems to be an increase in the fraction of smaller gouge particles (~10 µm) in some results (Figure 10).

Since the laser diffraction particle size analysis method requires an amount of gouge greater than 100 milligrams, we could not analyse samples recovered from the mining-induced fractures as the small amount of material we recovered was utilised in dynamic friction experiments (see Mngadi et al., 2020).

4.6. Energy Budget

In order to understand the distribution of energy dissipated during the faulting process, it is critical to understand the amount of energy consumed when constructing the new surfaces. Here, we follow the method used by Olgaard and Brace (1983) to estimate the surface energy. The energy density (W_A) of the fault gouge per unit volume is given below:

$$W_A = S\gamma\rho \quad (4)$$

where S is the specific surface area created during faulting.

γ is the specific surface energy, and

ρ is the density of the particles.

The energy density can be associated to the total energy dissipated during faulting or fracturing. The surface energy is given by equation (3) ($E_A = S_T\,\gamma$). Therefore, combining equation (3) and (4) we get:

$$E_A = W_A\, A\, \mu \quad (5)$$

where A is the area of the fault rupture plane, and

μ is the thickness of the fault gouge zone.

The equation of total energy dissipated by the earthquake process is obtained from Brune (1970) and is given below (6):

$$E_T = A\, d\, \bar{\sigma} \quad (6)$$

where d is the average fault displacement, and

$\bar{\sigma}$ is the average stress on the fault.

Combining equations (5) and (6), we get equation (7) below:

$$\frac{E_A}{E_T} = \frac{W_A}{\bar{\sigma}}\,\frac{\mu}{d} \quad (7)$$

Olgaard and Brace (1983) draw on work by Spottiswoode (1978) and McGarr et al. (1979), who reported typical values for mining-induced shear fractures: values of driving stress ($\bar{\sigma}$ = 40 - 70 MPa), fault gouge thickness (μ = 10 – 50 mm) and average displacement (d = 50 – 60 mm).

Taking γ is the specific surface energy of quartz from Brace and Walsh (1962) and choosing $\gamma \sim 0.7$ J/m^2, and our measurements of the density of the rock mass (ρ ~2.72 x 10^6 g/m^3), we measured and found the specific surface area approaches S ~0.277 m^{2}g^{-1} at lower confining stresses and S ~0.246 m^{2}g^{-1} at higher confining stresses (Figure 11). Therefore, the estimated fracture energy relative to the total energy release:

$$\frac{E_A}{E_T} = 0.15\% - 0.56\%$$

Table 7 lists the measured specific surface area, confining stresses and estimated fracture energy. The fracture energy values obtained suggest that a minor fraction of the total earthquake energy budget is consumed in creating new fracture surfaces (Table 7).

5. ANALYSIS AND DISCUSSION

5.1. Comparison between mining-induced and experimental fault gouge

Extensive research of mining-induced seismic events in the deep and high stress gold mines in the Witwatersrand have shown that the mining-induced seismicity are similar to earthquakes in active tectonic regions (e.g., fault mechanisms, physical appearance and geometrical layouts, rupture propagation, etc.), despite being associated with mining activity (Gane et al., 1946; Cook, 1963). Therefore, it is important to study these mining-induced seismic activities since the knowledge gained may be extended to understanding seismicity in active tectonic regions and develop better seismic hazard assessments.

In this study, we designed laboratory experiments under comparable underground stress conditions (i.e., confining stresses up to 20 MPa). These triaxial compressive strength experiments were conducted on drill core samples recovered near mining-induced normal faults. The results showed that the triaxial compressive strength increases with increasing confining stress. These findings agree with general literature that shows increasing rock compressive strength with increased confining stresses (Babacan et al., 2009). The triaxial compressive strength ranged between 64 MPa and 339 MPa for argillaceous and pebbly quartzite, respectively. This introduces dependence of triaxial compressive strength on the rock composition or mineral assembly. This agrees with the previous laboratory experiments conducted by Mngadi et al (2019). These new triaxial compressive strength experiments were performed at higher confining stresses between 5 and 20 MPa that are comparable to Spottiswoode (1978) who performed triaxial compressive strength experiments using the similar quartzite recovered from the Witwatersrand gold mines at confining stresses between 13 and 28 MPa.

The recovered recently formed mining-induced Ortlepp shear fractures are characterised by rough surfaces and fault gouge (see Mngadi et al., 2020). The fresh experimentally-induced shear fractures are characterised by the fault gouge and rough rupture surfaces, similar to mining-induced shear fractures. The physical observations of the experimental results are consistent with the mining-induced seismicity. This agrees with van Aswegen's (2007) observations that revealed mining-induced shear zones physical observations are very similar to brittle shear ruptures produced in the laboratory experiments subjected to compressive stresses and confining stresses of ~10 MPa to 100 MPa (van Aswegen, 2007).

5.2. Fault gouge

In the brittle upper part crust, comminution naturally occurs during faulting and earthquake process (Sibson, 1986). Mining induced shear fractures as discussed are characterised by the presence of the fault gouge (finely comminuted rock, termed 'rock flour' in South African gold mines) with thickness of up to ~50 mm. The Witwatersrand quartzites vary from almost pure quartz to argillaceous quartzites with significant clay fractions. The average mineral grain size distribution of intact rocks is 500 µm and up to 2 mm, and this was estimated from thin section analysis. The grain size is comparable to the value for Witwatersrand quartzites (~0.5 mm) used by Olgaard and Brace (1983).

Experimentally-induced fault gouge weight did not show a clear pattern with increasing confining stress. Rather, the generation of the fault gouge (weight) shows that it is largely dependent on rock composition rather than confining stresses. We observed that conglomerate rocks generate larger fault gouge volumes. This could be explained through rupture surface roughness, which is likely to be rougher for conglomerate rocks (e.g., they are exteremly heterogeneous consisting of cracks, pebbles and matrix). In addition, the wear rate of these rocks were found to be related to slip velocity. Mngadi et al. (2020) found that the wear rate or gouge generation of these quartzite rocks, in particular, argillaceous quartzite was higher at high slip velocities (200 mm/s – 1200 mm/s).

The SEM analysis of the experimentally-induced fault gouge showed that smaller fault gouge particles are sub-rounded, while the larger fault gouge particles are angular and flaky (Figure 8a and Figure 8b). In addition, SEM analysis revealed shattering of quartz grains to smaller particles. van Aswegen (2007) interpreted these observations to indicate that the deformation field is partly dilation, which is consistent with some shattering activity during dynamic rupture propagation when subjected to local tensile stresses (Brune et al., 1993; Ben-Zion and Sammis, 2003; Rockwell et al., 2009).

At confining stresses of 20 MPa, there appears to be an increase in the finer fault gouge particles (~10 µm). However, our results do not show conclusively that the grain size of experimental fault gouge decreases with increasing confining pressure. We suggest that it requires more experiments to examine the relation conclusively. Previously, increasing confining stresses and displacement were correlated positively to grain size reduction of the fault gouge particles (Engelder, 1974; Olgaard and Brace, 1983). Sammis et al. (1987) described the particle size reduction as suppression of microfracture extension

and followed by a decrease in the spacing of axial microfractures as the confining stress increases. In addition, it is suggested that fast deformation generates the finer fault gouge (van Aswegen, 2013).

The SEM micrographs analysis for the fault gouge generated by the mining induced shear fractures showed irregular, sub-rounded to angular to particles (Figure 8c and Figure 8d). In comparison, these fault gouge textures are similar, comprising a mixture sub-round and angular particles. This is consistent with the observations by Wilson et al. (2005), who showed that fault gouge from the San Andreas fault with a total of 160 km of slip, and the rupture zone of a recent mining-induced earthquake in a South African mine with a 0.4 m slip, display similar textures (Wilson et al., 2005; Reches and Dewers 2005).

For experimentally induced fault gouge, particle distribution size approaches ~1.9 µm, with an average of ~100 µm. Olgaard and Brace (1983), using the X-ray sedimentation technique, found that fault gouge particle size range between 1 and 50 µm. These findings are consistent with our particle size distribution, and in the same order of magnitude. However, their SEM observations indicated that particle size might approach ~0.1 µm (Olgaard and Brace, 1983). This is an order of magnitude less than our particle size results. Wilson et al. (2005) revealed that fault gouge particle size for both San Andreas fault and rupture zone in deep South African gold mines fluctuates with run time from 0.04 – 200 µm to less than ~1 µm after 72 – 190 hours. Wilson et al. (2005) circulated the samples to deflocculate them, which may have resulted in sedimentation of the larger particles inside the machine, leading to particle size distribution being affected. Wechsler et al. (2011) reported that the mean particle size for the majority of samples falls between 50 and 470 µm. These results are comparable to our findings. To be noted, Wechsler et al. (2011) also deflocculated their fault gouge samples before performing particle size distribution measurement, which may be less relevant to our study since in our fresh rock fractures there are no clay minerals to stick grains together (except for argillaceous quartzite).

The fault gouge particle size distribution clearly shows a bi-modal distribution (Figure 10). There is a third, less pronounced, population. These two pronounced populations were previously interpreted by Keulen et al. (2007) to mean that grain size reduction in fault zones may be developing through two phases: (a) initial rupturing that creates cracked grains; and (b) additional slip displacement resulting in comminution of rock fragments by wear and attrition (Keulen et al., 2007). This could be correlated to our SEM observations, which revealed that smaller fault gouge particles are sub-rounded indicating

wear and attrition (phase 2) after initial rupturing, while the larger fault gouge particles are angular and flaky, which may have undergone only phase one of the fault process.

5.3. Fracturing as a component of dissipated energy

Cook (1963) appreciated that some of the energy dissipated should be due to slip between sliding rock surfaces (e.g., fracturing). The understanding of the partitioning of energy is a key towards the understanding the physics of earthquakes. These experimentally induced fractures showed physical similarities to mining-induced shear fractures occurring ahead of the stope.

The densities and P-wave velocities of these different rock types; quartzite, pebbly quartzite, argillaceous quartzite and conglomerate are presented in Table 5. The average of seismic P-wave and S-wave velocities of 5532 m/s and 3116 m/s. These lithologies show an average density of ~2.72 g/cm^3. The specific surface area (S) obtained for our study ranged between 0.163 - 0.246 m^2/g. Oldgaard and Brace's (1983) value of S (0.7 m^2/g) is more than three times greater than our value (0.2 m^2/g) for the fresh fault gouge recovered in the Witwatersrand gold mines.

Our specific surface area results and density measurements were used to compute the energy consumed in creating a new fracture surface. We obtained low values (0.15% – 0.56%), this suggest that only a small portion of the total earthquake energy budget is consumed for breaking or shattering rocks. This is consistent with conclusions obtained by several researchers with estimates range from 1% or less (Olgaard and Brace, 1983; Yshioka, 1986; Chester et al., 2005; Rockwell et al., 2009; Wechsler et al., 2011). However, some estimates are extremely high, to as much as 50% (Reches and Dewers, 2005; Wilson et al., 2005; Barber and Griffith, 2017). However, as discussed above measuring method seem to have contributed to the skewed results.

Olgaard and Brace (1983) estimated the energy consumed in grain crushing of the fault gouge in rupture zones situated in deep South African gold mines to be ~1 - 10%. Motivated by clear physical similarities between the mining induced shear fractures observed in deep South African gold mines and shear ruptures generated from triaixal compressive strength laboratory experiments, Spottiswoode (1978) performed triaxial compressive strength experiments and examined the particle size distribution of the comminuted 'rock flour' generated from a series of laboratory experiments. They used quartzite rock sampled similar to our studies from the East Rand Proprietary Mines (ERPM) in the Witwatersrand Basin at confining stresses (13 - 27 MPa) similar to those expected underground. Spottiswoode (1978)

results were reviewed and reinterpreted by McGarr et al. (1979) and revealed that the estimated seismic efficiency to be 0.36 to 3.6%.

6. CONCLUSION

Here we compared mining induced shear fractures and traixial compressive strength laboratory experiments performed under confining stresses (5 – 20 MPa) similar to underground conditions. There were strong physical similarities between shear ruptures generated from triaxial compressive strength laboratory experiments and the mining induced shear ruptures occurring in deep South African gold mines ahead of the stop face. In addition, we measured the particle size distribution of the comminuted fault gouge generated from runs of laboratory experiments. The specific surface area (0.163 - 0.246 m^2/g) and density (2.72 g/cm^3) measurements were used to compute the energy consumed in creating a new fracture surface. We found very low values of energy consumed in creating a new fracture between 0.15% and 0.56% of the total energy partitioned. These results suggest that only a minor share of the total energy budget is consumed for creating a new fracture surface (breaking or shattering rocks).

7. REFERENCES

An, L.-J. and Sammis, C. (1994). Particle size distribution of cataclastic fault materials from southern California: A 3-D study. Pure and Applied Geophysics, 143, 203-227.

Babacan, A.E., Ersoy, H. and Gelisli, K. (2009). Determination of physical and mechanical properties of rocks with direct and indirect methods: A case study on the beige limestones in the Eastern Pontides, Proceedings of the 21st International Mining Congress and Exhibition of Turkey, Antalya, 123-130.

Barber, T. and Griffith, W.A. (2017). Experimental constraints on dynamic fragmentation as a dissipative process during seismic slip. Philosophical Transactions of the Royal Society, 375: 20160002. http://dx.doi.org/10.1098/rsta.2016.0002.

Biegel, R.L., Sammis, C.G. and Dieterich, J.H. (1989). The frictional properties of a simulated gouge having a fractal particle distribution. Journal of Structural Geology, 11, 7, 827- 846.

Bosman, J.D. and van Aswegen, G. (2003). Dynamic failure of pillar remnants – case studies. ISRM 2003 – Technology roadmap for rock mechanics, SAIMM, Johannesburg, pp 143 – 149.

Brace W. F. and Walsh J. B. (1962). Some direct measurements of the fracture energy of quartz and orthoclase. American Mineralogist, 47, 1111-1122.

Ben-Zion, Y. and Sammis, C.G. (2003). Characterization of fault zones. Pure Appl. Geophys. 160, 677–715.

Brummer, R.K. (1987). Fracturing and deformation at edges of tabular excavations: development of a numerical model describing such phenomena. Unpublished. PhD thesis, Rand Afrikaans University, p. 204.

Brune, J.N. (1970). Tectonic stress and the spectra of seismic shear waves from earthquakes. Journal of Geophysical Research, 75, 4997-5009.

Brune, J.N., Brown, S. and Johnson, P.A. (1993). Rupture mechanism and interface separation in foam rubber model of earthquakes: a possible solution to the heat flow paradox and the paradox of large overthrusts. Tectonophysics, 218, 59–67.

Chester, J.S., Chester, F.M. and Kronenberg, A.K. (2005). Fracture surface energy of the Punchbowl fault, San Andreas system. Nature, 437, 133–136.

Cook, N.G.W. 1963. The seismic location of rockbursts. In: Proceedings of the Fifth Rock Mechanics Symposium. Oxford: Pergamon Press, pp. 493-516.

Dankert B.T. and Hein, K.A.A. (2010). Evaluating the structural character and tectonic history of the Witwatersrand Basin. Precambrian Research, 177, 1-22.

Doan M.L. and Gary G. (2009). Rock pulverization at high strain rate near the San Andreas fault. Nature Geoscience, 2, 709–712. doi:10.1038/ngeo640.

Engelder J.T. (1974). Cataclasis and the generation of fault gouge. Bulletin of the Geological Society of America, 85, 1515-1533.

Folk, R.L. (1968). Petrology of Sedimentary Rocks. Texas: Hemphill Publication Co., 170p.

Gane, P.G, Hales, A.L. and Oliver, H.A. (1946). A seismic investigation of the Witwatersrand earth tremors. Bulletin of the Seismological Society of America, 36, 49-80.

Gay, N.C. (1972). Virgin rock stresses at Doornfontein Gold Mine, Carletonville, South Africa. Journal of Geology, 80, 61-80.

Gay, N.C. (1975). In-situ stress measurements in Southern Africa. Tectonophysics, 29, 447-459.

Gay, N.C. and Ortlepp, W.D. (1979). Anatomy of a mining-induced fault zone. Bulletin of the Geological Society of America, 90, 47-58.

Gupta, C.K. (2003). Chemical Metallurgy: Principles and Practice. WILEY-VCH Verlag GmbH & Co. KGaA, Weinheim. pp. 130.

Hadizadeh, J. and Johnson, W. (2003). Estimating local strain due to comminution in experimental cataclastic textures. Journal of Structural Geology, 25, 1973-1979.

Harvey, F., Joughin, W. and Ortlepp, D.W. (2006). Design of Ezulwini Shaft Pillar Extraction. SRK Consulting Engineers and Scientists, Technical report: Report number: 346813.

Heilbronner, R. and Keulen, N. (2006). Grain size and grain shape analysis of fault rocks. Tectonophysics, 427, 199-216. doi:10.1016/j.tecto.2006.05.020.

Hoek, E. and Brown, E.T. (2018). The Hoek-Brown failure criterion and GSI - 2018 edition. Journal of Rock Mechanics and Geotechnical Engineering, 11, 445-463.

Jager, A.J. and Ryder, J.A. (1999). A Handbook on Rock Engineering for Tabular Hard Rock Mines. Braamfontein. Johannesburg: SIMRAC.

Kanda, Y and Kotake, N. (2007). Chapter 12: Comminution Energy and Evaluation in Fine Grinding. In Salman, Agba D.; Hounslow, Michael J. Handbook of Powder Technology, 12, 529–551.

Kato, A., Ohnaka, M. and Mochizuki, H. (2003). Constitutive properties for the shear failure of intact granite in seismogenic environments. Journal of Geophysical Research, 108, doi:10.1029/2001JB000791.

Keulen, N., Heilbronner, R., Stunitz, H., Boullier, A.M. and Ito. H. (2007). Grain size distributions of fault rocks: A comparison between experimentally and naturally deformed granitoids. Journal of Structural Geology, 29, 1282-1300.

Marone, C. and Scholz, C. (1989). Particle-size distribution and microstructures within simulated fault gouge. Journal of Structural Geology, 11, 799–814.

McCarthy, T.S. (2006). The Witwatersrand Supergroup. In: The Geology of South Africa, MR Johnson, CR Anhaeusser, RJ Thomas, editor. Pretoria: Council for Geosciences, pp. 155–186.

McGarr, A. (2016). Anatomy of a Mining- Induced Fault Zone Revisited. U.S. Geological Survey, Menlo Park, CA.

McGarr, A., Sacks, I.S., Linde, A.T., Spottiswoode, S.M. and Green, R.W.E. (1982). Coseismic and other short-term strain changes recorded with Sacks-Evertson strainmeters in a deep mine, South Africa. Geophysical Journal of the Royal Astronomical Society, 70, 717-740.

McGarr, A., Spottiswoode, S.M., Gay, N.C. and Ortlepp, W.D. (1979). Observations relevant to seismic driving stress, stress drop, and efficiency. Journal of Geophysical Research, 84, 2251-2261.

McGarr, A. and Gay, N.C. (1978). State of stress in the earth's crust. Annual Review of Earth and Planetary Sciences, 6, 405-436.

Mngadi, S.B, Tsutsumi, A., Onoe, Y., Manzi, M.S.D., Durrheim, R.J., Yabe, Y., Ogasawara, H., Kaneki, S., Wechsler, N., Ward, A.K., Naoi, M., Moriya, H., Nakatani, M. and the DSeis team. (2020). The effect of gouge particles (“rock flour”) on rupture propagation along brittle shear fractures in deep and high-stress mines. International Journal of Rock Mechanics and Mining Sciences, 137, 104454. https://doi.org/10.1016/j.ijrmms.2020.104454.Mngadi, S.B., Durrheim, R.J., Manzi, M.S.D., Ogasawara, H., Yabe, Y., Yilmaz, H., Wechsler, N., Van Aswegen, G., Roberts, D., Ward, A.K., Naoi, M., Moriya, H., Ishida, A., SATREPS team and ICDP DSeis team. (2019). Integration of underground mapping, petrology, and high-resolution microseismicity analysis to characterise weak geotechnical zones in deep South African gold mines. International Journal of Rock Mechanics and Mining Sciences, 114, 79–91.

Mngadi, S.B. (2015). Integrated petrographic, geomechanical and seismological studies of rockmass behaviour during the extraction of the Cooke 4 shaft pillar. MSc thesis. The University of the Witwatersrand.

Monzawa, N. and Otsuki, K. (2003). Comminution and fluidization of granular fault materials: implications for fault slip behavior. Tectonophysics, 367, 127-143.

Moriya, H., Naoi M., Nakatani, M., van Aswegen, G., Murakami O., Kgarume T., Ward, A.K., Durrheim, R.J., Philipp, J., Yabe, Y., Kawakata, H. and Ogasawara, H. (2015). Delineation of large localized damage structures forming ahead of an active mining front by using advanced acoustic emission mapping techniques. International Journal of Rock Mechanics and Mining Sciences, 79, 157–165.

Ogasawara, H., Kato, H., Hofmann, G., Roberts, D., Piper, P., Clements, T., Ward, A.K., Yabe, Y., Yilmaz, H. and Durrheim, R.J. (2014b). BX CCBO in-situ stress measurements at earthquake prone areas in South African gold mines – a summary of mini-workshop. Proceedings of ARMA2014, Minneapolis, CD-ROM, paper number 14-7438.

Ogasawara, H., Kato, H., Hofmann, G., Piper, P., Clements, T. and Sakaguchi, K. (2013). In-situ stress measurements to constrain stress and strength near seismic faults in deep level South African gold mines. In Proceedings of the 6th International Symposium on In-situ Rock Stress, Sendai, 20-22 August 2013, 614-623.

Ogasawara, H., Liebenberg, B., Rickenbacher, M., Ziegler, M., Esterhuizen, V.H., Onstott, T.C., Durrheim, R.J., Manzi, M.S.D., Mngadi, S.B., Yabe, Y., Ogasawara, H., Kaneki, S., Cason, E., Vermeuren, J.G., van Heerden, E., Wiersberg, T., Zimmer, M., Kujawa, C., Conze, R., van Aswegen, G., Wechsler, N., Ward, A.K., Enslin, S., Tau, S., Bucibo, M.S. and the DSeis Team. (2019) status report: Drilling into seismogenic zones of M2.0–M5.5 earthquakes in South African gold mines (DSeis project). Proceedings of the 9th International Conference on Deep and High Stress Mining. The Southern African Institute of Mining and Metallurgy, Johannesburg, pp. 375-384. https://doi.org/10.36487/ACG_rep/1952_28_Ogasawara.

Olgaard, D.L. and Brace, W.F. (1983). The microstructures of gouge from a mining induced seismic shear zone. International Journal of Rock Mechanics and Mining Science and Geomechanics, Abstracts 20, 11-19.

Ortlepp, W.D. (1997). Rock Fracture and Rockbursts (South Africa Institute of Mining and Metallurgy, Monograph series M9, 1997).

Ortlepp, W.D. (1978). The mechanism of a rockburst, Proc. 19th U.S. Rock Mechanics Symp. Stateline, Nevada, pp. 476–483.

Reches, Z. and Lockner, D.A. (1994). The nucleation and growth of faults in brittle rocks. Journal of Geophysical Research, 99, 18159–18174.

Reches, Z., and Dewers, T. A. (2005). Gouge formation by dynamic pulverization during earthquake rupture. Earth and Planetary Science Letters, 235, 361–374.

Richardson, E. and Jordan, T. (2002). Seismicity in deep gold mines of South Africa - implications for tectonic earthquakes. Bulletin of the Seismological Society of America, 92, 1766–1782.

Robb, L.J., and Meyer, F.M. (1995). The Witwatersrand Basin, South Africa: Geological framework and mineralization processes. Ore Geology Reviews, 10, 67-94.

Rockwell, T.K., Sisk, M., Girty, G., Dor, O., Wechsler, N. and Ben-Zion, Y. (2009). Chemical and physical characteristics of pulverized Tejon Lookout Granite adjacent to the San Andreas and Garloc faults: implications for earthquake physics. Pure and Applied Geophysics, 166, 1725–1746.

Ryder, J.A. and Jager, A.J. (2002). A Textbook on Rock Mechanics for Tabular Hard Rock Mines. Braamfontein, Johannesburg: SIMRAC.

Sakaguchi, K., Obara, Y., Nakayama, T. and Sugawara. K. (1992). Accuracy of rock stress measurement by means of conical-ended borehole technique. Journal of the Japan Institute of Metals and Materials,108, 455-460.

Sammis, C. and Biegel, R. (1989). Fractals, fault-gouge, and friction. Pure and Applied Geophysics, 131, 255-271.

Sammis, C., Osborne, R., Anderson, J., Banerdt, M., and White, P. (1987). Self-similar cataclasis in the formation of fault gouge. Pure and Applied Geophysics, 124, 53–78.

SACS (South African Committee for Stratigraphy). (1980). Stratigraphy of South Africa. Part 1 (Comp L.E. Kent). Lithostratigraphy of the Republic of South Africa, South West Africa/Namibia and the Republics of Boputhatswana, Transkei and Venda. Pretoria: Geological Survey of South Africa.

SACS (South African Committee for Stratigraphy). (2006). A revised stratigraphic framework for Witwatersrand Supergroup. Lithostratigraphy of the Republic of South Africa. Pretoria: Geological Survey of South Africa.

Savage, H.M., and Brodsky, E.E. (2011). Collateral damage: Evolution with displacement of fracture distribution and secondary fault strands in fault damage zones. Journal of Geophysical Research, 116, B03405, doi:10.1029/2010JB007665.

Scholz, C.H. (2002). The Mechanics of Earthquakes and Faulting, 2nd edition. Cambridge University Press, Cambridge.

Shimamoto, T. and Logan. J.M. (1981). Effects of simulated fault gouge on the sliding behavior of Tennessee Sandstone: Nonclay gouges. Journal of Geophysical Research Solid Earth, 86, 2902-2914.

Sibson, R.H. (1986). Earthquakes and rock deformation in crustal fault zones. Annual Review of Earth and Planetary Sciences, 14, 149-175.

Spectris plc. (2005). Malvern Instruments: Instruction manual. Enigma Business Park (www.malvern.co.uk).

Spottiswoode, S.M. (1980). Source mechanism studies on Witwatersrand seismic events. PhD Thesis, University of the Witwatersrand, Johannesburg.

Spottiswoode, S.M. (1978). Fault gouge, driving stress, and seismic efficiency. Unpublished report. (Most of data is quoted in McGarr, A., Spottiswoode, S.M., Gay, N.C. and Ortlepp, W.D. (1979). Observations relevant to seismic driving stress, stress drop, and efficiency Journal of Geophysical Research, 84, 2251-2261.)

Sugawara, K. and Obara, Y. (1999). Draft ISRM suggested method for in situ stress measurement using the compact conical-ended borehole overcoring (CCBO) technique. International Journal of Rock Mechanics and Mining Sciences, 36, 307-322.

Turcotte, D. (1992). Fractals and Chaos in Geology and Geophysics. University Press, Cambridge.

van Aswegen, G. (2007). Ortlepp Shears – dynamic brittle shears of South African gold mines. In: Potvin, Y (Ed.) 1st Southern Hemisphere International Rock Mechanics Symposium, 16-19 September, Perth, Western Australia. pp. 111 – 120.

van Aswegen, G. (2013). Forensic rock mechanics, Ortlepp shears and other mining-induced structures. Key-note lecture. In: Malovichko, A. and Malovichko, D (Eds), 8 th International

Symposium on Rockburst and Seismicity in Mines (RaSiM8). GS RAS & MI UB RAS, Obninsk-Perm, ISBN 978-5-903258-28-4, pp. 11-29.

van Aswegen, G., Mngadi, S.B. Padilla, R. and Stonestreet, P. (In preparation). Detecting mining-induced seismic sources in borehole core.

Wechsler, N., Allen, E., Rockwell, T.K., Girty, G., Chester, J.S., Ben-Zion, Y. (2011). Characterization of pulverized granitoids in a shallow core along the San Andreas Fault, Littlerock, CA. Geophysical Journal International, 186, 401-417.

Wilson, B., Dewers, T., Reches, Z. and Brune, J.N. (2005). Particle size and energetics of gouge from earthquake rupture zones. Nature, 434, 749– 752.

Yuan, F., Prakash, V. and Tullis, T. (2011). Origin of pulverized rocks during earthquake fault rupture. Journal of Geophysical Research Solid Earth, 116, 1–18.

Yoshioka, N. (1986). Fracture energy and the variation of gouge and surface roughness during frictional sliding of rocks. Journal of Physics of the Earth, 34, 335–355.

List of Figures

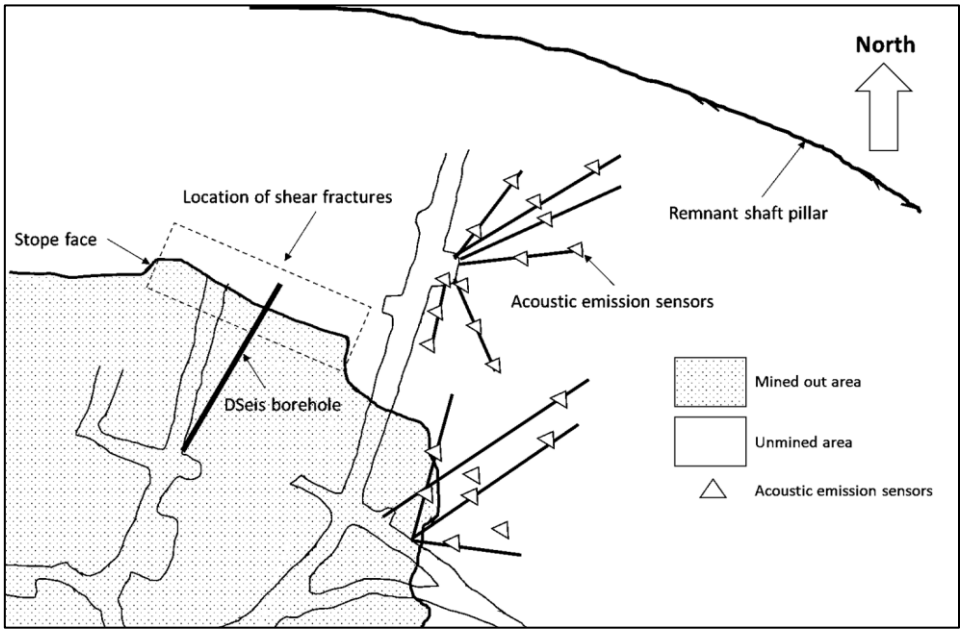


Figure 1. Remnant shaft pillar at 1.2 km depth showing the mined out area and unmined area, borehole configurations of SAPTREPS with anstalled acoustic emission sensors used to delineate fractures occuring ahead of the stope and DSeis Projects borehole, stope face, and the location of shear fractures associated with the stope face.

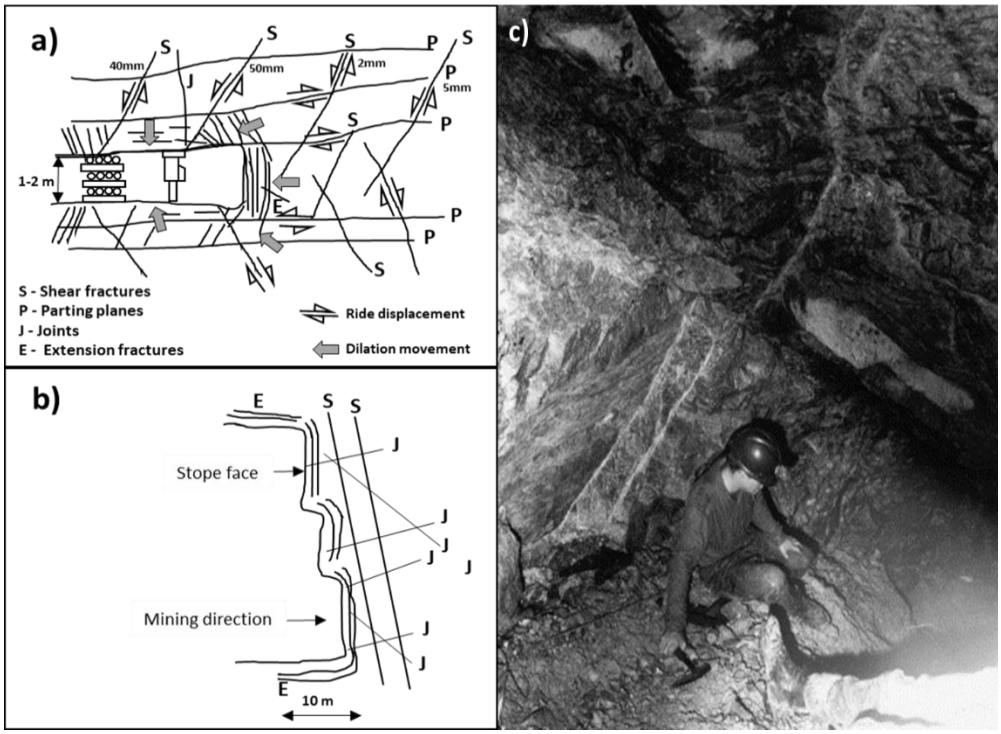


Figure 2. Shear fractures occuring ahead of the stope face. a) Vertical section. b) Plan view showing advancing stope face (Jager and Ryder, 1999). c) Shear fractures in the Western Claims pillar area of the ERPM gold mine situated ~ 2 km depth. Normal fault slip between 4 and 10 cm measured (Photograph by W. D. Ortlepp).

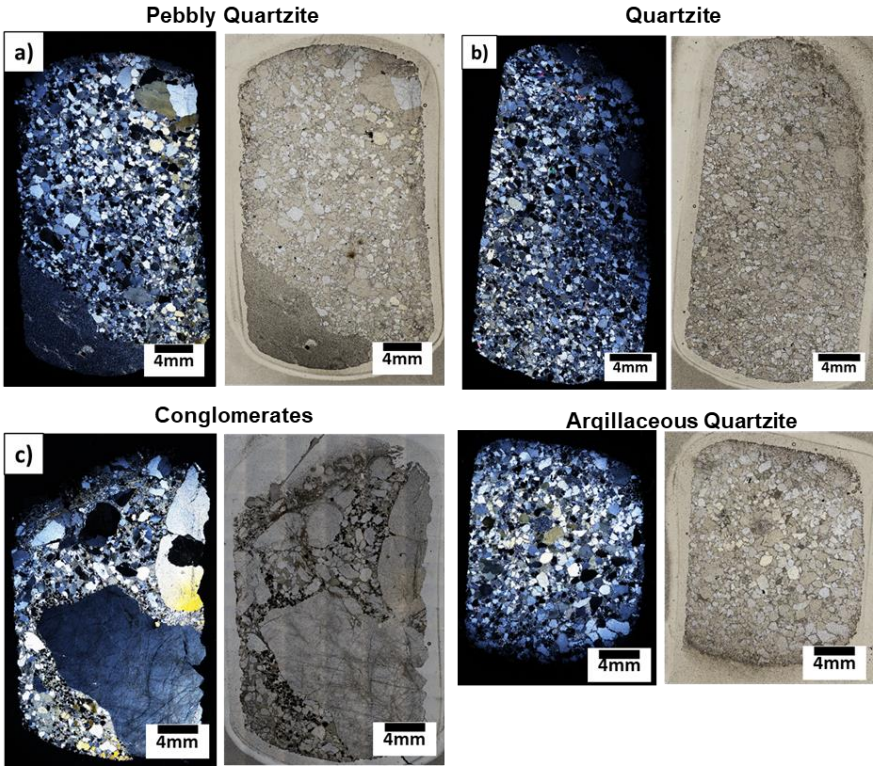


Figure 3. Thin-section micrographs confirm that the host rocks consist mainly of sand-sized quartz grains. The grain size distribution is estimated to be an average of 500 µm and up to 2 mm.

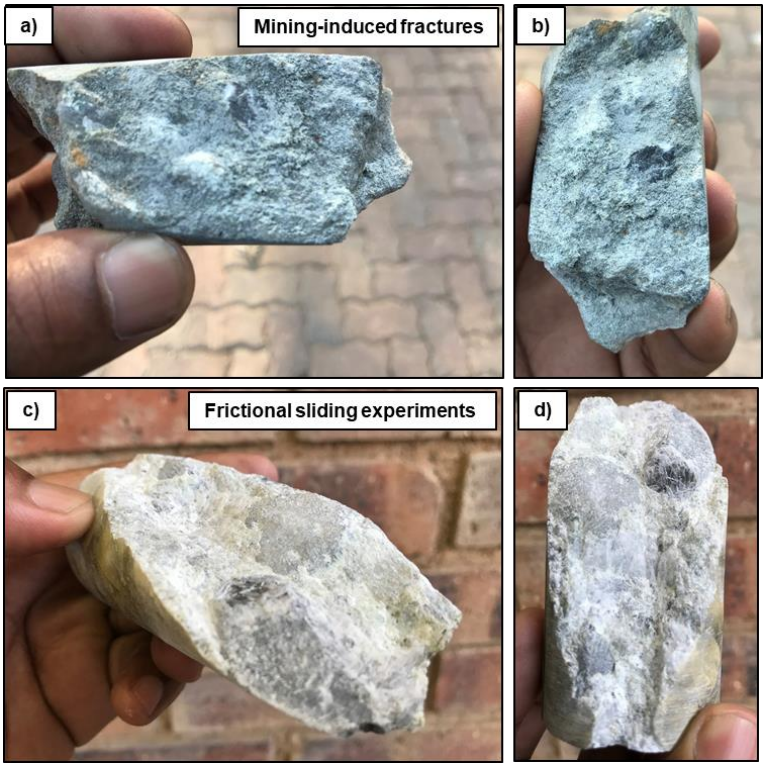


Figure 4. Illustration of shear fracture rupture surfaces generated from mining-induced Ortlepp shears (a & b) compared to the rupture surfaces generated from frictional sliding experiments (c & d).

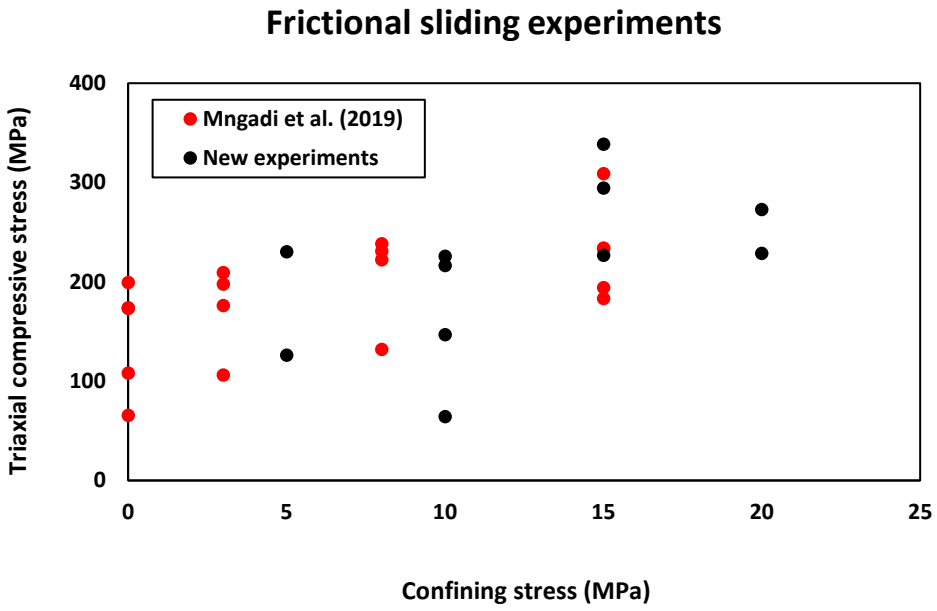


Figure 5. The uniaxial and triaxial compressive strength data shows a general increase in compressional strength with increasing confinement.

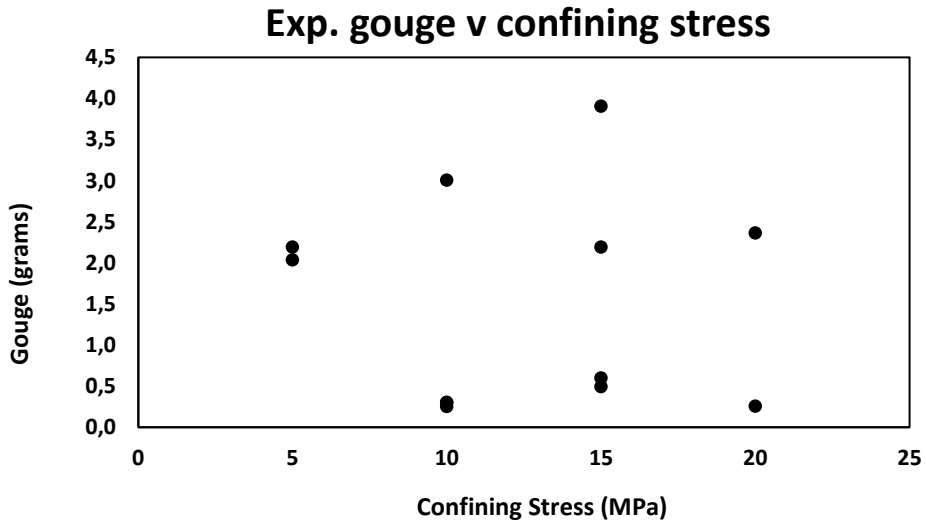


Figure 6. The weight of the gouge particles generated from frictional sliding experiments shown as a function of confining stress.

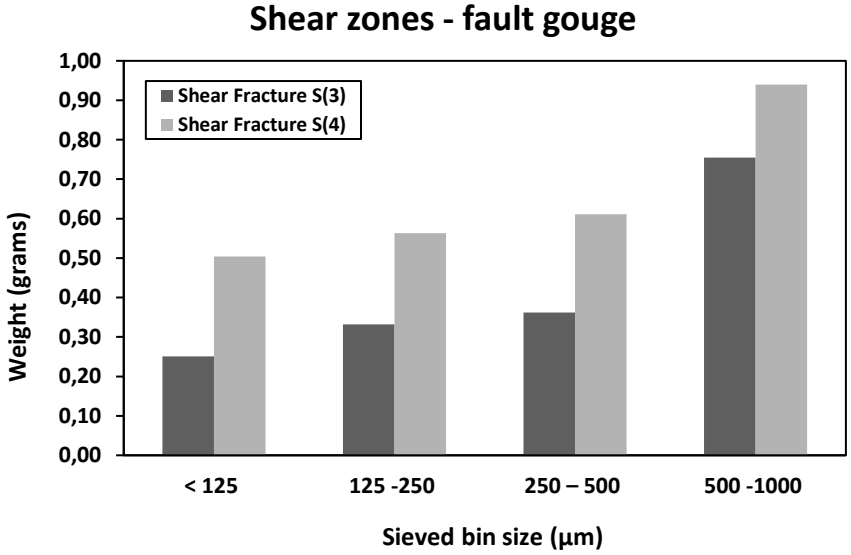


Figure 7. The particle size distribution of mining-induced brittle shear zones.

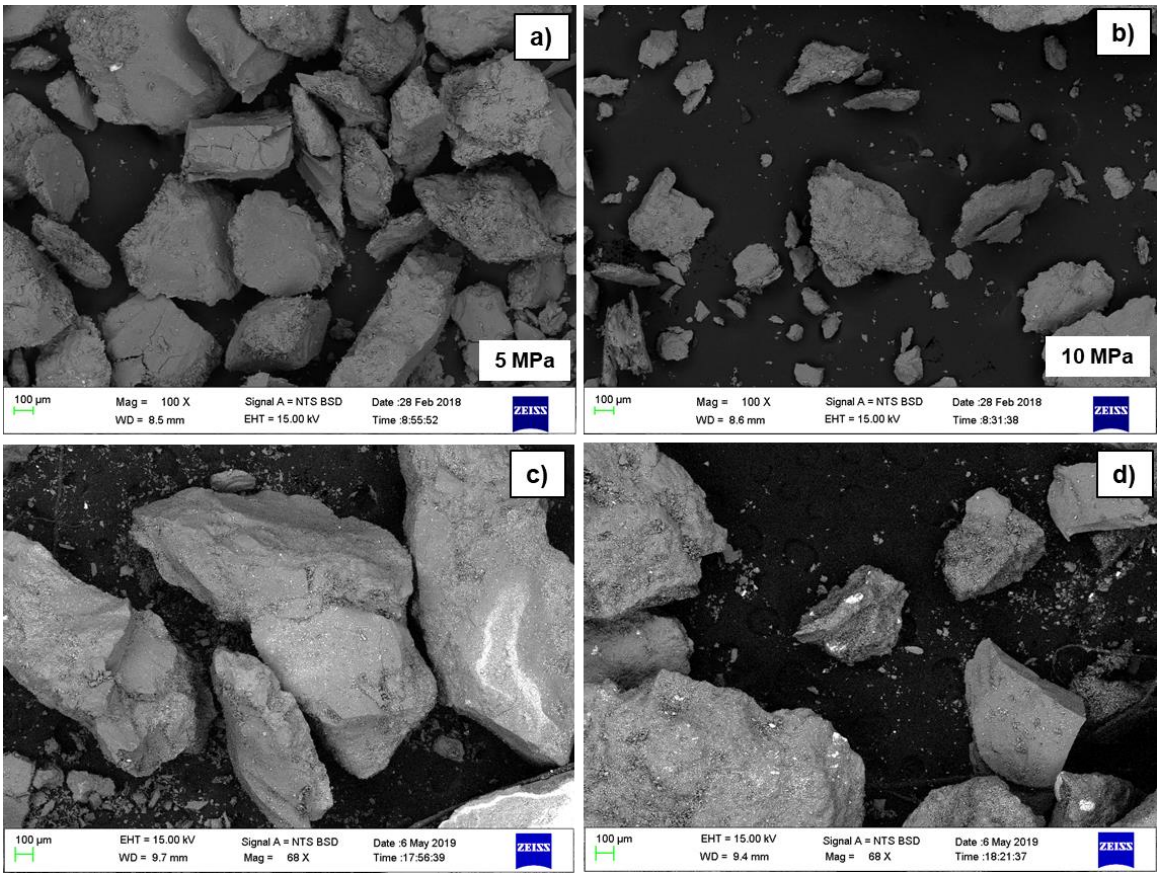


Figure 8. a-b) Scanning electron microscopy (SEM) analysis of fault gouge generated by the frictional sliding experiments, showing sub-rounded and angular particles. c-d) The SEM images of gouge samples collected from the fresh rock fractures, no aggregated pattern is observed. These fault gouge textures are similar to frictional sliding experiments showing sub-rounded and angular particles.

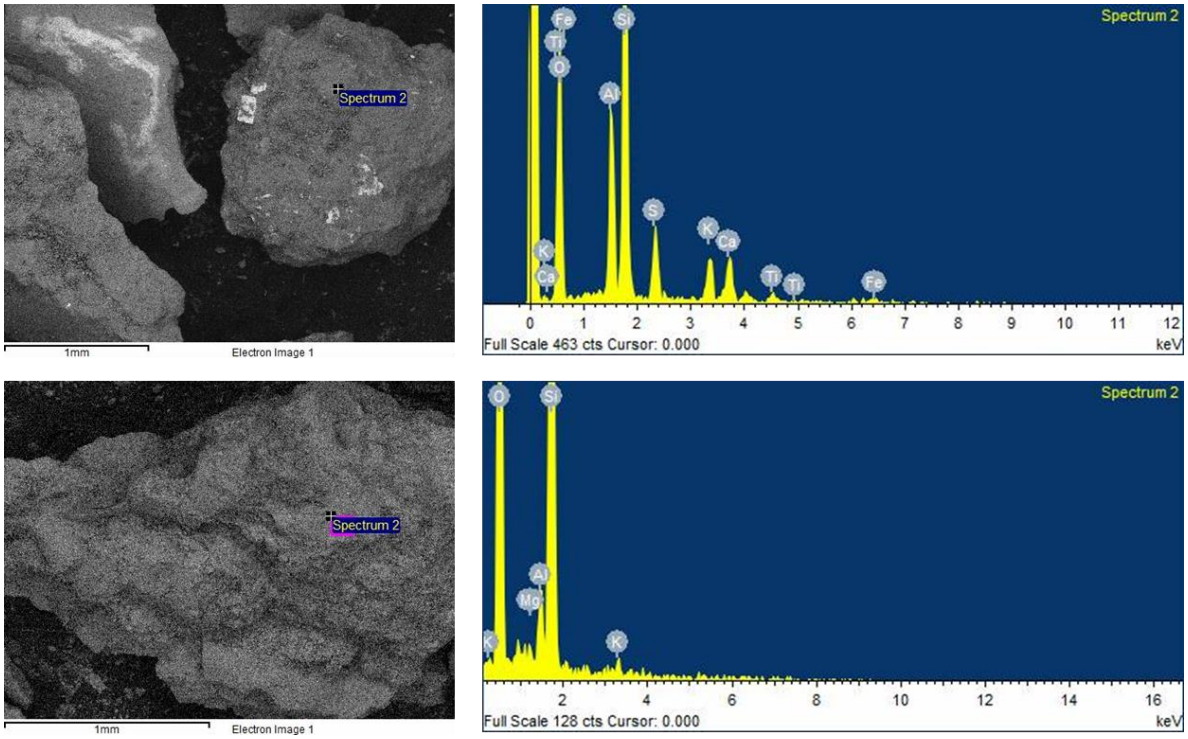


Figure 9. The Energy Dispersive X-ray Spectroscopy (EDS) shows the elemental composition of particles from experimentally-induced fractures. The spectra are clearly different meaning gouge particles vary in compostion.

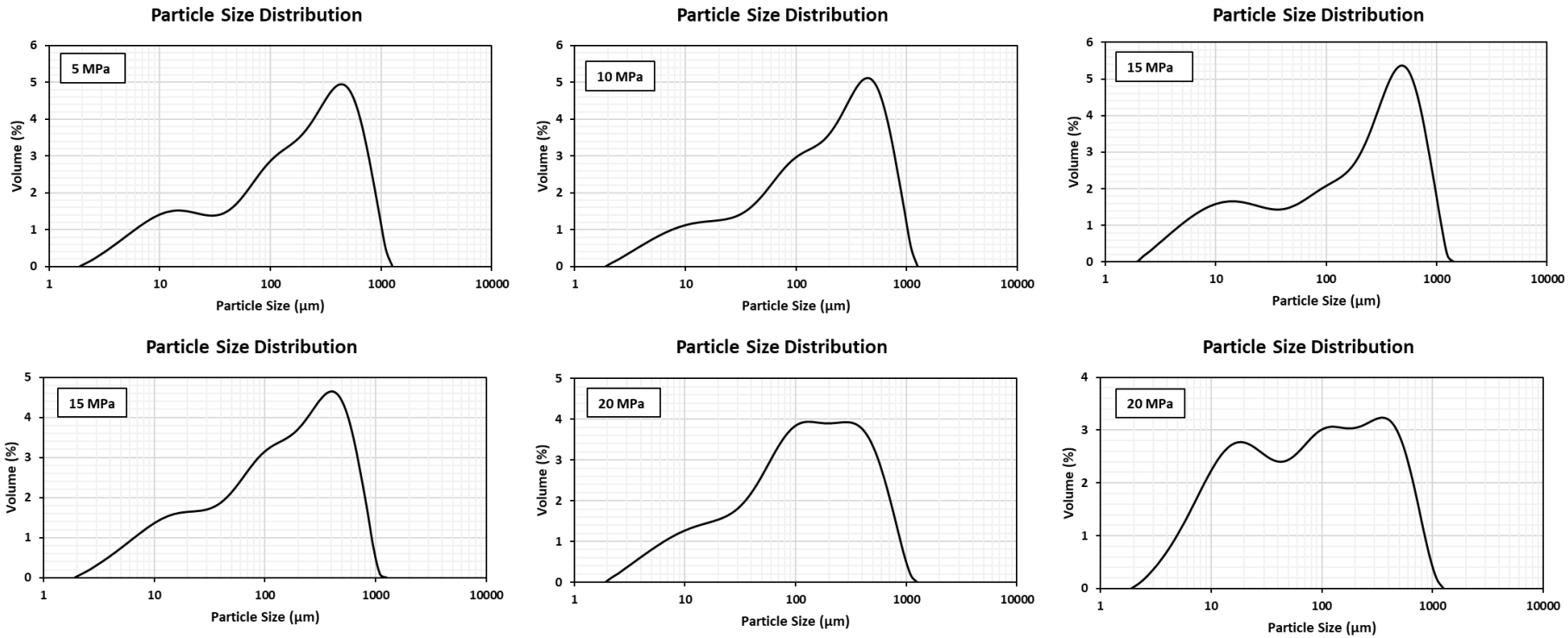


Figure 10. Fault gouge recovered from the frictional sliding experiments, particle size distribution approaches submicron scale ~1.9 µm.

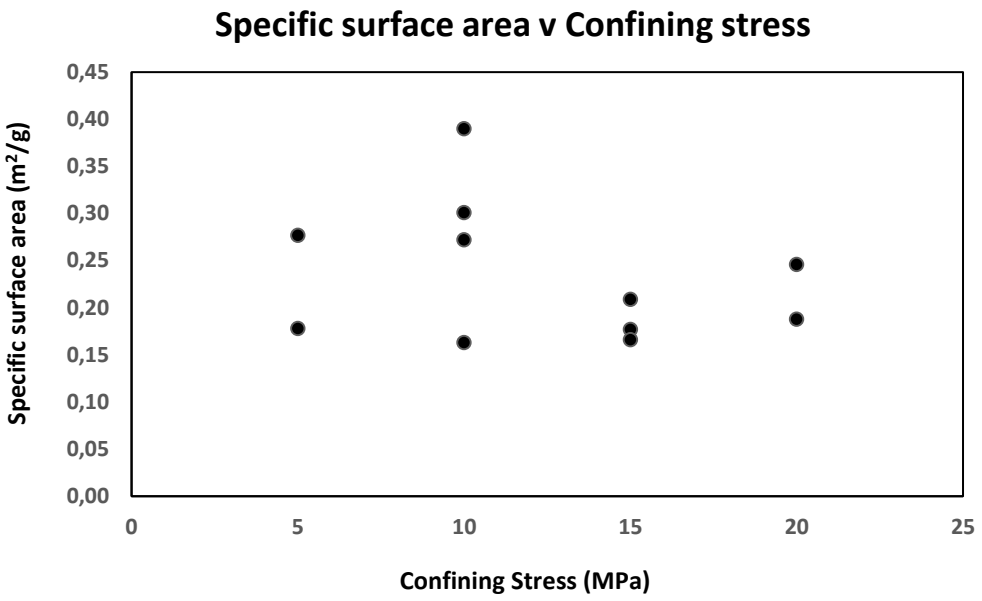


Figure 11. Measured specific surface area, SSA (i.e. surface area per unit mass) approach 0.277 m^2g^{-1} at lower confining stresses and 0.246 m^2g^{-1} at higher confining stresses.

List of Tables

Table 1: Three in-situ stress measurements were conducted in a single hole at Cooke 4 mine remnant shaft pillar at 1.0 - 1.2 km depth (Ogasawara et al. 2014b).

Principal Components	Stress (MPa)	Error (±)	*K-ratio*
σ_1	126.8	3.2	-
σ_2	41.0	3.1	0.3
σ_3	35.6	2.8	0.3
Principal Components	**Stress (MPa)**	**Error (±)**	***K-ratio***
σ_1	123	1.3	-
σ_2	41.5	1.4	0.3
σ_3	28.8	1.1	0.2
Principal Components	**Stress (MPa)**	**Error (±)**	***K-ratio***
σ_1	136.6	2.3	-
σ_2	47.7	1.8	0.3
σ_3	38.1	1.8	0.3
Av. Principal Components	**Av. Stress (MPa)**	**Av. Error (±)**	***Av. K-ratio***
σ_1	128.8	2.3	-
σ_2	43.4	2.1	0.3
σ_3	34.2	1.9	0.3

Table 2: Published research on rock type, particle size analysis, methods and fractal dimensions of fault rocks (modified from Keulen et al, 2007).

Authors (year)	Rock type	Location	Nat./Exp.	Method	Smallest Diameter (μm)
Folk (1968b).	Sandstone	Muddy Mountain thrust fault, Nevada	Natural and Experimental	sieve and pipette	100
Engelder (1974)	Sandstone	Uinta Mountains reverse fault, Utah	Natural and Experimental	thin-section, sieve and pipette	
“ ”	Sandstone	Bonita normal fault, New Mexico	Natural and Experimental	thin-section, sieve and pipette	50
“ ”	Sandstone	Muddy Mountain thrust fault, Nevada	Natural and Experimental	thin-section, sieve and pipette	25
“ ”	Sandstone	Hurricane fault, Utah,	Natural and Experimental	thin-section, sieve and pipette	
Gay and Ortlepp (1979)	Quartzite	East Rand Proprietary Mines, South Africa.	Natural	SEM	0.1
Spottiswoode (1980)	Quartzite	East Rand Proprietary Mines, South Africa.	Natural and Experimental	microscope	5.0
Olgaard and Brace (1983)	Quartzite	East Rand Proprietary Mines, South Africa.	Natural	SEM, TEM and Coulter counter	0.1
Sammis and Biegel (1989)	Granite	San Gabriel Mountains, California	Natural	LM and SEM	5
Marone and Scholz (1989)	Quartz sand	Ottawa	Experimental	SEM	1.5
An and Sammis (1994)	Granite	San Anreas Fault, Tejon Pass	Natural	Sieve and Coulter counter	2
“ ”	Gneiss	San Gabriel	Natural	Sieve and Coulter counter	2
“ ”	Tonalite	Lopez Canyon	Natural	Sieve and Coulter counter	2
Shao and Zou (1996)	Schist and gneiss	Qinling Mountain	Natural	LM and SEM	6
Monzawa and Otuki (2003)	Granite	Tanakura	Natural	LM	10
“ ”	Granite	It.-Shimotsutaki	Natural	LM	11
“ ”	Granite	Koi	Natural	LM	8.1
“ ”	Granite	Nojima	Natural	LM	7.7
Hadizadeh and Johnson (2003)	Sandstone	Masillon Ohio	Experimental	LM	3.5
Wilson et al. (2005)	Granite	San Anreas Fault, Tejon Pass	Natural	Coulter counter	0.04
Reches and Dewers (2005)	Quartzite	Bosman Fault, South Africa	Natural	Coulter counter	0.04
Chester et al. (2005)	Granite	San Anreas Fault, Punchbowl	Natural	LM and TEM	0.05
Heilbronner and Keulen (2006)	Granitoids	Verzasca	Experimental	SEM and digital	0.03
Keulen et al. (2007)	Granitoids	Nojima	Natural	SEM and digital	0.03
“ ”	Granitoids	Verzasca	Experimental	SEM and digital	0.03
Rockwell et al. (2009)	Granite	San Andreas Fault, Tejon Pass	Natural	Coulter counter and pipette	26
Wechsler et al. (2011)	Granitoids	San Andreas Fault, Littlerock	Natural	LM and Coulter counter	50

Table 3: Sieving of experimentally-induced gouge particles. Only two sieves were used, i.e. for particles less and greater than 1.0 mm size.

Rock type	Confining Stress (MPa)	Sieve size (mm)	Weight (g)	Stress failure (MPa)
Conglomerate	10	< 1.00	3.008	226
		> 1.00	3.314	
Quartzite	20	< 1.00	2.365	229
		> 1.00	1.635	
Quartzite	5	< 1.00	2.039	230
		> 1.00	1.376	
Quartzite	15	< 1.00	2.195	294
		> 1.00	2.241	
Quartzite	5	< 1.00	2.193	126
		> 1.00	0.71	
Conglomerate	15	< 1.00	3.906	227
		> 1.00	3.121	
Pebbly Quartzite	15	< 1.00	0.496	339
		> 1.00	0.118	
Argillaceous Quartzite	20	< 1.00	0.258	273
		> 1.00	0.076	
Quartzite	10	< 1.00	0.306	147
		> 1.00	0.137	
Argillaceous Quartzite	10	< 1.00	0.30	64
		> 1.00	0.029	
Pebbly Quartzite	10	< 1.00	0.254	217
		> 1.00	0.212	

Table 4: Summary of measurements of Poisson's ratio and Young's modulus (Mngadi, 2015).

Elastic Properties	Pebbly quartzite	Quartzite	Argillaceous quartzite	Conglomerate
Poisson's ratio	0.149	0.157	0.258	0.165
	0.153	0.197	0.233	0.228
	0.126	0.157	-	0.125
Av. Poisson's ratio	**0.142**	**0.171**	**0.245**	**0.173**
Young's modulus	74.47	77.92	56.16	34.56
	76.45	70.8	69.06	69.2
	81.88	73.73	-	76.34
Av. Young's modulus	**77.6**	**74.15**	**62.61**	**60.03**

Table 5: Density and seismic velocity measurements on rock samples (P-waves and S-waves).

Rock type	Density (g/cm^3)	P-wave velocity (m/s)	S-wave velocity (m/s)
Argillaceous quartzite	2.78	-	-
Pebbly quartzite	2.69	5631.58	2899.73
Conglomerate	2.74	5638.30	3430.42
Quartzite	2.69	5253.73	2901.10
Argillaceous quartzite	2.76	5711.23	3316.77
Pebbly quartzite	2.69	-	-
Conglomerate	2.69	5313.43	2717.56
Quartzite	2.68	5645.50	3430.87

Table 6: Particle size distribution and weights of sieved fault gouge from mining-induced fractures (Mngadi et al., 2020).

Shear zone S(3)		Shear zone S(4)	
Sieve size (µm)	**Weight (g)**	**Sieve size (µm)**	**Weight (g)**
< 125 µm	0.251 g	< 125 µm	0.504 g
125 -250 µm	0.332 g	125 -250 µm	0.563 g
250 – 500 µm	0.362 g	250 – 500 µm	0.611 g
500 -1000 µm	0.755 g	500 -1000 µm	0.940 g

Table 7: Measured specific surface area, with confining stresses and estimated fracture energy relative to the total energy release.

Confining stress (MPa)	Specific surface area (m^2/g)	Energy per unit volume (J/m^3)	Minimum (%)	Maximum (%)
5	0.177	3.36E+05	0.17%	0.40%
10	0.209	3.97E+05	0.20%	0.47%
15	0.246	4.68E+05	0.23%	0.56%
15	0.163	3.10E+05	0.15%	0.37%
15	0.178	3.38E+05	0.17%	0.40%
20	0.166	3.15E+05	0.16%	0.38%
20	0.188	3.57E+05	0.18%	0.43%

11. Discussion

This PhD thesis investigated mining-induced and naturally occurring faulting in deep South African gold mines, and compared the result to small scale laboratory tests. Rock mass stresses increase significantly during mining operations at greater depths and during the extraction of remnant shaft pillars. If these stresses exceed the rock mass strength, fractures can form around the excavation (Jager and Ryder, 1999). Shear fractures are often sources of large damaging seismic events (M 1-4), which pose risks to infrastructure and mine workers. In addition, the study examined a large seismic event that was possibly triggered by mining related activities such as continuous stress redistribution. Although not directly induced by mining, the Orkney M5.5 earthquake occurred in 2014, with its main rupture below mining levels. These events are often larger than M4 and are generally related to pre-existing weak structures such as dykes and faults. Lastly, the study compared and discussed seismogenic zones of naturally occurring and mining induced ruptures.

Manuscript 1 presents the petrological results, which show that the shaft pillar at Cooke 4 mine comprises of the Upper Elsburg reefs of Mondeor Formation that underlie the VCR (Venterspost Formation) and soft lavas (Westonaria Formation) (Harvey et al., 2006; Roberts and Schweitzer, 1999; Milev and Spottiswoode, 2002). The results from core logging and petrographic examination, confirmed by underground mapping, show that there are four sedimentary rock types making up the shaft pillar *viz.* quartzites, pebbly quartzites, argillaceous quartzite and conglomerates.

The study conducted uniaxial and triaxial compressive strength tests: quartzite (143-202 MPa) and pebbly quartzite (96-173 MPa) both show large ranges of uniaxial and triaxial compressive strengths. These uniaxial and triaxial compressive strength values are low compared to other quartzite rocks of the Witwatersrand Basin (200 – 300 MPa). This may be due to the heterogeneity of rock samples, or the presence of micro to macro-discontinuities such as stretched out matrix lenses and sedimentary foresets in quartzite. Micro-cracks are often visible in a stress-strain curve, and closure of these cracks occur during the initial loading. In addition, the core drilling directions were subparallel to the bedding planes, which may have affected the quartzite compressive strength (143 – 202 MPa). Rocks are often weaker along bedding planes (see Table 1 and Table 3: Manuscript 1) (Harvey et al., 2006; Briggs, 1982).

The compressive strength of conglomerate is lower (76-153 MPa) than pebbly quartzite (96-173 MPa). Argillaceous quartzite showed the lowest compressive strength (47-157 MPa). Quartzite, pebbly

quartzite and conglomerate typically have higher compressive strength than the hangingwall volcanic rocks such as soft tuffaceous lava (48 – 138 MPa) (Harvey et al., 2006; Roberts and Schweitzer, 1999). The Westonaria Formation (WAF) is consistently weaker (<100 MPa) and forms immediately above the Ventersdorp Contact Reef (VCR) (Glasspool and Ward, 2010; Roberts and Schweitzer, 1999) (see Table 3; Figure 15; Manuscript 1).

Microseismicity data could clearly delineated Ortlepp shear fractures forming ahead of the mining excavations, and further reveal that the turning point of these fractures occurs in the hangingwall (Figure 14; Manuscript 1). As discussed, the hangingwall is largely made up of tuffaceous soft lavas of the Westonaria Formation (Harvey et al., 2006). Underground mapping in the stope shows the layered argillaceous quartzite and conglomerate with numerous discontinuities from minor to medium scale faults. Some of these discontinuities were attributed to Ortlepp shears forming ahead of the stope. Moriya et al. (2015) analysed acoustic emission (AE) clusters that occurred ~20 m ahead of the stope, and characterised by a dip length of 10 m - 30 m. Moriya et al. (2015) reported that these AE clusters strike parallel to the stope face and dip ~65°. In addition, these AE clusters resembled typical Ortlepp shears (Moriya et al., 2015). The integration of these datasets allowed the development of a geotechnical fracture model for underground stopes (i.e., a weak/soft lava hanging wall and a quartzite/conglomerate footwall). This agrees with the fracture model developed by Roberts and Schweitzer (1999).

Manuscript 2 examines the propagation of Ortlepp shear dynamic ruptures at various slip velocities, and compares friction experiments conducted with and without the intervening gouge layer. The findings have an implication on the severity of rockbursts and seismicity during unstable rupture propagation in underground shear ruptures, which pose a risk to infrastructure and mine workers. After delineating these shear fractures and developing a fracture model using the integration of datasets such as high-resolution acoustic emission data and underground mapping, the DSeis team drilled into these fractures using the triple-tube technique to recover fragile fault rock material such as fault gouge, rock breccia and the host rocks described above.

The mineral composition has an effect on the frictional properties of rocks. The rock mass forming the remnant shaft pillar at Cooke 4 mine comprises mainly quartz and muscovite. In some instances, muscovite occurs in quantities greater than 10 wt%. Manuscript 1 studied these minerals in thin sections and conducted uniaxial compressive strength (UCS) tests. These rocks are relatively competent and

brittle, thus, South African gold mines are commonly called ‘hard rock’ mining environment. The fault gouge material recovered from the Ortlepp shears showed similar bulk composition as the surrounding host rocks, and that was interpreted to demonstrate that it had not undergone any modifications or major weathering. The fault gouge particles were relatively fresh.

The study compared the rock-on-rock and gouge friction experiments with previously published data (see Figure 15: Manuscript 2). Our findings are consistent and very much in line with the previously recorded weakening behaviour of quartz-rich rocks. Goldsby and Tullis (2002) conducted friction experiments on novaculite and quartzite at normal stresses of ~28 MPa, and quartzite at higher normal stress ~112 MPa. In 2004, Di Toro and co-workers performed friction experiments on novaculite at a normal stress of ~5 MPa. Hayashi and Tsutsumi (2010) carried out friction experiments on chert at a normal stress of ~1.5 MPa. Di Toro et al. (2011) performed friction experiments on quartz sandstone, novaculite and other materials at normal stresses greater than 5MPa. Rowe et al. (2019) conducted friction experiments on novaculite at a normal stress of ~ 2.5 MPa. Kanagawa et al. (2020) carried out friction experiments on intact agate and silica-gel gouge at a normal stress of ~1.5 MPa at sub-seismic to seismic velocities (1 - 1000 mm/s).

The friction experiments with and without the fault gouge, the quartzite rocks were used. At lower slip velocities, the measured steady-state friction values can be as high as ~0.8. This shows that our experimental data, with and without the fault gouge, obey Byerlee’s law (i.e., friction coefficient ~0.8). At higher slip velocities, a lower friction coefficient of ~0.2 was measured. These findings indicate that friction has a strong velocity dependence at higher slip rates for quartzite rocks.

Particularly, results of friction experiments on bare rocks surfaces (i.e., without the fault gouge layer) revealed a weakening behaviour at lower slip velocity (~ 5 mm/s). This agrees with friction experiments performed by Di Toro et al. (2004) on bare rocks (rock-on-rock friction experiments) (Arkansas novaculite) at lower slip velocities of 0.001 - 100 mm/s that showed weakening behaviour (i.e., considerable fall in the frictional resistance) at slip velocities greater than 1 mm/s. It should be noted that the quartzite used in our experiments comprises of slightly lower quartz abundance compared to the novaculite used by Di Toro et al. (2004) in their friction experiments at 5 MPa normal stress.

Rowe et al. (2019) conducted friction experiments on a similar rock type (novaculite) at sub-seismic slip velocities of ~ 0.1 - 100 mm/s and normal stresses of 2.5 MPa. The weakening behaviour

occurred at lower slip velocities, revealing the peak friction coefficient of ~0.7 being reduced to a steady-state value of ~0.45 – 0.6 (at slip velocities ~ 0.1 mm/s, 1 mm/s and 10 mm/s). Further, Kanagawa et al. (2020) used agate to perform friction experiments on both bare rock surfaces and with intervening gouge at sub-seismic slip velocity (1 – 100 mm/s) and normal stress of 1.5 MPa. The agate rock comprises of cryptocrystalline silica, chalcedony and 'microgranular' quartz. In addition, the X-ray diffraction of the agate rock revealed clear quartz peaks. Kanagawa et al. (2020) revealed that quartz rocks tend to weaken at lower slip velocities ~ 1 mm/s, compared to other common rock forming minerals where weakening occurs at higher slip velocities such as ~ 100 mm/s. This is clearly observed in our friction experiments conducted in quartz rocks. Here, I clearly observe slip weakening at low slip velocities of ~ 5 mm/s at comparable normal stresses (2 MPa vs 1.5 MPa).

Kanagawa et al. (2020) discussed that since the density, heat capacity, thermal diffusivity and peak friction coefficient of common rock-forming minerals do not vary significantly. The temperature (ΔT) at an asperity contact is largely dependent on indentation strength (Si). Correlations between Si and indentation hardness (Hi) can be drawn, and the mineral quartz has a considerably higher Hi (~12 GPa) compared to other 'common' rock-forming minerals such as micas 1 – 2 GPa, calcite 1.5 GPa, amphiboles 3.4 – 5 GPa, pyroxenes 3.4 – 6.5 GPa, feldspars 6 GPa and olivine 6.5 – 8.4 GPa (Spray, 2010). Consequently, at slip velocity (V), normal stress (σ) and area (A), the temperature (ΔT) at asperity contacts in quartz rocks will be greater than other common rock-forming minerals. This means larger frictional heat is produced at asperities, potentially accountable for weakening behaviour at lower slip velocities. At slip velocities of ~ 5 mm/s (Eq. (7): Manuscript 2), it is estimated that for our quartz rocks the flash weakening temperature is approximate ~ 574° C (Rice, 2006).

The weakening behaviour of the artificial and natural fault gouge is dependent on slip velocity. For instance, the frictional strength of the artificial gouge at low slip velocity of ~10 mm/s persisted at relatively high values, ranging from peak friction of ~ 0.86 to a steady-state value of ~ 0.72 over a slip weakening displacement (Dc) of ~ 6.9 m. At sub-seismic slip velocities of 100 mm/s, the weakening behaviour occurred from peak friction of 0.97 to steady-state friction of ~0.69 over slip weakening displacement of 9.6 m. At high seismic slip velocities (~1200 mm/s), dramatic weakening behaviour occurred from peak friction of ~0.91 to steady-state friction of ~ 0.26 over slip weakening displacement (Dc) of ~7.1 m. This dramatic weakening could be modelled by an exponential function (Mizoguchi et al., 2007).

The natural gouge recovered from DSeis drilling was sheared at sub-seismic slip velocities (~100 mm/s), the frictional strength decreased from peak friction of ~0.92 – 0.98 to steady-state friction of ~0.67– 0.71 over a slip weakening displacement of ~ 6.1 – 12.8 m, similar to artificial gouge at sub-seismic velocities. There are clear differences in the slip weakening displacement (Dc) between friction experiments performed with the fault gouge and on bare rock surfaces (rock-on-rock). The friction experiments performed with the intervening fault gouge tend to have larger slip weakening displacement, Dc, 6.9 – 13.6 m, whereas, the slip weakening displacement (Dc) for rock-on-rock friction experiments is shorter and averages ~0.5 – 3.8 m.

The strain is distributed or spread within a gouge layer before it is localized (Marone et al., 1990; Beeler et al., 1996). The strain distribution results in a more 'gradual' temperature increase during slip, delaying the activation of flash heating weakening mechanisms (Violay et al., 2014). This means the critical consequence of having a fault gouge layer is to delay flash heating. This is because there are more 'contacts' in a fault gouge to accommodate sliding, lowering the average slip velocity. As a result, the potential for activation of flash heating is reduced (Platt et al. 2014; Yao et al. 2016). This is observed in our friction experiment, the weakening distance for friction experiments with intervening gouge layer is large compared to rock-on-rock friction experiments. Rock-on-rock friction experiments weaken at lower slip velocities and over short slip displacement.

Applying the flash heating in equation 7 of Manuscript 2, ΔT was calculated. In Table 8 (Manuscript 2), the input parameters used are listed. For instance, at sub-seismic and seismic velocities, ~100 mm/s and 1200 mm/s, ΔT ~ 2568 °C and 3631 °C, respectively (Table 9: Manuscript 2). These findings agree with flash heating calculations performed by Kanagawa et al. (2020) on quartz rocks. At similar slip velocity of 100 mm/s, they found flash heating of ~2500 °C. This temperature is larger than the melting temperature of quartz (~1700 °C), and may suggest that melting occurred during experiments (Kanagawa et al., 2020). Therefore, for both our friction experiments (with and without intervening gouge layer), we suggest that the weakening mechanism are largely induced and controlled by flash heating. This is consistent with previous studies of friction experiments performed in quartz rocks that reveal a weakening behaviour at sub-seismic to seismic slip velocities ~1-1000 mm/s (Goldsby and Tullis, 2011; Platt et al., 2014; Yao et al. 2016; Rowe et al., 2019; Kanagawa et al., 2020).

The rock-on-rock friction experiment performed by Di Toro et al. (2004) shows a shorter slip weakening displacement of Dc < 500 mm at lower slip velocity of ~ 3 mm/s. In our friction experiments,

the weakening behaviour occurs at slip velocity of ~ 5 mm/s over a larger slip weakening displacement of 3.8 m compared to Di Toro et al. (2004). This may be due to the higher normal stress of 5 MPa, compared to the normal stress of 2 MPa. In addition, these critical results show the importance of normal stress in scaling Dc. Thus, these results mean that at higher normal stresses Dc computed from friction experiments may be the same order of magnitude, consistent with underground mining-induced Ortlepp shear fractures (i.e. slip displacements up to ~ 100 mm). This suggests that our results could be valid at deep level mining operations, which consists of high normal stresses.

Manuscript 3 examined the Orkney M_L 5.5 earthquake. The structure hosting the event was delineated using the in-mine seismic network and legacy 2-D reflection seismic data acquired for gold exploration by Anglo Gold Ashanti. The ICDP-DSeis team drilled into this seismogenic zone below the Moab Khotsong mine. In total, three holes were drilled. The drill core recovered from the ICDP-DSeis drilling of Holes A and B comprised of the Jeppestown Subgroup of the West Rand Group. The drill cores recovered from Hole A and Hole B showed strong lithological similarities, which were described in detail by Rickenbacher (2018). The holes A and B intersected the Roodepoort Formation, Crown Formation and Babrosco Formation of the Jeppestown Subgroup (Rickenbacher, 2018). These recovered drill cores are characterised by metasedimentary rocks, basalts and various intrusive rocks, including dykes and sills (Armstrong et al., 1991; Ogasawara et al., 2017; Rickenbacher, 2018). Rickenbacher's (2018) petrological analysis was limited to hand specimens and thin section analysis. Nonetheless, the studies revealed that intrusive rocks were largely similar in mineral composition, with variations in the extent of alteration (Rickenbacher, 2018). These analyses were focused on Hole A and B, at that time the Hole C was not yet drilled.

The study focused petrological analysis on Hole C (branch). At borehole depth (from the collar) of ~608 m, XRD analysis of the recovered host rocks and fault gouge material occurring adjacent to the lamprophyre dyke were performed. The fault gouge samples comprise of mainly talc and biotite (>40 wt%). This agrees with XRD analysis conducted by Kaneki et al (2018), where the fault gouge showed the presence of talc (Kaneki et al., 2018). These minerals have low friction, and often characterise seismogenic processes (Moore and Lockner, 2004; Ogasawara et al., 2019). This distinctive characteristic of low frictional behaviour comes from their structure that consists of strong covalent bonds within layers, and weak van der Waals forces between layers. In addition, these minerals consist

of low basal plane energies, allowing easy shearing along the tribological interface (Pawlak et al., 2008; Bucholz et al., 2012).

The DSeis petrological analysis (XRD results) and in-mine seismicity data revealed the composition and alteration of lamprophyre dykes, and the geometry of the NNW-SSE-striking structure that hosted the M5.5 event. The re-processed 2-D legacy reflection seismic data revealed that the study area is characterised by several sub-vertical structures that tend to branch. These sub-vertical structures are related to the attenuation of seismic amplitudes (see Figure 18: Manuscript 3). There appears to be no substantial displacement related to the majority of these structures, and this may indicate that these are strike-slip faults or they have throws below the seismic resolution limit. The structures are, therefore, interpreted as a combination of faults and dykes (i.e., dykes may have intruded into pre-existing faults). It is, however, hard to differentiate between the dykes and faults on the reflection seismic section with little displacement or offset. Hence, the DSeis drill core from Hole A, B and C to control the reflection seismic interpretation was used. The lamprophyre dyke was mapped adjacent to the fault and gouge material, which validates our interpretation of the reflection seismic section.

In addition, the reflection seismic section revealed high amplitude reflections that tend to die down laterally. These structures are high amplitude and were interpreted as sills. Once more, this interpretation was constrained through geological core logging and geophysical borehole logging, which revealed dolerite sills. Geophysical borehole logging and laboratory tests revealed that these seismic reflectors are due to the acoustic impended contrasts between the high P-wave velocity (6.7 - 6.5 km/s) and density (2.99 – 3.06 g/cm^3) of the intrusive rocks and adjacent metasedimentary rocks P-waves (5.9 - 5.5 g/cm^3) and density (2.71 - 2.86 g/cm^3).

The re-processed 2-D legacy reflection seismic data revealed the numerous strike-slip faults, as well as dykes and sills intruded into the West Rand Group rocks. Hughes et al. (in prep.) dated the lamprophyre dykes between the ages of ~177.2 and 131.8 Ma. The age data is consistent with the interpretation of the structural relationship on the reflection seismic data, suggesting that lamprophyre dykes may have intruded into an existing fault displacing all Witwatersrand Supergroup strata.

Lamprophyre dykes have also been reported in the Bushveld Complex. They tend to be related to rockburst and seismicity (Daya, 2019; Hughes et al. in prep.). This failure is said to be caused by decomposition and gas outbursts. In addition, when dykes and sills intersect, large damaging seismic

events tend to occur (van Heerver, 1982), which we find in our study area. Typically, dykes tend to intrude mechanically weak zones. These zones of defect or discontinuity (faults, etc.) tend to be related to stress concentration over time, especially around mining operations and when the fault strength is exceeded faults may be reactivated. This is consistent with the work performed by Yabe et al. (2019), measuring the differential stress in the drill core using the diametrical core deformation analysis (DCDA) stress-measurement technique (Funato and Ito, 2017). The stress measurements revealed the localisation in specific zones adjacent to (1) the M5.5 rupture in Hole B; (2) the upper edge of the aftershock; and (3) the hypersaline brine fissure in Hole A (Yabe et al., 2019).

The study also conducted friction experiments at sub-seismic slip velocity (100 mm/s) on the M5.5 fault gouge recovered from deep drilling at Moab Khotsong mine. The fault gouge was sheared at slip velocities of ~100 mm/s and applied normal stress of ~2 MPa. The peak friction coefficient reached ~1.0, and weakening to steady-state friction of ~0.66. The slip weakening distance occurred over ~9.1 m (Figure 21; Table 8: Manuscript 3). This is comparable to friction coefficient values obtained from Ortlepp shear fractures (Cooke 4 mine) at slip velocity of 100 mm/s and normal stress of 2 MPa. The natural gouge sample S (3) revealed peak friction of ~0.98 and weakened to steady-state friction of ~0.67 over a slip weakening displacement of ~12.8 m (Manuscript 2). Also, the natural gouge sample S(4) at similar experimental conditions, revealed peak friction of 0.92 and weakened to steady-state friction of 0.71, over a slip weakening displacement of ~6.1 m. These results indicate that the weakening behaviour of natural gouge samples from Cooke 4 and Moab Khotsong mines is similar (see Table 8: Manuscript 3) (Manuscript 2).

The seismogenic zone at Cooke 4 mine is controlled by mechanical damage induced by mining-related stresses (Manuscript 1; Manuscript 2). At Moab Khotsong mine, the investigation showed that there are three processes controlling the M5.5 earthquake seismogenic zone: (a) intersection between lamprophyre dyke and dolerite sills, which creates a mechanical zone of weakness; (b) tectonic and/or mining-related stresses; and (c) chemical processes resulting from water and rock interaction (Wiersberg et al., 2019).

To understand Ortlepp shear fractures fully, Manuscript 4 investigates the energy partitioning of these shear fractures and compares them to experimentally induced fractures. It is accepted that Ortlepp shears can be simulated by the shear zones reproduced in the laboratory experiments under triaxial compressive strength tests (van Aswegen, 2008). Thus, the study conducted triaxial

compressive strength tests with high confining stresses up to 20 MPa (machine limit), comparable to underground stress conditions. These triaxial compressive strength tests were performed on drill core recovered close to mining-induced normal faults. Spottiswoode (1979) also performed triaxial compressive strength experiments using the similar quartzite recovered from the Witwatersrand gold mines at confining stresses between 13 and 28 MPa.

The results showed that the triaxial compressive strength increases with increasing confining stress. These findings are generally consistent with the literature (Manuscript 1). The triaxial compressive strength ranged between the minimum of 64 MPa and maximum of 339 MPa. These differences in strength can be explained since the Witwatersrand quartzite fluctuates in composition from almost pure quartz quartzite to argillaceous quartzite with substantial clay minerals. The densities and P-wave velocities of quartzite, pebbly quartzite, argillaceous quartzite and conglomerate were measured (see Table 5: Manuscript 4). The measured average values of seismic P-wave and S-wave velocities is 5532 m/s and 3116 m/s, respectively. These lithologies indicate a typical density of ~2.72 g/cm^3.

Mining induced shear fractures as discussed in Manuscript 4 are characterised by the presence of a fault gouge (finely comminuted rock termed ‘rock flour’ in South African gold mines) often with a thickness of up to ~50 mm. In the study of the fault gouge particles, the specific surface area (S) measured were between 0.163 m^2/g and 0.246 m^2/g. These results show three-fold difference compared to the specific surface area values (0.7 m^2/g) attained by Olgaard and Brace (1983) on fresh fault gouge, which they recovered from deep mines in South Africa. The specific surface area and density measurements were used to calculate the energy consumed in creating a new fracture surface. The study obtained low values (0.15% – 0.56%), this suggests that only a minor share of the total earthquake energy budget is consumed in breaking or shattering rocks. This agreed with findings by several scholars with estimates ranging from 1% or less, and this appears to be the consensus (Olgaard and Brace, 1983; Yoshioka, 1986; Chester et al., 2005; Rockwell et al., 2009; Wechsler et al., 2011). Nonetheless, some estimations are very high, to as much as 50% (Reches and Dewers, 2005; Wilson et al., 2005 Barber and Griffith, 2017). In these cases, the measuring method seems to have contributed to the skewed results and is often criticised.

Olgaard and Brace (1983) computed the energy consumed (~1% - 10%) in grain crushing for quartzite rocks in rupture zones occurring in deep and high stress South African gold mines.

Spottiswoode (1979) performed triaxial compressive tests and examined the particle size distribution of the comminuted 'rock flour' generated from a series of laboratory experiments. Similar to our studies, they used quartzite rock types from the East Rand Proprietary Mines (ERPM) in the Witwatersrand Basin. They used confining stresses of 13 - 27 MPa, comparable to our studies and underground conditions. Spottiswoode's (1979) findings were revised and reinterpreted by McGarr et al. (1979) revealing estimated seismic efficiency of 0.36% to 3.6%. This suggests that the seismic efficiency may be comparable to order of magnitude of the energy required in creating a new fracture surface.

There remains a key unresolved aspect of these brittle Ortlepp shear fractures occurring ahead of the stope face – a consistent and accepted 'criteria' used to identify these seismic sources in the diamond drill core. Manuscript 5 develops new criteria that may be used to identify these seismic sources in drill core to mitigate risks posed by rockburst and seismicity, especially in deep and high-stress underground mines. Identification of these seismic sources in drill core will assist mine workers to improve roof support (based on seismic source patterns), and evacuate mining crew where there is potential hazard around and ahead of the stope. The core analysis is the best and direct method to characterise in-situ fractures. Using the triple-tube core barrel drilling technique (Ogasawara et al., 2019; Manuscript 2), comprehensive analysis of newly formed shear fractures were performed for the Cooke 4 core, with negligible core loss in some areas.

In the study area, a 'densely fractured' rock mass consisting of shear fractures occurring ahead of the stope face were targeted. Thus, it is critical that a cautious unconventional drilling approach is used, a "triple tube" drilling method with stationary inner metal split spoon complemented by a kitchen foil to ensure best core recovery. However, disadvantages associated with core recovery and examination using this triple-tube drilling method is that a turnaround time can be slow and relatively expensive (see Table 4: Manuscript 5). With the new recommended identification criteria of a seismic source, the core examination should be at least faster and straightforward.

Important features of a shear fracture are the existence of the fault gouge and rock breccia. Detail surface geometry of the shear rupture is often characterised by soft slickensides and cross fabric. The presence of the fault gouge and rock breccia at the suspected shear fracture position in the core tray may be a good indication of a shear rupture zone. To achieve this level of detail and core recovery, not only triple tube drilling is required but also a clear procedure and carefulness during drill core transportation from drill site to the core shed must be in place. The drilling site is often underground and

the core shed is usually on surface. Therefore, vibrations during the core transportation could shake off the drill core resulting in shearing of the fine material from the fracture surfaces. In addition, we strongly discourage washing or hosing of the core before their examination. The geological core logging should be performed directly after drilling with comprehensive high-resolution photographic records and good lighting, if not in direct sunlight, a flash should be used.

Examination of this detailed fresh mining-induced Ortlepp shear fractures provides evidence and insight into their formation, physics and mechanics. In our study, we could observed soft slickensides, which is evidence for shear displacement occurring along the rupture zone. They also indicate that rock failure may have occurred tens of meters ahead of the mining excavation (van Aswegen, 2013). This is consistent with acoustic emissions data analysed by Moriya et al. (2015) and Manuscript 1 that delineated brittle shear fractures forming tens of meters ahead of the stope face, reminiscent of typical Ortlepp shears. In cases where shear rupture surfaces had no slickensides, which may suggest that the shear mechanism was dilatational or transtensional, meaning that shear failure may have occurred close to the stope face (van Aswegen, 2013).

The rupture surface roughness may indicate the dilatation mechanism during shear displacement, and influence the initial direction of slip (Reches and Lockner, 1994). The rupture surface of our shear fractures are corrugated, which may mean that the shear displacement was largely controlled by a dilatational mechanism. Reches and Dewers (2005) reported that the fault gouge is mainly generated from a process of stress intensity and volumetric strain (Reches and Dewers, 2005; van Aswegen, 2008). Manuscript 2 also suggest that the wear process generates a considerable amount of gouge.

Manuscript 2 concluded that the presence of the fault gouge influences fault rupture propagation processes along underground brittle shear zones. The presence of the fault gouge in the rupture zone and the wear rate, may cause strengthening of the fault (or brittle shear fracture), and delays the weakening or the unstable rupture propagation at low to high slip velocities (~1.0 – 100 mm/s).

12. Conclusion and Future work

12.1. Conclusion

In deep levels South African gold mines, shear fractures develop and progress ahead of tabular active mining stopes. Normal faulting occurs since mining activities increase the vertical maximum principal stress. At depths greater than 1000 m such as the Cooke 4 mine, I delineated the evolution of these shear fractures using high-resolution acoustic emission network down to Mw -5. The integration of multidisciplinary datasets *viz.* microseismic data, geochemistry, geology, petrophysics and rock mechanics has enabled the development of a fracture model for different geotechnical zones (i.e., weak/soft lava hangingwall and quartzite/conglomerate footwall). In addition, the turning point of these shear fractures occur in weaker or soft strata, which has implications for the fall of ground and support design.

In 2017, using existing underground seismicity data and underground mapping, the DSeis team used 1.5 m-long triple-tube drilling to recover these shear fractures occurring ahead of the stope at Cooke 4 mine in the remnant pillar. The DSeis team drilled and successfully recovered both the host rocks, fault gouge, breccia and fault rocks associated with these shear fractures. The shear fracture system was well preserved. These recovered shear fracture systems were compared to shear ruptures generated from triaxial compressive tests with confining stresses up to 20 MPa, similar to stress levels in the remnant pillar at Cooke 4 mine. The energy budget was estimated, and revealed that the energy consumed during the creating a new fracture surface is extremely low (0.15% and 0.56%) and it is comparable to seismic efficiency.

Further, the study performed a series of friction experiments to examine the effect of the fault gouge (namely rock flour in South African mines) generated by mining-induced shear fractures occurring ahead of the stope during rupture propagation. These friction experiments revealed that the presence of the fault gouge and its formation during rupture propagation temporally strengthens the fault at lower slip velocities (i.e., slip weakens faster without the presence of the fault gouge). These results have vital implications for the severity of rockburst and seismicity.

At Cooke 4 mine, a detailed examination of the recovered drill core samples and fault rocks allowed us to develop a criterion that may be used to distinguish newly formed shear ruptures from pre-existing geological discontinuities and drilling-induced fractures in any drill core. We developed a new criteria to identify the intersection of seismic sources in a diamond drill core.

At Moab Khotsong mine, the study examined the architecture, physics and mechanics of the 'unusual' M5.5 strike-slip earthquake that occurred below the mining level. Distinct from shear fractures occurring at mining levels with a normal-slip fault displacement at Cooke 4 mine, this fault had the M5.5 earthquake was within the legacy 2-D reflection seismic data acquired in 1992 for gold exploration. This data was re-processed and re-interpreted to make clear the geological structures hosting the M5.5 earthquake. The re-processed and re-interpreted legacy 2-D reflection seismic data revealed that the geological structure hosting the M5.5 earthquake crosscuts the entire Witwatersrand Supergroup, the Transvaal Supergroup, and potentially up to the base of the Karoo Basin.

Using the in-mine seismicity data to delineate the M5.5 rupture plane, the DSeis team successfully drilled and recovered the fragile core, host rocks, rock breccia, sampled hypersaline brine, dolerite sills and lamprophyre dyke. The integration of 2-D reflection seismic data, in-mine seismicity data, geological core logging and geophysical borehole logging (gamma, density and velocity) allowed us to fully describe and make clear a near-vertical structure, striking NNW-SSE, intruded by sills and dykes.

Here, the investigations suggest that the lamprophyre dyke is relatively younger and that it intruded into an existing fault and older dolerite sills. The M5.5 earthquake occurred as a result of reactivation as a left-lateral strike-slip fault. I suggest that three active processes are influencing the M5.5 earthquake seismogenic zone: (a) the fault zone architecture (e.g., interception of lamprophyre dykes and dolerite sills); (b) the mechanical process induced by tectonic and/or mining-related stresses; and (c) the chemical processes caused by the fluids. This is different from Cooke 4 mine normal faults that are largely controlled by the mechanical processes induced by mining-related stress.

12.2. Future work

I. The dynamic rupture process during large earthquakes has been analysed using slip weakening models (Ida, 1972). In the model, the friction coefficient decreases from peak friction (μ_p) to steady-state friction coefficient (μ_s) over a slip weakening displacement (Dc). For Dc, there are differences between our friction experiments and underground observations. The Dc obtained from our experiments at low normal stress of 2 MPa are estimated between 0.5 to 3.8 m, which is one order of magnitude larger than the values estimated from seismic wave analysis (Ide and Takeo, 1997; Olsen et al., 1997) and our underground observations, even for earthquake magnitudes of M 4. However, the D_c values at higher normal stresses approach the same order of magnitude compared to D_c values observed underground from classical Ortlepp shears (see Di Toro et al., 2004). Deep and high stress underground mines have higher normal stresses; under those high normal stress conditions steady-state will be reached over shorter shear displacement. Therefore, future work should analyse the slip weakening displacement of the underground shear fractures at higher normal stresses, similar to underground conditions, to examine the slip weakening displacement changes with the normal stress.

II. Furthermore, future work can consider the effect of the gouge thickness. How much gouge is needed to delay weakening? We think this is a very important question. However, we didn't investigate the amount of gouge thickness needed for slip weakening to be delayed. This important question should form part of future studies. Previous work on the effect of gouge thickness to D_c, Marone and Kilgore (1993) performed gouge friction experiments using quartz sand to simulate a granular gouge layer and varied the initial thickness of the gouge layer and particle size to examine their influence on D_c at slower slip velocities (0.001 – 0.01 mm/s) compared to our experiments and larger normal stress of 25 MPa. The friction experiments revealed that critical slip distance D_c scales with shear strain in the simulated fault gouge. They reported that D_c is 'controlled' by the gouge thickness containing the localized shear.

III. What is the role of slip localization on this slip weakening effect? Study of samples after laboratory tests may be crucial to answering these questions, which are essential to allow extrapolation to nature. I tried to conduct post-experiment observations as I wanted to see if there was evidence of shear localisation on the gouge samples and if that could be comparable to any physical

observation underground. The samples were cut, however, the gouge was not observed on thin sections; perhaps the epoxy didn't work properly.

13. The ICDP DSeis team

S.B. Mngadi, M.S.D. Manzi, R.J. Durrheim, H. Ogasawara, A. Ishida, H.Y. Ogasawara, K. Sugimura, T. Noda, M. Kanematsu, R. Tadokoro, M. Higashi, S. Yoshida, K. Suzuki, Y. Mima, B. Liebenberg, E. van Heerden, C. van der Nest, B. Freese, B. Watson, L. Linzer, S. Enslin, S. Tau, D. Ligaraba, T.J. Mabaso, T. Lepote, N. Masondo, M. Ziegler, M. Richenbacher, N. Berset, Y. Yabe, T. Ito, Y. Mukuhira, S. Abe, T.C. Onstott, M. Lau, D.M. Nisson, Z. Garvin, R. Harris, T.L. Kieft, E. Cason, J. Vermeulen, E. van Heerden, J.C. Castillo, L. Scheepers, G. Hofmann, Y. Jooste, M. Rodel, T. Hirono, Y. Yokoyama, A. Funato, D. Roberts, N.Z. Nkhosi, J. Machake, T. Wiesberg, M. Zimmer, C. Kujawa, C. Janssen, A. Schleicher, R. Conze, N. Wechsler, H. Kato, A.K. Ward, S. Morema, V. Visser, K. Bosman, W. Meintjes, M. Grobbelaar, C. Claill, A. Cichowicz, S. Bucibo, G. van Aswegen, T.L. Kieft, J.J. Mori, A.Tsutsumi, M. Naoi, S. Kaneki, T. Yasutomi, W.L. Ellsworth, M. Boettcher, S.A. Shapiro, C. Dinske, S. Sangaraju, S.N. Somala , H. Gupta, P. Dight, Y. Yamamoto, T. Ishikawa, T. Matsuzaki, K. Arai, Tadai, T. Komatsu, N. Shibuya, S. Yanagimoto, Y. Katayama.

14. References

Adams, G.R, Jager, A.J. and Roering, C. (1981). Investigation of rock fracture around deep level gold mine stopes. In: Proceedings of the 22nd U.S. Rock Mechanics Symposium. M.I.T, pp. 159-185.

Arellano, J.P. (2012). Copper Mining and its Impact on Chile's Development. Integration and Trade. Integración y Comercio, 35, 45-57.

Armstrong, R.A., Compston, W., Retief, E.A., Williams, I.S. and Welke, H.J. (1991). Zircon ion microprobe studies bearing on the age and evolution of the Witwatersrand triad. Precambrian Research, 53, 243–266.

Anon. (1924). Report of the Witwatersrand Earth Tremors Committee. Cape Town: The Government Printer, Union of South Africa, pp. 64.

Bam, J., Ntsebeza, L. and Zinn, A. (2018). Whose history counts: decolonising African pre-colonial historiography. Stellenbosch, South Africa, pp. 179–199.

Barber, T. and Griffith, W.A. (2017). Experimental constraints on dynamic fragmentation as a dissipative process during seismic slip. Philosophical Transactions of the Royal Society, 375: https://doi.org/10.1098/rsta.2016.0002.

Beach, A. and Smith R. (2007). Structural geometry and development of the Witwatersrand Basin, South Africa. In: Deformation of the Continental Crust: The Legacy of Mike Coward. Geological Society of London, pp. 533–542. https://doi.org/10.1144/GSL.SP.2007.272

Beeler, N.M., Tullis, T.E., Blanpied, M.L. and Weeks, J.D. (1996). Frictional behavior of large displacement experimental faults. Journal of Geophysical Research, 101, 8697–8715.

Ben-Zion, Y. and Sammis, C.G. (2003). Characterization of fault zones. Pure Applied Geophysics, 160, 677–715.

Biegel, R.L., Sammis, C.G. and Dieterich, J.H. (1989). The frictional properties of a simulated gouge having a fractal particle distribution. Journal of Structural Geology, 11, 827-846.

Bosman, J.D. and van Aswegen, G. (2003). Dynamic failure of pillar remnants – case studies. ISRM 2003 - Technology roadmap for rock mechanics, SAIMM, Johannesburg, pp. 143 – 149.

Boulton, C., Yao, L., Faulkner, D.R., Townend, J., Toy, V.G., Sutherland, R., Ma, S. and Shimamoto, T. (2017). High-velocity frictional properties of Alpine Fault rocks: mechanical data, microstructural analysis, and implications for rupture propagation. Journal of Structural Geology, 97, 71-92. doi.org/10.1016/j.jsg.2017.02.003.

Brace, W.F. (1961). Dependence of fracture strength of rocks on grain size. In: Proceedings of the 4th Rock Mechanics Symposium, Pennstate, 99–103.

Briggs, D.J. (1982). Mechanical properties of quartzites and associated rock types. Chamber of Mines South Africa Research Organization and Mining Technology Laboratory; Report number: 13/83

Brune, J.N., (2001). Fault-normal dynamic unloading and loading: an explanation for “non-gouge” rock powder and lack of fault-parallel shear bands along the San Andreas Fault, EOS, Transactions American Geophysical Union, Fall Meeting, Abstract S22B-0655, 82(47).

Bucholz, E.W., Zhao, X., Sinnott, S.B. and Scott S. (2012). Perry friction and wear of pyrophyllite on the atomic scale. Tribology Letters, 46, 159 – 165.

Chester, J.S., Chester, F.M. and Kronenberg, A.K. (2005). Fracture surface energy of the Punchbowl fault, San Andreas system. Nature, 437, 133–136. https://doi.org/10.1038/nature03942

Cook, N.G.W. (1962). A study of failure in the rock surrounding underground excavations, PhD Thesis, University of the Witwatersrand, Johannesburg.

Cornet, F.H., Bernard, P. and Moretti, I. (2004). The Corinth Rift Laboratory. Comptes Rendus Geosciences, 336, 235-241.

Coward, M.P., Spencer R.M. and Spencer C.E. (1995). Development of the Witwatersrand Basin, South Africa. Geological Society of London, Special Publication, 95, 243–269.

Dankert, B.T. and Hein, K.A.A. (2010). Evaluating the structural character and tectonic history of the Witwatersrand Basin. Precambrian Research, 177, 1-22.

De Kiewiet. C.W. (1941). A History of South Africa, Social and Economic. New York: Oxford University Press, pp. 292.

Dieterich, J.H. (1978). Time-dependent friction and the mechanics of stick-slip. Pure Applied Geophysics, 116, 790–805.

Di Toro, G., Goldsby, D.L. and Tullis, T.E. (2004). Friction falls towards zero in quartz rock as slip velocity approaches seismic rates. Nature, 427, 436– 439.

Di Toro, G., Han, R., Hirose, T., De Paola, N., Nielsen, S., Mizoguchi, K., Ferri, F., Cocco, M. and Shimamoto, T. (2011). Fault lubrication during earthquakes. Nature, 471, 494-498.

Duffey, A. (2012). Mapungubwe: Interpretation of the Gold Content of the Original Gold Burial M1, A620. Journal of African Archaeology, 10, 175–187.

Durrheim, R.J., Anderson, R.L., Cichowicz, A., Ebrahim-Trollope, R., Hubert, G., Kijko, A., McGarr, A., Ortlepp, W.D., and van der Merwe. N. (2006). The risks to miners, mines, and the public posed by large seismic events in the gold mining districts of South Africa. In Proceedings of the 3rd International Seminar on Deep and High Stress Mining, Quebec City, Canada.

Durrheim, R.J., Ogasawara, H., Nakatani, M., Yabe, Y., Milev, A. Cichowicz, A., Kawakata, H., Moriya, H. and the JST-JICA SA Research Group. (2010). Observational Study to Mitigate Seismic Risks in Mines: a new Japanese - South African collaborative project. In: Van Sint Jan, M., Potvin, Y. (Eds.). Proceedings of the 5th International Seminar on Deep and High-Stress Mining, Australian Centre for Geomechanics, Perth, Australia, 215-225.

Durrheim, R.J., Ogasawara, H., Nawakata, M., Yabe, Y., Naoi, M., Ward, A.K., Murphy, S.K., Wienand, J., Lenegan, P., Milev, A.M., Murakami, O., Yoshimitsu, N., Kgarume, T., Chichowicz, A. and the SATREPS research group. (2012). A Japanese - South African collaboration to mitigate seismic risks in mines: establishment of experimental sites. In: Potvin, Y. (Eds.). Proceedings of the 6th International Seminar on Deep and High-Stress Mining, Australia, Australian Centre for Geomechanics, Perth, Australia, 173-187.

Durrheim, R.J., Ogasawara, H., Nakatani, M., Yabe, Y., Naoi, M., Moriya, H., Cichowicz, A., Satoh, T., Hironori, K.H., Milev, A., Kgarume, T., Brink, V.Z., Ward, A.K., Ribeiro, L., Manzi, M.S.D., Mngadi, S.B., the SATREPS Team. (2017). Observational Studies in South African Mines to Mitigate Seismic Risks: Challenges and Achievements. In: Proceedings of the AfriRock International Symposium. 3-5 October 2017. Cape Town, South Africa.

Förster, A., Hötzl, H., Rettenmaier, D., Cornet, F. and Borm, G. (2004). The ICDPDGLab AIGION Fault Drilling Gulf of Corinth/Greece: A thermohydraulic approach to seismicity and geodynamics. Abstract at ICDP Conference “Continental Scientific Drilling 2005: A Decade of Progress and Challenges for the Future” Potsdam, Germany.

Funato, A. and Ito, T. (2017). A new method of diametrical core deformation analysis for in-situ stress measurements, International Journal of Rock Mechanics and Mining Sciences, 91, 112-118.

Gane, P.G. Hales, A.L. and Oliver H.A. (1946). A seismic investigation of the Witwatersrand earth tremors. Bulletin of the Seismological Society of America, 36, 49-80.

Gay, N.C. and Ortlepp, W.D. (1979). Anatomy of a mining-induced fault zone. Bulletin of the Geological Society of America, 90, 47- 58.

Gibowicz, J. and Kijko, A. (1994). An introduction to mining seismology. Academic Press San Diego, 55, 1-399.

Glasspool, M. and Ward, A.K. (2010). Ezulwini Mine: mandatory code of practice to combat rockburst and rockfall related accidents. SRK Consulting Engineers and Scientists Technical Report. Report number: DME16/3/2/1-A3.

Goldsby, D.L. and Tullis, T.E. (2002). Low frictional strength of quartz rocks at sub-seismic slip rates. Geophysical Research Letters, 29(17), 1844. doi:10.1029/2002GL015240.

Goldsby, D.L. and Tullis, T.E. (2011). Flash heating leads to low frictional strength of crustal rocks at earthquake slip rates: Science, 334, 216– 218. doi: 10.1126 /science .1207902.

Harvey, F., Joughin, W. and Ortlepp, D.W. (2006). Design of Ezulwini Shaft Pillar Extraction. SRK Consulting Engineers and Scientists Technical report. Report number: 346813.

Hayashi, N. and Tsutsumi, A. (2010). Deformation textures and mechanical behavior of a hydrated amorphous silica formed along an experimentally produced fault in chert. Geophysical Research Letters, 37, L12305. doi.org/10.1029/201.

Hazzard, J.F., Maxwell, S.C. and Young, R.P. (2000). Micromechanical modeling of cracking and failure in brittle rocks. Journal of Geophysical Research, 105, 683-697.

Heap, M.J., Vinciguerra, S. and Meredith, P.G. (2009). The evolution of elastic moduli with increasing crack damage during cyclic stressing of a basalt from Mt. Etna volcano. Tectonophysics, 471, 153–160.

Heesakkers, V., Murphy, S.K., van Aswegen, G., Domoney, R., Addams, S., Dewers, T., Zechmeister, M. and Reches, Z. (2005). The Rupture Zone of the M=2.2 Earthquake that Reactivated the Ancient Pretorius Fault in TauTona Mine, South Africa. Eos Transactions, AGU, 86, Fall Meeting Supplementary, Abstract S31B-04.

Heesakkers, V., Murphy, S. and Reches, Z. (2011a). Earthquake rupture at focal depth. Part I: Structure and rupture of the Pretorius Fault, TauTona Mine, South Africa. Pure and Applied Geophysics, 168, 2395- 2425.

Heesakkers, V., Murphy, S., Lockner, D.A. and Reches, Z. (2011b). Earthquake rupture at focal depth. Part II: Mechanics of the 2004 M2.2 earthquake along the Pretorius Fault, TauTona Mine, South Africa. Pure and Applied Geophysics, 168, 2427-2449.

Herron, A.D. (2011). First step in seismic interpretation. Geophysical monograph series number 16. Tulsa, Oklahoma. Society of Exploration Geophysicists. The International Society of Applied Geophysics.

Hickman, S., Zoback, M. and Ellsworth, W. (2004). Introduction to special section: Preparing for the San Andreas Fault Observatory at Depth. Geophysical Research Letters, 31. L12S01.

Hughes, H.S.R., Kinnaird, J.A., Mcdonald, I., Kramers, J.D. and Nex, P.A.M. (In press). A major swarm of orangeite dykes exposed in platinum mines across the Western Bushveld Complex, South Africa.

Jaeger, J.C. and Cook, N.G.W. (1979). Fundamentals of Rock Mechanics. 3rd edition, London, Chapman and Hall, pp. 593.

Jager, A.J. and Ryder, J.A. (1999). A Handbook on Rock Engineering Practice for Tabular Hard Rock Mines. SIMRAC, Braamfontein, South Africa.

Kanagawa, K., Murayama, H., Sugita, A., Takahashi, M., Sawai, M., Furukawa, N. and Hirose, T. (2020) Weakening of quartz rocks at subseismic slip rates due to frictional heating, but not to lubrication by wear materials of hydrated amorphous silica or silica gel. Tectonophysics, 784, 228429. https://doi.org/10.1016/j.tecto.2020.228429.

Kaneki, S., Yokoyama, Y., Hirono, T., Yabe, Y. and Ogasawara, H. (2018). Mineralogical characteristics of fault rocks recovered from aftershock zone of the M5.5 Orkney earthquake in South Africa (ICDP DSeis project). Seismological Society of Japan Fall Meeting, Abstracts.

Katsuichiro, G., Tomohiro, Y., Mai, P.M. and Mori, N. (2017). Tsunami simulations of mega-thrust earthquakes in the Nankai-Tonankai trough (Japan) based on Stochastic rupture scenarios. Geological Society London Special Publications, 456(1). doi: 10.1144/SP456.1

Kgarume, T., Spottiswoode, S., Milev, A., Nakatani, M., Naoi, M., Yabe, Y., Philipp, J., Durrheim, R.J., Ogasawara, H. and Ward, A.T. (2013) Using acoustic emissions to study rock mass degradation due to stope fracturing. In: Proceedings of the 13th Biennial SAGA Conference. 6–9 October 2013, Kruger National Park, South Africa.

Keulen, N., Heilbronner, R., Stunitz, H., Boullier, A.M. and Ito. H. (2007). Grain size distributions of fault rocks: A comparison between experimentally and naturally deformed granitoids. Journal of Structural Geology, 29, 1282 -1300.

Knill, J.L., Cratchley, C.R., Early, K.R., Gallois, R.W., Humphreys, J.D., Newbery, J., Price D.G. and Thurrell, R.G. (1970). Geological Society Engineering Group Working Party report on the logging of rock cores for engineering purposes. Quarterly Journal of Engineering Geology and Hydrogeology, 3, 1-24.

Lama, R.D. and Vutukuri, V. (1978). Handbook on mechanical properties of rocks – Testing techniques and results. Trans tech publications, 3, 209-320.

Landau, L.D. and Lifshitz, E.M. (1986). Theory of elasticity. (3rd Edition). Wheaton and Co. Ltd, Great Britain.

Lenhardt, W.A. (1989). Seismic event characteristics in a deep level mining environment. Proceedings of the Rock at Great Depth Seminar. (ed. Maury, V. and Fourmaintraux, D.). Balkema, Rotterdam, 727-732.

Ligege R. (2013). Cooke 4 shaft Geologist. Personal communication.

Logan, J.M., Friedman, M., Higgs, N., Dengo, C. and Shimamoto, T. (1979). Experimental studies of simulated fault gouge and their application to studies of natural fault zones. Proceedings of the VIII. Analysis of Actual Fault Zones in Bedrock. United States Geological Survey. Open-file Reports, 79-1239, 305-343.

Ma, K.F., Hung, J.O., Wang, C.Y., Song, S.R., Tonaka, H., Ito, H., Mori, J., Yeh, E.C. and Chen, W.M. (2005). Dynamics of Chi-Chi earthquake rupture: Discovery from Seismological Modeling and Taiwan Chelungpu-fault Drilling Project (TCDP). Abstract at ICDP Conference "Continental Scientific Drilling 2005: A Decade of Progress and Challenges for the Future" Potsdam, Germany, http://www.icdp-online.de/news/future_abstracts.htm.

Marone, C. and Kilgore, B. (1993). Scaling of the critical slip distance for seismic faulting with shear strain in fault zones. Nature, 362, 618–621.

Marone, C. and Scholz, C. H. (1989). Particle-size distribution and microstructures within simulated fault gouge. Journal of Structural Geology, 11, 799-814.

McCarthy, T.S. (2006). The Witwatersrand Supergroup. In: The Geology of South Africa, MR Johnson, CR Anhaeusser, RJ Thomas, editor. Pretoria: Council for Geosciences, 155–186.

McCarthy, T. and Rubidge, B. (2005). The Story of Earth and Life. Struik Publishers. Cape Town, South Africa.

McGarr, A. (2000). Energy budgets of mining-induced earthquakes and their interactions with nearby stopes. International Journal of Rock Mechanics and Mining Sciences, 37, 437–443.

McGarr, A. and Green, R.W.E. (1975). Measurement of tilt in a deep-level gold mine and its relationship to mining and seismicity. Geophysical Journal of the Royal Astronomical Society, 43, 327-345.

McGarr, A., Spottiswoode, S.M., Gay, N.C. and Ortlepp, W.D. (1979). Observations relevant to seismic driving stress, stress drop, and efficiency. Journal of Geophysical Research, 84, 2251-2261.

McGarr, A. and Gay. N.C. (1978). State of Stress in the Earth's Crust. Annual Review of Earth and Planetary Sciences, 6, 405-436.

McGarr, A., Spottiswoode, S.M., Gay, N.C. and Ortlepp, W.D. (1979). Observations relevant to seismic driving stress, stress drop, and efficiency. Journal of Geophysical Research, 84, 2251-2261.

McGarr, A., Sacks, I.S., Linde, A.T., Spottiswoode, S.M. and Green, R.W.E. (1982). Coseismic and other short-term strain changes recorded with Sacks-Evertson strainmeters in a deep mine, South Africa. Geophysical Journal of the Royal Astronomical Society, 70, 717-740.

Milev, A.M. and Spottiswoode, S.M. (2002). Effect of the rock properties on the mining-induced seismicity around the Ventersdorp Contact Reef, Witwatersrand Basin, South Africa. Pure and Applied Geophysics, 159,165–177.

Mizoguchi, K., Hirose, T., Shimamot, T. and Fukuyama, E. (2007). Reconstruction of seismic faulting by high-velocity friction experiments: An example of the 1995 Kobe earthquake. Geophysical Research Letters, 34(1): L01308. doi:10.1029/2006gl027931.

Mngadi, S.B. (2015). Integrated petrographic, geomechanical and seismological studies of rockmass behaviour during the extraction of the Cooke 4 shaft pillar. MSc Thesis. The University of the Witwatersrand, Johannesburg.

Mngadi, S.B., Durrheim, R.J., Manzi, M.S.D., Ogasawara, H., Yabe, Y., Yilmaz, H. Wechsler, N., van Aswegen, G., Roberts, D., Ward, A.K., Naoi, M., Moriya, H., Nakatani, M., Ishida, A., SATREPS. and ICDP DSeis Team. (2019). Integration of underground mapping, petrology, and high-resolution microseismicity analysis to characterise weak geotechnical zones in deep South African gold mines. International Journal of Rock Mechanics and Mining Sciences, 114, 79–91.

Mngadi, S.B, Tsutsumi, A., Onoe, Y., Manzi, M.S.D., Durrheim, R.J., Yabe, Y., Ogasawara, H., Kaneki, S., Wechsler, N., Ward, A.K., Naoi, M., Moriya, H., Nakatani, M. and the DSeis team. (2020). The effect of gouge particles (“rock flour”) on rupture propagation along brittle shear fractures in deep and high-stress mines. International Journal of Rock Mechanics and Mining Sciences, 137, 104454. https://doi.org/10.1016/j.ijrmms.2020.104454.

Monzawa, N. and Otsuki, K. (2003). Comminution and fluidization of granular fault materials: implications for fault slip behavior. Tectonophysics, 367, 127-143.

Moore, D.E., Lockner, D.A., Tanaka, H. and Iwata, K. (2004). The coefficient of friction of chrysotile gouge at seismogenic depths. International Geology Review, 46, 385–398. doi:10.2747/0020-6814.46.5.385.

Mori, J. and Ellsworth, W. (2013). Active fault and earthquakes. Unravelling the Workings of Planet Earth – Science Plan for 2014-2019, pp. 24-31.

Moriya, H., Naoi, M., Nakatani, M., Murakami, O., Kgarume, T., Ward, A.K., Durrheim, R., Philipp, J., Yabe, Y., Kawakata, H. and Ogasawara, H. (2015). Delineation of large localized damage structures forming ahead of an active mining front by using advanced acoustic emission mapping techniques. International Journal of Rock Mechanics and Mining Sciences, 79, 157–165.

Myers, R.E., McCarthy, T.S. and Stanistreet, I.G. (1989). A tectono-sedimentary reconstruction of the development of the Witwatersrand Basin, with particular emphasis on the Central Rand Group. Economic Geology Research Unit, 216, 497–540.

Naoi, M., Nakatani, M., Yabe, Y., Kwiatek, G., Igarashi, T. and Plenkers, K. (2011). Twenty thousand aftershocks of a very small (M2) earthquake and their relation to the mainshock rupture and geological structures. Bulletin of the Seismological Society of America, 101, 2399-2407.

Naoi, M., Nakatani, M., Horiuchi, S., Yabe, Y., Philipp, J., Kgarume, T., Morema, G., Khambule, S., Masakale, T., Ribeiro, L., Miyakawa, K., Watanabe, A., Otsuki, K., Moriya, H., Murakami, O., Kawakata, H., Yoshimitsu, N., Ward, A., Durrheim, R.J. and Ogasawara, H. (2014). Frequency–magnitude distribution of -3.7 < Mw < 1 mining-induced earthquakes around a mining front and b value invariance with post-blast time. Pure and Applied Geophysics, 171, 2665-2684.

Naoi, M., Nakatani, M., Otsuki, K., Yabe, Y., Kgarume, T., Murakami, O., Masakale, T. Ribeiro, L., Ward, A.T., Moriya, H., Kawakata, H., Durrheim, R.J. and Ogasawara, H. (2015a). Steady activity of microfractures on geological faults loaded by mining stress Tectonophysics, 649, 100-114.

Naoi, M., Nakatani, M., Kgarume, T., Khambule, S., Masakale, T., Ribeiro, L., Philipp, J., Horiuchi, S., Otsuki, K., Miyakawa, K., Watanabe, A., Moriya, H., Murakami, O., Yabe, Y., Kawakata, H., Yoshimitsu, N., Ward, A., Durrheim, R.J. and Ogasawara, H. (2015b). Quasi-static slip patch growth to 20 m on a geological fault inferred from acoustic emissions in a South African gold mine. Journal of Geophysical Research Solid Earth, 120, 1692-1707.

Nkosi, Z.N. (2016). Seismological and mineralogical studies of the world's deepest gold-bearing horizon, the Carbon Leader Reef, West Wits Line goldfields (South Africa): Implications for its poor seismic reflective character. MSc Thesis. University of the Witwatersrand, Johannesburg.

Norrish, K. and Hutton, J.T. (1969). An accurate X-ray spectrographic method for the analysis of geologic samples. Geochemica et Cosmochimica Acta, 33, 431-454.

O'Connor, C. (2017). Challenges Facing the South African Mining Industry. South African Minerals to Metals Research Institute, viewed 23 March 2017, < http://saae.co.za/challenges-facing-the-south-african-mining-industry-by-prof-cyril-oconnor/>.

Ogasawara, H., Durrheim, R.J., Nakatani, M., Yabe, Y., Milev, A., Cichowicz, A., Kawakata, H. and Moriya, H., (2009). JST-JICASA Research Group A. Japanese - South African Collaboration to Mitigate Seismic Risks in Deep Gold Mines. In: Proceedings of the 1st Hard Rock Safety Conference, Johannesburg, 115–134.

Ogasawara, H., Nakatani, M. Durrheim, R.J., Naoi, M., Yabe, Y., Moriya, H., Hofmann, G.F., Stander, C., Roberts, D.P., de Bruin, P., Oelofse, J., Kato, H., Cichowicz, A., Birch, D., Ngobeni, D., Milev, A., Kgarume, T., Satoh, T., Horiuchi, S., Kawakata, H., Murakami, O., Yoshimitsu, N., Ward, A.T., Wienand, J., Lenegan, P., Yilmaz, H., Mngadi, S.B., Piper, P.S., Clements, T.N., Nakao, S., Okubo, M., Ishii, H. and Visser, A.V. (2014a). Observational studies of the rock mass response to mining in highly stressed gold mines in South Africa, Proceedings of 7th International Congress on Deep and High Stress Mining, Sudbury, Canada, 16-18 September, M. Hudyma and Y. Potvin (eds.), Australian Centre for Geomechanics, 123-137.

Ogasawara, H., Kato, H., Hofmann, G., Roberts, D., Piper, P., Clements, T., Ward, A.T., Yabe, Y., Yilmaz, H. and Durrheim, R.J. (2014b). BX CCBO In-situ Stress Measurements at Earthquake Prone Areas in South African Gold Mines—a Summary of Mini-workshop on 13 Feb 2014, Paper 14-7438 Presented at 48th US Rock Mechanics/Geomechanics Symposium, Minneapolis.

Ogasawara, H., Durrheim, R.J., Yabe, Y., Ito, T., van Aswegen, G., Grobbelaar, M., Funato, A., Ishida, A., Ogasawara, H., Mngadi, S.B, Manzi, M.S.D., Ziegler, M., Ward, A.K. Hofmann, G., Moyer, P., Boettcher, M., Dight, P., Ellsworth, W., Liebenberg, B., Wechsler, N., Onstott, T., Berset, N. and the DSeis Team. (2017). Drilling into Seismogenic Zones of M2.0 – M5.5 Earthquakes from Deep South African Gold Mines (DSeis): Establishment of Research Sites. International Rock Mechanics Symposium AfriRock - Rock Mechanics for Africa, 237-248. Ogasawara, H., Liebenberg B., Yabe

Y., Durrheim R., Ziegler M., Manzi M.S.D., Mngadi S.B., Onstott, T., Kaneki S., Yokoyama Y. and the ICDP DSeis team. (2019). An overview of the completed ICDP project, Drilling into Seismogenic zones of M2.0-5.5 earthquakes in South African gold mines (DSeis). In: Proceedings of the EGU General Assembly. 7–12 April 2019, Abstracts 21: EGU2019-6503-1. Vienna, Austria.

Ogasawara, H., Liebenberg, B., Yabe, Y., Yokoyama, Y., Hirono, T., Nisson, D.M., Onstott, T.C., Kieft, T.L., Esta van Heerden, Wiersberg, T., Noda, T., Manzi, M.S.D. Mngadi, S.B. Durrheim, R.J., Yamamaoto, Y., Ito, T., Funato, A., Ziegler, M., Mori, J.J., Carsten, D. and The ICDP DSeis team. (2020). The seismogenic zones of an M2.0-5.5 earthquakes successfully recovered in deep South African gold mines: the outcomes and the follow-up plan. EGU General Assembly 2020. 4–8 May 2020, Online.

Olgaard, D.L. and Brace, W.F. (1983). The microstructures of gouge from a mining induced seismic shear zone. International Journal of Rock Mechanics and Mining Science and Geomechanics Abstracts, 20, 11-19.

Ortlepp, W.D. (1978). The mechanism of a rockburst. In: Proceedings of the 19th U.S. Rock Mechanics Symposium. Nevada, 476-483.

Ortlepp, W.D. (1992). Note on fault-slip motion inferred from a study of micro-cataclastic particles from an underground shear rupture. Pure and Applied Geophysics, 139, 677-695.

Ortlepp, W. D. (1997). Rock Fracture and Rockbursts. South Africa Institute of Mining and Metallurgy, Monograph series M9, 1997.

Pawlak, Z., Pai, R., Bayraktar, E., Kaldonski, T. and Oloyede, A. (2008). Lamellar lubrication in vivo and vitro: friction testing of hexagonal boron nitride. Biosystems, 94, 202–208.

Perez, M.A. (2014). Mapping brittleness and stress. GeoConvention 2014: FOCUS, Apache Canada.

Platt, J., Proctor, B., Mitchell, T., Hirth, G., Goldsby, D., Di Toro, G., Beeler, N. and Tullis, T. (2014). The role of gouge and temperature on flash heating and its hysteresis: American Geophysical Union. Fall Annual Meeting, Abstract, S11C-4360.

Reches, Z. and Lockner, D.A. (1994). The nucleation and growth of faults in brittle rocks. Journal of Geophysical Research, 99, 18159–18174.

Reches, Z., DAFSAM and NELSAM teams. (2006). Building a Natural Earthquake Laboratory at Focal Depth (DAFSAM-NELSAM Project, South Africa). Scientific drilling, 3. doi:10.2204/iodp.sd.3.06.2006.

Reches, Z. and Lockner, D.A. (2010). Fault weakening and earthquake instability by powder lubrication. Nature, 467, 452–455.

Reches, Z. and Ito, H. (2007). Scientific drilling of active faults: past and future. In: Harms U., Koeberl C., Zoback M.D. (eds.) Continental Scientific Drilling. Springer, Berlin, Heidelberg. pp. 235-258. https://doi.org/10.1007/978-3-540-68778-8_6.

Reches, Z. and DAFSAM - NELSAM. (2006). Building a natural earthquake laboratory at focal depth (DAFSAM-NELSAM Project, South Africa). Scientific drilling, 3. doi:10.2204/iodp.sd.3.06.2006.

Reches, Z. and Dewers, T.A. (2005). Gouge formation by dynamic pulverization during earthquake rupture. Earth and Planetary Science Letters, 235, 361–374.

Rice, J.R. (2006). Heating and weakening of faults during earthquake slip. Journal of Geophysical Research, 111: B05311. doi.org/10.1029/2005JB004006.

Rickenbacher, M. (2018). Geological and geotechnical rock mass model from two deep DSEIS boreholes drilled at Moab Khotsong. MSc Thesis. Swiss Federal Institute of Technology Zurich, Zurich.

Rickman, R., Mullen, M.J., Petre, J.E., Grieser, W.V. and Kundert, D. (2008). A practical use of shale petrophysics for stimulation design optimization: All shale plays are not clones of the Barnett Shale. In SPE Annual Technical Conference and Exhibition. Society of Petroleum Engineers.

Robb, L.J. and Meyer, F.M. (1995). The Witwatersrand Basin, South Africa: Geological framework and mineralization processes. Ore Geology Reviews, 10, 67-94.

Roberts, M.K.C. and Schweitzer, J.K. (1999) Geotechnical areas associated with the Ventersdorp contact reef, Witwatersrand Basin, South Africa. Journal of the Southern African Institute of Mining and Metallurgy, 99, 157–166.

Rockwell, T.K., Sisk, M., Girty, G., Dor, O., Wechsler, N. and Ben-Zion, Y. (2009). Chemical and physica characteristics of pulverized Tejon Lookout Granite adjacent to the San Andreas and Garloc faults: implications for earthquake physics. Pure Applied Geophysics, 166, 1725–1746.

Rowe, C.D. and Griffith, W.A. (2015) Do faults preserve a record of seismic slip: A second opinion. Invited Review, Journal of Structural Geology, 78, 1-26.

Ryder, J.A. and Jager, A.J. (2002). A textbook on rock mechanics for tabular hard rock mines. Braamfontein, Johannesburg: SIMRAC.

SACS (South African Committee for Stratigraphy). (1980). Stratigraphy of South Africa. Part 1 (Comp L.E. Kent). Lithostratigraphy of the Republic of South Africa, South West Africa/Namibia and the Republics of Bophuthatswana, Transkei and Venda. Pretoria: Geological Survey of South Africa.

SACS (South African Committee for Stratigraphy). (2006). A revised stratigraphic framework for Witwatersrand Supergroup. Lithostratigraphy of the Republic of South Africa. Pretoria: Geological Survey of South Africa.

Sadd, M.H. (2005). Elasticity: Theory, Applications, and Numeric. Elsevier, Oxford, pp. 445.

Sammis, C., King, G. and Biegel, R. (1987). The kinematics of gouge deformation. Pure Applied and Geophysics, 125, 777-812.

Sammis, C., Osborne, R., Anderson, J., Banerdt, M., and White, P. (1986). Self-similar cataclasis in the formation of fault gouge. Pure and Applied Geophysics, 124, 53-78.

Scholz, C.H. (2002). The Mechanics of Earthquakes and Faulting, Cambridge University, Press.

Shao, S.M. and Zou. J.C. (1996). Fractal research of fault gouge. Acta Seismologica Sinica, 9, 485-491.

Shimamoto, T. and Tsutsumi, A. (1994). A new rotary-shear high-velocity frictional testing machine: Its basic design and scope of research (in Japanese with English abstract). Journal of Structural Geology, 39, 65– 78.

Simm, R. and Bacon, M. (2014). Seismic Amplitude. An Interpreters Handbook. Cambridge University Press, New York.

Spectris plc. (2005). Malvern Instruments: Instruction manual. Enigma Business Park (www.malvern.co.uk).

Spottiswoode, S.M. (1980). Source mechanism studies on Witwatersrand seismic events, PhD Thesis, University of the Witwatersrand, Johannesburg.

Spottiswoode, S.M. (1979). Fault gouge, driving stress, and seismic efficiency. Unpublished Report (1978). (Most of data is quoted in McGarr, A., Spottiswoode, S.M., Gay, N.C. and Ortlepp W.D. (1979). Observations relevant to seismic driving stress, stress drop, and efficiency. Journal of Geophysical Research, 84, 2251-2261)

Spottiswoode, S.M. and McGarr, A. (1975). Source parameters of tremors in a deep-level gold mine. Bulletin of the Seismological Society of America, 65, 93-112.

Spray, J.G. (2010). Frictional melting processes in planetary materials: from hypervelocity impact to earthquakes. Annual Review of Earth and Planetary Sciences, 38, 221–254.

Statistics South Africa. (2018). Gross domestic product, fourth quarter 2017. P0441. Viewed on 23 June 2021. <https://www.dmr.gov.za/Portals/0/files/P04414thQuarter2017(1).pdf?ver=2018-03-09-063718-170>.

Steacy, S.J. and Sammis, C.G. (1991). An automaton for fractal patterns of fragmentation. Nature, 353, 250–252.

Tanaka, H., Wang, C.Y., Chen, W.M., Sakaguchi, A., Ujiie, K., Ito, H. and Ando, M. (2002). Initial science report of shallow drilling penetrating into the Chelungpu fault zone, Taiwan. Terrestrial, Atmospheric and Oceanic Sciences, 13, 227-251.

Tchalenko, J.S. (1970). Similarities between shear zones of different magnitudes. Geological Society of America Bulletin, 81, 41-60.

Tsutsumi, A., Fabbri, O., Karpoff, A.M., Ujiie, K. and Tsujimoto. A. (2011). Friction velocity dependence of clay-rich fault material along a megasplay fault in the Nankai subduction zone at intermediate to high velocities. Geophysical Research Letters, 38, L19301. doi:10.1029/2011gl049314.

Ujiie, K. and Tsutsumi, A. (2010). High-velocity frictional properties of clay-rich fault gouge in a megasplay fault zone, Nankai subduction zone. Geophysical Research Letters, 37, L24310. doi.org/10.1029/2010GL046002.

USGS report prepared by Flanagan, D.M. (2019). Mineral commodity summaries - USGS Publications.

van Aswegen, G. (2008). Ortlepp Shears – dynamic brittle shears of South African gold mines. In: Potvin, Y (Ed.) 1st Southern Hemisphere International Rock Mechanics Symposium, 16-19 September 2008, Perth, Western Australia, 111 – 120.

van Aswegen, G. and Stander, M. (2013). Origins of some fractures around tabular stopes in deep South African mines. Journal of the Southern African Institute of Mining and Metallurgy, 112, 729–735.

Vermaakt, D.T. and Chunnet, I.E. (1994). Tectono-sedimentary processes which controlled the deposition of the Ventersdorp Contact Reef within the West Wits Line. In: Proceedings of the 15th Congress of the Council for Mining and Metallurgical Institutions (eds. Anhaeusser C.R.). South African Institute of Mining and Metallurgy, 3, 117–130.

Violay, M., Nielsen, S., Gibert, B., Spagnuolo, E., Cavallo, A., Azais, P., Vinciguerra, S. and Di Toro, G. (2014). Effect of water on the frictional behavior of cohesive rocks during earthquakes. Geology, 42, 27–30.

Vorster, C.J. (2003). Samindaba (South African Mineral Deposits Database) with special reference to new website programme year 2002/2003. 2003-0054

Wechsler, N., Allen, E., Rockwell, T.K., Girty, G., Chester, J.S. and Ben-Zion, Y. (2011). Characterization of pulverized granitoids in a shallow core along the San Andreas Fault, Littlerock, CA. Geophysical Journal International, 186, 401-417.

Wechsler, N., Van Aswegen, G., Yabe, Y., Mngadi, S., Kamhaji, L., Ward, A., Morema, S., Durrheim, R., Ogasawara, H. and ICDP Dseis team. (2018). Recovery of ruptures from seismogenic zone at Cooke 4 mine (DSeis - ICDP scientific drilling project in the South-African gold mines). Abstract EGU 2018-9721, Vienna, 12 April 2018.

Wibberley, C.A.J., Petit, J-P and Rives, T. (2000). Micromechanics of shear rupture and the control of normal stress. Journal of Structural Geology, 22, 411-427.

Wiersberg, T., Zimmer, M., Kujawa, C., Liebenberg, B., Ogasawara, H., Onstott, T.C., Cason, E., Vermeulen, Jan-G and van Heerden, E. (2019). Investigations on fault zone gases in South African gold mines. Abstract EGU2019-5670, 7-12 April 2019, Vienna.

Wilson, B., Dewers, T. Reches, Z. and Brune, J. (2005). Particle size and energetics of gouge from earthquake rupture zones. Nature, 434, 749–752.

Wöhrl, T. and de Wall. H. (2014). The On-Site Geoscientist. GFZ. Potsdam.

Yabe, Y., Philipp, J., Nakatani, M., Morema, G., Naoi, M., Kawakata, H., Igarashi, T., Dresen, G., Ogasawara, H. and JAGUARS-Group. (2009). Observation of numerous aftershocks of an Mw1.9 earthquake with an AE network installed in a deep gold mine in South Africa. Earth Planets Space, 61, E49–E52.

Yabe, Y., Nakatani, M., Naoi, M., Philipp, J., Janssen, C., Watanabe, T., Katsura, T., Kawakata, H., Georg, D., and Ogasawara, H. (2015). Nucleation process of an M2 earthquake in a deep gold mine in South Africa inferred from on-fault foreshock activity, Journal of Geophysical Research, 120, 5574-4495.

Yabe, Y., Abe, S., Ito, T., Ishida, A., Sugimura, K., Kanematsu, M., Higashi, M., Tadokoro, R., Ogasawara, H., Funato, A., Kato, H., Watson, B., Mngadi, S.B., Durrheim, R.J., Hofmann, G. and Scheepers, L. (2019). In-situ stress around source faults of seismic events in and beneath South African deep gold mines', in W Joughin (ed.), Proceedings of the Ninth International Conference on Deep and High Stress Mining. The Southern African Institute of Mining and Metallurgy, Johannesburg, 399-411.

Yao, L., Ma, S., Platt, J.D., Niemeijer, A.R. and Shimamoto, T. (2016). The crucial role of temperature in high-velocity weakening of faults: Experiments on gouge using host blocks with different thermal conductivities. Geology, 44, 63–66.

Yoshioka, N. (1986). Fracture energy and the variation of gouge and surface roughness during frictional sliding of rocks. Journal of Physics of the Earth, 34, 335–355.

Yue-Gau Chen, Wen-Shan Chen, Jian-Cheng Lee, Yuan-Hsi Lee, Chyi-Tyi Lee, Hui-Cheng Chang and Ching-Hua Lo. (2001). Surface rupture of 1999 Chi-Chi earthquake yields insights on active tectonics of central Taiwan. Bulletin of the Seismological Society of America, 91, 977-985. doi: 10.1785/0120000721.

Zoback, M., Hickman, H. and Ellsworth, W. (2006). Structure and properties of the San Andreas Fault in central California: Preliminary results from the SAFOD experiment. European Geosciences Union, Geophysical Research Abstracts, 8, 02474.

15. Appendix

This draft manuscript may still need some work before submission to the journal. This manuscript has been put in an Appendix because I am the second author. The first author contributed to the conceptualisation of the manuscript and the first draft of the manuscript.

15.1. Detecting mining-induced seismic ruptures in borehole core

[1]Gerrie van Aswegen, [2]Siyanda Brightboy Mngadi, [3]Rene Padilla and [4]Peter Stonestreet

[1]Institute of Mine Seismology, Republic of South Africa

[2]University of the Witwatersrand Johannesburg, Republic of South Africa.

[3]Codelco División El Teniente, Rancagua, Chile.

[4]Newcrest Mining Limited, Melbourne, Australia.

ABSTRACT

Detailed core logging is one of the clearest, direct and effective methods to identify and characterise in-situ shear fractures. However, conventional single and double core barrel rotary drilling methods are often unable to reasonably recover “intensely fractured” core in a hard rock environment (e.g., Witwatersrand Basin). The amount of core recovered is inversely proportional to the intensity of fractures, and core samples may be sheared or disturbed, loosing evidence. The DSeis team used unconventional triple-tube drilling method to drill into intensely fractured rock mass to recover highly fragile core, shear fractures forming ahead of the stope face. Unprecedented details of the core was recovered despite minor core loss in some areas. This allowed us to resolve one of the important unresolved aspect – developing criteria (establish new rules) to identify the intersection of a seismic source in a diamond drill core. Critical features of a seismic source (shear fracture) are the presence of the fault gouge “rock flour”, rock breccia (comminuted rock fragments), and in many cases, detail surface geometry of the shear fracture with soft slickensides and cross fabric. Also, the existence of the fault gouge “rock flour” and rock breccia in the core tray at the fracture location may be a good first-pass indication of a shear rupture zone. We could distinguish freshly formed shear fractures from pre-existing geological discontinuities and drilling induced fractures in the core. This proves that we can see newly formed shear fractures in the core. We focus on examples from El Teniente mine and the DSeis borehole at Site 7, Cooke 4 Shaft.

1. INTRODUCTION

Mining remains critical for developing economies such as South Africa and Chile. South African mining industry continues to be one of the significant contributors to the gross domestic product (GDP), and employs many South Africans. The Witwatersrand Basin has produced more than ~1,672 Moz of gold since discovered, which is equivalent to more than a third of gold ever produced in the world. In addition, estimations suggest that the remaining inferred resource is ~965 Moz (Tucker et al., 2016).

In Chile, copper production has and continues to play a critical role in the GDP. Pre 1994 copper production added US$ 3 billion annually to the GDP. Since 2006, it has increased tenfold to US$ 30 billion annually (Arellano, 2012). In 2019, Chile was the largest copper producer globally; according to the United States Geological Survey (USGS) the global copper production reached 20 million metric tonnes, and Chile produced 5.6 million tonnes (USGS report, 2019).

Extracting ore in deep and high stress comes with various complex challenges such as underground rockfalls and rockbursts associated with large seismic events. These pose a risk to mine workers, mine infrastructure and people living near mining towns. Ore extraction at greater depths (>1000 m below the surface) especially, in a highly stressed remnant shaft pillar induces stress fracturing around and ahead of an underground opening (Ryder and Jager, 2002). In this paper, we develop and discuss the criteria that could be used to identify seismic sources in drill core in an advancing stope to mitigate the risk posed by these stress-induced brittle fractures with the special attention on two cases in deep mines - Cooke 4 Shaft and El Teniente mine (Figure 1).

Deep level mining requires knowledge about geological or mining-induced structures that may have deformed dynamically. Knowledge of the location and orientation of such structures form an important sub-set of the structural model used in mine- and support design. Also, for purposes of accurately locating seismic sources and understanding their characteristics, it would be useful to be able to detect them in the diamond drill core. Note that the hypocentre location estimated from seismograms are generally not very accurate and only reflects the site of rupture initiation. Large slip events can span hundreds of square metres and the area of maximum displacement can be far away from the "location" as reflected in the seismic database.

Geologists and rock mechanics practitioners are often frustrated at not being able to study the walls of tunnels because they are covered with shotcrete and other support materials very soon after an advance. Even where the walls are captured by photogrammetry, particular details may not be

discernible. So, even where the tunnel development is associated with hundreds of seismic events such that some of the sources must be exposed by the advancing tunnel, no record of seismic sources are found in geological or geotechnical databases.

The important underdeveloped or vague aspect of shear fracture mapping and analysis is a criterion that may be used to identify the intersection of a seismic source in a diamond drill core. In this paper, we set up the criteria that may be used to identify these seismic sources in drill core. We use case studies from El Teniente mine and the Cooke 4 mine (Pereira et al., 2003; Hormazabal et al., 2014; Ogasawara, et al., 2017 and 2019). The latter core was drilled specifically to intersect a series of shear rupture surfaces detected by acoustic emission (AE) monitoring (Moriya et al., 2015; Wechsler et al., 2018; Mngadi et al., 2019).

AEs are commonly used to map the growth and evolution of fractures both in deep and high-stress underground mines and enhanced geothermal systems (EGS). AEs can be detected at ranges of several tens to hundreds of meters in competent rock (Lacy and Smith, 1989; Naoi et al., 2014; 2015a; Moriya et al., 2015). These microseismic clusters often indicate localised damage or a fractured zone (Wills et al., 1992). The recorded waveform from AEs are also carefully used to compute and characterise dynamic source properties such as (a) dimensions; (b) slip orientation; (c) fracture orientation, and (e) stress. However, these computations are often not accurate, and not compared to true physical observations because of the difficulty to drill in seismogenic zones (Mori and Ellsworth, 2013).

Mining-induced seismicity in deep mines poses a risk to mineworkers and the public. They also present an unusual opportunity to study the true physical nature and physics of earthquakes near source regions (Durrheim et al., 2017), and provide a unique opportunity to compare the ‘exhumed’ shear ruptures (features observed on a core from holes that intersect the rupture) and microfracturing monitoring results.

Other common methods of fracture detection and analysis include “conventional” geophysical well-logging techniques. These geophysical well-log techniques are based on physical property effects, often ‘indirectly’ associated with fractures. The magnitude of anomalies may be qualitatively related to the "size" of the fracture, but nearly impossible to define precisely. Another limitation in geophysical well-logging of fractures is resolution of some of the borehole logging, which highly depends on the

sampled rock volume and averages around the sampled region resulting in measurements being relatively insensitive to the presence of individual fractures.

With the advancement of technology and the availability of new logging devices such as micro-logging (improved devices with closely spaced sources of the neutron, gamma density, magnetic susceptibility and electrical resistivity), the vertical resolution has better-quality for the detection of fractures compared to conventional techniques. The short source to detector logging devices samples small enough rock volume which significantly improves the spatial resolution compared to surface methods and surface to borehole methods.

2. TERMINOLOGY

Since the study of the seismic sources in mines is limited to a few South African cases, there is not a definitive set of terms in general use in the mining environment. Below several references to **Ortlepp shears** are made and there is a specific definition for them – specifically, they are *dynamic brittle shears that develop through previously intact rock proximal to a mine opening*. If a shear rupture occurs along an existing discontinuity some distance from a mine opening we would not call it an Ortlepp shear.

The purpose of this paper is to set criteria to distinguish a planar (sub-planar) discontinuity that has experienced a 'recent' dynamic shear breakthrough rupture failure. We prefer to use the term "**shear rupture surface**" without trying to define whether it is a pre-existing discontinuity, which experienced a fresh dynamic slip, or whether it is a newly formed dynamic brittle shear through intact rock.

We use the term **cross fabric** for a linear fabric found along several shear rupture surfaces observed in recovered core samples. It is interpreted to have the same mechanical origin as some very strong linear patterns found along Ortlepp shear zone walls, being the intersection lines of the en-echelon extension fractures within the shear zone with the shear zone wall.

3. BACKGROUND

A long history of studying Ortlepp shears in South African gold mines provides the background to this paper (Ortlepp, 1999, van Aswegen, 2007, 2013). The characteristics of mining induced, dynamic, brittle shears include the presence of finely comminuted rock material referred to as "rock

flour". Similar material would inevitably be formed during dynamic deformation in the natural environment during the tectonic evolution of the rock mass (e.g., Reches and Dewers, 2005). Because of the very fine grain size and consequent large surface exposure, such material in natural fault gouges are readily altered to form fault rocks of varying kinds depending on the primary composition and that of circulating fluids and the prevailing pressure/temperature conditions (metamorphic grade). The powdery component of the fault rock is thus bound in clay minerals, micas or harder minerals (mostly siliceous) so that no trace of rock flour is left.

In the case of mining induced brittle shears in the relatively cool mining environment and (mainly) because of the limited time between the instance of dynamic deformation and the exposure by mining (or drilling), the rock flour remains as evidence of the recent dynamic origin of the structures. In some cases where rockburst damage is severe, it may be possible to see parts of the seismic source daylighting in an underground excavation. The majority of mine seismic events are, however, never seen. As recorded by mine seismic systems, tunnel development in deep, hard rock mines is associated with large numbers of seismic events, albeit generally small. Modern photogrammetry tools allow detail structural mapping of the tunnel walls despite the walls being covered by shotcrete soon after the photography. It is statistically impossible for such tunnels not to intersect seismic sources. One does not, however, find fresh seismic sources in the mapping.

Diamond drilling is commonly used in mines for various purposes. Mostly the core is logged geologically and geotechnically. In many cases, it would be statistically impossible for a drill hole not to have crossed one or more seismic sources. Yet, even in the most seismically active mines, one does not find discontinuities being marked as seismic sources in those logs. The purpose of this paper is to provide some historical background information and example photographs as a guide to the recognition of seismic sources in drill core.

4. CORE-RECOVERY

One of the ICDP-DSeis drilling sites is Cooke 4 mine situated 40 km southwest of Johannesburg in the Central Rand Group of the Archean Witwatersrand Basin, South Africa. The mine is located in a highly-stressed (vertical stress of ~127 MPa) remnant shaft pillar at 1000 m below the surface. Before drilling, detailed observational and high resolution monitoring studies were conducted by the SATREPS team, South Africa- Japan collaboration. The SATREPS project installed a dense network of acoustic

emission sensors (2010 - 2015). Acoustic emissions (AEs) down to Mw -5 were recorded and used to characterise both temporal and spatial evolution of mining induced fractures forming ahead and around the stope (Naoi et al., 2014; 2015a). Using AEs, Moriya et al. (2015) delineated brittle shear fractures which extend tens of meters ahead of the stope face, and are characterised by localised damage with the geometry that resembles typical Ortlepp shears.

The ICDP-DSeis team drilled into these fragile mining-induced brittle shear ruptures and host rocks using highly specialised drilling technique 'triple-tube' with a 1.5 m core barrel and metal split spoons. The tinfoil was used supplementary to maximise core and fragile rupture recovery (Mngadi et al., 2020).

The second set of core samples were recovered from the El Teniente mine from routine geological drilling. However, some of the structures were well preserved, mapped and are described in detail below. El Teniente mine is situated 80km south of Santiago in the Andes in Chile and is the world's biggest underground copper mine. The El Teniente mine exploits the porphyry copper and molybdenum deposits and lies 1880 m below surface. The porphyry copper and molybdenum deposits occur in andesites, diorites and hydrothermal breccias. These rocks surround a pipe of hydrothermal breccias commonly referred to as the 'Braden Pipe' (Pereira et al., 2003; Hormazabal et al., 2014). The copper deposit and pipe formation developed in the Pliocene, with the Braden Pipe forming the shape of an inverted cone with dimensions of 1200 m diameter at surface and ~3000 m vertical extent (Pereira et al., 2003).

5. GEOPHYSICAL BOREHOLE LOGGING AND GEOLOGICAL CORE LOGGING

The ICDP-DSeis team completed drilling full-core wire-line NQ hole, which is the smallest borehole diameter that allows downhole geophysical logging (Ogasawara et al., 2017). The core recovery was nearly 100%, even with frequent borehole breakouts. The core was "intensely fractured", characterised by rock breccia or rather several comminuted rock fragments, which made it almost impossible to orient the core in certain areas (see Figure 2). To quantify or measure the "fracture density" or the intensity of fracturing, we used the rock quality designation (RQD) index. The RQD is defined as the sum length of all recovered core samples greater than 10 cm in length (good quality) divided by the total length of the drilled core. It is expressed in terms of percentage. In our study, the RQD for the core is 67% (Table 1).

Detailed geophysical borehole logging, core scanning and geological core logging were conducted. The core recovered from the triple-tube drilling penetrated four main rock types viz. argillaceous quartzite, conglomerate 'reefs', pebbly quartzite and quartzite of Mondoer formation, Central Rand Group (Mngadi et al., 2019).

Several fractures were mapped in detail on the core and distinguished. Some of the observed fractures were drilling-induced and others form naturally from in-situ stress concentration induced by mining excavations (see Figure 3). The differences in drilling-induced and shear fractures are presented in sections 6.4 and 6.5 below. We could identify the intersection of a seismic source in the diamond drill core. In section 6, we describe the criteria used to identify seismic sources in drill core.

In addition to core logging, geophysical well logs were used to delineate fractures encountered in a borehole (Figure 3). Our result shows that the natural gamma-ray log is the most responsive or sensitive to borehole variations when correlated with the mapped shear fracture ruptures and changes in lithologies. It is followed by a bed-resolution density log, which is most responsive to lithological changes and in some cases, indicative of fractures. However, this response is generally inconsistent and not unique. Magnetic susceptibility and short-spaced density logs were the less responsive or sensitive to shear fractures, and even to lithology changes. To be noted, we could not carry out the borehole televiewer survey in the DSeis hole at Cooke 4 due to the malfunction of the recorder during the survey, and while we struggled to get a new recorder, the site was walled off. These could be some of the drawbacks of geophysical logging.

However, we performed an unrolled and rolled scan of the drill core. The International Continental Scientific Drilling Program protocol was used to conduct the scanning of the core. These were digitised. Images of fractures and lithology are presented (Figure 4). These images could clearly show fractures and different lithologies. Nonetheless, it is difficult to identify and distinguish "Ortlepp" shear fractures and drilling-induced fractures purely from these images. Also, geological features such as veins could be observed.

6. CHARACTERISTICS OF MINING INDUCED SHEAR RUPTURE SURFACES

From our insight of the internal characteristics of Ortlepp shears, and true physical observations of the core recovered at seismogenic depths in South African mines we list basic characteristics of dynamic brittle shears as one would expect to see in drill core (Table 2):

6.1. Fault gouge “rock flour”

The slip surface should be powdery such that powder remains on the thumb (the finger usually used for this highly scientific exercise). Depending on the nature of the fracture zone (some yield more and some less rock flour) and the drilling process (how much of the surface area of the fracture was disturbed and material washed away) there could be finely comminuted material left along the fracture surface, especially in depressions along the rough surface. An extreme example of rock flour from a seismic source is shown in Figure 5. An example of a shear rupture surface in the core is shown in Figure 6. See also Figure 7.

6.2. No cohesion

The drill core should be broken at the intersection, unlike some old fault surfaces that, through recrystallisation, gained cohesion strength.

6.3. Finely broken rock in the core tray.

Fine rock fragments in the core tray at the fracture would be characteristic of dynamic damage (Figure 8).

6.4. Rough at cm-scale

Unlike most joints and mining-induced extension fractures, shear rupture surfaces are not smooth on cm-scale, but rather corrugated (Figure 6, Figure 11, Figure 12, and Figure 15).

6.5. Distinguishable from extension fractures

Extension fractures may be distinguished from shear fractures based on the presence of fractographic striations referred to as plumose structure in geological texts. Figure 9 shows a case where the core fracture appears to have been induced by the drill operator, hitting the core with something like a hammer – the fractographic striations indicate that the rupture initiated at the edge of the core. Maybe the core was too long to fit in the core box. It must be noted, however, that the evolution of a shear fracture may include an initial phase of extension, in which case one may find slip striations superimposed on fractographic striations (van Aswegen, 2013, Figure 15).

6.6. Soft slickensides

The slickensides on the slip surface can be expected to be weak and rubbed off easily. Geologically old slickensides are generally strong due to recrystallization. In clay-rich fault rock, it may be as weak as the fault rock itself, but would still be distinguished from "fresh" slickensides since they would not easily be rubbed off (Figure 10).

6.7. Cross fabric

Depending on the maturity of the shear zone, one could expect a cross lineation at right angles to the slickensides. These would be the intersections of the extension fractures within the brittle shear, with the shear zone wall (Figure 10, Figure 11, Figure 12 and Figure 13).

6.8. Slickensides are consistent with stress state

A simple test to check whether the slickensides are indeed reflecting recent slip is to compare their orientation (and sense of slip if distinguishable) with the expected direction of a slip in the current stress state. For this purpose, the orientation of stress as indicated by moment tensor stress inversion in the particular volume of interest is the recommended stress orientation estimate to use.

6.9. No slickensides

A shear rupture surface can show minimal or no slickensides if the shear mechanism was dilatational (transtensional shear). This is a fairly frequent mechanism where the shear failure occurs very close to a mine opening (see van Aswegen, 2013, Figure 30), but an unlikely mechanism tens of metres away from a mine opening. Within a complex fault zone, there may, of course, be jogs that could cause a local transtensional shear as the rupture jumps across the jog, but statistically, it would be unlikely to hit such a position.

6.10. Evidence easily destroyed

It is important to examine and photograph fractures as soon as possible (Figure 14 and Figure 15). It is very easy for the comminuted rock along the surface of the fracture – the most important

evidence of dynamic failure – to get destroyed and/or washed away during core handling and cleaning. The common practice of hosing down the core before logging could destroy the evidence.

6.11. Shiny

Some authors ascribe a shiny surface as reflecting fast slip. Such surfaces have not been positively associated with shear rupture surfaces in mines, but should nevertheless be noted when observed (Figure 16).

7. DISCUSSION

In Sections 2 and 3, we clarify the terminology used to describe these dynamic brittle “Ortlepp" shear fractures and discuss the background (characteristics and the origin of these brittle shear Ortlepp fractures), respectively. In a rock mass, there are various types of discontinuities, a mechanical breakdown that weakens the rock mass strength viz. joints, bedding planes, fractures and shear zones (Ryder and Jager, 2002). In deep and high-stress mining, these discontinuities are important to identify and take precautions through various means such as support or adjusting mining direction or mining method. With the advancement in technology, many simple rock surface observations (e.g., tunnel or stope walls) to sophisticated geophysical mapping techniques are available for mapping exposed or buried discontinuities such as fractures.

In our study area, Moriya et al. (2015) used high-resolution AEs sensors around the mining stope to monitor the damage accumulation in detail at focal depths over a period of months during mining activities, with measurement sensitivity down to M_w -5. The study delineated and described these brittle shear fractures to have the geometry similar to Ortlepp shears. Mngadi et al. (2019) used the integration of datasets to reveal that the shear fracture turning point occurs in the soft strata (e.g., hangingwall weak/soft lavas), and developed the fracture model for different geotechnical zones for the similar underground environment (viz., hangingwall weak/soft lava and footwall quartzite/conglomerate). These have a serious effect on the fall of ground (FOG), seismicity, support and safety.

With these recent developments, there remains a key unresolved aspect of these brittle shear fractures – that is consistent and accepted “criteria” used to identify the seismic source in the diamond drill core. This paper sets up a criterion that may be used to identify these seismic sources in drill core

(Ogasawara et al., 2017 and 2019), and compare with existing mapping techniques that are used for shear fracture mapping, especially in deep and high-stress underground mines.

7.1. Geophysical logging and core scanning

The International Society for Rock Mechanics (ISRM) recommends several standard procedures to follow in the field for rock characterisation and analysis of rock discontinuities (ISRM, 2007). Fractures are two dimensional zones of 'anomalous' physical properties (Ryder and. Jager, 2002). For that reason, geophysical logging is commonly used for the detection and characterisation of fractures, and to measure in situ properties adjacent to a borehole (Keys and Sullivan, 1979). There are several advantages of geophysical well logs: consistent one-dimensional profile of rock properties; in situ measurements of rock properties; and independent measurements of rock properties.

In some mines, particularly gold and platinum mines, the ground penetrating radar (GPR) is used on a semi-routine or need basis to delineate fractures in the hangingwall, ahead of the stope face and "fracture intensity" in support pillars - before and after pre-conditioning (Kgarume et al., 2019). Challenges relating to underground GPR applications include logistics of data acquisition; in-mine safety requirements, data processing turn-around time, integration of GPR visualisation and interpretation with mine plans (Kgarume et al., 2019). Also, photogrammetry and LiDAR have become routine supplementary approaches for characterisation of rock discontinuities in underground excavations such as tunnels (Hua et al., 2011; Lato and Vöge, 2012).

We conducted geophysical borehole logging and core scanning. The recovered core samples were "intensely fractured" and therefore, idealised geophysical log responses (or anomalies) associated with individual shear fractures were difficult to resolve. In the study, the natural gamma-ray log was the most sensitive to changes in lithologies. These high anomalies could be correlated mostly to conglomerate rock types and, to a lesser degree, to individual shear fracture ruptures. The bed-resolution density log showed low density contrast on quartzite and pebbly quartzite, compared to high density on conglomerate rock types. Laboratory measurements show that argillaceous rocks and conglomerate have slightly higher density values compared to quartzite and pebbly quartzite (Mngadi, 2015). This agrees with the observed geophysical well log results, and true density values which may be extracted from laboratory experiments (Table 3). In general, the geophysical well log responses to shear fractures were generally inconsistent. In very few instances, the geophysical anomaly could be

correlated with the mapped or observed shear fracture on the core. Even in those cases, the anomaly is not unique. This is contrary to the acoustic emission method, which could delineate the shear fractures and their spatial and temporal evolution (Moriya et al., 2015; Mngadi et al., 2019).

For better resolution and fracture identification, the borehole wall imaging technique is one of the most effective methods for detecting fractures in the borehole. This method allows the intersection of fractures with the borehole to be "seen" by providing photographs of the borehole wall (Paillet et al., 1990). Further, a modern digital borehole scanner offers higher resolution and real colour images of a borehole wall. This enables identification of fracture, mineralisation, fault gouge and alteration (Cohen, 1996). The most commonly used acoustic imaging method for fracture detection and characterisation is the borehole televiewer (BHTV). Nonetheless, there are some challenges associated with borehole wall imaging methods: cameras require clear borehole fluids; commonly produce oblique borehole images; and lighting sources often produce shadows (Paillet et al., 1990). The DSeis team attempted to conduct the borehole televiewer survey. However, due to the malfunction of the recorder during the survey, the survey could not be completed. While the team was trying to get a new recorder, the site was walled off. This is evidence of the risk associated with the malfunction of the equipment during a critical time, which is a serious drawback. However, we could conduct “unrolled and rolled” scan images of the drill core. Fracture and lithology images could be evidently “seen” with some of the detailed geological features such as veins.

The clearest, obvious and most direct method to characterise in-situ fractures is examination of the actual core. Cores with “intense fracturing” are commonly drilled and recovered through conventional single or double barrel rotary drilling techniques. These conventional drilling methods are not suitable for “densely fractured” core in a hard rock environment, such as in our study area. This is because the amount of core recovered is often inversely proportional to the “density of the fractures” and the amount of weathering related to fractures. Unique to our study is that we target “densely fractured” rock mass. Therefore, a careful unconventional drilling approach was employed – “triple tube” drilling with stationary inner metal split spoon and supplemented by kitchen foil to ensure optimal core recovery. The use of the triple-tube drilling method to recover "densely fractured” core and examination can be slow and hence more expensive (Table 4). However, with the new proposed seismic source identification criteria, the core examination should be quick and straightforward.

Examination of recovered core samples, geophysical borehole logging and borehole wall imaging all provide a small volumetric sample of the fracture, especially when core diameters are only a few centimeters (in our study the diameter was ~42 mm) (Table 4). In general, these methods may not necessarily represent the whole adjacent rock mass or fracture zone. Even with these limitations, cores samples offer critical “direct” evidence of the host rocks and fracture properties. In addition, core examination allows other fundamental scientific questions to be addressed – such as how these shear fractures form and why some result in damaging seismic events or aseismic rockfall (FOG)? Therefore, we suggest that the use of the core is the most critical and effective method. There will be further gains when the core description is correlated with geophysical well logs from the borehole, especially in cases of suspected core loss or intensely fractured rock mass. In regions of core losses, geophysical well logs may be used to estimate fracture properties. This integrated approach of core examination and geophysical logs provides information on fractures that are not accessible when individual methods are applied independently.

7.2. Criteria to detect mining-induced seismic sources in borehole core

With over a century-long history in mining, surprisingly, not much has been done to develop a uniform and consistent “criteria” that would help mining practitioners identify seismic sources in cores, which could be used to mitigate the risk associated with large shear fractures such as falls of ground (FOG), rockbursts and seismicity. Using the triple-tube core barrel drilling technique (Ogasawara et al., 2019; Mngadi et al., 2020), a series of detailed observations of newly formed shear fractures were conducted for the Cooke 4 core, despite minor core loss in some areas (~67% RQD). These were supplemented by high-resolution core photographs, and comprehensive descriptions of newly-formed shear fractures were produced (Section 6). These were used to establish new 'criteria' that may be used to identify and distinguish freshly-formed shear fractures from drilling-induced fractures, old joints and pre-existing geological discontinuities in core samples (Section 6). Using these new set of rules or criteria, geologists and various practitioners should be able to recognise dynamic shear rupture surfaces. A critical feature of a shear rupture zone is the presence of the fault gouge “rock flour” and rock breccia (comminuted rock fragments), while detailed study of the surface geometry of the shear fracture will often reveal soft slickensides and cross fabric. The existence of the rock flour and rock breccia at the fracture location in the core tray may be an indication of a shear rupture zone. This proves

that one can see newly formed shear fractures in the core, while conventional drilling methods are unlikely to preserve such detail.

To achieve this, in addition, a clear protocol and extreme care during core transportation from drill site (often underground) to the core shed (usually on surface) must be in place. The vibrations during the transportation of the core boxes could shake off (or shear) the fine material from the fracture surfaces. Also, we do not recommend washing or hosing of the core before examination. The core logging should be conducted immediately after drilling with detailed high resolution (down to 0.2 mm or improved) photographic records and good lighting, preferably not direct sunlight if a flash is used.

7.3. Formation of mining-induced shear fractures

This study examined the "true physical nature" of recently formed brittle shear fractures recovered from focal depths, which are characterised by rock flour, comminuted rock fragments (rock breccia), rough rupture surfaces (cm-scale), with often soft slickensides. Analysis of this unprecedented, detailed evidence provided us with insight into the formation, physics and mechanics of the mining-induced earthquakes. For instance, in our study we observed soft slickensides that provided evidence that shear displacement occurred along the rupture zone, and that rock failure may have occurred tens of metres ahead of the mining excavation (van Aswegen, 2013). This agrees with the acoustic emissions study conducted by Moriya et al. (2015) that delineated brittle shear fractures forming tens of metres ahead of the stope face, resembling typical Ortlepp shears. In some cases, shear rupture surfaces had no slickensides, which suggests that the shear mechanism was dilatational or transtensional, and that shear failure may have occurred close to the stope face (van Aswegen, 2013). Also, this could be evidence that brittle shear fractures nucleate and grow by interaction among dilating cracks that are parallel to maximum compressive stress in a self-organising manner, which agrees with observations by Reches and Lockner (1994).

Further, the roughness of the rupture surface may indicate dilatational mechanisms during shear displacement that may influence the initial direction of slip (ISRM, 1978; Reches and Lockner, 1994). We observed that the rupture surface of our recovered shear fractures were corrugated, which may mean that the shear displacement was largely controlled by dilatational mechanism. Also, the rupture surface roughness contribute to initial shear strength, and it declines with filling thickness (e.g., rock

flour or fault gouge). Reches and Dewers (2005) concluded that the rock flour is mostly generated through stress intensity and volumetric strain (Reches and Dewers, 2005; van Aswegen, 2008).

Also, a considerable amount of gouge is generated by the wear process (Mngadi et al., 2020). Both these interpretations agree with the view that faults propagate from the nucleation zone by in-plane growth as mixed-mode II and mode III fracture (Lockner et al., 1991). In addition, Mngadi et al. (2021) suggest that the presence of "rock flour" may influence fault rupture propagation processes along underground brittle shear zones. The presence of "rock flour" in the rupture zone and the rate of generation rock flour, may cause strengthening of the fault (or brittle shear fracture), and temporarily prevent the unstable rupture propagation weakening process at low to high slip velocities (~1.0 – 100 mm/s). However, if there is initially very little to no 'rock flour' during rupture propagation, fault frictional strength will weaken more quickly.

8. CONCLUSIONS

In this paper, we developed and discussed the criteria that could be used to identify seismic sources in drill core. We document a list of criteria for recognising seismic source intersections in drill core. Having studied the cores and presented extensive photographs as evidence, geologists and various practitioners should be able to recognise dynamic shear rupture surfaces. The most important aspect of a shear rupture surface is the presence of finely comminuted rock fragments and rock flour, with soft slickensides in many cases. A cross fabric is also present in many cases. The presence of fine rock fragments and rock flour in the core tray at the fracture location is also characteristic. The preservation of evidence (rock flour, soft slickensides) along the fracture surface is important, requiring:

- The best available drilling technology (e.g., a 1.5 m triple-tube core-barrel with a split-spoon stainless-steel liner).
- Extreme care during core transportation. The vibrations during the transportation of the core boxes from the drill site at depths to the core shed usually on the surface could shake off (or shear) the fine material from the fracture surfaces.
- Preferably, no washing/hosing down of the core, and core logging should be conducted immediately after drilling, with detailed high resolution, down to 0.2 mm or better. The photographs should be taken in good light, but not in direct sunlight. If a flash is used, it should be strongly diffused.

9. ACKNOWLEDGMENTS

This work would not have been possible without access to the Site 7, Cooke 4 shaft drill core. The drilling project was part of the ICDP and JSPS Core-to-Core program, JSPS-NRF bilateral program sponsored drilling project into seismic sources in the South African gold mines. The authors thank the School of Geosciences at the University of the Witwatersrand, Johannesburg, South Africa, Center of Excellence for Integrated Mineral and Energy Resources Analysis (CIMERA), The Council for Scientific and Industrial Research (CSIR), Prof Hiroshi Ogasawara of the Rutsemeiken University, Kyoto, Japan, Tony A. Ward from Sibanye gold limited and Yasuo Yabe from the Graduate School of Science, Tohoku University, Sendai, Japan whom were responsible for Cooke 4 ICDP drilling, Lesedi Drilling (Pty) Ltd. (for drilling after mine closure was very tough). We also thank the management of the New Mine Level, El Teniente mine, for permission to view and photograph core from several NML boreholes.

10. REFERENCES

Arellano, J. (2012). Copper Mining and its impact on Chile economic development. Integration & Trade Journal, 16, 35.

Cohen, A. (1996). Hydrogeologic Characterization of Fractured Rock Formations: A Guide for Groundwater Remediators. The report in preparation, Lawrence Berkeley Laboratory, Berkeley, Calif.

Durrheim, R.J., Ogasawara, H., Nakatani, M., Yabe, Y., Naoi, M., Moriya, H., Cichowicz, A., Takashi Satoh, T., 7 Hironori Kawakata, H., Milev, A., Kgarume, T., Brink, V.Z., Ward, A.K., Luiz Ribeiro, L., Manzi, M.S.D., Mngadi, S. and the SATREPS Team. (2017). Observational Studies in South African Mines to Mitigate Seismic Risks: Challenges and Achievements. ISRM AfriRock - Rock Mechanics for Africa, 175-188.

Hua, X., Zhanga, Z., Duana, Y., Zhanga, Y., Zhua, J. and Long, H. (2011). International Archives of the Photogrammetry, Remote Sensing and Spatial Information Sciences, XXXVIII-5/W12

Hormazabal, E., Pereira, J., Barindelli, G. and Alvarez, R. (2014). Geomechanical evaluation of large excavations at the New Level Mine - El Teniente. Caving 2014, Santiago, Chile.

ISRM, (1978). Suggested Methods for the Quantitative Description of Discontinuities in Rock Masses .The International Society for Rock Mechanics on Commission for Standardisation of Laboratory and field tests.

Keys, W. S., and Sullivan, J. K. (1979). Role of borehole geophysics in defining the physical characteristics of the Raft River geothermal reservoir, Idaho. Geophysics, 44, 1116–1141.

Kgarume, T., van Schoor, M., and Nontso, Z. (2019). The use of 3D ground penetrating radar to mitigate the risk associated with falls of ground in Bushveld Complex platinum mines. The Southern African Insitute of Mining and Metallurgy. 119, 973-982.http://dx.doi.org/10.17159/2411-9717/603/2019.Lacy, L.L. and Smith. X. (1989). Fracture azimuth and geometry determinations. Pp. 357–375 in SPE Monograph 12: Recent Advances in Hydraulic Fracturing. Richardson, Tex.: Society of Petroleum Engineers.

Lato, M.J. and Vöge, L.M. (2012). Automated mapping of rock discontinuities in 3D LiDAR and photogrammetry models. International Journal of Rock Mechanics and Mining Sciences, 54, 150-158. DOI: 10.1016/j.ijrmms.2012.06.003

Lockner, D.A., Byerlee, J.D., Kuksenko, V., Ponomarev, A. and Sidrin, (1991). A. Quasi-static fault growth and shear fracture energy in granite. Nature, 350, 39-42.

Mngadi, S.B, Tsutsumi, A., Onoe, Y., Manzi, M.S.D., Durrheim, R.J., Yabe, Y., Ogasawara, H., Kaneki, S., Wechsler, N., Ward, A.K., Naoi, M., Moriya, H., Nakatani, M. and the DSeis team. (2020). The effect of gouge particles (“rock flour”) on rupture propagation along brittle shear fractures in deep and high-stress mines. International Journal of Rock Mechanics and Mining Sciences, 137, 104454. https://doi.org/10.1016/j.ijrmms.2020.104454.

Mngadi, S.B., Durrheim, R.J., Manzi, M.S.D., Ogasawara, H., Yabe, Y., Yilmaz, H., Wechsler, N., Van Aswegen, G., Roberts, D., Ward, A.K., Naoi, M., Moriya, H., Ishida, A., SATREPS team and ICDP DSeis team. (2019). Integration of underground mapping, petrology, and high-resolution microseismicity analysis to characterise weak geotechnical zones in deep South African gold mines. International Journal of Rock Mechanics and Mining Sciences, 114, 79–91. https://doi.org/10.1016/j.ijrmms.2018.10.003.

Mngadi, S.B., Durrheim, R.J., Manzi, M.S.D., Yabe, Y., Wechsler, N., Ogasawara, H., van Aswegen, G., Ward, A., Morema, S. and ICDP DSeis team. (2018). An overview of endeavours to recover drill core from fragile mining-induced fractures at Cooke 4 mine, South Africa and the analysis of gouge from experimentally-induced fractures. Abstract SSJ Fall Meeting 2018, Fukushima, 9 -11 Oct 2018.

Mngadi, S.B. (2015). Integrated Petrographic, Geomechanical and Seismological Studies of Rockmass Behaviour during the Extraction of the Cooke 4 shaft pillar. MSc thesis. The University of the Witwatersrand.

Mori, J. and Ellsworth, W. (2013). Active fault and earthquakes. Unravelling the Workings of Planet Earth – Science Plan for 2014-2019. International Continental Scientific Drilling Program, GFZ, pp. 24-31.

Moriya, H., Naoi M., Nakatani, M., van Aswegen, G., Murakami O., Kgarume T., Ward, A.K., Durrheim, R.J., Philipp, J., Yabe, Y., Kawakata, H and Ogasawara, H. (2015). Delineation of large localized damage structures forming ahead of an active mining front by using advanced acoustic emission mapping techniques. International Journal of Rock Mechanics and Mining Sciences 79, 157–165.

Naoi, M., Nakatani, M., Horiuchi, S., Yabe, Y., Philipp, J., Kgarume, T., Morema, G., Khambule, S., Masakale, T., Ribeiro, L., Miyakawa, K., Watanabe, A., Otsuki, K., Moriya, H., Murakami, O., Kawakata, H., Yoshimitsu, N., Ward, A.K, Durrheim, R. and Ogasawara, H. (2014). Frequency–

magnitude distribution of -3.7 ≤ MW ≤ 1 mining-induced earthquakes around a mining front and b value invariance with post-blast time. Pure and Applied Geophysics, 171, 2665-2684.

Naoi, M., Nakatani, M., Kgarume, T., Khambule, S., Masakale, T., Ribeiro, L., Philipp, J., Horiuchi, S., Otsuki, K., Miyakawa, K., Watanabe, A., Moriya, H., Murakami, O., Yabe, Y., Kawakata, H., Yoshimitsu, N., Ward, A.K., Durrheim, R.J. and Ogasawara, H. (2015). Quasi-static slip patch growth to 20 m on a geological fault inferred from acoustic emissions in a South African gold mine. Journal of Geophysical Research: Solid Earth, 120, 1692-1707. https://doi.org/10.1002/2014JB011165.

Ogasawara, H., Liebenberg, B., Rickenbacher, M., Ziegler, M., Esterhuizen, V.H., Onstott, T.C., Durrheim, R.J., Manzi, M.S.D., Mngadi, S.B., Yabe, Y., Ogasawara, H., Kaneki, S., Cason, E., Vermeuren, J.G., van Heerden, E., Wiersberg, T., Zimmer, M., Kujawa, C., Conze, R., van Aswegen, G., Wechsler, N., Ward, A.K., Enslin, S., Tau, S., Bucibo, M.S. and the DSeis Team. (2019) status report: Drilling into seismogenic zones of M2.0–M5.5 earthquakes in South African gold mines (DSeis project). Proceedings of the 9th International Conference on Deep and High Stress Mining. The Southern African Institute of Mining and Metallurgy, Johannesburg, pp. 375-384. https://doi.org/10.36487/ACG_rep/1952_28_Ogasawara.

Ogasawara, H. (2019). Operational Report about Drilling into Seismogenic zones of M2.0-5-5 earthquakes in South African gold mines (DSeis), ICDP Operational Reports, in preparation.

Ogasawara, H Liebenberg, B., Rickenbacher, M., Ziegler, M., Esterhuizen, v. H., Onstott, T.C., Durrheim, R.J., Manzi, M.S.D., Mngadi, S., Yabe, Y., Ogasawara, H.Y., Kaneki, S., Cason, E., Vermeuren, J.G., van Heerden, E., Wiersberg, T., Zimmer, M., Kujawa, C., Ronald Conze, R., van Aswegen, G., Wechsler, N., Ward, A.K., Stephanie Enslin, S., Tau, S., Bucibo, M.S., and the DSeis Team. (2017). Drilling into Seismogenic Zones of M2.0 – M5.5 earthquakes from Deep South African Gold Mines (DSeis): Establishment of Research Sites. ISRM AfriRock - Rock Mechanics for Africa, 3-5 October, Cape Town, South Africa.

Ortlepp, W.D. 1997. Rock Fracture and Rockbursts - an illustrative study. Monograph Series M9, SAIMM, Johannesburg, South Africa.

Paillet, F. L., Barton, C., Luthi, S., Rambow, F. and Zemanek. J. (1990). Borehole Imaging. SPWLA Reprint Series. Houston, Tex.: Society of Professional Well Log Analysts.

Pereira, J, Russo, A. and Karzulovic, A. (2003). 'Geomechanical Properties of the Braden Breccias at El Teniente Mine, Chile', Soil and Rock America 2003. 12th Panamerican Conference on Soil Mechanics and Geotechnical Engineering. 39th U.S. Rock Mechanics Symposium. Cambridge, EEUU. 22-26 June 2003, pp 723-727.

Reches, Z. and Dewers, T. A., 2005. Gouge formation by dynamic pulverization. Earth and Planetary Science Letters, 235, 361–374.

Reches, Z. and Lockner, D. (1994). Nucleation and growth of faults in brittle rocks. Journal of Geophysical Research, 99, 159-173.

Ryder J.A. and Jager A.J. (2002). A Textbook on Rock Mechanics for Tabular Hard Rock Mines. Braamfontein, Johannesburg: SIMRAC.

Tucker, R.F., Viljoen, R.P. and Viljoen, M.J. (2016). A Review of the Witwatersrand Basin - The World's Greatest Goldfield. Episodes, 39, 104-133. https://doi.org/10.18814/epiiugs/2016/v39i2/95771.

Ulusay, R. (2007). The ISRM Suggested Methods for Rock Characterization, Testing and Monitoring: 2007 - 2014.

van Aswegen, G. (2007). Ortlepp Shears – dynamic brittle shears of South African gold mines. In: Potvin, Y (Ed.) 1st Southern Hemisphere International Rock Mechanics Symposium, 16-19 September, Perth, Western Australia. pp. 111 – 120.

van Aswegen, G. (2013). Forensic rock mechanics, Ortlepp shears and other mining-induced structures. Key-note lecture. In: Malovichko, A. and Malovichko, D (eds.), 8th International Symposium on Rockburst and Seismicity in Mines (RaSiM8). 2013 GS RAS & MI UB RAS, Obninsk-Perm, ISBN 978-5-903258-28-4, pp 11-29.

Wechsler, N., Van Aswegen, G., Yabe, Y., Mngadi, S., Kamhaji, L., Ward, A., Morema, S., Durrheim, R., Ogasawara, H. and ICDP DSeis team. (2018). Recovery of ruptures from the seismogenic zone at Cooke 4 mine (DSeis - ICDP scientific drilling project in the South-African gold mines). Abstract EGU 2018-9721, Vienna, 12 April 2018.

Wills, P.B., De Martini, D.C. Vinegar, H.J. and Shlyapobersky. J. (1992). Active and passive imaging of hydraulic fractures. Geophysics: The Leading Edge of Exploration, 11, 15–23.

List of Figures

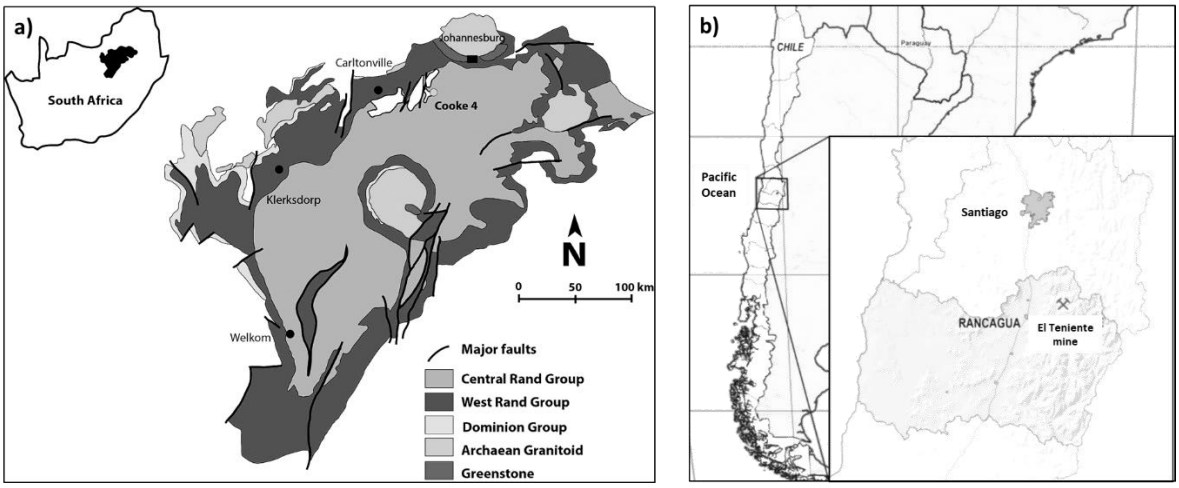


Figure 1.a) The Cooke 4 shaft is located 40km southwest of Johannesburg in the Central Rand Group, Witwatersrand Basin, South Africa (modified from Dankert and Hein, 2010). b) The El Teniente mine is situated in the central part of Chile, 80km south of Santiago and east of Rancagua cities (modified from Hormazabal et al., 2014).

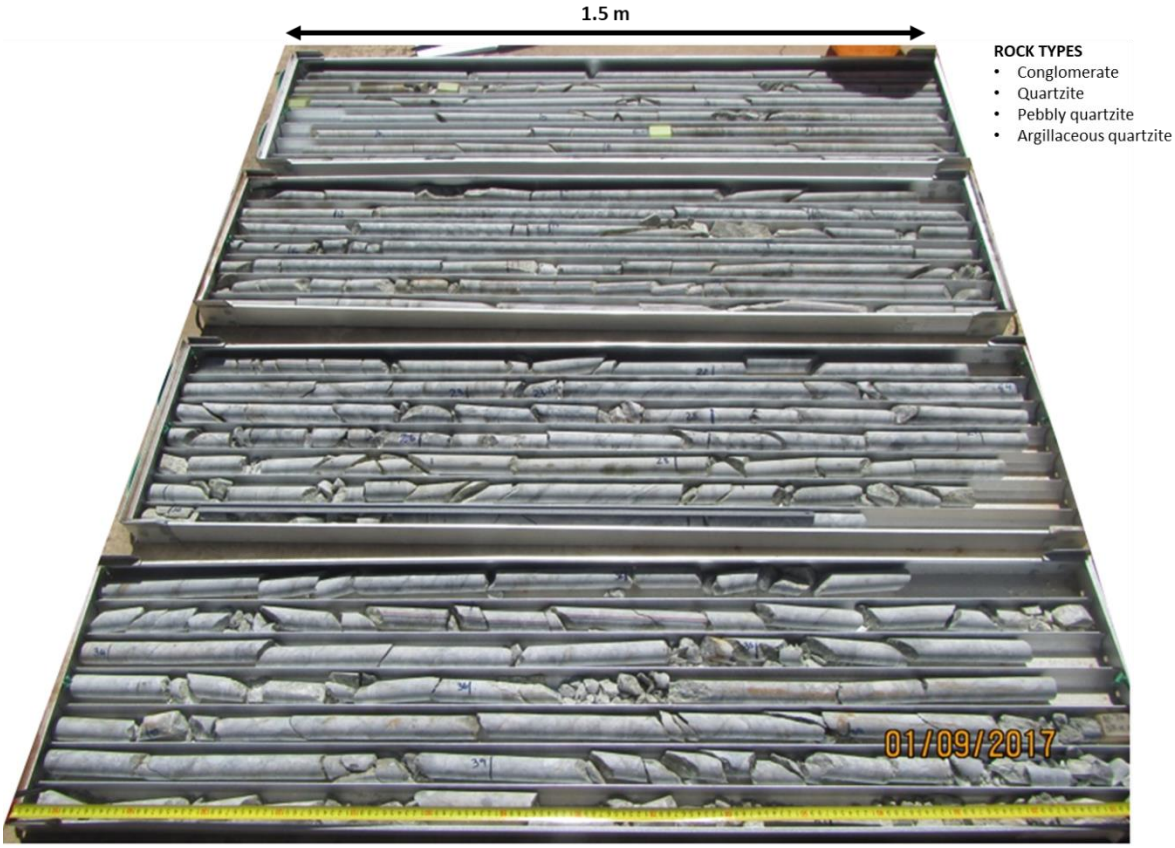


Figure 2. Highly fractured drill core recovered from Cooke 4 mine, 1000 m-1200 m deep.

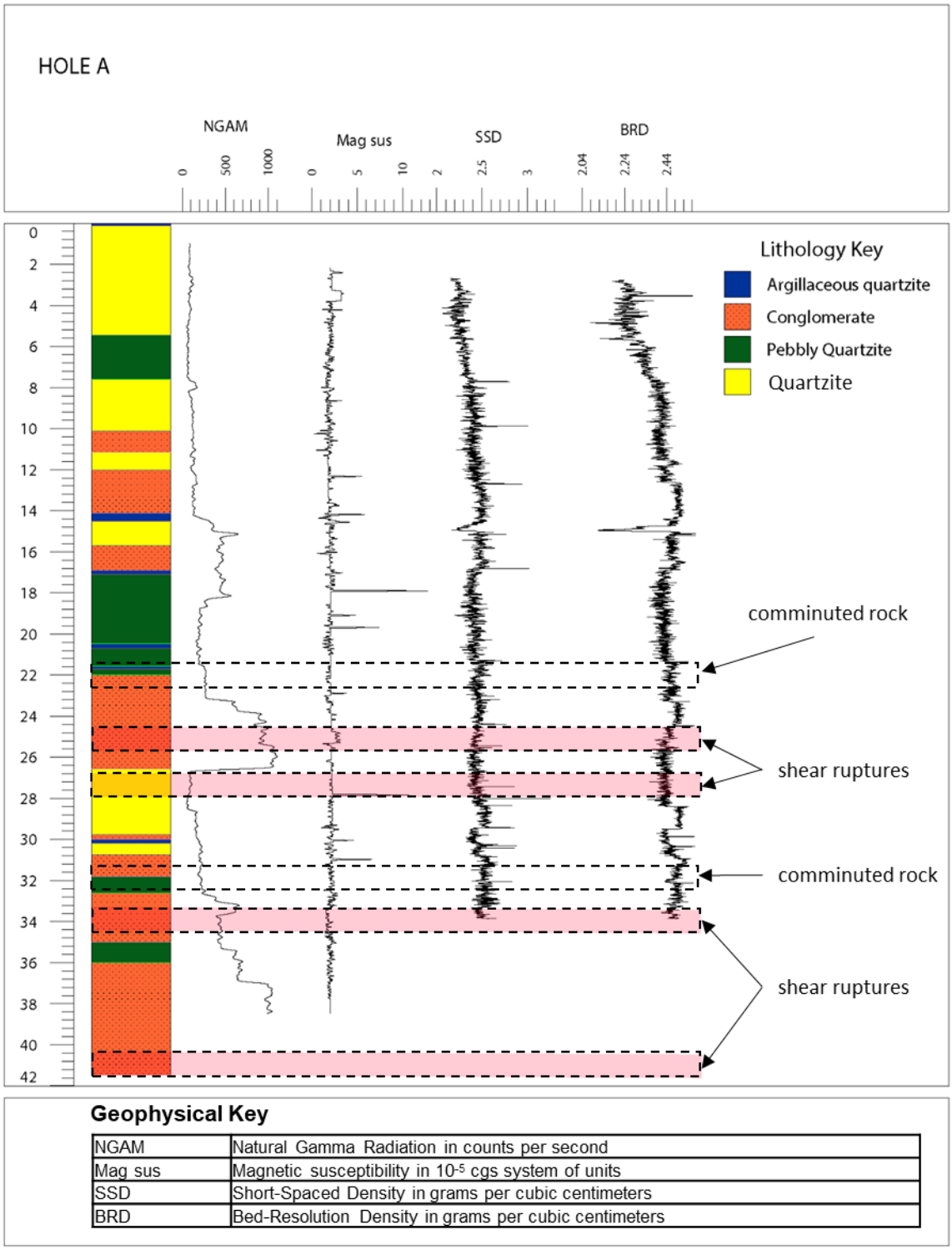


Figure 3: Recovered drill core was mapped - geological, structural and geophysical, with a detailed analysis of mining-induced ruptures or shear fractures (Modified from Mngadi et al., 2020).

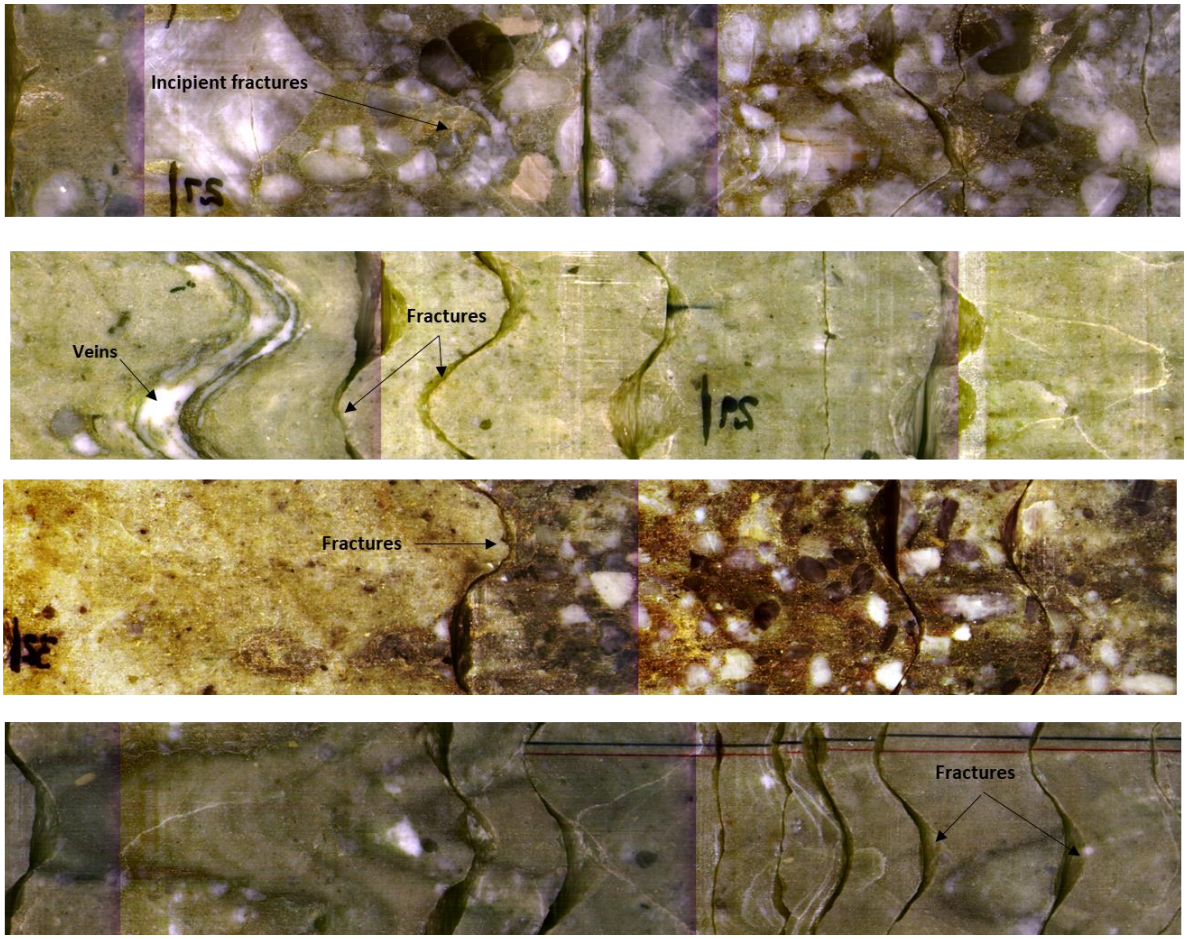


Figure 4: Unrolled and rolled scans of the drill core. Several fractures, veins, pebbles and different lithology can be identified.



Figure 5: A handful of rock flour from a major Ortlepp shear in a South African gold mine. The removal of the shot glass left a negative angle of repose similar to what you get in cake flour - if your mother allowed you to play games on the kitchen table while baking.



Figure 6: Rock flour preserved on a shear rupture surface at 34 m, Site 7, Cooke 4 Shaft.



Figure 7. Rough shear rupture surface at 7m, borehole SG0573, El Teniente NML. Note the powder easily rubbed off the fracture surface.



Figure 8: Comminuted rock in the core tray at a shear rupture intersection - at 32 m, Site 7, Cooke 4 Shaft, DSEIS project.



Figure 9: Fractographic striations along a fracture at approximately 170 m, borehole S6:0690, El Teniente NML. The initiation of the rupture was at the edge of the core, suggesting the core was broken by an impact (hammer?), possibly to make the core fit into the core box.



Figure 10: Relatively soft, but geologically old slickensides in the anhydrite filling of a smooth fault ~44 m, SG569, El Teniente NML. The scratch was done by a knife.



Figure 11: Archetypical Ortlepp shear (Ortlepp, 1997, p. 43).



Figure 12: Shear fracture with finely comminuted rock particles clinging to the rupture surface. Note the significant undulation/roughness of the surface and the cross fabric nearly orthogonal to the slickensides. Cooke 4 shaft, Site 7 at 21.6 m.



Figure 13. Slickensides and a cross fabric along an apparently fresh shear fracture. In this case, the fracture developed along a pre-existing vein in CMET. Borehole SG0573, NML, at approximately 106.5 m.



Figure 14: Apparently fresh slickensides with a prominent orthogonal cross fabric. At 17 m, SG0573, NML, El Teniente.

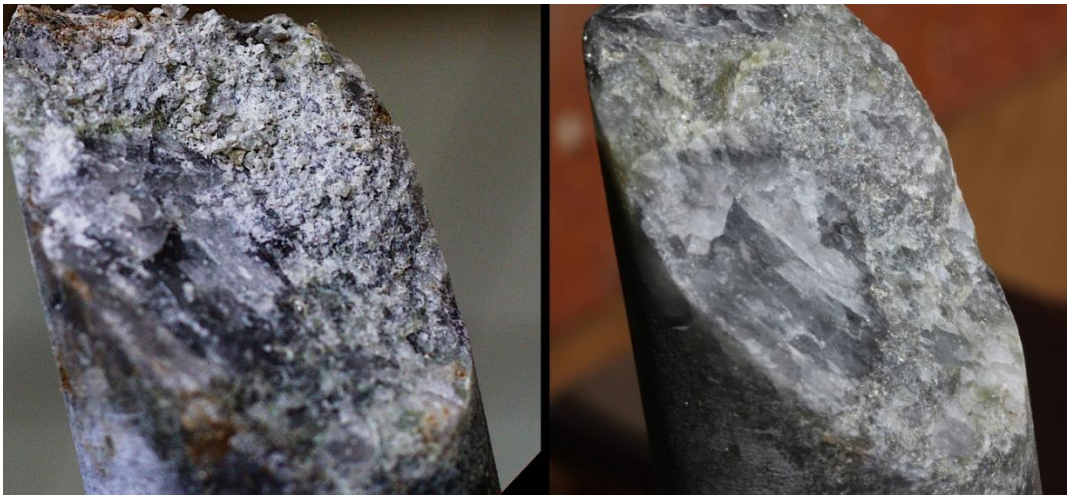


Figure 15: Shear fracture at Site 7, Cooke 4 Shaft at 25.2 m. The photograph on the left was taken in August 2017 when the core was delivered from underground to the office of the Rock Mechanics Department. Note how comminuted rock clings to the surface at the top. The photograph on the right was taken in April 2019 at the CSIR Mining core shed (Johannesburg) after core logging and other analyses.



Figure 16: Similar to Figure 11, shear fracture at 39.5m.



Figure 17: Shiny slickensides of unclear age at 154 m, SG0573, NML, El Teniente.

List of Tables

Table 1: The rock quality designation (RQD) for the drilled core from Cooke 4 mine, expressed in terms of percentage for two sections of 3 m.

Box	Slot	Section	Section Length (cm)	No. of core pieces > 10 cm	Length of core pieces > 10 cm (cm)	RQD (%)	Slot Pieces	Scanned	Match	Comments
1	1	1	152	6	134	71	8	Yes	yes	
	2	2	150	5	81		14	Yes	no	Piece 3 is broken and piece 9 is also broken
	3	1	152	5	131	81	7	Yes	no	Piece 5 is broken
	4	2	140	5	106		9	Yes	no	Piece 7 is broken
	5	1	143	5	130	91	6	Yes	no	
	6	2	148	6	134		8	Yes	yes	
	7	1	159	7	154	97	8	Yes	no	
2	1	2	132	6	128		6	Yes	no	
	2	1	152	5	139	78	7	Yes	yes	
	3	2	143	4	90		10	Yes	no	Piece 6-10 are broken
	4	1	153	5	118	74	10	Yes	no	Piece 3-6 are broken
	5	2	150	5	105		11	Yes	no	Piece 11 is broken
	6	1	147	2	46	55	19	Yes	no	
	7	2	148	7	118		8	Yes	no	
3	1	1	145	5	96	70	15	Yes	no	
	2	2	153	5	112		10	Yes	no	
	3	1	155	7	102	50	14	Yes	no	
	4	2	148	3	50		18	Yes	no	
	5	1	150	5	86	44	14	Yes	no	
	6	2	142	2	43		16	Yes	no	
	7	1	123	3	64	63	13	Yes	no	
4	1	2	124	5	92		11	Yes	no	Piece 7 is broken
	2	1	152	5	60	61	18	Yes	no	
	3	2	142	7	118		9	Yes	no	
	4	1	147	6	93	66	11	Yes	no	Piece 2,8 are broken
	5	2	151	6	104		14	Yes	no	
	6	1	155	3	60	35	14	Yes	no	Piece 4, 14 are broken
	7	2	155	4	50,00		13	Yes	no	Piece 13 is broken

Table 2: Summary of the criteria or expected checklist in drill core.

Internal characteristics of Ortlepp shears	
1.	Fault gouge “rock flour”
2.	No cohesion
3.	Finely broken rock in the core tray.
4.	Rough at cm-scale
5.	Distinguishable from extension fractures.
6.	Soft slickensides
7.	Shiny surface as reflecting fast slip

Table 3: Measured density and compression and shear wave seismic velocities.

Rock type	**Density (g/cm^3)**	**P-wave velocity (m/s)**	**S-wave velocity (m/s)**
Argillaceous quartzite	2.78	-	-
Pebbly quartzite	2.69	5631.58	2899.73
Conglomerate	2.74	5638.30	3430.42
Quartzite	2.69	5253.73	2901.10
Argillaceous quartzite	2.76	5711.23	3316.77
Pebbly quartzite	2.69	-	-
Conglomerate	2.69	5313.43	2717.56
Quartzite	2.68	5645.50	3430.87

Table 4: Methods of identifying shear fractures (seismic source) in a drill core in a sequence of (a) relative accessibility, (b) relative costs; (c) relevance and (d) interpretability (modified from Ryder and Jager, 2002).

	Underground mapping	**Geophysical well logging and core scanning**	**New criteria – identifying seismic source intersections in drill core**
Specimen size	Unlimited	Borehole size (~42 mm diameter)	~ 42 mm (diameter)
Setup difficulty	Low	Moderate	Moderate
Degree of Control	Low	Low	High
Measurement accuracy	Moderate and restricted	Moderate	Very high
Relative costs	Moderate	Expensive	Expensive
Relevance	High	Moderate	High
Interpretability	Difficult	Moderate to difficult	Easy